

# Sheffield Hallam University

*Imaging the distribution of agrochemicals in plants by MALDI-MSI.*

ANDERSON, David Michael Germaine.

Available from the Sheffield Hallam University Research Archive (SHURA) at:

<http://shura.shu.ac.uk/19276/>

## A Sheffield Hallam University thesis

This thesis is protected by copyright which belongs to the author.

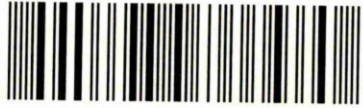
The content must not be changed in any way or sold commercially in any format or medium without the formal permission of the author.

When referring to this work, full bibliographic details including the author, title, awarding institution and date of the thesis must be given.

Please visit <http://shura.shu.ac.uk/19276/> and <http://shura.shu.ac.uk/information.html> for further details about copyright and re-use permissions.

Sheffield City Campus  
Sheffield S1 1WB

101 930 646 7



**REFERENCE**

ProQuest Number: 10694156

All rights reserved

INFORMATION TO ALL USERS

The quality of this reproduction is dependent upon the quality of the copy submitted.

In the unlikely event that the author did not send a complete manuscript and there are missing pages, these will be noted. Also, if material had to be removed, a note will indicate the deletion.



ProQuest 10694156

Published by ProQuest LLC (2017). Copyright of the Dissertation is held by the Author.

All rights reserved.

This work is protected against unauthorized copying under Title 17, United States Code  
Microform Edition © ProQuest LLC.

ProQuest LLC.  
789 East Eisenhower Parkway  
P.O. Box 1346  
Ann Arbor, MI 48106 – 1346



*Sheffield Hallam University*

# Imaging the Distribution of Agrochemicals in Plants by MALDI-MSI

**David Michael Germaine Anderson**

**BSc Hons**

**A thesis submitted in partial fulfilment of the requirement of  
Sheffield Hallam University  
for the degree of Doctor of Philosophy**

February 2009

Collaborating Organisation

Syngenta (Jealotts Hill International Research Station, Jealotts Hill, Bracknell)

# Contents

<b>1.0 ABSTRACT</b>	<b>6</b>
<b>CHAPTER ONE: TECHNIQUES FOR THE DETERMINATION OF AGROCHEMICALS DISTRIBUTION IN PLANTS</b>	<b>9</b>
<b>1.1 INTRODUCTION</b>	<b>10</b>
<b>1.2 METHODS FOR DETECTING TRANSLOCATION</b>	<b>12</b>
1.2.1 <i>Fluorescence microscopy</i>	12
1.2.2 <i>Autoradiography</i>	17
1.2.3 <i>Secondary ion mass spectrometry (SIMS)</i>	22
<b>1.3 CURRENT APPLICATIONS OF MALDI IMAGING</b>	<b>24</b>
1.3.1 <i>Introduction</i>	24
1.3.2 <i>Lasers for MALDI-MSI</i>	26
1.3.3 <i>Stigmatic ion optics for high-resolution MALDI-MSI.</i>	29
1.3.4 <i>Desorption electrospray ionisation (DESI) imaging</i>	32
1.3.5 <i>Whole body MALDI imaging</i>	34
<b>1.4 MASS SPECTROMETRY FOR THE ANALYSIS OF PLANT TISSUE</b>	<b>41</b>
<b>1.5.1 ION FORMATION MECHANISMS IN UV-MALDI</b>	<b>51</b>
1.5.2 <i>Similar to Primary Ion Formation a Number of Mechanisms have been Proposed for Secondary Ion Formation</i>	55
(ii) <i>Proton Transfer</i>	55
1.6 <i>Suppression effects</i>	56
<b>1.6 CONCLUSIONS</b>	<b>57</b>
<b>1.7 REFERENCES</b>	<b>58</b>
<b>CHAPTER TWO: DETECTION OF AGROCHEMICALS ON LEAF</b>	<b>68</b>
<b>2.1 INTRODUCTION</b>	<b>69</b>
<b>2.2 METHODS</b>	<b>71</b>
2.2.1 <i>Conventional MALDI-MS analysis</i>	71
2.2.2 <i>Indirect MALDI imaging analysis of azoxystrobin from leaf surface</i>	72

2.2.3 Absorption of mesotrione using cell stripping and direct analysis of leaf (matrix sinapinic acid)	73
2.2.4 Comparison of 9-aminoacridine and sinapinic acid and the effect of gold sputter coating.	74
2.2.5 Direct MALDI imaging analysis of mesotrione on plant tissue - examination of the absorption of mesotrione using cell stripping	75
2.2.6 Direct MALDI imaging analysis of mesotrione in leaf veins after foliar absorption	76
2.2.7 Effect of laser fluence for the detection of mesotrione	77
2.2.8 Assessment of suppression effects on the detection of mesotrione using plant extract	78
<b>2.3 RESULTS</b>	<b>80</b>
2.3.1 Mesotrione spot samples	80
2.3.1.1 Azoxystrobin spot samples	81
2.3.2.1 Indirect MALDI imaging analysis of azoxystrobin from leaf surface. Initial azoxystrobin result from indirect imaging method	82
2.3.2.2 Results from revised indirect imaging method	84
2.3.3 Absorption of mesotrione using cell stripping and direct analysis of leaf (matrix sinapinic acid)	86
2.3.4 Comparison of 9-aminoacridine and sinapinic acid and the effect of gold sputter coating.	88
2.3.5 Direct MALDI imaging analysis of mesotrione on plant tissue - examination of the absorption of mesotrione using cell stripping	93
2.3.6 Direct MALDI imaging analysis of mesotrione in leaf veins after foliar absorption	97
2.3.7 Effect of laser fluence for the detection of mesotrione	103
2.3.8 Assessment of suppression effects on the detection of mesotrione using plant extract	109
<b>2.4 DISCUSSION</b>	<b>114</b>
<b>2.5 CONCLUSIONS</b>	<b>117</b>
<b>2.6 REFERENCES</b>	<b>118</b>
<b>CHAPTER THREE: DETECTION OF TRANSLOCATED AGROCHEMICALS IN PLANT STEMS</b>	<b>120</b>
<b>3.1 INTRODUCTION</b>	<b>121</b>
3.1.1 Translocation in the xylem and phloem	121
3.1.2 IR-LDI and IR-MALDI with water as a matrix	125
<b>3.2 METHODS</b>	<b>126</b>
3.2.1 Uptake of azoxystrobin via the roots in soya bean plants	126
3.2.2 Method for encasing stem sections in ice	127
3.2.3 Uptake of azoxystrobin via the roots in sunflower plants	129
3.2.4 Uptake of nicosulfuron via the roots (hydroponics experiment)	130

3.2.5 Absorption of nicosulfuron via foliar application	131
3.2.6 Nicosulfuron and azoxystrobin uptake following stem application experiment	133
3.2.7 Nicosulfuron and azoxystrobin uptake following stem application experiment, using Labcyte Portrait 630 matrix applicator	135
3.2.8 IR-LDI analysis of mesotrione and fluazifop-p-butyl	135
3.2.9 IR-MALDI Analysis of uptake of nicosulfuron following foliar application	136
3.2.10 IR-MALDI analysis of uptake of nicosulfuron via the roots (hydroponics experiment)	137
3.2.11 IR-MALDI analysis of uptake of azoxystrobin via the roots (hydroponics experiment) for IR method	138
<b>3.3 RESULTS</b>	<b>139</b>
3.3.1 Uptake of azoxystrobin via the roots in soya bean plants	139
3.3.3 Uptake azoxystrobin via the roots in sunflowers plants	142
3.3.4 Uptake of nicosulfuron via the roots (hydroponics experiment)	144
3.3.5 Absorption of nicosulfuron following foliar application	151
3.3.6 Nicosulfuron and azoxystrobin uptake following stem application experiment	154
3.3.7 Nicosulfuron and azoxystrobin uptake following stem application experiment, using Labcyte Portrait 630 matrix applicator	157
3.3.8 IR-LDI from analysis of fluazifop-p-butyl	160
3.3.9 IR-MALDI analysis from nicosulfuron following uptake via the roots and foliar application	168
3.3.10 IR-MALDI analysis from azoxystrobin uptake	175
<b>3.4 DISCUSSION</b>	<b>178</b>
<b>3.5 CONCLUSION</b>	<b>179</b>
<b>3.6 REFERENCES</b>	<b>180</b>
<b>CHAPTER FOUR: DETECTION OF SULFONYLUREA HERBICIDE TRANSLOCATION</b>	<b>183</b>
<b>4.1 INTRODUCTION</b>	<b>184</b>
<b>4.2 METHODS</b>	<b>186</b>
4.2.1 Sulfonylurea herbicides analysis by conventional MALDI analysis	186
4.2.2 Limit of detection for sulfonylurea herbicides by conventional MALDI analysis	187
4.2.2 Limit of detection of sulfonylurea herbicides on control plant stem tissue sections	187
4.2.3 Absorption of sulfonylurea herbicides via foliar application	188
<b>4.3 RESULTS</b>	<b>190</b>
4.3.1 Positive ion MALDI-MS spectra and limit of detection of sulfonylurea herbicides	190

4.3.1.1 Chlorsulfuron positive MALDI-MS	190
4.3.1.2 Chlorimuron-ethyl positive MALDI-MS	192
4.3.1.3 Imazosulfuron positive MALDI-MS	194
4.3.1.4 Pyrazosulfuron-ethyl positive MALDI-MS	196
4.3.2 MALDI-MSI of spiked control sections	198
4.3.2.1 MALDI-MSI of chlorimuron-ethyl spiked sections	198
4.3.2.2 MALDI-MSI of chlorsulfuron spiked sections	199
4.3.3 MALDI-MSI of sulfonylurea herbicides 24 hour following foliar application	200
4.3.3.1 MALDI-MSI of chlorsulfuron	200
4.3.3.2 MALDI-MSI of chlorimuron-ethyl	202
4.3.3.3 MALDI-MSI of imazosulfuron	205
4.3.3.4 MALDI-MSI of pyrazosulfuron	208
<b>4.4 DISCUSSION</b>	<b>208</b>
<b>4.5 CONCLUSION</b>	<b>209</b>
<b>4.6 REFERENCES</b>	<b>211</b>
<b>CHAPTER 5: CONCLUSIONS</b>	<b>212</b>
<b>5.1 CONCLUSIONS</b>	<b>213</b>
<b>5.2 REFERENCES</b>	<b>218</b>
<b>APPENDIX 1: PUBLICATIONS ARISING FROM THIS THESIS</b>	<b>220</b>
<b>APPENDIX 2: EXAMINATION OF THE DISTRIBUTION OF NICOSULFURON IN SUNFLOWER PLANTS BY MALDI-MSI</b>	<b>223</b>

## 1.0 Abstract

Pesticides are widely used in agriculture to control weeds, pests and diseases. Successful control is dependent on the compound reaching the target site within the organism after spray or soil application. This is influenced by a range of physiological and environmental factors. One such factor is uptake into foliar tissue and roots and subsequent movement through the plant. Uptake and translocation (and metabolism) can affect the speed and persistence of action, crop selectivity and weed spectrum, thus understanding these issues is of great importance.

Conventional methods for determining uptake and movement of herbicides and pesticides include autoradiography, liquid scintillation and chromatographic techniques such as HPLC. Autoradiography using radiolabelled compounds provides the best indication of a compound's movement within the plant system which is an established technique but relies on radiochemical synthesis. The cost and time taken means that only a relatively few agrochemicals can be studied in this way.

MALDI is a highly adaptable soft ionisation technique that was established in the late 1980's through the developmental research of Tanaka and Hillenkamp. The versatility of MALDI-MS has been extended in recent years with the advent of protein profiling and imaging directly from the surface of thin biological tissue sections. Research by Caprioli *et al* has resulted in the successful profiling and imaging of proteins from thin sections of healthy mouse brain and mouse brain containing tumor and the profiling of proteins from a neurotoxin induced rat model

of Parkinson's disease. Recently the imaging technique has been further developed by research groups to include the detection and imaging of small organic molecules on the surface of porcine epidermal tissue and the surface of rodent brain tissue. In preliminary studies undertaken to support the grant application for this project the detection and imaging of compounds on the surface of a plant leaf or inside a plant stem using MALDI-MS was demonstrated.

In this project the technique of imaging matrix assisted laser desorption ionisation mass spectrometry has been used to examine the uptake and distribution of a range of compounds of agrochemical interest into growing plants. The agrochemicals of interest are azoxystrobin, mesotrione, fluazifop-p butyl and nicosulfuron. Azoxystrobin is a broad spectrum fungicide which inhibits mitochondrial respiration in fungi; the compound is absorbed through the roots and translocated in the xylem. Mesotrione is a selective phloem mobile herbicide which inhibits HPPD, an enzyme involved in carotene synthesis and results in bleaching of the leaves. Fluazifop-p butyl is absorbed as its ester, which is quickly hydrolysed to its carboxylic acid (fluazifop acid) that is mobile in the xylem and the phloem. Fluazifop acid works as a fatty acid synthesis inhibitor, by inhibition of acetyl CoA carboxylase (ACCase). Nicosulfuron is both xylem- and phloem-mobile which inhibits branched chain amino acid synthesis by means of the acetolactate synthase (ALS) enzyme.

MALDI-MS images of mesotrione in tissue underlying the waxy cuticle layer following removal using a tape stripping method have been generated. MALDI-MS images have been generated from azoxystrobin following uptake via the roots in soya and sunflower plants. Nicosulfuron translocation following uptake via the

roots and foliar application has been determined in sunflowers and a phase I metabolite has been identified 48 hours following uptake via the roots and 24 hours following foliar application using MALDI-MSI. Nicosulfuron and azoxystrobin translocation has been determined in the same plant following application of the compounds to the plant stem. The methods developed were used to determine the extent of translocation of four sulfonylurea herbicides 24 hours following foliar application. Additionally, a preliminary method was assessed to determine whether MALDI-MSI can be used to assess translocation of agrochemicals.

**Chapter One: Techniques for the Determination of  
Agrochemicals Distribution in Plants**

## 1.1 Introduction

In order for effective weed management with herbicides and fungicides several factors need to be considered.

- Chemical application and placement
- Chemical uptake
- Chemical translocation (movement within the plant)
- Chemical metabolism (breakdown within the plant)
- Chemical toxicity or activity

The techniques that are of interest are those that are used for the detection of chemical uptake and translocation within the plant. The uptake of chemicals is dependent on the chemical application methodology, which in turn is related to the physiochemical properties of the chemical because several barriers have to be overcome before translocation and metabolism can occur. The two major ways in which agrochemicals are applied are via spraying of leaf surfaces resulting in foliar absorption or uptake via the roots from soil application and subsequent translocation in the plant transport systems. Herbicides are classed into two groups selective and non-selective where selective herbicides are active against specific species and non-selective which kill all plant material<sup>1</sup>. The applications of these various herbicides depends on the desired outcome, a non selective herbicide can be applied to the soil in areas which require clearing such as foot paths or before planting crops. Foliar applied selective herbicides are useful in post emergence weed control because large areas can be sprayed quickly without detrimental effects to the crop. Another benefit of foliar applied selective

herbicides is treatment of established perennial weeds because they are translocated around the plant preventing re-growth from roots or underground stems<sup>2</sup>.

Fig. 1 shows a horizontal cross sectional representation of a plant stem. Transport systems in plants are comprised of two networks, the xylem and the phloem. The xylem is made up of dead cells, which can transport water and certain nutrients due to the capillary effect. The phloem is composed of living cells which move amino acids and sugars in both directions, up and down the plant<sup>3</sup>.

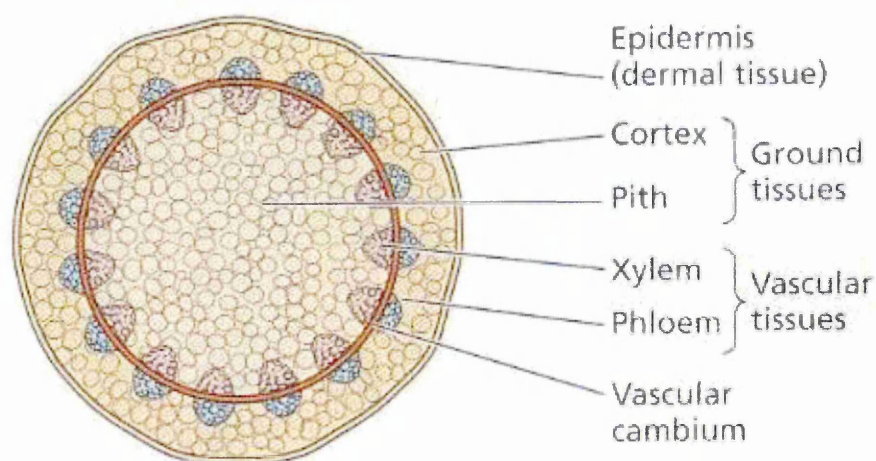


**Fig. 1 Horizontal cross sectional representation of a plant stem<sup>3</sup>.**

The uptake, translocation and metabolism of agrochemicals can affect the speed and persistence of action, crop selectivity and weed spectrum<sup>4</sup>. For these reasons agrochemical companies require detection techniques to assess the uptake of compounds in the early stages of development.

Conventional methods for determining uptake and movement of herbicides and pesticides include autoradiography, liquid scintillation and chromatographic

techniques such as HPLC. Foliar uptake can be measured by removing the surface residue with solvent and quantifying it or extracting the compound from the leaf itself for analysis. This can be achieved by HPLC or scintillation counting<sup>5</sup>. Translocation is usually determined by autoradiography using radiolabelled compounds. The same technique can be used to study root uptake by the use of a <sup>14</sup>C labeled compound in the nutrient solution of plants grown in hydroponics<sup>5,6,7</sup>. These are established techniques but rely on radiochemical synthesis. HPLC can be used but it depends on the ease with which the compound can be analysed and is a destructive method. It would be of extreme benefit to researchers if an analytical technique could be employed in the early stages of agrochemical development that enabled the detection of the movement into leaves and roots and its subsequent translocation.

## **1.2 Methods for detecting translocation**

### **1.2.1 Fluorescence microscopy**

Confocal laser scanning microscopy (CLSM) employs an Ar/Kr laser, in order to excite fluorescent compounds *in vivo* so they can be visualised while migrating through sample tissue. The technique has recently been used for visualising stomatal infiltration of surfactant into leaves, the wax layer of apple, phenolic compounds in plant tissues, and fluorescent dyes in pepper fruit cuticle<sup>17</sup>. CLSM is able to determine the distribution of fluorescent compounds in relatively thick samples (2mm excised segment of petiole and epidermal cells were peeled off the mesophyll and lower epidermis tissue) to a very high degree of lateral and axial resolution<sup>8</sup>.

In a study performed by Zhiqian and Gaskin<sup>8</sup> two fluorescent compounds were used, Oregon Green 488 (2, 7-difluorofluorescein, Oregon Green here after, used as sodium salt) and Rhodamine B (*N*-[9-(2-carboxyphenyl)-6-(diethylamino)-3*H*-xanthen-3-ylidene]-*N*-ethyl-ethanaminium chloride), to assess translocation pathways through plant tissue. Whilst the compounds have similar molecular masses and polarities to pesticides, such compounds are expected to diffuse into plant transport systems the same way as the comparable xenobiotic. The structure of these compounds can be seen in Fig. 2.

The results obtained demonstrated that the absorption of Oregon Green (hydrophilic) into bean leaves was a lengthy process, the uptake being only 4% 2 hours after application and only 6.5% after 4 hours. Rhodamine B, a moderately lipophilic compound had a much faster absorption rate with the rate of absorption being, 10% after 2 hours and 15% after 4 hours after application.

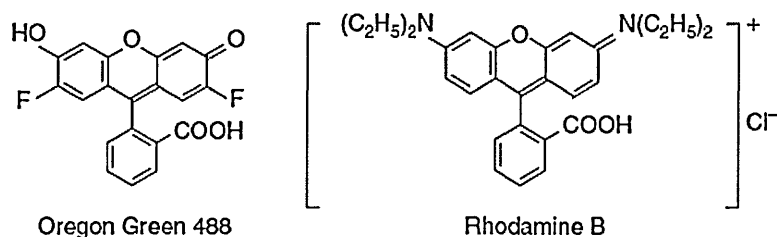


Fig. 2 Chemical structures of Oregon Green and Rhodamine B. <sup>8</sup>

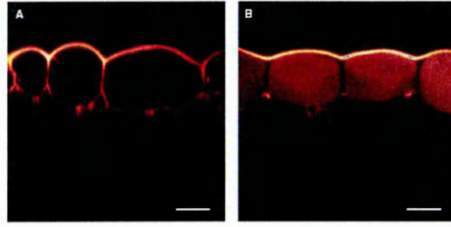


Fig. 3 Distribution of (A) Oregon Green and (B) Rhodamine B within the cuticle of bean leaves 1 hour after application onto the leaf surface. Both images are cross sections. Bar = 20 $\mu$ m.<sup>8</sup>

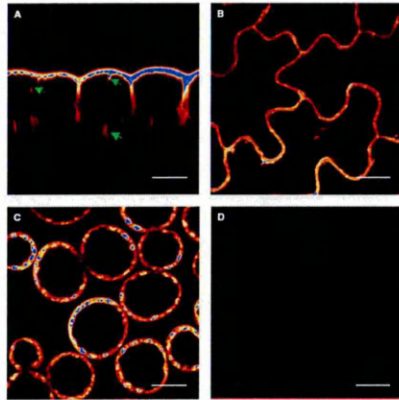


Fig. 4 Distribution of Oregon Green in bean leaves 2 hours after application: (A) Cross section of the treated area. (B) Horizontal section (10 $\mu$ m below the leaf surface.) (C) Horizontal section (40 $\mu$ m below the leaf surface). (D) Horizontal section (40 $\mu$ m below the surface of an untreated leaf.) Bar = 20 $\mu$ m.<sup>8</sup>

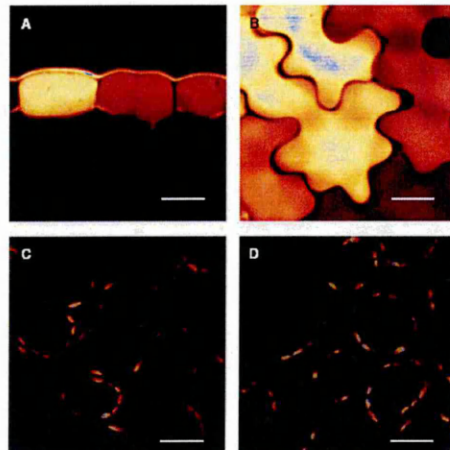


Fig. 5 Distribution of Rhodamine B in bean leaves 2 hour after application: (A) cross section of the treated area. (B) Horizontal section (10 $\mu$ m below the surface.) (C) Horizontal section (40 $\mu$ m below the surface.) (D) Horizontal section (40 $\mu$ m below the surface of an untreated leaf.) Bar = 20 $\mu$ m.<sup>8</sup>

**Horizontal section (40µm below the surface). (D) Horizontal section (40µm below the surface of an untreated leaf.) Bar = 20µm. <sup>8</sup>**

Fig. 4 (A-C) show the distribution of Oregon Green 2 hours after application in bean leaves. Fig. 4 A shows a cross section of the treated area, Fig. 4 B shows a horizontal section taken 10µm below the leaf surface and Fig. 4 C a section taken 40µm below the leaf surface. Fig. 4 D is the equivalent section taken 40µm below the leaf surface from an untreated control. Fig. 4A shows Oregon Green with strong fluorescence in the epidermal cell wall but also in the cytoplasm of the epidermal cells (Fig. 4A upper arrows). This is evidence that this hydrophilic compound is able to diffuse through the plasma membrane as well as the cuticle. No fluorescence was observed in the vacuole of the epidermal cells but a considerable amount was observed in the mesophyll cells (4A lower arrow). The image shown in Fig. 4B of a horizontal-section 10µm below the leaf surface, confirmed the presence of Oregon Green in the cell walls and the cytoplasm of the epidermal cells but not in the vacuole. Fig. 4C, a section of the mesophyll tissue (40µm below the leaf surface), demonstrates that the dye was present in the cell walls and cytoplasm of the palisade cells 2 hours after application. The image shown in Fig. 4D is from a section through an untreated leaf as a control and shows no interference from endogenous compounds.

The image in Fig. 5A-C shows Rhodamine B 2 hours after application in a cross section sample (5A) of the treated area and horizontal sections taken at 10µm (5B) and 40µm (5C) below the treated leaf surface and a control section from an untreated leaf 40µm below the leaf surface (5D). The image in Fig. 5A shows Rhodamine B in the vacuole of the epidermal cells in a significant concentration.

This suggests that moderately lipophilic compounds can diffuse readily across the tonoplast and the plasma membrane of the epidermal cells, unlike Oregon Green. The horizontal section (10 $\mu$ m below the surface of the leaf) shown in Fig. 5B is evidence of the presence of Rhodamine B in the vacuole because strong fluorescence is observed here. Fig. 5C shows no evidence of Rhodamine B the fluorescence observed being that of chlorophyll autofluorescence. This is confirmed by a control untreated leaf (Fig. 5D) cut to the same depth.

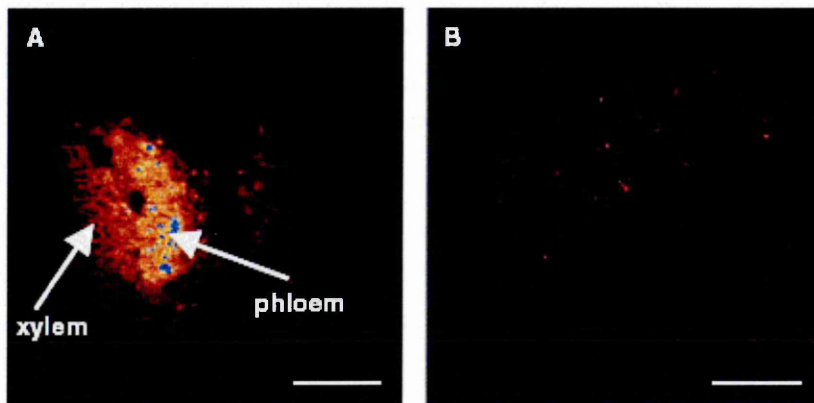


**Fig. 6 Distribution of the fluorescent dyes in the petiole of bean leaves 2 hours after application (A) cross section of a leaf petiole after treatment by Oregon Green. (B) Cross section of a leaf petiole Rhodamine B. Bar = 100 $\mu$ m.<sup>8</sup>**

Phloem translocation was assessed by sectioning the petiole region of treated leaves. In Fig. 6A strong fluorescence can be observed in the phloem and weak fluorescence in the xylem. The presence of Rhodamine B in the xylem may be due to lateral diffusion from the phloem. There is no evidence for the translocation of Rhodamine B in Fig. 6B the fluorescence observed is again due to the autofluorescence of chlorophyll.

These data show that CFMS can yield informative results on the localisation of the chemicals inside the leaf tissues such as the diffusion pathways and also show the sub-cellular distribution after foliar application. The technique is limited however as the distribution of the agrochemicals within the whole plant system cannot be studied. Another major limitation is that actual agrochemical compounds cannot be excited by the laser since only compounds which exhibit fluorescence can be observed.

### **1.2.2 Autoradiography**

Autoradiography is a method used to detect the abundance of radioisotopes in a sample. The technique originates from the work of Niepce de St. Victor in 1867 who observed the blackening of silver chloride and silver halide emulsions by uranium nitrate and uranium tartrate<sup>9</sup>.

Autoradiography can be performed on samples, plants and whole animals. The process of obtaining results in conventional autoradiography involves exposing a photosensitive film to the sample for a period of time. The photosensitive layer is made up of silver halide grains emulsified within gelatin. The size of the grains defines the sensitivity and the resolution detected.

Autoradiography has been used to show the distribution of a number of agrochemicals in a range of plant species and is currently the established methodology used to visualize the distribution of pesticides within plant systems.

A study conducted by Bolsinger *et al*<sup>10</sup> used autoradiography to assess the uptake of pymetrozine, a highly selective insecticide against plant-sucking insects (such

as aphids). The compound provokes a feeding stop and results in death by starvation. The compound achieves best results when ingested by the pest organisms, rather than direct topical contact. Effective distribution at the feeding sites creates the best efficiency<sup>10</sup>. Autoradiography provided results showing good mobility of the compound around the plants transport system, the pesticide can also be seen moving within the leaf.

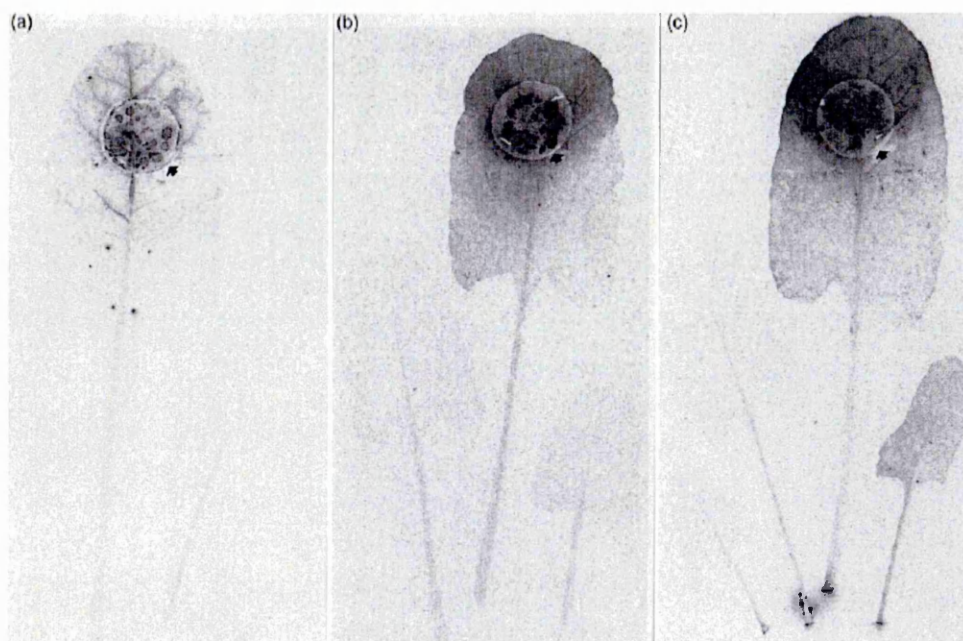


**Fig. 7** Autoradiographs of sugar beet leaves (a) 4 hours (b) three days and (c) six days after [<sup>14</sup>C] pymetrozine treatment of one leaf disc (arrow) per plant. <sup>10</sup>

Fig. 7 a-c shows autoradiography data of <sup>14</sup>C labelled pymetrozine on sugar beet leaves 4 hours (a), 72 hours (b) and 144 (c) hours after application. The circle observed in the leaf is where the leaf was inoculated. The grey regions observed in the images represent the abundance of radioisotope <sup>14</sup>C pymetrozine in that area. The data in Fig. 7 a, showing the compound 4 hours after application, show

that the compound has already started to move into the main veins and in Fig. 7 b and c it can be seen moving into the petiole and into the younger untreated leaves. The results also show an increased density of compound at the apical points (point at which growth occurs) in both treated leaves and untreated leaves.

This distribution pattern was also observed in tomato plants after stem application in the same study.

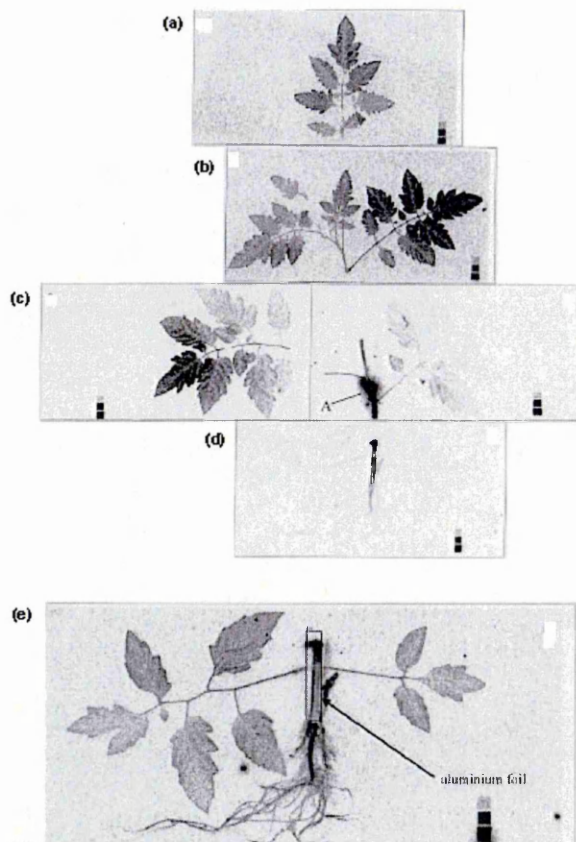


**Fig. 8** Autoradiographs of a tomato plant 40 hours after application of [ $^{14}\text{C}$ ] pymetrozine to the internode indicated by the letter A (right side of plate c). Plates (a-d) were exposed for 2 hours, imaging plate (e) was exposed to the part below the application site for 18 hours (aluminium foil present as shielding to prevent overexposure).<sup>10</sup>

Fig. 8 shows the translocation of  $^{14}\text{C}$  pymetrozine around a whole tomato plant 40 hours after application at point A (right side of plate c). The radiolabelled

compound was applied at point A in the diagram and can be seen to relocate around the plant to untreated areas and again to the apical points and down towards the roots. These data gave evidence for transport in both the xylem and in the phloem due to the bidirectional movement of the compound.

Autoradiography can also be used to assess the efficiency of additives used to enhance the uptake, absorption and translocation of agrochemicals.

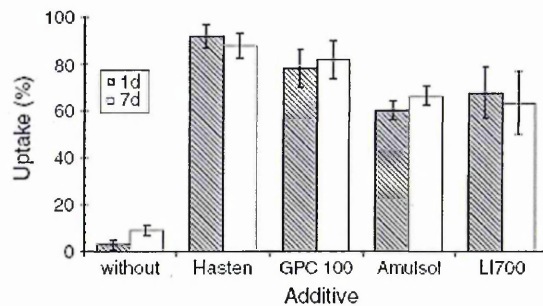


**Fig. 9 Uptake % (y axis) into hop leaves of [<sup>14</sup>C] imidacloprid in combination with various additives (x axis) after 2 time points, 1 day (grey), and 7 days (white).<sup>11</sup>**

The bar graph in Fig. 9 shows the results for the uptake of <sup>14</sup>C radiolabelled imidacloprid with various additives 1 day and 7 days after application using liquid scintillation counting<sup>11</sup>. With the addition of the additives the % uptake has been increased significantly.

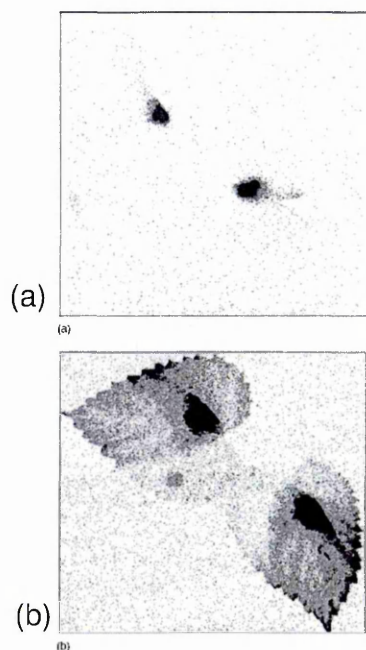


**Fig. 10 (a) Translocation of  $^{14}\text{C}$  imidacloprid without additive. (b) Translocation of  $^{14}\text{C}$  imidacloprid with LI 700. <sup>11</sup>**

Fig. 10 (a) shows the distribution of  $^{14}\text{C}$  imidacloprid on the leaf without the addition of an additive. Fig.10 (b) shows the distribution of  $^{14}\text{C}$  imidacloprid on the leaf with the addition of an additive (LI 700).

Autoradiography is currently the best method for assessing translocation of agrochemicals as it has been shown to generate an excellent visual representation of the abundance of the radiolabelled compound distributed around the plant tissue at any desired time point. This tissue can be subject to further analysis to obtain quantification of the compound using scintillation counting.

Drawbacks to autoradiography are that the radiosynthesis of compounds is expensive and time consuming and thus is not very suitable for compounds in the early stages of development. Also the results do not give any differentiation between the distribution of metabolites and the parent compound since images

generated show the distribution of all compounds that contain the radioisotope. In addition there is a wish in the agrochemical industry to move away from the safety issues involved in handling radiolabelled materials.

### **1.2.3 Secondary ion mass spectrometry (SIMS)**

SIMS analyzes the secondary ions emitted when a sample is irradiated with a primary ion beam. Static SIMS uses a primary ion beam of very low current density (low-dose particle bombardment) which is an extremely sensitive technique for analysing the top few molecular layers of a sample with little damage to molecules <sup>12</sup>.

SIMS has been used to examine the role of boron in plant physiology <sup>13</sup>. The primary functions of boron are unclear although some hypotheses propose that it is linked to plant cell wall stabilisation by polysaccharide cross-linking, membrane integrity, phenol metabolism and others <sup>13</sup>. Boron has no radioactive isotopes of practical use thus preventing the use of autoradiographic imaging. SIMS has already been used for boron mapping in animal tissues following ion mass neutron capture therapy for cancer <sup>14</sup>.

A study reported by Dérue *et al* <sup>13</sup> used SIMS analysis of flax seedlings (*Linum usitatissimum*) enriched with boron, to generate images of boron and calcium distribution at a cellular level. The seedlings were allowed to germinate before being placed in a hydroponics system. Control samples were prepared by adding H<sub>3</sub>BO<sub>3</sub> to the growth solution 2 days before analysis. The samples were prepared using a vapour phase technique developed in-house, this ensured there was known boron relocation which was not too extensive. Once the samples were

completely dehydrated they were mounted in resin and sliced using a diamond knife to a thickness of 2  $\mu\text{m}$ . The samples were analysed using  $\text{O}_2^+$  as the primary ion beam, images (256 x 256 pixels) were edited in grey scale. The high spatial-resolution images generated can be seen in Fig. 11 (A-F).

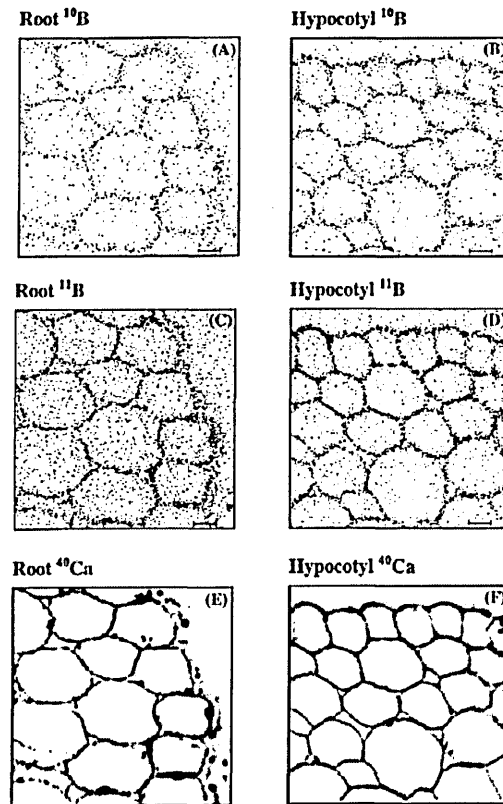


Fig. 11 Images of the distribution of  $^{10}\text{B}^+$ ,  $^{11}\text{B}^+$  (A-D) and  $^{40}\text{Ca}^+$  (E and F) in root (A, C and E) and hypocotyl (B, D and F) section of flax seedlings. <sup>13</sup>

Fig. 11 shows the distribution of  $^{10}\text{B}^+$ ,  $^{11}\text{B}^+$  and  $^{40}\text{Ca}^+$  in the root (A, C and E) and the hypocotyl sections of the boron enriched control flax seedlings (B, D and F). The two boron isotopes are normalised to  $^{12}\text{C}^+$ , the non-normalized image of  $^{40}\text{Ca}^+$  shows the details of the anatomical structure of the tissues. Fig. 11 A-F shows that the boron is mainly present in the cell-contours including the cell wall. Boron can also be seen in the resin surrounding the tissue. SIMS clearly has the

potential to analysis agrochemicals at a cellular level but not on a large scale. Other drawbacks are that the technique is very destructive and samples can only be analysed once due to the damage caused by the primary ion beam on the surface of the samples and the instrumentation is very expensive.

## 1.3 Current applications of MALDI imaging

### 1.3.1 Introduction

MALDI is a highly adaptable soft ionisation technique that was established in the late 1980's through the developmental research of Tanaka<sup>15</sup> and Hillenkamp<sup>16</sup>. The versatility of MALDI-MS has been extended in recent years with the advent of protein profiling and imaging directly from the surface of thin biological tissue sections<sup>17,18,19</sup>. Research by Caprioli *et al*<sup>19</sup> has resulted in the successful profiling and imaging of proteins from thin sections of healthy mouse brain and mouse brain containing tumor and the profiling of proteins from a neurotoxin induced rat model of Parkinson's disease<sup>8</sup>. Recently the imaging technique has been further developed by research groups to include the detection and imaging of small organic molecules on the surface of porcine epidermal tissue<sup>20</sup> and the surface of rodent brain tissue<sup>21</sup>.

Matrix assisted laser desorption ionisation imaging (MALDI-MSI) was first developed by the Caprioli group in 1997<sup>22</sup>. This technique has been used to image the distribution of a wide range of compounds, including proteins, lipids, pharmaceuticals, metabolites and other small molecules<sup>23,24</sup>. The first demonstration of the use of MALDI to directly study pharmaceutical compounds in animal tissue was performed by Troendle *et al*<sup>25</sup>. In this work the anti cancer drug

paclitaxel was detected in a rat liver incubated in a solution containing paclitaxel and also in a dosed xenograft. They also detected the antifungal drug siperone from spiked sections of rat liver tissue. The results gave rise to the idea that MALDI-MSI could provide a powerful investigative tool for pharmaceutical research and development.

The Caprioli group in collaboration with Schering-Plough <sup>21</sup> reported the distribution of anti-tumour drug dosed mouse tumour tissue and rat brains. By using selected reaction monitoring, spectral interference from matrix and endogenous metabolites (which limits the sensitivity of MALDI-TOF MS for drug analysis) was avoided. Images were generated from the product ions showing the distribution of the anti tumour drugs in both tumour and brain tissue. Imaging MALDI-MSI has progressed to the stage when it offers a complementary technology to autoradiography for imaging the distribution of xenobiotic compounds. Additional functionality is obtained since separate images for the distribution of the parent compounds and its metabolites in whole body tissue sections may be generated <sup>26</sup>.

Time of flight (TOF) mass analysers are particularly well suited to MALDI due to the pulsed nature of laser desorption as well as their high mass range. TOF analysers separate ions while they pass through a field free drift region, as the ions are accelerated by the applied voltage at the focusing lens the molecules acquire varying velocities, smaller ions travel faster and strike the detector before larger ions <sup>12</sup>. Currently MALDI imaging is limited by laser spot size and fluence. As the laser size decreases so does the sensitivity because the area of desorbed ions is

decreased. The energy of the laser may be increased meaning more ions are desorbed but this can also lead to high degrees of fragmentation and a significant loss in sensitivity <sup>27</sup>.

### 1.3.2 Lasers for MALDI-MSI

A study published by the mass spectrometry and instrument manufacturer Bruker compared nitrogen ( $N_2$ ) lasers with Nd:YAG assessing laser focus for improved MALDI performance <sup>28</sup>. This study looks beyond the obvious difference in wavelength and measures the beam profile at the target surface. Using a Bruker Ultraflex II MALDI-TOF instrument with a modified laser setup, allowed  $N_2$ , Nd:YAG (Gaussian) and Nd:YAG structured A or B to be used on the same instrument within seconds. The behaviour of the different lasers was assessed on the same sample.

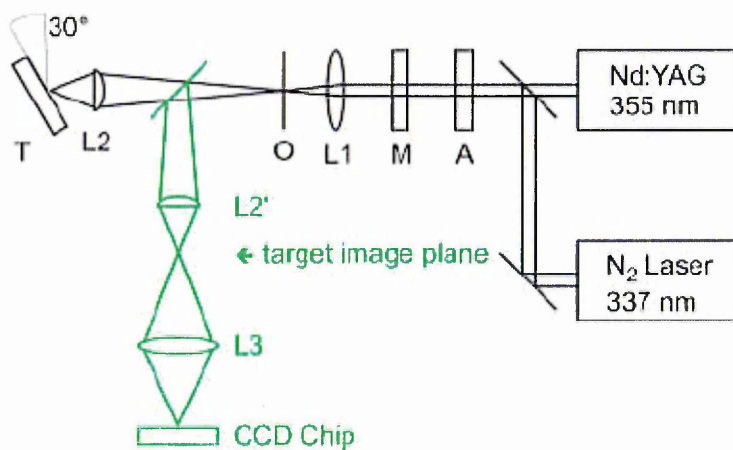


Fig. 12 Optical setup for modulation of the laser profile. A = attenuator, M = modulation, L1 = lens, O = round aperture, L2 = Lens, T = sample target and L3 = lens 3. The elements in green are required only for measuring laser profiles. <sup>28</sup>

The optics for modulating the beam profile are shown in Fig. 12. The laser beam first passes through the attenuator (A), which adjusts the laser fluence (laser power). This is followed by a modulator which shapes the beam profile using interference principles. Lens 1 (L1) focuses the modulated beam to an image plane and the outer interference structures are cut out using an aperture limiting the boundaries of the profile. Lens 2 (L2) focuses the laser onto the target and is used to alter the beam from Nd:YAG structured A, B and Gaussian. The beam profiles at the target surface were measured by using a CCD camera (seen in green, Fig. 12), the CCD camera produced bitmaps of a single laser shot which could be interpreted using their in-house software.

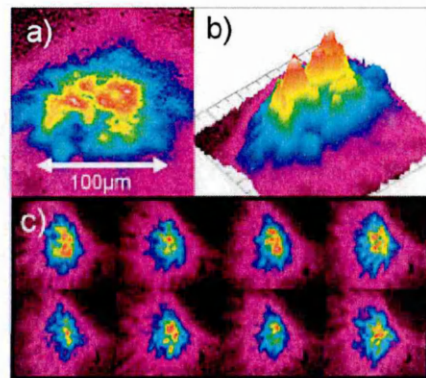


Fig. 13 Typical profile of nitrogen laser a) view from top, b) 3D view from side, c) beam profile of eight consecutive laser shots. <sup>28</sup>

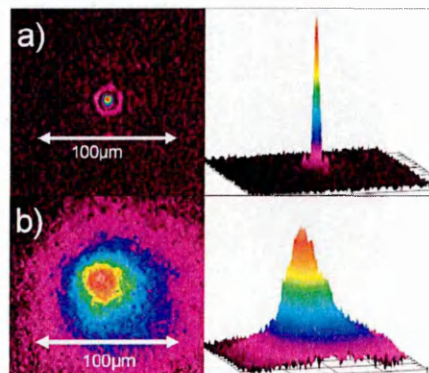
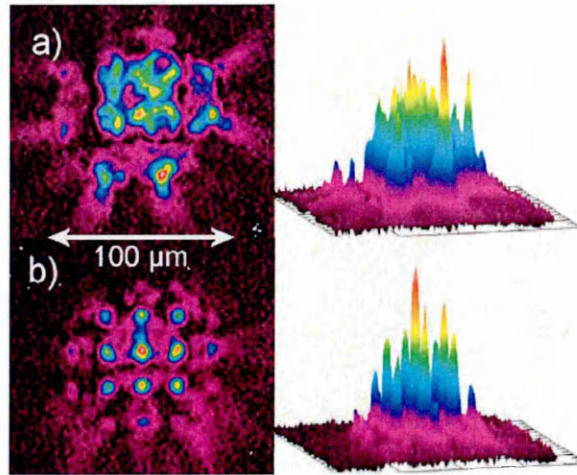


Fig. 14 Beam profile of a Nd:YAG (Gaussian) laser a) fully focused Nd:YAG (Gaussian) approximately 5µm b) defocused Nd:YAG (Gaussian) approximately 45 µm. <sup>28</sup>



**Fig. 15 Beam profiles of the two structured beams a) Nd:YAG (structured A) approximately 60  $\mu\text{m}$  b) Nd:YAG (structured B) approximately 45  $\mu\text{m}$ .<sup>28</sup>**

The images generated in Fig. 13 show the laser beam profile of the nitrogen laser where the different colours represent different energy, red being the highest energy and black zero energy. Fig. 13 a) shows the beam profile from above showing that the energy from the beam is dispersed across an area around 100  $\mu\text{m}$ . Fig. 13 b) shows a 3-D view from the side indicating laser fluence is more intense in the centre of the beam. Fig. 13 c) shows replicate shots of the same profile.

Fig. 14 shows the beam profiles of the Nd:YAG (Gaussian) (a. fully focused and b. defocused). The focused laser in Fig. 14 a) covers an area of approximately 5  $\mu\text{m}^2$ , the defocused laser Fig. 14 b) covers an area of approximately 45  $\mu\text{m}^2$ .

Fig. 15 shows the beam profiles of the two structure beams a) is the profile for structure A which has a diameter around 60  $\mu\text{m}^2$  and b) shows structure B has a diameter of approximately 45  $\mu\text{m}^2$ .

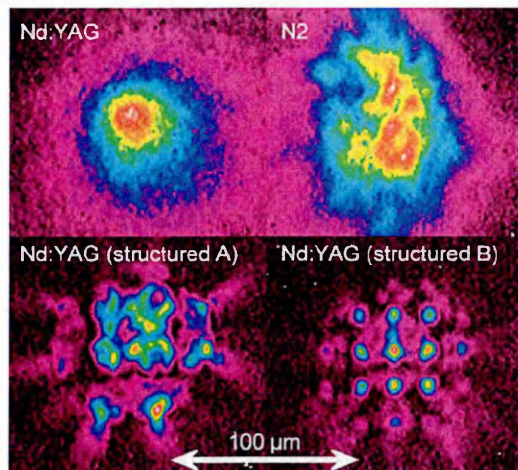


Fig. 16 Direct comparison of all four beam profiles used in these experiments.<sup>28</sup>

Fig. 16 shows a direct comparison of all four beam profiles assessed in this study. The conclusions drawn from these experiments are that using a structured beam profile instead of a Gaussian beam a frequency-tripled Nd:YAG laser shows that results are comparable and on occasion can be better than those obtained with a nitrogen laser. With the extended life expectancy of the Nd:YAG this can make it a more suitable laser for imaging applications.

### 1.3.3 Stigmatic ion optics for high-resolution MALDI-MSI.

A novel approach to MALDI imaging has been reported by the FOM Institute for Atomic and Molecular Physics in Amsterdam in conjunction with a number of other establishments<sup>27</sup>. The method of Stigmatic imaging mass spectrometry was devised by extensively modifying a Physical electronics TRIFT II triple focusing time of flight mass spectrometer equipped with a phosphor screen/CCD. The ions are still separated by the varying velocities acquired according to their mass. The difference is in the ion optics, the ions desorbed by a laser with a spot size spot of

≈200μm and the ions retain their original spatial distribution during the time of flight separation. These ions are then detected by a position sensitive detector so that spatial resolution is independent of the laser spot size. The utilization of the stigmatic ion optics results in ion images with a spatial resolution of 4 μm. Whilst the spatial resolution achieved in this approach depends on the quality of the ion optics and the resolution of the detector (rather than the laser spot size large spot size), large spot sizes can be employed to give better sensitivity and greatly increase image acquisition times.

Ron Heeren presented his work with the stigmatic mass microscope at the 17<sup>th</sup> International Mass Spectrometry Conference (IMSC) in August 2006 and published a paper in the International Journal of Mass Spectrometry<sup>27</sup>. The data presented demonstrate the potential of the instrument by analysing endogenous analytes in mouse, rat and human pituitary glands<sup>27</sup>. Analysis of mouse or rat pituitary glands with a conventional MALDI imaging instrument with a high degree of spatial resolution would be difficult due the small nature of the gland (10<sup>2</sup>-10<sup>3</sup> μm). The data reported show that the high resolution achievable with the stigmatic mass microscope allows localization of neuropeptide distribution within the different cell clusters within a single pituitary section.

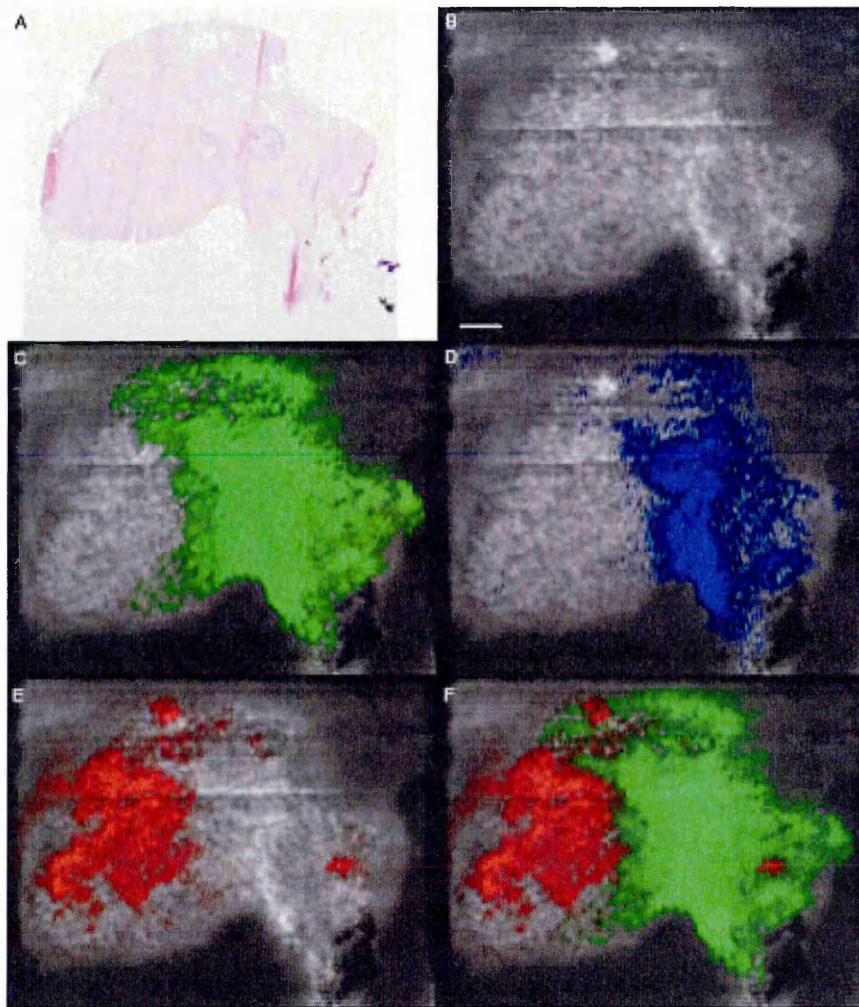


Fig. 17 Molecular image of human pituitary by MALDI-IMS (A) optical image of a H&E stained section. (B) Total ion count MALDI image in greyscale of section adjacent to the one in the optical image. Neuropeptide distribution overlaid on the greyscale total ion count image with (C) vasopressin in green (D) oxytocin in blue (E)  $\alpha$ -MSH in red. (F) Overlay of vasopressin (green) and  $\alpha$ -MSH (red). (b) scale bar = 1 mm.<sup>27</sup>

The data shown in Fig. 17 demonstrate the high resolution achievable with the stigmatic ion optic approach with a resolving power of 4  $\mu$ m and very fast acquisition time. One of the drawbacks of this technique is poor mass resolution which will affect the image generated from ions when ions with a similar m/z are present in the tissue.

### 1.3.4 Desorption electrospray ionisation (DESI) imaging

Another recent development in instrument technology for imaging mass spectrometry uses two ionization techniques, electrospray ionization (ESI) and desorption ionization (DI) combined to create desorption electrospray ionization or DESI. The method was developed by Graham Cooks group at Purdue University and a paper published in Science in 2004<sup>29</sup>, DESI uses an electrosprayed solvent to examine condensed phase samples at atmospheric pressure and allows direct and rapid analysis of surfaces with very little or no sample preparation. A study performed by the group from Purdue University in Indianapolis assesses DESI's resolution and application to identify lipids in a rat brain. They assessed the DESI image resolution using a printed image of ( $m^*$ )<sup>30</sup>.

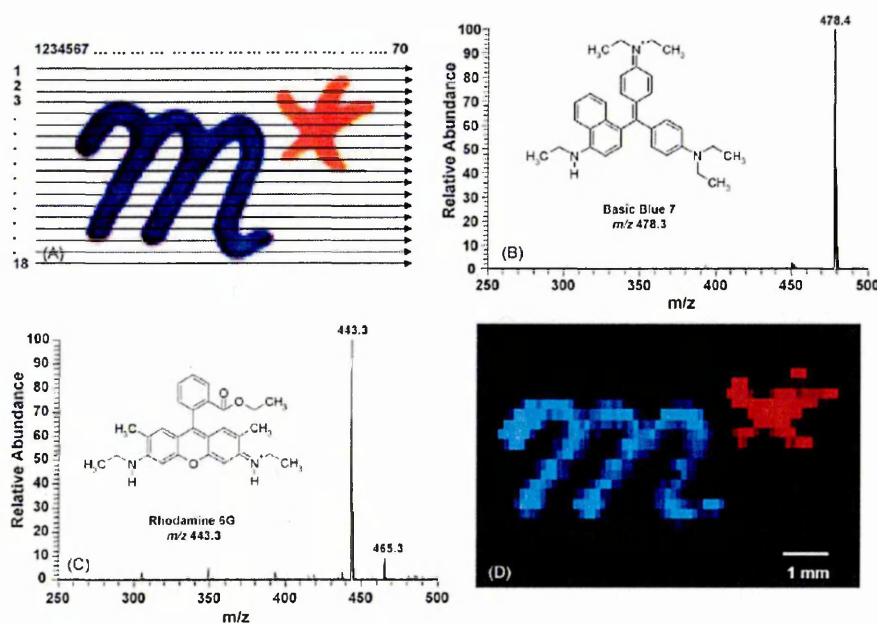


Fig. 18 (A) digitally scanned optical image of the  $m^*$  symbol written on glossy photographic paper. Arrows indicate the direction of each scan. (B) Positive ion DESI mass spectrum of the basic blue 7 dye from the paper. (C) Positive ion DESI mass spectrum of rhodamine 6G dye from the paper. (D) Molecular ion image of the  $m^*$  symbol recorded by DESI<sup>30</sup>.

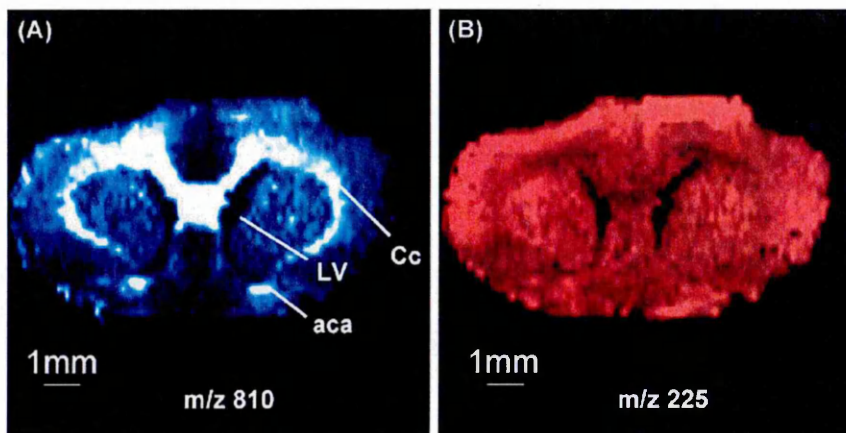


Fig. 19 (A) DESI image at  $m/z$  810 from a  $4\mu\text{m}$  coronal section of a rat brain tissue. (B) DESI image at  $m/z$  225 from the same tissue section.<sup>30</sup>

Fig. 18 shows that the DESI image produced by the protonated masses of basic blue and rhodamine 6G overlaid generates an image of the  $m^*$  which has clearly retained the original spatial distribution and is clearly visible.

Fig. 19 A and B are images generated from the rat brain section, showing that regions of the brain can be identified. Fig. 19 A is an image generated by a peak at  $m/z$  810 corresponding to the deprotonated form of phosphatidyl serine (38:4). The signal is found to be most intense in the white matter region of the brain, specifically the corpus callosum. Fig. 19 B is an image generated from a peak at  $m/z$  225 which is the deprotonated form of myristoleic acid (14:1) and shows the compound uniformly distributed across the tissue section.

The benefits of DESI as an imaging technique are that samples can be analysed at atmospheric pressure and its ability to ionise lipids and simple sample preparation with no need for a matrix. Limitations of DESI include poor sensitivity and spatial resolution, as the appropriate amount of liquid must be delivered to the

surface with sufficient force to liberate analyte from the surface as charged droplets to obtain high signal. Redistribution of the analyte on the surface of the sample can occur resulting in misrepresentation of the analyte distribution. If the solvent and gas flow rates are reduced to prevent this redistribution the sensitivity of the technique is compromised<sup>31</sup>.

### **1.3.5 Whole body MALDI imaging**

Stoeckli *et al* have reported the use of MALDI-MSI to map the distribution of compounds and their metabolites in whole body samples<sup>26</sup>. This technology would be very beneficial to the drug development industry and contract research organisations because there is a lot of interest in the fate of drug metabolites. Companies are keen to see results in this area because it can speed up the path to clinical trials and hence production and profit. The method of whole body drug distribution is traditionally performed by autoradiography techniques. Although this method produces very accurate results, information on metabolites is limited and radiolabelled compounds in the early stages of development are expensive and can be time consuming to produce.

The research of Stoeckli *et al*<sup>26</sup> has been focused on developing a robust method protocol for whole body imaging of rats and mice with results which are comparable to autoradiography. Although there are major advantages to autoradiography, i.e. standardised methods, high sensitivity and established methodology for quantification there are also limitations since the parent compound is indistinguishable from metabolites. MALDI imaging poses the

advantage of acquiring massive amounts of data from the imaged tissue which not only include the distribution of the analyte compound but also endogenous metabolite data. This allows not only the compound and metabolite distribution but the potential to gain information on the organism's response to drug treatment i.e. pharmacological data.

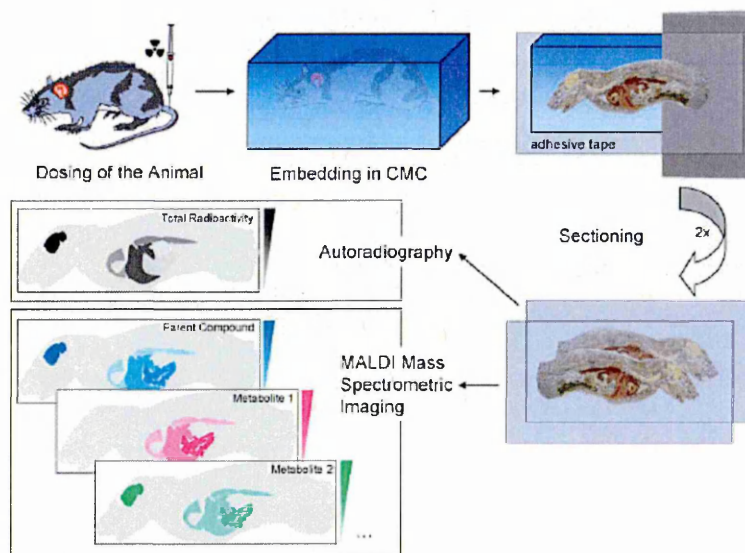
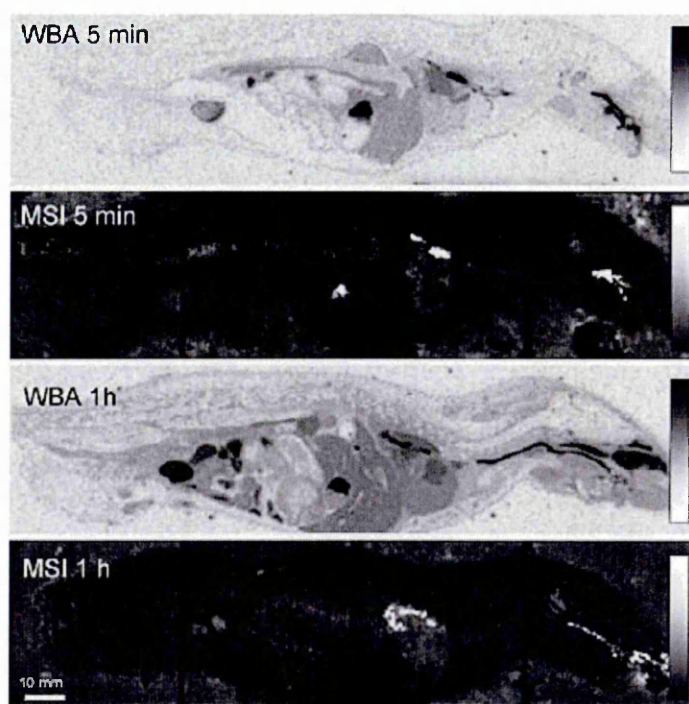


Fig. 20 MALDI MSI sample preparation process for whole-body tissue sections. <sup>26</sup>

Fig. 20 shows the sample preparation stages required to produce sections for whole body imaging MALDI experiments. The process starts with dosing of the animal which is left for the desired time period before it is sacrificed. The samples were prepared by rapidly freezing the sacrificed animals by immersion into hexane in a dry ice bath (-75 °C) then immersing the shaved animal into a 2% semi liquid gel of sodium carboxymethylcellulose (CMC). The animal is then sectioned longitudinally on a cryostat capable of sectioning whole animals. This procedure was optimised since speed is a crucial factor in retaining tissue structure. The samples were then freeze dried after preparation to prevent degeneration of the

tissue. The samples were then mounted onto the sample plates using double sided adhesive tape ensuring uniform mounting without air bubbles and contamination. Optical images were taken using a flat bed scanner to allow the optical image to be superimposed with the molecular images generated by MALDI imaging. Matrix solution was applied by airspray deposition. As the size of the sample is limited by the size of the target plate the images of whole body samples had to be done in sections, software was then used to bring the imaged sections together.



**Fig. 21 Comparison of MSI with whole body autoradiography (WBA) sections after (0.5 mg/kg) intratracheal administration of compound. <sup>26</sup>**

Fig. 21 shows the comparable whole body autoradiography (WBA) and mass spectrometry images 5 minutes and 1 hour following dosing. The MALDI-MS images show the compound is present in the same regions as observed with the autoradiography results although the technique is apparently not as sensitive as

autoradiography because some of the regions in the 1 hour result are not seen in the mass spectrometry image. This could however be due to the radiolabel being present on metabolites of the compound since autoradiography is not able to distinguish between the distributions of the radiolabelled compound or a metabolite of the compound with the radiolabel present.

There are three problems which need to be overcome in order to use MALDI-MSI for quantification: substance specific ionization yield, tissue specific ion suppression and the dependence of detected signal on the amount/property of the deposition matrix. These factors result in quantifiable data being difficult to obtain because signal suppression is dependent on not only the compound but also the tissue. The paper by Stoeckli *et al*<sup>26</sup> suggests that calibration needs to be performed separately by spiking the compounds on each of the tissues or better still homogeneously spiking whole-body tissue sections and imaging the subsequent sections. The method described in this paper to assess the tissue specific suppression was to spray 4 mL of a compound solution 0.25 mg/mL over a control whole body rat section.

Fig. 22 shows the tissue specific suppression of signal, the areas of blue and dark grey indicate regions of high signal suppression and the lighter grey regions indicate regions with higher signal. Although this result is valuable it can only give an indication of tissue specific suppression. As the compound was applied to the surface it will still be present on the surface of the cells and not within the tissue structure as it would be in a dosed sample section. This will affect the availability of compound for co-crystallisation with the matrix and subsequent ionisation also

the concentration present on the tissue will vary to that of a dosed sample section compared to a control produced using this method.

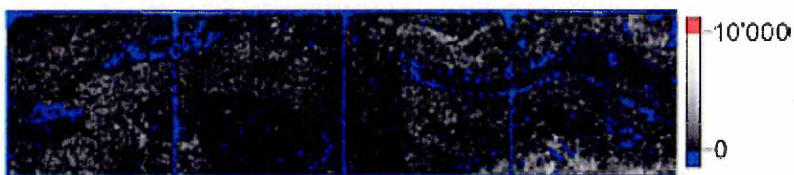


**Fig. 22 Tissue specific suppression of signal, measured intensity distribution of the compound homogeneously deposited over the sample (detectable signal = blue colour).**<sup>26</sup>

Following this, the study tackles the problem of spatial resolution and as mentioned before the limitations of this type of instrument with regards to laser spot size and sample preparation. The laser spot size was assessed by forming an ablation pattern onto a coloured surface, which were interpreted as ellipsoid of dimensions being  $\sim 80 \mu\text{m} \times 50 \mu\text{m}$ . The critical process of matrix application causing lateral diffusion of analyte leading to loss of spatial resolution was assessed by one of the special features using BIOMAP [<http://maldi-msi.org>].

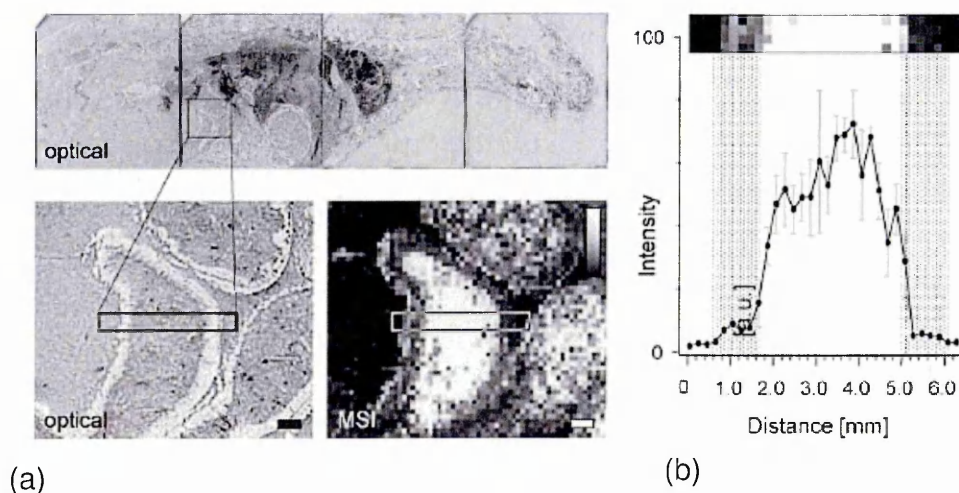


**Fig. 23 (a) MALDI-MS image and optical image across an intestinal lobe. (b) Compound distribution in defined area observed using MSI and intensity against distance line graph.**<sup>26</sup>

Fig. 23 (a) shows the comparison of an optical image of an intestinal lobe compared to the MALDI-MS image of a rectangular section of the same intestinal lobe, where a high ion signal was observed. Fig. 23 (b) assesses the lateral diffusion of the ion of interest following matrix application with a line graph of intensity against distance.

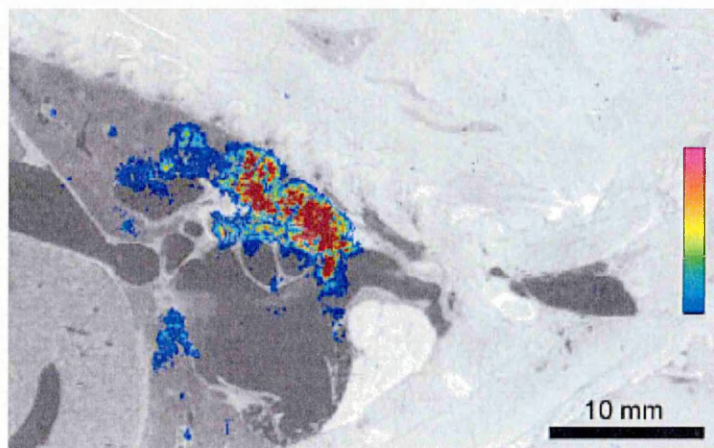


**Fig. 24 High resolution image (100x100 $\mu$ m) indicating minimal lateral diffusion of compound following matrix application.<sup>26</sup>**

Fig. 24 shows a high resolution (100x100  $\mu$ m) MALDI-MS image overlaid with the optical image of the section of the sacrificed rat. This was further evidence that matrix application with aerospray deposition caused minor lateral diffusion of the compound in these experiments with the maximum measured displacement being less than 500  $\mu$ m.

One of MALDI imaging's advantages over autoradiography is its ability to detect multiple analytes simultaneously. The paper includes results showing the excretion pathway of the compound.

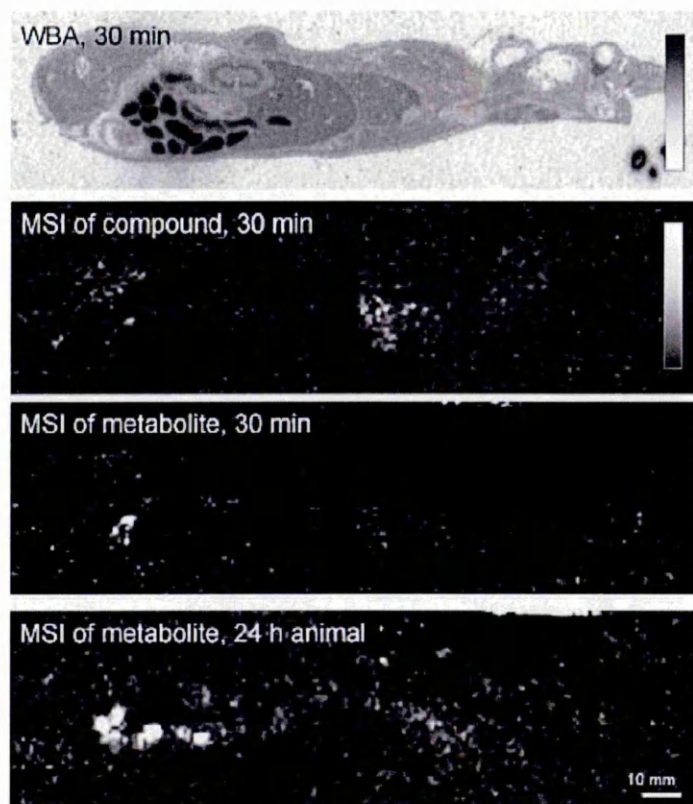


Fig. 25 whole body autoradiography (WBA) image 30 minutes after administration compared to MALDI-MS image of compound after 30 minutes, MALDI-MS image of metabolite after 30 minutes and MALDI-MS image of metabolite 24 hours after administration.<sup>26</sup>

Fig. 25 shows the whole body autoradiography (WBA) image 30 minutes after administration compared to the MALDI-MS images of the metabolite 30 minutes and 24 hours after the administration of the compound. First of all masses for the known metabolites from a liver metabolite study were assessed, although the results of the compound distribution were not comparable to the autoradiography results. After this MS images were generated for all the masses corresponding to the protonated, sodiated and potassiated known metabolites. Images were generated with a mass corresponding to the protonated glucuronide distributed within the intestine. Since glucuronidation is a common mechanism for excretion this result was deemed positive although it had to be confirmed by MS/MS.

This study shows clear evidence that MALDI-MSI can produce comparable results to autoradiography with the added bonus that metabolite distribution can be studied without the need for radiolabelled compounds. These results will further the interest in the technique by the pharmaceutical industry and contract research organisations because these results will be beneficial for drugs in the early stages of development and may shorten the time period before clinical trials and speed up the drug development to production process.

## 1.4 Mass spectrometry for the analysis of plant tissue

MALDI-MSI and profiling has been widely used in the study of plant material. Stahl *et al*<sup>32</sup> employed MALDI-MS and high performance anion-exchange chromatography (HPAEC) in 1997 to analyse 2 high molecular weight fructans from *Dahlia variabilis* L. and also carried out direct tissue analysis on the epidermal and paraenchymal tissue of onion bulbs (*Allium cepa* L.).

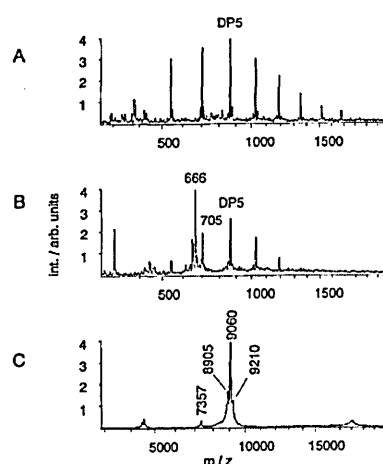


Fig. 26 (A) Spectrum from onion parenchyma tissue. (B) Spectrum from onion epidermis tissue. (C) Spectrum from crystalline rim of DHB on edge of onion leaf base epidermal tissue.<sup>32</sup>

Fig. 26 A shows spectra taken from onion parenchyma tissue, B. onion bulbs leaf base epidermal tissue and C spectrum of desorbed ions from the outermost crystalline rim of the matrix dihydroxybenzoic acid (DHB) from the leaf base epidermal tissue. The data show that fructans with a maximum degree of polymerization of 5 were observed in both tissue types (Fig. 26 A, B). Oligosaccharides were also observed in the spectrum obtained from the microcrystalline rim surrounding the tissue indicating that analyte molecules had leaked out during sample preparation (Fig. 26 C). A peak at  $m/z$  666 was observed in the epidermal tissue (6B) but not the parenchyma tissue (6A) which following further investigation of a single epidermal cells vacuole was found to be a monopotassium adduct ion of a noncarbohydrate compound of mass 627.

The study found that various isomeric fructans and more than 50 compounds were detected from both techniques with  $m/z$  values ranging from <2000 up to 10000.

In 2004 Sluszny *et al*<sup>33</sup> reported probing the biotic-abiotic boundary of plants using laser desorption/ionization mass spectrometry (LDI-MS), by using transition metals, metal powders and colloidal suspension to create ionized species via attachment of metal ions.

Fig. 27 shows the spectrum of the  $C_{12}$ - $C_{60}$  n-alkane standard mixture as silver adducts, the upper spectrum is an enlarge view of the  $m/z$  350-900 region and the lower spectrum is an enlarged view of the  $C_{26}$  alkane. The data observed in Fig. 27 indicate there is a large difference in the ionization efficiencies of the varying alkanes and that there is little sensitivity for alkanes smaller than  $C_{20}$ .

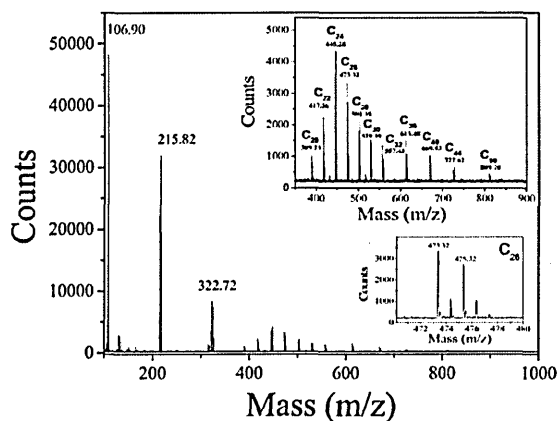


Fig. 27 LDI-MS spectrum of n-alkane standard mixture as silver adducts. The upper spectrum is an enlarged view of the m/z 350-900 region and the lower spectrum is an enlarged view of the C<sub>26</sub> alkane.<sup>33</sup>

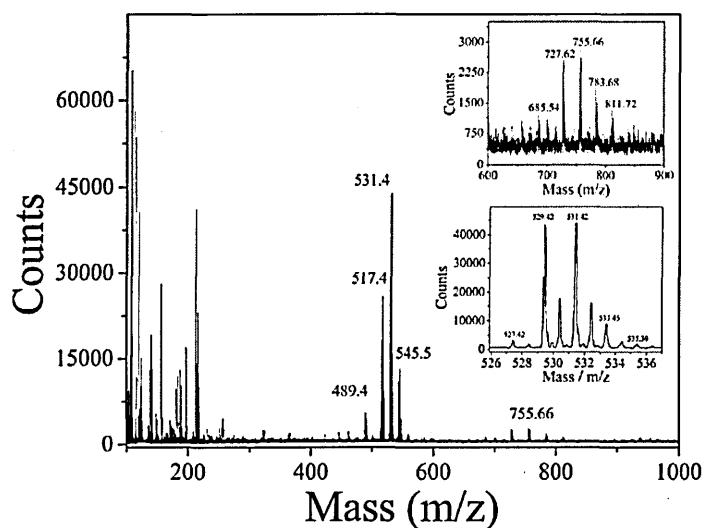


Fig. 28 Spectrum from direct analysis of *Arabidopsis thaliana* tissue. The upper spectrum shows an enlarged view of the peaks for the <sup>107</sup>Ag adducts of esters and the lower spectrum show an enlarged view of the peaks around m/z 529.4.<sup>33</sup>

Fig. 28 shows LDI-TOF data from the analysis of *Arabidopsis thaliana* tissue. The upper spectrum shows an enlarged view of the peaks for the <sup>107</sup>Ag adducts of esters and the lower spectrum show an enlarged view of the peaks around m/z

529.4. Fig. 28 presents 4 major peaks one of which is  $m/z$  529.4 which when enlarged (Fig. 28 lower spectrum) has a peak pattern similar to that observed in Fig. 27 lower spectrum.

The published data demonstrated that LDI-MS could be used to analyse cuticle waxes made up of long-chain non-polar hydrocarbons and that these could be identified by direct tissue analysis with nearly identical mass spectra being obtained by direct analysis and extraction.

Wu *et al*<sup>34</sup> profiled alkaloid distribution in four commonly used Chinese medicinal herbs by using direct tissue analysis MALDI-MS. The results demonstrated the feasibility of MALDI-MS to provide rapid and reliable plant component profiles by direct analysis of plant tissue. This reduced damage to the components observed using the traditional sample preparation methods. This work was also performed on *Strychnos nux-vomica* seeds profiling regions of the endosperm and epidermis without the need for complex sample preparation, clear differences were observed between the endosperm and epidermis regions with several additional alkaloids present in the epidermis region<sup>35</sup>.

Robinson *et al*<sup>36</sup> have generated MALDI-MS images of carbohydrates from wheat stems (*Triticum aestivum*). A range of hexose sugars present in wheat stems were identified using MALDI-MS and liquid chromatography electrospray ion trap mass spectrometry and presented images showed the distribution of these sugars within stem sections from both the longitudinal axis and the horizontal axis.

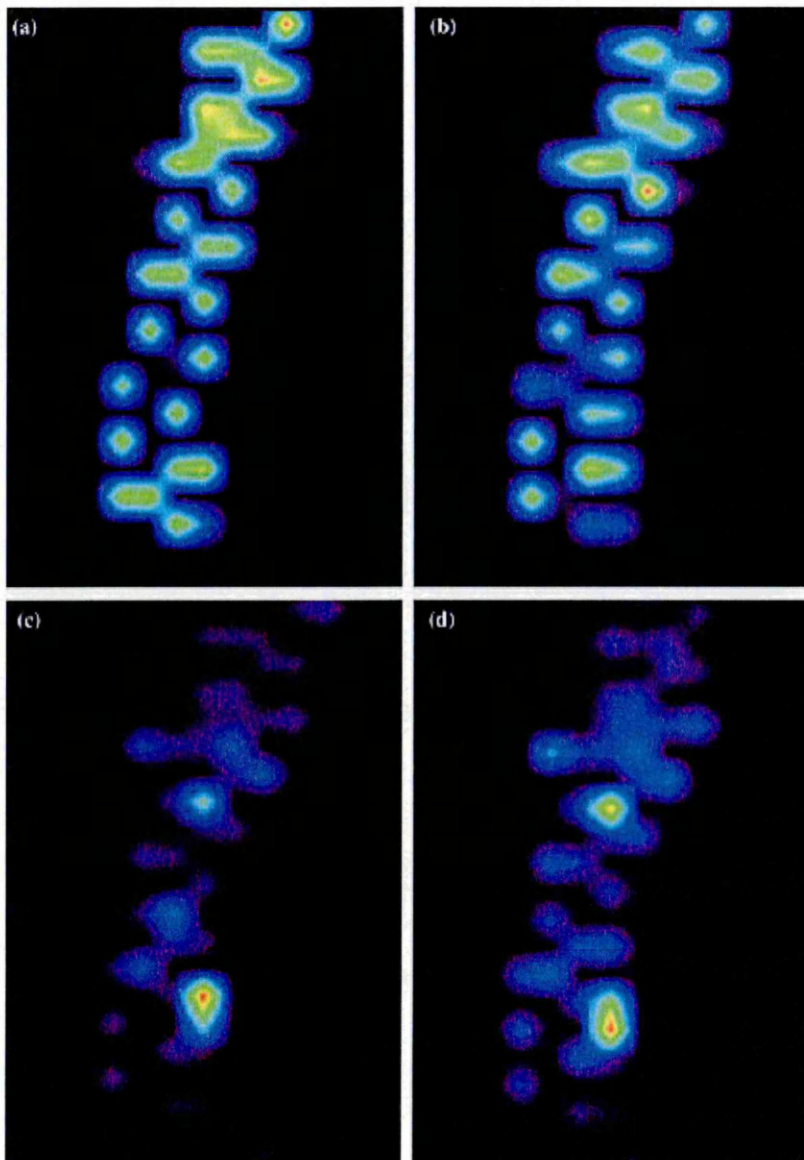
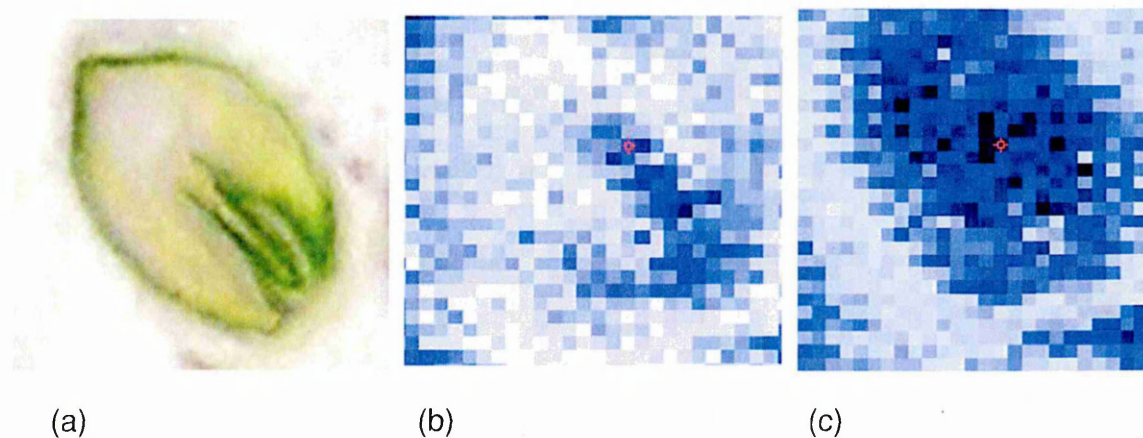


Fig. 30 (a-d) MALDI-MS images of a longitudinal section of a wheat stem. (a) Image generated from m/z 228, (b) image generated from m/z 381, (c) image generated from m/z 705 and (d) image generated from m/z 1353. <sup>36</sup>

Fig. 30 (a-d) shows MALDI-MS images of a longitudinal section of wheat stem. Fig. 30 (a) was generated from m/z 228 the potassium adduct of  $\alpha$ -cyano-4-hydroxycinnamic acid ( $\alpha$ -CHCA), (b) was generated from m/z 381 the potassium adduct for hexose disaccharide, (c) was generated from m/z 705 the potassium

adduct for hexose tetrasaccharide and (d) was generated from  $m/z$  1353 the potassium adduct hexose octasaccharide.

Burrell *et al*<sup>37</sup> generated images of a range of metabolites in wheat grains by looking in positive and negative ion mode using  $\alpha$ -cyano-4-hydroxycinnamic acid and 9-aminoacridine respectively. The images show the distribution and variation in abundance of metabolites in specific regions of a wheat grain at a micromolar concentration.



**Fig. 31 Optical and MALDI-MS images of a wheat grain section. (a) Optical image of wheat grain section, (b) Image generated from  $m/z$  175.1195 and (c) Image generated from  $m/z$  381.0799.<sup>37</sup>**

Fig. 31 shows (a) optical image of the wheat grain, (b) the distribution of arginine at  $m/z$  175.1195 with the darker regions indicating higher abundance and (c) the distribution of sucrose at  $m/z$  381.0799. The images in Fig. 31 show that MALDI-MSI is able to distinguish the localization of the two compounds within the wheat grain which are quite different. The sample stage moved 100  $\mu\text{m}$  in the x and y dimensions between laser acquisitions at each point on the sample which is equal

to the pixel size in the image. The average size of a cell within a wheat grain ranges from 10-150  $\mu\text{m}$ <sup>38</sup>.

In a previous study Mullen *et al*<sup>39</sup> have reported preliminary investigations into the determination of agrochemicals in soya plants by MALDI-MSI. The results show that mesotrione can be detected on the surface of a leaf by direct analysis of the freeze dried leaf and indirect blotting method. Azoxystrobin was also detected both on the surface of a leaf and with the plants transport system<sup>39</sup>.

For direct and blotting analysis the compounds were pipetted directly onto the leaf surface. Root absorbance into the plant systems was performed using a hydroponics setup adding the compound to the nutrient solution.

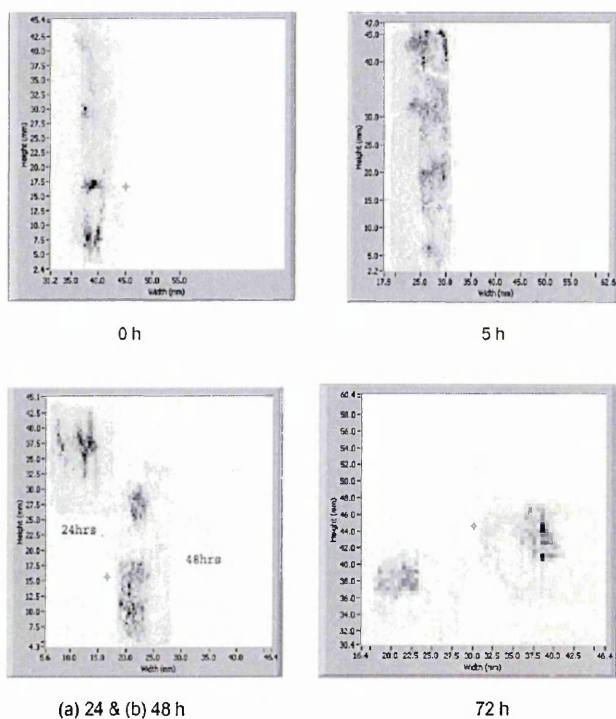


Fig. 32 MALDI-MS images generated from the direct analysis of mesotrione on the surface of soya leaves at 0, 5, 48 and 72 hours after application. Images were generated from the abundance of the fragment ion at  $m/z$  291.03.<sup>39</sup>

Fig. 32 shows MALDI-MS images generated from the direct analysis of mesotrione on the surface of freeze dried soya bean leaves 0, 5, 24, 48 and 72 hours following application.

Fig. 33 shows MALDI-MS images generated from the direct analysis of azoxystrobin on the surface of freeze dried soya bean leaves 0, 5, 24, 48 and 72 hours following application. The images observed in Fig. 32 and 33 show that the spatial resolution of the compound distribution varies from image to image, this could be improved with method development. With further modifications a quantification method might be developed to assess the absorption rate from foliar application. Fig. 34 shows MALDI-MS images generated from the blot analysis of azoxystrobin on the surface of a cellulose membrane taken from the leaf surface 0, 5, 24 and 72 hours following application.

The images generated using the blot analysis show improved and reproducible spatial resolution for the distribution of the compound.

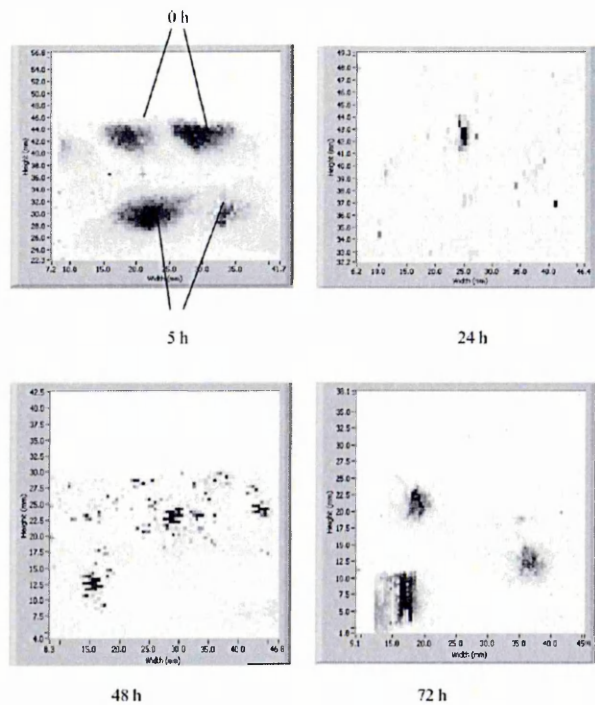


Fig. 33 Images generated from the direct analysis of azoxystrobin on the surface of soya leaves at 0, 5, 48 and 72 hours after application. Images were generated from the abundance of the fragment ion at  $m/z$  372.04.<sup>39</sup>

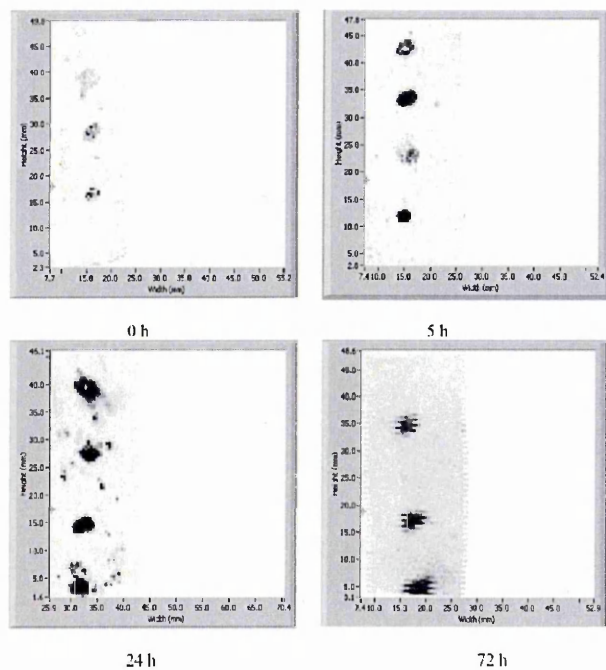


Fig. 34 Images generated from blot analysis of azoxystrobin on the surface of soya leaves at 0, 5, 24 and 72 hours after initial application. Images were generated from the abundance of the fragment ion at  $m/z$  372.04.<sup>39</sup>

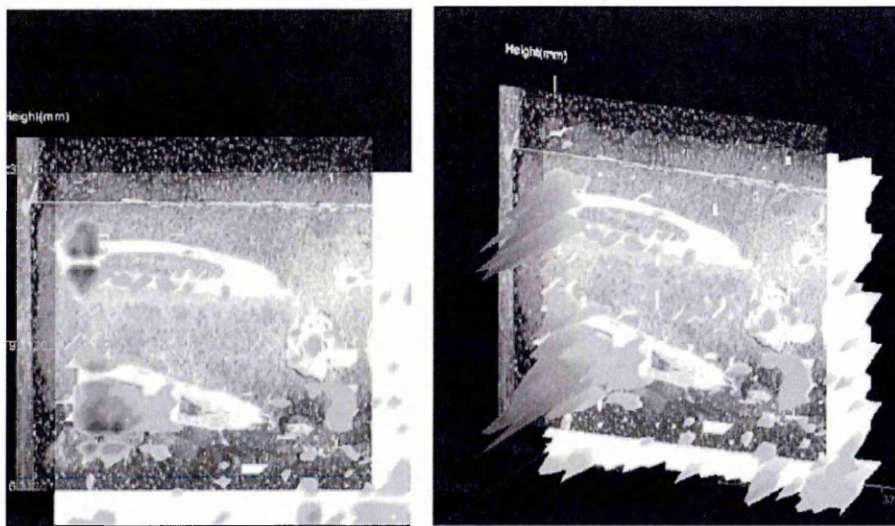


Fig. 35 Image generated from the overlay of the azoxystrobin mass spectrometry image over a digital image of the sample. Image generated from the fragment ion at  $m/z$  372.04.<sup>39</sup>

The image in Fig. 35 was generated from the azoxystrobin hydroponics experiment with 2 horizontal stem section samples using oMALDI server 5.0 3-D display. These data indicate that the compound was localised to specific regions towards the centre of the stem in the lower stem section and in the outer edge in the upper stem section. The abundance is visualised as a 3-D plot using peaks and colour (black and white image does not demonstrate this) as a measure of a compound abundance.

This study provides evidence that MALDI-MSI has great potential as an analytical technique to detect and assess the foliar and root uptake of agrochemicals, to reveal their distribution through the plant once absorbed and translocated.

## 1.5.1 Ion Formation Mechanisms in UV-MALDI

Although the exact reaction methods associated with MALDI are not yet fully understood, there have been many proposed ionisation mechanisms<sup>40</sup>. There are many different theories regarding the reactions that occur in ion formation in the MALDI process. There is an increasing consensus amongst researchers that a two-step model exists, first primary ionisation event being followed by extensive secondary reactions in the plume. These secondary reactions occur in the desorbed expanding plume material as matrix and analyte molecules interact<sup>41</sup>.

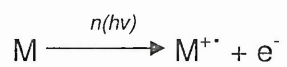
A number of mechanisms have been proposed for the primary ionisation event.

### (i) Desorption of Preformed Ions

An important primary ion formation pathway is the desorption of preformed ions<sup>42</sup>. In this mechanism the ions observed in the MALDI spectrum, e.g. metal adducts are believed to be already present in the sample and are ejected in to the gas phase by the laser pulse.

### (ii) Multiphoton Ionisation

Multiphoton ionisation is the formation of matrix radical cations by absorbing the energy from a number of laser photons, it can be represented by the following equation whereby a matrix cation radical is formed<sup>43</sup>.



M = Matrix molecule

M<sup>+·</sup> = Radical cation

e = electron

h = Plank's constant (the proportionality constant between the photon energy (E)

and the frequency of the corresponding radiation frequency)

$\nu$  = radiation frequency (electromagnetic wave)

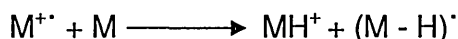
### (iii) The Cluster Model

Introduced by Karas *et al*<sup>44</sup>, this model assumes that a large protonated analyte clusters are preformed in the chemical matrix<sup>45</sup>. The concept behind the cluster model is that post irradiation of the sample by the laser, the clusters are desorbed and in the gas phase neutral matrix molecules are desolvated and analyte ions are created.

### (iv) Gas-phase Proton Transfer

Since reactions between matrix molecules do occur in the plume, the formation of reaction intermediates may be a fundamental requirement for the protonation of analytes<sup>46</sup>.

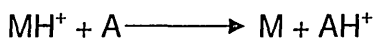
Protonated matrix formation



The radical formed in the above reaction can be converted into  $(M-H)^-$  if it reacts with a free electron.



Reactions can also occur between the matrix and the analyte, very often these reactions produce protonated species. These are thought to occur after secondary proton transfer reactions have taken place in the plume.

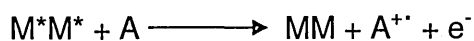
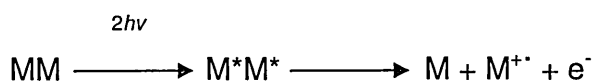


The creation of ions by gas phase reactions has been reported as a feasible mechanism for ionisation by Wang *et al*<sup>47</sup>.

#### (v) Energy Pooling

This details the role of MALDI matrix excitation states and explains the energetic processes underpinning a 'diffusely excited solid'. The internal energy of two or more excited state matrix molecules pooling together (represented in the equation as  $M^*M^*$ ) to form one matrix radical cation ( $M^{+\cdot}$ )<sup>41</sup>.

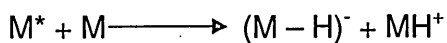
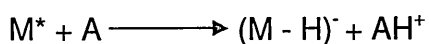
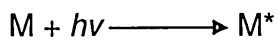
This approach is conceivable as clusters often form in MALDI plumes, the following equations detail the process.



#### (vi) Excited-state Proton Transfer

This is a popular theory that involves one photon where a single excited matrix molecule ( $M^*$ ) can efficiently transfer a labile proton to the analyte/matrix molecule in the ground state<sup>41</sup>.

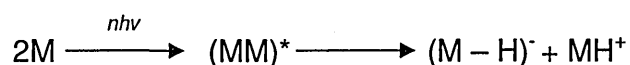
The following equations detail this theory:



### (vii) Disproportionation Reactions

It is proposed that disproportionation reactions may hold the key to the fact that some matrices perform better in positive ion mode and others in negative ion mode <sup>48, 49</sup>.

The following equations detail this theory:



### (viii) Thermal Ionisation

Thermal ionisation is a very likely mechanism when particle suspension matrices have been utilised in the experiment. This is due to the fact that this particular type of matrix is composed of fine particles and do not possess a chromophore or have the ability to co-crystallise with the analyte. Thermal ionisation can occur in two ways, at the particle surface as expressed using the Saha-Langmuir equation <sup>50</sup> or via a disproportionation reaction that incorporates electron affinity of the matrix. It has also been inferred that laser induced damage on the crystalline surface, approximately 1  $\mu\text{m}$  in thickness, causes desorption of ions to occur. When comparing a UV laser to an IR laser the IR laser penetrates much deeper into the sample <sup>41,50</sup>.

### 1.5.2 Similar to Primary Ion Formation a Number of Mechanisms have been Proposed for Secondary Ion Formation

#### (i) Electron Transfer

A feasible reaction in the plume may involve electron transfer, this process is detailed in the following equation whereby reactions are thought to occur between the matrix radical cation and an analyte molecule.



The electron transfer reactions have been supported by published literature when the compounds of interest have low ionisation potentials <sup>50</sup>.

#### (ii) Proton Transfer

Gas phase proton transfer reactions with neutral matrix and neutral analyte molecules when the primary ions are radical cations have been reported in the literature <sup>51</sup>. The free energy change of matrix-analyte and analyte-analyte reactions in the plume can be selected in the mass spectrum.

$$\Delta G = RT \ln(K)$$

K = Calculated from the relative abundances of ions in the mass spectrum that are thought to be involved in charge transfer reactions in the plume <sup>51</sup>.

#### (ii) Cationisation

Cationisation is the term given to the process where the analyte is primarily ionised by the forming of metal ion adducts. This has been shown to be a process commonly observed with carbohydrates and synthetic polymers <sup>52, 53, 54, 55</sup>.

Zhang *et al.* have investigated the role of the matrix in the cationisation process<sup>56</sup>.

## 1.6 Suppression effects

Matrix ions including protonated, cationized matrix and radical cations can be completely suppressed by analytes at certain concentration ratios. This effect relates to the secondary reactions and depends on the analyte polarity i.e. basic analyte strongly deplete protonated matrix<sup>41</sup>.

Analyte suppression effects can occur in the presence of multiple analytes via secondary reactions as they undergo reactions with matrix ions and each other



If B has a lower ionisation potential than A, B will react more efficiently with  $M^+$  than A and  $A^+$  will signal will decrease. Charge transfer between  $A^+$  and B can also occur reducing  $A^+$  signal

This can cause further issues in the analysis of mixtures, as is the case for direct tissue analysis. The individual proton accepting efficiencies of each analyte in the case of positive ion mode, will differ causing them to react differently with  $M^+$ . This results in the analyte with the higher proton accepting efficiency being observed at high intensity and the analyte with the lower proton accepting efficiency being suppressed. As the number of  $M^+$  matrix ions formed in the primary reactions are limited and is related to the laser fluence<sup>41</sup>.

## 1.6 Conclusions

There are a number of methods currently available to assess the translocation of agrochemicals in plants each with their own benefits and limitations. Confocal microscopy and SIMS yield very informative results at a cellular level, although they are not suitable for visualisation of compounds throughout the whole plant system. DESI offers an attractive alternative because it can be performed by direct tissue analysis at atmospheric pressure although initial results obtained by Syngenta suggested its sensitivity towards agrochemicals is limited. Autoradiography certainly provides the most informative results for compound distribution within the plant systems but radiosynthesis is very expensive and can be time consuming for new compounds in the early stages of development.

MALDI has yielded excellent results from the analysis of endogenous compounds in plant tissue and MALDI-MSI is a proven technique in many areas with rapidly growing interest from mass spectrometry operators, research groups and instrument manufactures leading to new developments for applications and instrument design.

MALDI-MSI has great potential and with further method development should be able to yield much more information than autoradiography such as metabolite distribution and quantification. The aims of this research degree are to utilize the MALDI-MSI technique to show the extent of translocation of various agrochemicals following uptake via the roots and absorption following foliar application after varying time points. It is also proposed to utilize the ability of MALDI-MSI to obtain data for agrochemical metabolite distribution in the plant after translocation.

## 1.7 References

1. Ashton F. M and Crafts A. S. Mode of Action of Herbicides. Wiley International Publication, USA.
2. Hassall K. A. The Biochemistry and Uses of Pesticides second edition. MacMillan LTD. Japan.
3. Esau K. (1965) Plant Anatomy. Wiley International Edition, Japan.
4. Taiz L. and Zeiger E. Plant Physiology fourth edition Sinaver Associations Inc.
3. Wyss P. and Bolsinger M. (1997) Translocation of Pymetrozine in Plants. *Pesticide Science* 50: 195-202.
6. Bartlett M. G., Fraser D. W., Hawkes T. E. M., Holt T. R., Townson D. C., Wichert D. C. and Rex A. (2001) Mesotrione: a new selective herbicide for use in maize. *Pesticide Management Science* 57: 120-128.
7. Mäkelä P., Peltonen-Sainio P., Jokinen K., Pehu E., Setälä H., Hinkkanen R. and Somersalo S. (1996) Uptake and translocation of foliar-applied glycinebetaine in crop plants. *Plant Science* 121: 221-230.
8. Zhiqian L. and Gaskin R. E. (2004) Visualisation of the uptake of two model xenobiotics into bean leaves by confocal laser scanning microscopy: diffusion

pathways and implication in phloem translocation. *Pest Management Science* 60: 434-439.

9. Rogers, A.W. (1973) *Techniques of Autoradiography*, 2nd Edition, Elsevier Scientific Publishing Company, Amsterdam.

10. Wyss P. and Bolsinger M. (1997) Translocation of Pymetrozine in Plants. *Pesticide Science* 50: 195-202.

11. Weichel L. and Nauen R. (2004) Uptake, translocation and bioavailability of imidacloprid in several hop varieties. *Pest Management Science* 60: 440-446.

12. Hoffmann E-D. and Stroobant (2005) *Mass Spectrometry Principles and Applications*. John Wiley & Sons Ltd. England

13. Dérue C., Gibouin D., Verdus M-C., Lefebvre F., Demarty M., Ripoll C. and Thellier M. (2002) Appraisal of SIMS Applicability to Boron Studies in Plants. *Microscopy Research and Technique* 58: 104-110.

14. Bennett, B. D., Zha X. H., Gay I. and Morrison G. H. (1992) Intracellular Boron Localization and Uptake in Cell-Cultures using Imaging Secondary Ion Mass-Spectrometry (ion microscopy) for Neutron-Capture Therapy for Cancer. *Biology of the Cell* 74: 105-108.

15. Tanaka K., Waki H., Ido Y., Akita S., Yoshida Y., Yoshida T., and Matsuo T. (1988) Protein and polymer analyses up to  $m/z$  100 000 by laser ionization time-of-flight mass spectrometry. *Rapid Communications in Mass Spectrometry* 2: 151-153.
16. Karas M. and Hillenkamp F. (1988) Laser desorption ionization of proteins with molecular masses exceeding 10,000 daltons. *Analytical Chemistry* 60: 2299-2301.
17. Chaurand P., Schwartz S. A., and Caprioli R. M. (2004) Assessing Protein Patterns in Disease Using Imaging Mass Spectrometry. *Journal of Proteome Research* 3: 245-252.
18. Chaurand P., Schwartz S. A. and Caprioli R. M. (2004) Profiling and Imaging Proteins in Tissue Sections by MS. *Analytical Chemistry* 76 (5): 86A-93A.
19. Schwartz S. A., Weil R. J., Johnson M. D., Toms S. A. and Caprioli R. M. (2004) Protein Profiling in Brain Tumors Using Mass Spectrometry. *Clinical Cancer Research* 10: 981-987.
20. Bunch J., Clench M. R. and Richards D. S. (2004) Determination of pharmaceutical compounds in skin by imaging matrix-assisted laser desorption/ionisation mass spectrometry. *Rapid Communications in Mass Spectrometry* 18: 3051-3060.

21. Reyzer M. L., Hsieh Y., Ng K., Korfmacher W. A. and Caprioli R. M. (2003) Direct analysis of drug candidates in tissue by matrix-assisted laser desorption/ionization mass spectrometry. *Journal of Mass Spectrometry* 38: 1081-1092.
  
22. Caprioli R. M., Farmer T. B. and Gile J. (1997) Molecular Imaging of Biological Samples: Localization of Peptides and Proteins Using MALDI-TOF MS. *The Journal of Analytical Chemistry* 69: 4751-4760.
  
23. Atkinson S.J., Prideaux B., Bunch J., Warburton K.E. and Clench M.R. (2005) Imaging Matrix assisted laser desorption ionisation mass spectrometry - A new technique for drug distribution studies. *Chimica Oggi-Chemistry Today* 23: 5-8.
  
24. Goodwin R.J., Pennington S.J. and Pitt A.R. (2008) Protein and peptides in pictures: Imaging with MALDI mass spectrometry. *Proteomics* 18: 3785-3800.
  
25. Troendle F.J., Reddick C. D., and Yost R.A. (1999) Detection of pharmaceutical compounds in tissue by matrix-assisted laser desorption/ionization and laser desorption/chemical ionization tandem mass spectrometry with a quadrupole ion trap. *Journal of The American Society for Mass Spectrometry* 10: 1315-1321.
  
26. Stoeckli M., Staab D. and Schweitzer A. (2006) Compound and metabolite distribution measured by MALDI mass spectrometric imaging in whole-body tissue sections. *International Journal of Mass Spectrometry* 260: 195-202.

27. Altelaar A.F. M., Taban I. M., McDonnell L. A., Verhaert P. D.E.M., Lange R. P.J., Adan R. A.H., Mooi W. J., Heeren R. M.A. and Piersma S. R. (2007) High-resolution MALDI imaging mass spectrometry allows localization of peptide distributions at cellular length scales in pituitary tissue sections. *International Journal of Mass Spectrometry*. 260: 203-211.
28. Holle A., Haase A., Kayser M. and Höhndorf J. (2006) Optimizing UV laser focus profiles for improved MALDI performance. *Rapid Communications in Mass Spectrometry* 41: 705-716.
29. Takáts Z., Wiseman J. M., Gologan B. and Cooks G. R. (2004) Mass spectrometry Sampling Under Ambient Conditions with Desorption Electrospray Ionization. *Science* 306: 471-473.
30. Ifa D. R., Wiseman J. M., Song Q. and Cooks G. R. (2007) Development of capabilities for imaging mass spectrometry under ambient conditions with desorption electrospray ionization (DESI). *International Journal of Mass Spectrometry* 259: 8-15.
31. Kertesz V. and Berkei G. J. V. (2008) Improved imaging resolution in desorption electrospray ionization mass spectrometry. *Rapid Communication in Mass Spectrometry* 22: 2639-2644.

32. Stahl B., Linos A., Karas M., Hillenkamp F and Steups M. (1997) Analysis of fructans from higher plants by matrix-assisted laser desorption/ionization mass spectrometry *Analytical Biochemistry* 246: 195-204.
33. Slusznycy C. and Yeung E. S. (2004) In-situ probing of the biotic-abiotic boundary of plants by laser desorption/ionization time-of-flight mass spectrometry. *Journal of the American Society for Mass Spectrometry* 16: 107-115.
34. Wu W., Liang Z., Zhao Z. and Cai Z. (2007) Direct analysis of alkaloid profiling in plant tissue by using matrix-assisted laser desorption/ionization mass spectrometry *Journal of Mass Spectrometry*. 42: 58-69.
35. Wu W., Gao C., Liang Z., Hu H., Zhao Z. and Cai Z. (2007) Alkaloid profiling in crude and processed *Strychnos nux-vomica* by matrix-assisted laser desorption/ionization-time of flight mass spectrometry. *Journal of Pharmaceutical and Biomedical Analysis*. 45 430-436.
36. Robinson S., Warburton K., Seymour M., Clench M. and Thomas-Oates J. (2006) Localization of water-soluble carbohydrates in wheat stems using imaging matrix-assisted laser desorption ionization mass spectrometry. *New Phytologist* 173: 438-444.
37. Burrell M. M., Earnshaw C. J. and Clench M. R. (2007) Imaging Matrix Assisted Laser Desorption Ionisation Mass Spectrometry: a technique to map

plant metabolites within tissues at high spatial resolution. *Journal of Experimental Botany* 58: 757-763.

38. Tosi P., Parker M., Gritsch C. S., Carzaniga R., Martin B., and Shewry P. R. (2009) Trafficking of storage proteins in developing grain of wheat. *Journal of Experimental Botany*. 60(3): 979–991

39. Mullen A. K., Clench M. R., Crosland S. and Sharples K. R. (2005) Determination of agrochemical compounds in soya plants by imaging matrix-assisted laser desorption/ionisation mass spectrometry. *Rapid Communications in Mass Spectrometry* 19: 2507-2516.

40. Karbach V. and Knochenmuss R. (1998) Do Single Matrix Molecules Generate Primary Ions in Ultraviolet Matrix-assisted Laser Desorption/Ionization. *Rapid Communications in Mass Spectrometry* 12, 968-974.

41. Knochenmuss R. (2006) Ion formation mechanisms in UV-MALDI. *Analyst*. 131, 966-986.

42. E. Lehmann and R. Zenobi (1998) Detection of Specific Noncovalent Zinc Finger Peptide- Oligodeoxynucleotide Complexes by Matrix-Assisted Laser Desorption/Ionization Mass Spectrometry, *Angew. Chem. Int. Ed.* **37** 3430–3432.

43. Brown T., Clipston N. L., Simjee N., Luftmann H., Hungerbuhler H. and Drewello T. (2001) . *International Journal of Mass Spectrometry*. 210, 249-263.

43. Karas M., Kruger R. (2003) Ion formation in MALDI: the cluster ionisation mechanism. *Chemical Reviews* 103, 427-439.
44. Liao P. C., Allison J. (1995) Ionisation processes in matrix assisted laser desorption/ionisation mass spectrometry: matrix dependent formation of  $[M+H]^+$  and  $[M+Na]^+$  ions of small peptide and some mechanistic comments. *Journal of Mass Spectrometry* 30, 408-423.
45. Ehring H., Karas M. and Hillenkamp F. (1992) Role of photoionisation and photochemistry in ionisation processes of organic molecules and relevance for matrix-assisted laser desorption/ionisation mass spectrometry. *Organic Mass Spectrometry*. 27, 427-480.
46. Wang *et al.* Wang B. H., Dreisewerd K., Bahr U., Karas M. and Hillenkamp F. (1993) Gas-Phase cationization and protonation of neutrals from MALDI. *Journal of the American Society for Mass Spectrometry* 30, 408-423.
47. Busch K. L. (1995) Desorption-ionisation mass spectrometry. *Journal of Mass Spectrometry*. 30, 230-240.
48. Breuker K., Knochenmuss R. and Zenobi R. (1999) Gas-phase basicities of deprotonated matrix-assisted laser desorption/ionisation molecules. 184, 25-38.
49. Lehmann E., Knochenmuss R. and Zenobi R. (1997) Ionisation mechanisms in matrix-assisted laser desorption/ionisation mass spectrometry: contribution of pre-formed ions. *Rapid Communications in Mass Spectrometry*. 11, 1483-1492.

50. Knochenmuss R., Stortelder A., Breuker K., Zenobi R. (2000) Secondary ion-molecule reactions in matrix-assisted laser desorption/ionisation. *Journal of Mass Spectrometry* 35, 1237-1245.
51. Karas M. Gluckmann M. and Schafer J. Ionisation in the matrix-assisted laser desorption/ionisation: single charged molecular ions are the lucky survivors. *Journal of Mass Spectrometry*. 35, 1-12.
52. Wong C. K. L. and Chan T-W. D. (1997) Cationization processes in matrix-assisted laser desorption/ionization mass spectrometry: Attachment of divalent and trivalent metal ions. *Rapid Communications in Mass Spectrometry*. 11, 513-519.
53. Bogan M. J. and Agnes G. R. (2003) Time-of-flight mass spectrometry analysis of ions produced from adjacent sample spots irradiated simultaneously by a single 337 nm laser. *Rapid Communication in Mass Spectrometry* 17 2557-2562.
54. Erb W. J., Hanton S. D. and Owen K. G. (2006) A study of gas-phase cationisation in matrix-assisted laser desorption/ionisation time of flight mass spectrometry. *Rapid Communications in Mass Spectrometry*. 20, 2165-2169.
55. Zhang J. and Zenobi R. (2004) Matrix-dependent cationisation in MALDI mass spectrometry. *Journal of Mass Spectrometry* 39, 808-816.

56. Zhang J. and Zenobi R. (2004) Matrix-dependent cationisation in MALDI mass spectrometry. *Journal of Mass Spectrometry* 39, 808-816.

## **Chapter Two: Detection of Agrochemicals on Leaf**

## 2.1 Introduction

The structure of a leaf is generally comprised of epidermis tissue which sandwiches both the palisade and spongy mesophyll between an upper and lower layer (Fig. 1). These tissues are highly specialized for light absorption<sup>2</sup>.

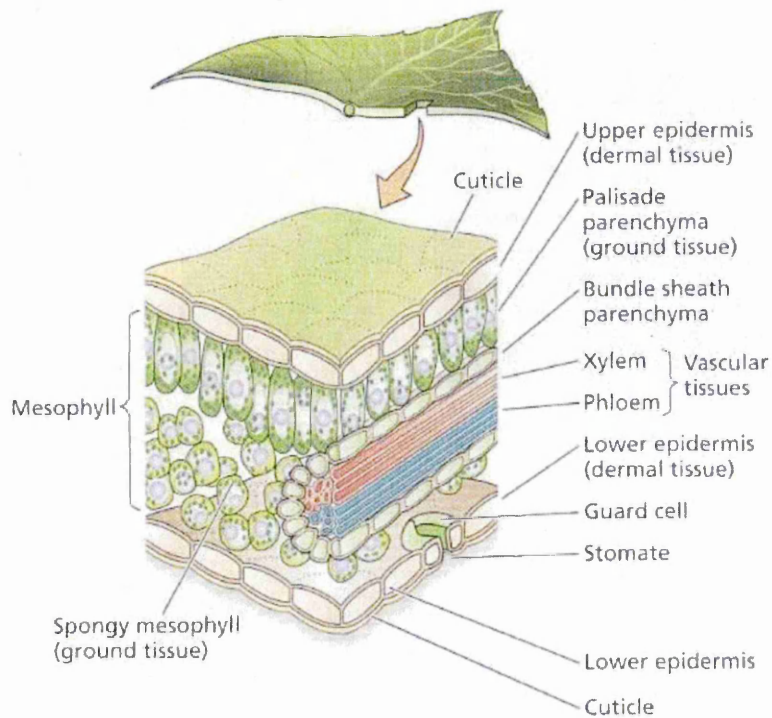


**Fig. 1 Cross sectional representation of leaf cell structure. <sup>1</sup>**

The epidermis layer is typically transparent and the individual cells are often convex and hence can act as lenses so that more light reaches the chloroplasts present in the cells underlying this layer. Below the epidermis layer the palisade mesophyll cells are arranged like pillars that stand in parallel columns. Some leaves have several layers of columnar palisade cells although the high chlorophyll content of the first layer allows little transmission of light to the lower layers. Below this is the spongy mesophyll layer where the cells are arranged irregularly to form

air spaces around the stomata where carbon dioxide can enter the plant. The stomata are pores in the lower epidermis which are regulated by specialist epidermal cells called guard cells which lead to the gas space in the spongy mesophyll layer <sup>2</sup>.

The outer epidermal layer is coated in epicuticular waxes forming the outermost boundary layer of the plant (cuticle). This layer consists mainly of two components, the biopolymer cutin and lipids which form a complex mixture of long chain aliphatic components, primary and secondary alcohols, aldehydes and ketones also cyclic components like triterpenes or flavonoids <sup>3</sup>. The major function of this layer is to prevent water loss by acting as a barrier which in turn also prevents compounds absorbing into the leaf by creating a hydrophobic water-repellent surface. Both relative humidity and water stress affect the development of the cuticle causing it to thicken to combat water loss. Diffusion and translocation can be affected by a number of factors such as temperature, water stress and relative humidity. Relative humidity affects diffusion and translocation of foliar applied herbicides directly because a hydrated cuticle is easy to penetrate and the droplet's drying time is reduced.

The efficacy of foliar-applied herbicides depends on the diffusion of the herbicide into the target plant and translocation around the plant. The diffusion and translocation of herbicides by both the leaves and roots increases with increasing temperature, within physiological limits. Lower temperatures increase the viscosity of water and decrease the permeability of the colloidal gels of cell walls <sup>4</sup>. The

optimum translocation temperature varies between species due to genetic differences.

The aims of this chapter are to show the detection of pesticides on the surface of leaves and to demonstrate their penetration of the waxy cuticle layer at the start of foliar diffusion. It is also proposed to observe translocation from leaf tissue into leaf veins towards the petiole following foliar application.

## **2.2 Methods**

### **2.2.1 Conventional MALDI-MS analysis**

Preparation of mesotrione for the analysis of conventional MALDI spots was carried out using a standard stock solution of mesotrione 1.7 mg/mL in acetone: 0.1% Tween® (Sigma Aldrich, Dorset, UK), (v/v), (50:50).

Sample preparation for azoxystrobin was carried out using a standard stock solution of azoxystrobin 1.9 mg/mL in acetone: 0.1% Tween® (v/v), (50:50).

#### Matrix solution preparation

10 mg/mL solutions of the desired matrix were prepared in 10 mL volumetric flasks using acetone as a solvent. The solutions were sonicated for 5 minutes to ensure all organic acid had been dissolved.

### MALDI sample preparation

1  $\mu\text{L}$  of the above solutions were combined with 1  $\mu\text{L}$  of the appropriate matrix solution i.e sinapinic acid (Sigma Aldrich, Dorset, UK) for mesotrione and  $\alpha$ -cyano-4-hydroxycinnamic acid ( $\alpha$ -CHCA) (Sigma Aldrich, Dorset, UK) for azoxystrobin. Solutions were mixed and 1  $\mu\text{L}$  was pipetted onto a well of a conventional stainless steel MALDI target.

### Instrumentation

Spectra were obtained using an Applied Biosystems/MDS Sciex Q-star pulsar star pulsar / hybrid quadrupole time of flight mass spectrometer (Concord, Ontario, Canada) fitted with an orthogonal MALDI source and a nitrogen laser at a laser power of 20  $\mu\text{J}$  and a laser repetition rate of 20 Hz.

### **2.2.2 Indirect MALDI imaging analysis of azoxystrobin from leaf surface**

Soya bean leaves were spotted with 2x 1  $\mu\text{L}$  and 2x 2  $\mu\text{L}$  of a 1.9 mg/mL solution of azoxystrobin 50:50 acetone:0.1% Tween® (Sigma Aldrich, Dorset, UK), one spot of each volume on each side of the midrib avoiding the main veins in the leaf. The solutions were then left to dry before removing the leaf at the petiole. This sample was then secured to a flat surface using double sided tape. A standard cellulose membrane (Whatman®, Kent, UK) (5cm diameter) was saturated in acetone. Excess solvent was removed and the membrane was air dried for 30 seconds before placing it on the inoculated leaf surface area. The compound was then transferred to the membrane under defined pressure (moderately firm pressing with finger tips) for 30 seconds. Cellulose membranes were coated with

approximately 20 mL of matrix,  $\alpha$ -CHCA (10 mg/mL 0.1% TFA in acetone) using an Iwata gravity-fed pneumatic air spray gun (Iwata Media Inc., Portland, OR, USA). Matrix coated membranes were then mounted into a MALDI target using conductive tape.

The appropriate areas were then imaged using an Applied Biosystems/MDS Sciex Q-star pulsar / hybrid quadrupole time of flight mass spectrometer (Concord, Ontario, Canada) fitted with an orthogonal MALDI source and an Nd:YAG laser at a laser power of 3.2  $\mu$ J and a laser repetition rate of 1000 Hz . Images were acquired with a spatial resolution of 200  $\mu$ m x 200  $\mu$ m.

### **2.2.3 Absorption of mesotrione using cell stripping and direct analysis of leaf (matrix sinapinic acid)**

Soya bean leaves were spotted with 2x 5  $\mu$ L of a 2.5 mg/mL solution of mesotrione 50:50 acetone: 0.1% Tween®, one spot each side of the midrib avoiding the main veins in the leaf. The solutions were then left for the desired time period (6, 24, 48 and 72 hours) before removing the leaf at the petiole. This sample was then secured to a flat surface and the top layer of cells was removed using a d-squame disc (CuDerm, Texas, USA), the sample was then placed between two microscope coverslips ensuring it remained flat. The sample was then freeze dried for 24 hours before being attached to the MALDI target plate. The matrix (10 mg/mL sinapinic acid in acetone, ~10 mL) (Sigma Aldrich, Dorset, UK) was applied using an Iwata gravity-fed pneumatic air spray gun (Iwata Media Inc., Portland, OR, USA) by passing the compressed air gun over the sample 15 times, ensuring the sample tissue did not get saturated and even coverage had been achieved.

The appropriate areas of the leaf were imaged using an Applied Biosystems Voyager-DE PRO MALDI time-of-flight mass spectrometer (Concord, Ontario, Canada) equipped with a N<sub>2</sub> laser (337 nm wavelength) in negative ion mode with sample stage increments of 150 micron along the x and y dimensions. 100 shots per pixel at a laser power of 2674 were used for the image acquisition experiment. Images were acquired using MMSIT software and processed using BIOMAP [<http://maldi-msi.org>]

#### **2.2.4 Comparison of 9-aminoacridine and sinapinic acid and the effect of gold sputter coating.**

Soya bean leaves were spotted with 2 µl of a 2.5 mg/mL mesotrione solution in 50/50 acetone 0.1% Tween® (Sigma Aldrich, Dorset, UK). This was performed four times. The spots were left to dry before the leaf was removed from the plant. The leaf sample was then trimmed down using a surgical blade and the appropriate areas were sandwiched between 2 microscope cover slips and freeze dried for 24 hours. Two samples were sprayed with sinapinic acid (Sigma Aldrich, Dorset, UK), (10 mg/mL, 100% acetone, ~10 mL) and two samples were sprayed with 9-aminoacridine (Sigma Aldrich, Dorset, UK), (10mg/mL, 100% acetone, ~10mL) using an Iwata gravity-fed pneumatic air spray gun (Iwata Media Inc., Portland, OR, USA) by passing the compressed air gun over the sample 15 times, ensuring the sample tissue did not get saturated and even coverage had been achieved. These 4 samples were then mounted onto a target plate. One of each of the 9- aminoacridine and the sinapinic acid coated samples was then sputter coated in gold ≈1 µm thickness (Emitech K950, Ashford, Kent, UK,).

The appropriate areas of the leaf were imaged using an Applied Biosystems Voyager-DE PRO MALDI time-of-flight mass spectrometer (Concord, Ontario, Canada) equipped with a N<sub>2</sub> laser (337 nm wavelength) in negative ion mode with sample stage increments of 150 micron along the x and y dimensions. 100 shots per pixel at a laser power of 2674 were used for the image acquisition experiment. Images were acquired using MMSIT software and processed using BIOMAP [<http://maldi-msi.org>].

### **2.2.5 Direct MALDI imaging analysis of mesotrione on plant tissue - examination of the absorption of mesotrione using cell stripping**

Soya bean leaves were spotted with 5 µL of the 2.5 mg/mL solution of mesotrione avoiding the main veins in the leaf. The solutions were then left for the desired time period (0, 1, 2 and 3 hours) before removing the leaf at the petiole. These samples were then secured to a flat surface and the top layer of cells was removed using d-squame strips (CuDerm, Texas, USA), the sample was then freeze dried for 24 hours. The sample was then freeze dried for 24 hours before being attached to the MALDI target plate. The matrix (10 mg/mL 9-aminoacridine (Sigma Aldrich, Dorset, UK) 100% acetone, ~10 mL) was applied using an Iwata gravity-fed pneumatic air spray gun (Iwata Media Inc., Portland, OR, USA) by passing the compressed air gun over the sample 15 times, ensuring the sample tissue did not get saturated and even coverage had been achieved followed by a layer of gold sputter coating, ≈1 µm thickness. (Emitech K950, Ashford, Kent, UK.). The appropriate areas of the leaf were imaged using an Applied Biosystems Voyager-DE PRO MALDI time-of-flight mass spectrometer (Concord, Ontario, Canada) equipped with a N<sub>2</sub> laser (337 nm wavelength) in negative ion mode with

sample stage increments of 150 micron along the x and y dimensions. 100 shots per pixel at a laser power of 2674 were used for the image acquisition experiment. Images were acquired using MMSIT software and processed using BIOMAP [<http://maldi-msi.org>].

## **2.2.6 Direct MALDI imaging analysis of mesotrione in leaf veins after foliar absorption**

### Control Image

A small section of leaf vein tissue was removed from the plant and the outer most tissue was removed (disrupted to expose the underlying tissue). This tissue was spiked with 1 $\mu$ L of a 2.5 mg/mL mesotrione in 50/50 acetone/0.1% Tween® (Sigma Aldrich, Dorset, UK) solution pipetted onto it. The solution was left to dry and the sample was then freeze dried for 24 hours before being attached to the MALDI target plate. The matrix (10mg/mL 9-aminoacridine 100% acetone, ~10mL), (Sigma Aldrich, Dorset, UK) was applied using an Iwata gravity-fed pneumatic air spray gun (Iwata Media Inc., Portland, OR, USA) by passing the compressed air gun over the sample 15 times, ensuring the sample tissue did not get saturated and even coverage had been achieved followed by a layer of gold sputter coating,  $\approx$ 1  $\mu$ m thickness. (Emitech K950, Ashford, Kent, UK,)

### Sample tissue

A leaf was inoculated with mesotrione near to the apex (leaf tip) on the upper surface. The leaf was then left for a range of time points (5 hours and 20 hours) on the plant. After this time period had elapsed the leaf was removed from the plant and secured to a flat surface and the veins leading to the petiole were

disrupted using a scalpel blade. The sample was then freeze dried for 24 hours before being attached to the MALDI target plate. The matrix (10mg/mL 9-aminoacridine 100% acetone, ~10mL), (Sigma Aldrich, Dorset, UK) was applied using an Iwata gravity-fed pneumatic air spray gun (Iwata Media Inc., Portland, OR, USA) by passing the compressed air gun over the sample 15 times, ensuring the sample tissue did not get saturated and even coverage had been achieved followed by a layer of gold sputter coating,  $\approx 1 \mu\text{m}$  thickness (Emitech K950, Ashford, Kent, UK,).

The appropriate areas of the leaf were imaged using an Applied Biosystems Voyager-DE PRO MALDI time-of-flight mass spectrometer (Concord, Ontario, Canada) equipped with a  $\text{N}_2$  laser ( $\lambda = 337\text{nm}$ ) in negative ion mode with sample stage increments of 150 micron along the  $x$  and  $y$  dimensions, 100 shots per pixel at a laser power of 2674 were used for the image acquisition experiment. Images were acquired using MMSIT software and processed using BIOMAP [<http://maldi-msi.org>]

### **2.2.7 Effect of laser fluence for the detection of mesotrione**

A range of solutions of mesotrione in 50:50 acetone: 0.1% Tween® (Sigma Aldrich, Dorset, UK) were prepared from a stock solution of mesotrione (1.0 mg/mL) in acetone. The concentration range was 0.001, 0.01, 0.025, 0.05, 0.1 mg/mL. 10  $\mu\text{L}$  of these solutions were combined with 10  $\mu\text{L}$  of the matrix solution 9-aminoacridine (Sigma Aldrich, Dorset, UK), (15 mg/mL). 1  $\mu\text{L}$  of these analyte:matrix solutions were pipetted on to the spot target plate in duplicate. The first series of spots was run at 2603 laser power. The second series of spots were

run at 2728 laser power using conventional MALDI-MS analysis with an Applied Biosystems Voyager-DE PRO MALDI time-of-flight mass spectrometer (Concord, Ontario, Canada) equipped with a UV-VQ Nd:YAG laser ( $\lambda = 355\text{nm}$ ) (Elforlight, Daventry, UK) in negative ion mode. The intensities generated were entered into an Excel spread sheet and graphs were generated to compare the intensities of the matrix ion, fragment ion and deprotonated molecule to assess the effect of laser power on the ion intensity of the fragment ion and deprotonated molecule for mesotrione. Using the matrix as an internal standard, the analyte to matrix ratio was calculated to generate the calibration curve.

### **2.2.8 Assessment of suppression effects on the detection of mesotrione using plant extract**

In this experiment 0.5 grams of plant tissue was macerated using a pestle and mortar with the addition of 1mL of 50:50 acetone: 0.1% Tween® (Sigma Aldrich, Dorset, UK). The MALDI sample solutions were prepared by combining 10  $\mu\text{L}$  of the stock solutions with 10  $\mu\text{L}$  of the macerated tissue solution and 20  $\mu\text{L}$  of 9-aminoacridine (Sigma Aldrich, Dorset, UK), (15 mg/mL). These solutions were compared to control solutions which were prepared by replacing tissue extract with an equal volume of 50:50 acetone: 0.1% Tween® (Sigma Aldrich, Dorset, UK) solution as a blank. The spots were then run using conventional MALDI-MS analysis with an Applied Biosystems Voyager-DE PRO MALDI time-of-flight mass spectrometer (Concord, Ontario, Canada) equipped with a UV-VQ Nd:YAG laser ( $\lambda = 355\text{nm}$ ) (Elforlight, Daventry, UK) in negative ion mode at the 2728 laser power setting. This higher laser power (2728) was chosen over the lower laser power (2603) due to the advantageous effects observed in ionization of

mesotrione using the higher laser power resulting in the total ion counts for the matrix and ions relating to mesotrione being much greater. The intensities generated were entered into an Excel spread sheet and graphs were generated to compare the intensities of the matrix ion, fragment ion and deprotonated molecule to assess the effect of the plant tissue on the ion intensity of mesotrione. Using the matrix as an internal standard, the analyte to matrix ratio was calculated to generate the calibration curve.

## 2.3 Results

### 2.3.1 Mesotrione spot samples

The spectrum in Fig. 2 shows the mesotrione deprotonated molecule at  $m/z$  338.07 and a fragment ion at  $m/z$  291.09.

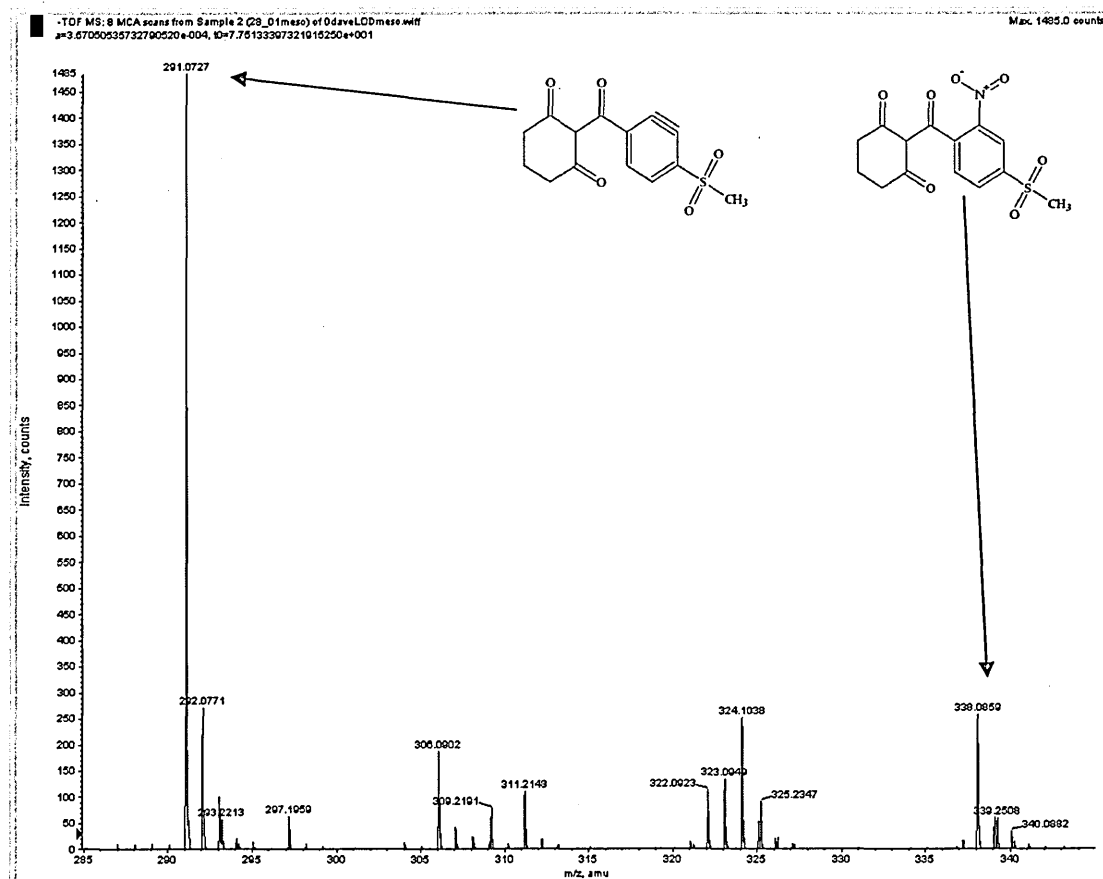


Fig. 2 Negative MALDI-MS spectrum of mesotrione (1.7mg/mL) with sinapinic acid (10mg/mL in acetone) 50:50. Showing the  $[M+H]^+$  ion at  $m/z$  338.07 and a fragment ion at  $m/z$  291.09 and their structures.

The intensity for the fragment ion is greater than that of the deprotonated molecule as the loss of the proton from mesotrione results in an unstable ion species and subsequent fragmentation. These ions were chosen to generate images of the distribution of mesotrione across tissue surfaces, owing to their intensity and structural significance for mesotrione.

### 2.3.1.1 Azoxystrobin spot samples

The spectrum in Fig. 3 shows the azoxystrobin protonated molecule at  $m/z$  404.07 and a fragment ion at  $m/z$  372.04.

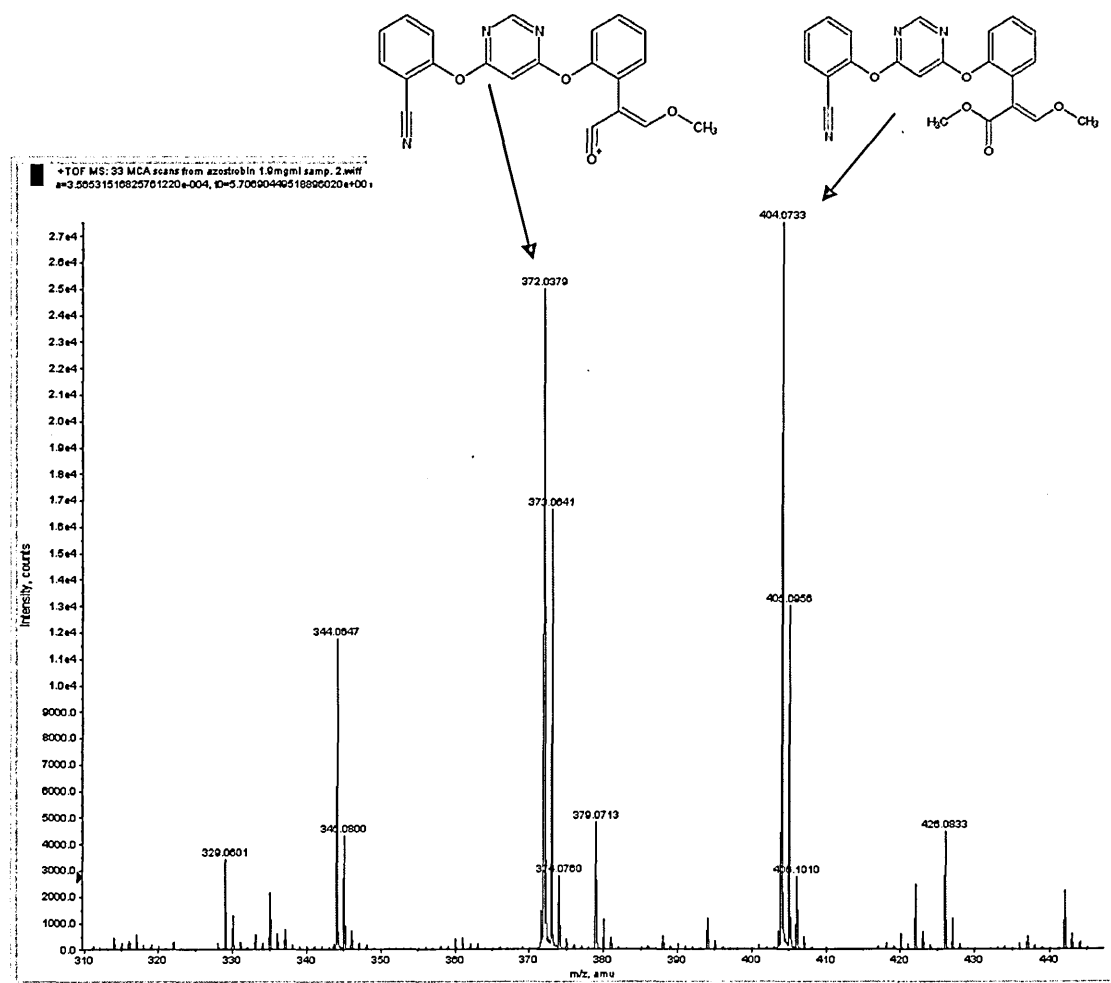


Fig. 3 Positive MALDI-MS spectrum of azoxystrobin (1.9mg/mL) with CHCA (10mg/mL in acetone) 50:50. Showing the  $[M+H]^+$  ion at 404.07 and a fragment ion 372.04 and their structures.

These ions were chosen to generate images to show the distribution of azoxystrobin across tissue and cellulose membrane surfaces.

### **2.3.2.1 Indirect MALDI imaging analysis of azoxystrobin from leaf surface. Initial azoxystrobin result from indirect imaging method**

The image in Fig. 4 generated from the protonated molecule of  $\alpha$ -CHCA from the cellulose membrane shows that a moderately homogeneous matrix coverage was achieved across the cellulose membrane using the gravity feed airgun. It can be seen that the matrix is evenly distributed across the membrane with high ion intensities shown throughout the sample surface. This ion was used to normalise the images in Fig. 5 and 6.

Fig. 5 shows the distribution of the fragment ion of azoxystrobin ( $m/z$  372.09) across the cellulose membrane from 2x 1 $\mu$ L of a 1.9mg/mL solution, (0.0019  $\mu$ g on sample). The spatial integrity of the spot's original location has been lost in this sample. This is possibly due to excessive solvent usage during blotting and/or saturation of the membrane during application of the matrix. This has resulted in azoxystrobin spreading from its original application point and the original spot distribution is unclear. However, the presence of the compound is clearly visible in treated areas. Areas with high abundance of azoxystrobin can easily be distinguished from areas of low abundance through the highly contrasting areas of the image.

Fig. 6 shows the distribution of the protonated molecule of azoxystrobin ( $m/z$  404.12) across the cellulose membrane following application of the compound to the surface of the cellulose membrane. Due to the original distribution of the original location of the compound being distorted the method described in 2.2.1 was repeated. The compound spots were placed further apart on the leaf and more care was taken to ensure the membrane was not too 'wet' before being

applied to the surface of the leaf and that the membrane did not become saturated during the matrix application.

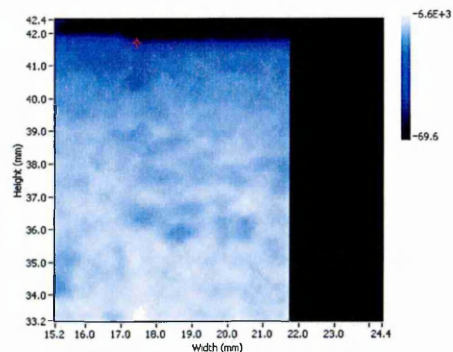


Fig. 4 MALDI-MSI of matrix coverage of protonated  $\alpha$ -CHCA ( $m/z$  190.05) used to normalize the fragment ion and protonated molecule images.

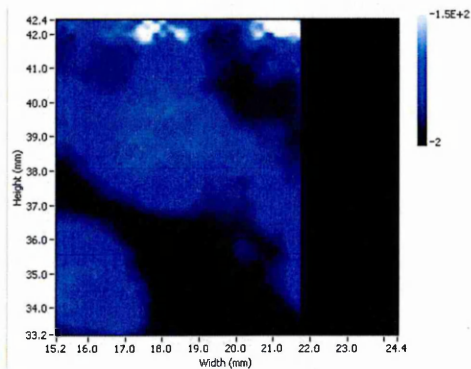


Fig. 5 MALDI-MSI of azoxystrobin's fragment ion at  $m/z$  372.09 on cellulose membrane.

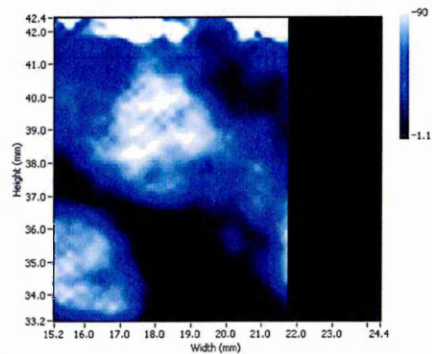


Fig. 6 MALDI-MSI of azoxystrobin's protonated molecule at  $m/z$  404.12.

### 2.3.2.2 Results from revised indirect imaging method

The image in Fig. 7 is of the protonated molecule of  $\alpha$ -CHCA. The image shows good coverage, the matrix is evenly distributed across the membrane and shows good intensity throughout. This ion was used to normalise the images in Fig. 8 and 9.

The image in Fig. 8 is generated from the fragment ion of azoxystrobin at  $m/z$  372.09 shows that the original spots distribution of the 1  $\mu$ L lower left and lower right spots (0.0019  $\mu$ g on sample). The 2  $\mu$ L upper right and upper left spots (0.0038  $\mu$ g on sample) has being retained and can clearly be distinguished from one another. The signal is present with good intensity (indicated by the scale of ion intensity on the right of the image).

Fig. 9 shows the distribution of the protonated molecule at  $m/z$  404.12. Again the original distribution for both spot's volumes location has been retained. The signal for the protonated molecule is present with good intensity (indicated by the intensity scale on the right of the image).

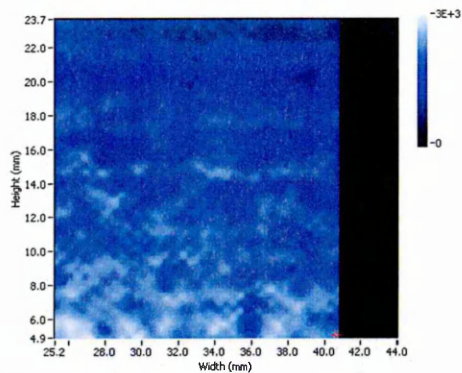


Fig. 7 MALDI-MSI of matrix coverage of the protonated molecule of  $\alpha$ -CHCA ( $m/z$  190.05) used to normalize the fragment ion and protonated molecule images.

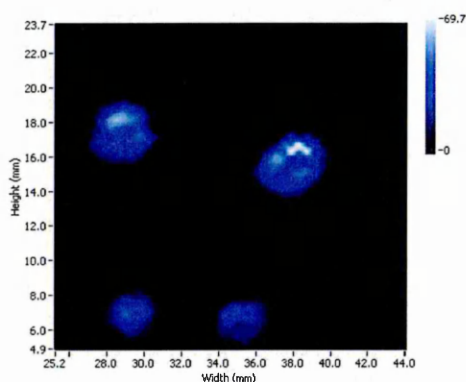


Fig. 8 Image of azoxystrobin fragment ion at  $m/z$  372.09, normalized using the protonated molecule of  $\alpha$ -CHCA.

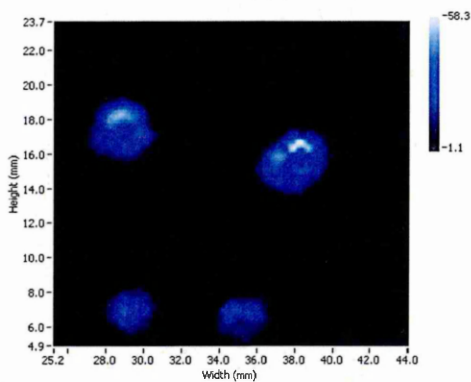


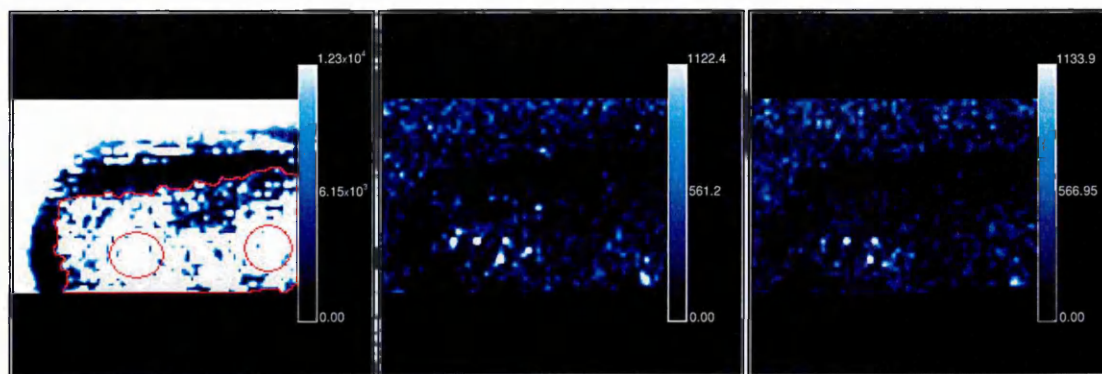
Fig. 9 Image of azoxystrobin protonated molecule at  $m/z$  404.12 ( $2 \times 0.0017\text{mg}$ ), normalized using the protonated molecule of  $\alpha$ -CHCA.

### 2.3.3 Absorption of mesotrione using cell stripping and direct analysis of leaf (matrix sinapinic acid)

Fig. 10 shows MALDI-MS images generated from a sample prepared 6 hours after application of mesotrione. Fig. 11 shows the MALDI-MS images generated from a 24 hour sample. Fig. 12 shows MALDI-MSI generated from a 72 hour sample. The images in Fig. 10 generated from the fragment ion at  $m/z$  291.03 (b.) and the deprotonated molecule at  $m/z$  338.03 (c.) suggests that not enough mesotrione has translocated through the waxy cuticle layer after 6 hours to produce a MALDI signal using sinapinic acid as a matrix. This suggests that the MALDI-MSI method is not sensitive enough to detect mesotrione translocation through the waxy cuticle at this time point.

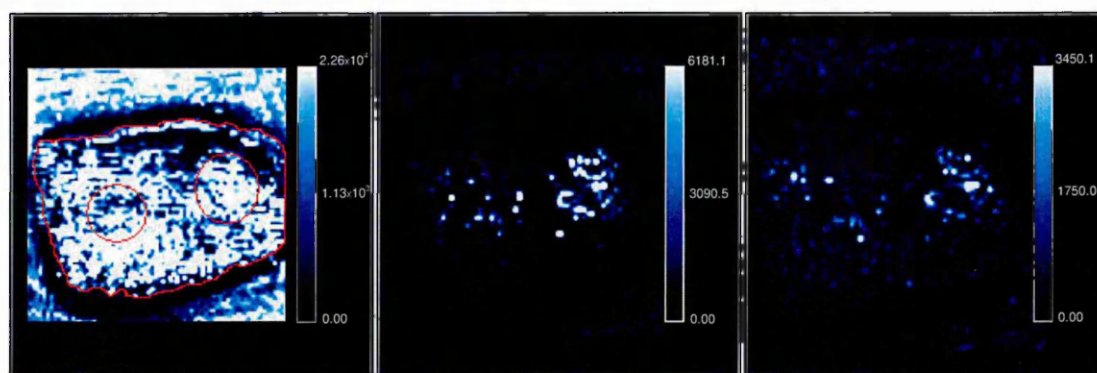
Fig. 11 shows that enough mesotrione is present in the cells underlying the waxy cuticle layer to produce a MALDI signal allowing images to be generated from the fragment ion mass ( $m/z$  291.03, b.) and the deprotonated molecule ( $m/z$  338.03, c.). These images were generated from reasonably intense peaks although it can be seen, that the intensity observed is not uniform in the area where the compound is present.

Fig. 12 b. shows a spot at the left hand side of the sample tissue which can be clearly distinguished with good spatial integrity; the intensity in the image generated by the fragment ion mass ( $m/z$  291.03) shows the spot clearly. A sufficient amount of compound has penetrated through the waxy cuticle surface layer into the underlying tissue of the leaf 72 hours following application. The spot applied to the right area of the leaf was damaged during cell stripping this is why no compound is visible in this region.



(a.) (b.) (c.)  
 Fig. 10 MALDI-MS images of 6 hour sample matrix coverage represented by the

deprotonated molecule of sinapinic acid (a m/z 223.06 red outline indicates leaf tissue and spot location), a mesotrione fragment ion (b m/z 291.03) and the deprotonated molecule of mesotrione (c m/z 338.03).



(a.) (b.) (c.)  
 Fig. 11 MALDI-MS images of 24 hour sample matrix coverage represented by the

deprotonated molecule of sinapinic acid (a m/z 223.06 red outline indicates leaf tissue and spot location), a mesotrione fragment ion (b m/z 291.03) and the deprotonated molecule of mesotrione (c m/z 338.03).

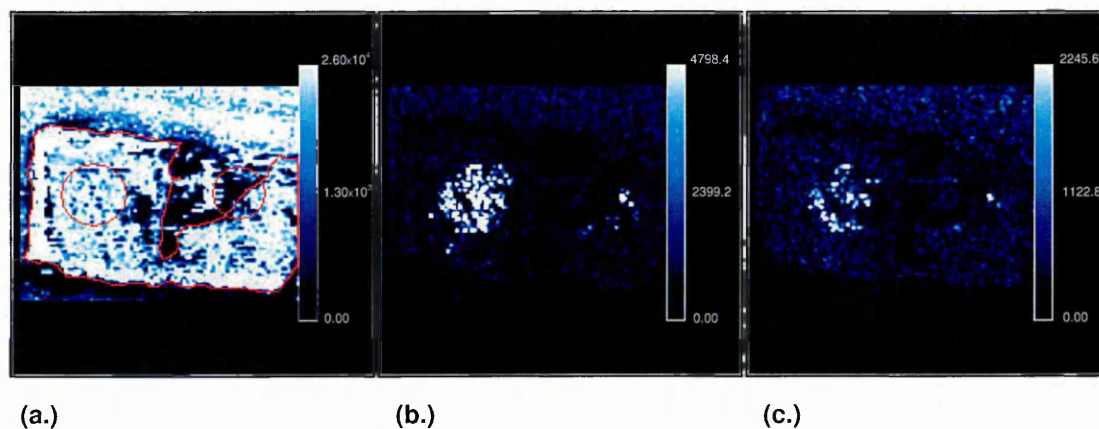


Fig. 12 MALDI-MS images of 72 hour sample matrix coverage represented by the deprotonated molecule of sinapinic acid (a  $m/z$  223.06 red outline indicates leaf tissue and spot location), a mesotrione fragment ion (b  $m/z$  291.03) and the deprotonated molecule of mesotrione (c  $m/z$  338.03).

### 2.3.4 Comparison of 9-aminoacridine and sinapinic acid and the effect of gold sputter coating.

Fig. 13 shows MALDI-MS images generated from the direct tissue analysis of mesotrione using sinapinic acid as a matrix. Fig. 13 (a.), the image of the matrix coverage shows good intensity across the majority of the sample tissue surface. The image generated from the fragment ion at  $m/z$  291.03 (Fig. 13 b.) shows the spot's original location, with good intensity towards the centre although the spatial distribution around the edge of the spot is not clear. This could be due to the compound spreading during the matrix application step. The image produced from the  $m/z$  of the deprotonated molecule is not as clear, indicating reduced sensitivity compared to the fragment ion.

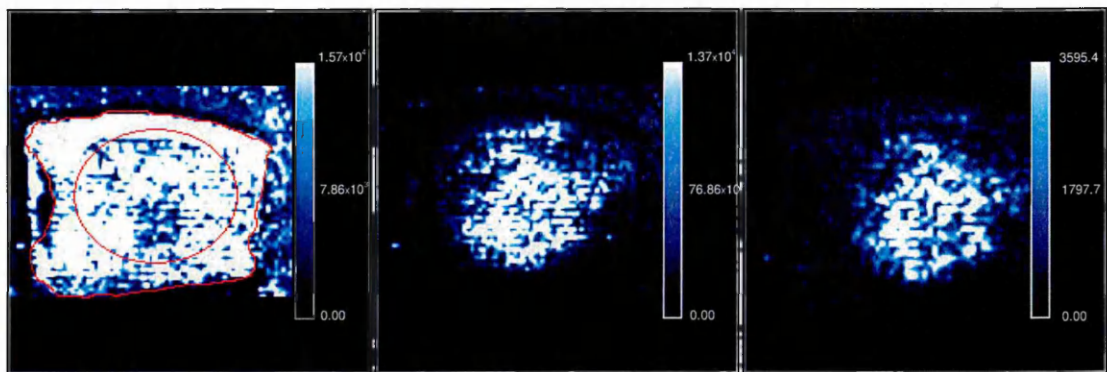
Fig. 14 (a) shows a MALDI-MS image generated from a sample with sinapinic acid as a matrix with the addition of a layer of gold sputtered onto the sample surface following matrix application. Fig. 14 shows that mass resolution was greatly

improved with the addition of the gold sputter due to a reduction sample's electric potential as a result of charging which occurs during analysis insulating samples such as tissues<sup>4</sup>. Since ions are constantly being drawn off the surface of the tissue sample an electric potential is generated on the sample, which affects the time of flight of ions causing peaks to broaden. This in turn has resulted background noise affecting the images produced, because the broader peaks begin to overlap with background noise causing blurring of images. The maintenance of the spatial distribution of the original spot applied to the leaf has been improved in the image generated by the fragment ion of  $m/z$  291.03 (Fig. 14 b.) although poor sensitivity is observed with the deprotonated molecule of  $m/z$  338.03 (Fig.14 c.).

Fig. 15 shows MALDI-MSI generated using 9-aminoacridine (9-AA) as a matrix. Fig. 15 (a) shows the image of the distribution of the deprotonated  $[M-H]^-$  ion of 9-AA ( $m/z$  193). The 9-AA coverage is more homogenous and present at a greater intensity than sinapinic acid. 9-AA is a moderately strong base in contrast to traditional MALDI matrices which are acidic in nature, 9-AA's ability to readily accept protons makes it a very effective matrix in negative ion mode<sup>6</sup>. One of the reasons for this is due to the application of the matrix using the gravity feed airgun being easier for the operator to achieve because the bright yellow colour makes an even coverage more apparent to the naked eye. Fig. 15 (b) the fragment ion ( $m/z$  291.03) and (Fig. 15 c) the deprotonated molecule ( $m/z$  338.03), are of much greater intensity because 9-AA improves the sensitivity for the detection of both the fragment ion and the deprotonated molecule of mesotrione. The spatial integrity of the original spot location also is retained.

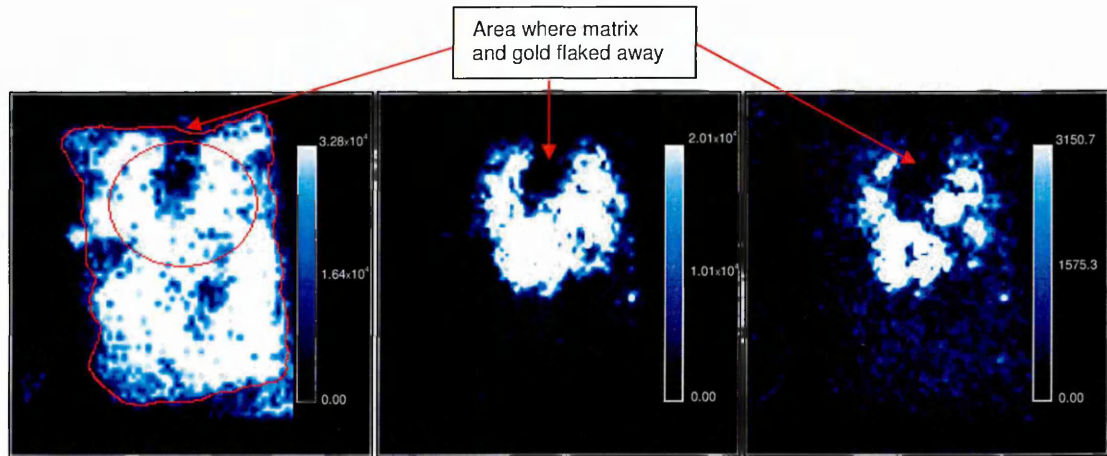
Fig. 16 shows MALDI-MSI generated from a sample with 9-AA as a matrix with the addition of a layer of sputtered gold. During transportation of the sample seen in Fig. 16 the coverage of the 9-AA became disrupted because an area of the matrix and the gold flaked away from the sample. This can be seen at the top middle section of the sample on the image generated by the deprotonated molecule of 9-aminoacridine (Fig. 16 a). This in turn affected the images produced for the fragment ion and deprotonated molecule of mesotrione (Fig. 16 b and Fig. 16 c) respectively. Again for both the images generated from the fragment ion mass and the deprotonated molecule the intensity has been greatly improved over that observed with sinapinic acid. The spatial integrity of the spot's original location has also been improved and is the best observed from this comparison experiment, with the image spots appearing smoother and the edges of the spot more clearly defined with exception of the area where the matrix and gold flaked away. This is since mass resolution has been greatly improved by the addition of the gold sputter coating. As a result of the significant increase in peak resolution the effects of background noise have also been reduced and the sensitivity for the mesotrione fragment ion (Fig. 16 b.  $m/z$  291.03) and deprotonated molecule (Fig.16 c.  $m/z$  338.03) have also been improved.





(a.) (b.) (c.)

Fig. 15 MALDI-MSI of mesotrione, direct analysis images of 9- aminoacridine coverage (a.  $m/z$  193.08 red outline indicates leaf tissue and spot location), a mesotrione fragment ion (b.  $m/z$  291.03) and the deprotonated molecule of mesotrione (c.  $m/z$  338.03).

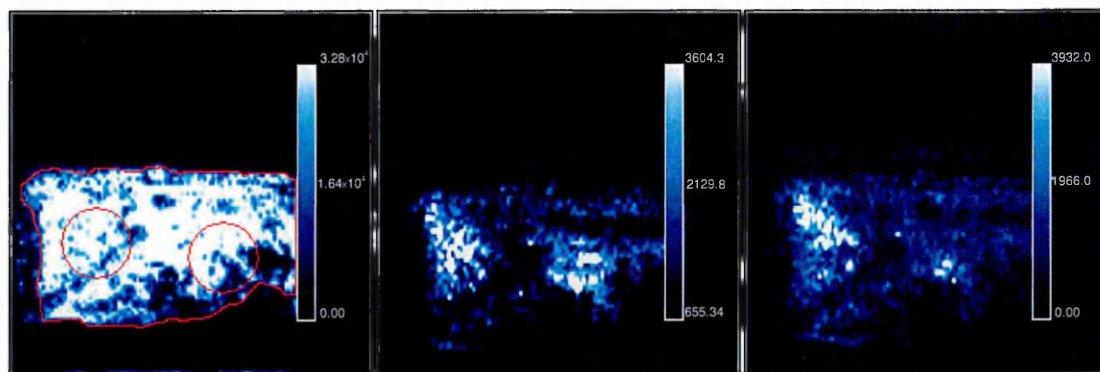


(a.) (b.) (c.)

Fig. 16 MALDI-MSI of mesotrione, direct analysis images of 9- aminoacridine and gold sputter coating coverage (a.  $m/z$  193.08 red outline indicates leaf tissue and spot location), a mesotrione fragment ion (b.  $m/z$  291.03) and the deprotonated molecule of mesotrione (c.  $m/z$  338.03).

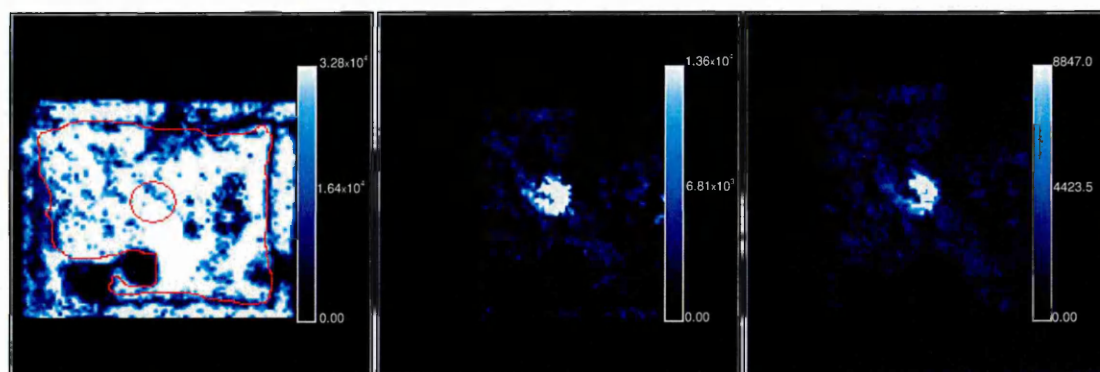
### **2.3.5 Direct MALDI imaging analysis of mesotrione on plant tissue - examination of the absorption of mesotrione using cell stripping**

Fig. 17 shows the MALDI-MS images generated as a control, 2x 2 $\mu$ L spots were pipetted onto the leaf surface and left just long enough to dry before the leaf was removed and prepared for tape cell stripping. Fig. 18 shows MALDI-MSI generated from a sample 1 hour following application of the compound. Fig. 19 shows an optical microscope image of the cells removed by the tape strip. The area on the left of this image shows a greater density of cells because a number of layers had been removed. Fig. 20 shows the MALDI-MS images generated from a sample 2 hours following application.



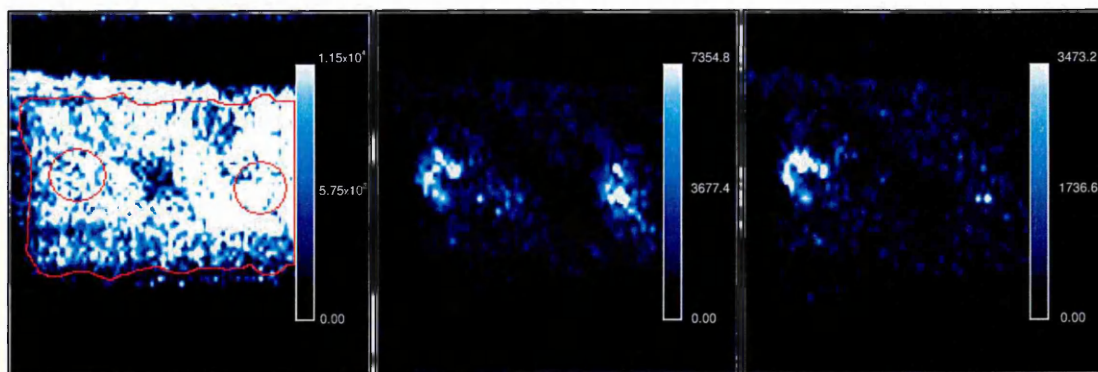
(a.) (b.) (c.)

Fig. 17 MALDI-MSI of 0 hour sample showing matrix coverage (a. m/z 193.08 red outline indicates leaf tissue and spot location), a mesotrione fragment ion (b. m/z 291.03) and mesotrione's deprotonated molecule (c. m/z 338.03).



(a.) (b.) (c.)

Fig. 18 MALDI-MSI 1 hour sample showing matrix coverage (a. m/z 193.08 red outline indicates leaf tissue and spot location), a mesotrione fragment ion (b. m/z 291.03) and the deprotonated molecule of mesotrione (c. m/z 338.03).



(a.) (b.) (c.)

Fig. 19 MALDI-MSI of 2 hour sample showing matrix coverage (a.  $m/z$  193.08 red outline indicates leaf tissue and spot location), a mesotrione fragment ion (b.  $m/z$  291.03) and the deprotonated molecule of mesotrione (c.  $m/z$  338.03).

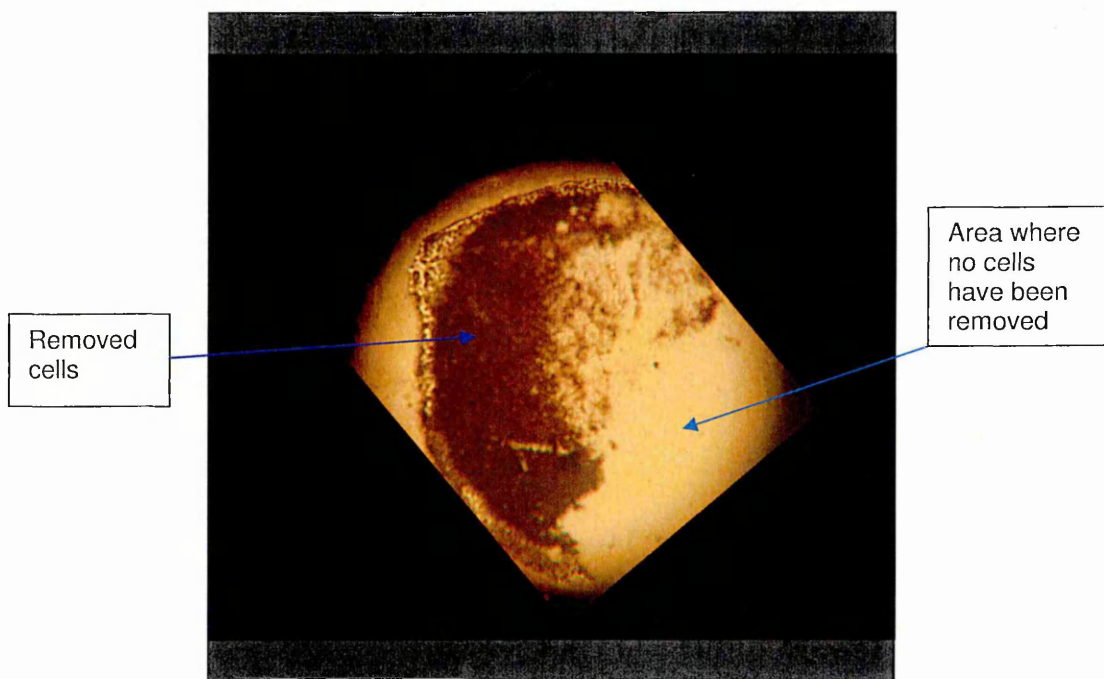


Fig. 20 Optical microscope image shows d-squame strip underside of the spot area removed from the leaf surface.

Fig. 17 shows that both the image from the mesotrione fragment ion (Fig. 17 b.) and the deprotonated molecule (Fig. 17 c.) show that the compound has

penetrated through the waxy cuticle layer. This indicates that compound has been absorbed during the drying period whilst still in the solution phase.

Fig. 18 shows the fragment ion at  $m/z$  291.03 (Fig. 18 b.) and the deprotonated molecule at  $m/z$  338.03 (Fig. 18c.) yield high signal intensity and that good spatial integrity has been retained. Since the localisation of the spot shape is preserved the compound has moved into the tissue in the region where it was originally applied and has not diffused into surrounding tissue by a significant amount 1 hour after application.

In this instance the removal of several layers of cells with the d-squame strip was clear to the naked eye so further examination was undertaken using the optical microscope (Fig. 20).

Fig. 19 shows both the fragment ion at  $m/z$  291.03 (Fig. 19 b.) and the deprotonated molecule at  $m/z$  338.03 (Fig. 19 c.) are clearly visible at high intensity, indicated by the dark areas observed in the images. The spatial distribution of the compound suggests mesotrione has started to diffuse laterally into the surrounding leaf tissue as it is translocating towards the phloem.

Fig. 20 shows an optical microscope image of the cells removed by the tape strip. On the area on the right side, just the waxy cuticle layer has been removed. This corresponds with the MALDI-MS image observed with the fragment and deprotonated molecule (Fig. 18 (b.) and (c.) respectively). The fragment ion can be seen in areas where several layers of cells have been removed providing evidence that mesotrione has penetrated into the tissue below the surface cells

into the underlying palisade mesophyll layer. Considerable care needs to be taken when performing the cell stripping method because the removal of several layers as opposed to just the surface layer could result in false negative results.

### 2.3.6 Direct MALDI imaging analysis of mesotrione in leaf veins after foliar absorption

#### Control result

Fig. 21 shows MALDI-MS images generated from a small section of leaf vein tissue with 1  $\mu\text{L}$  of a 2.5 mg/mL mesotrione in 50/50 acetone/0.1% Tween® solution pipetted onto it.

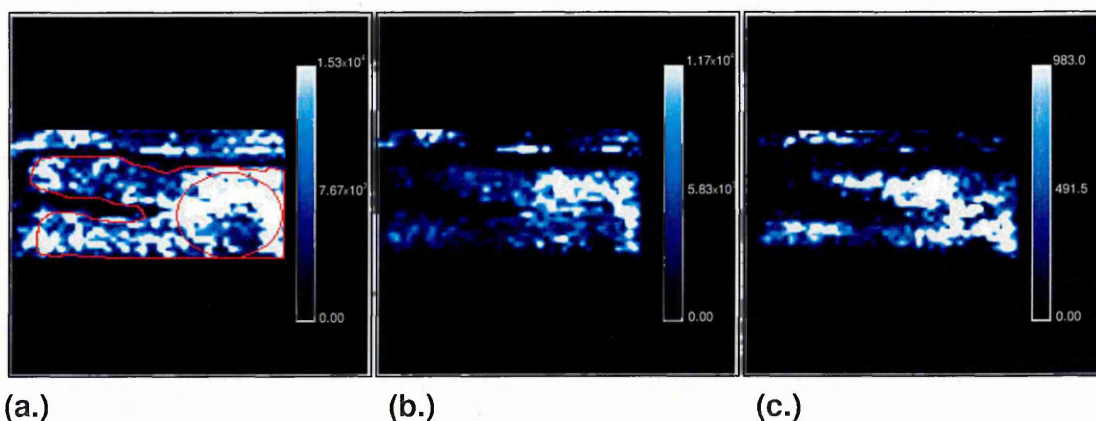


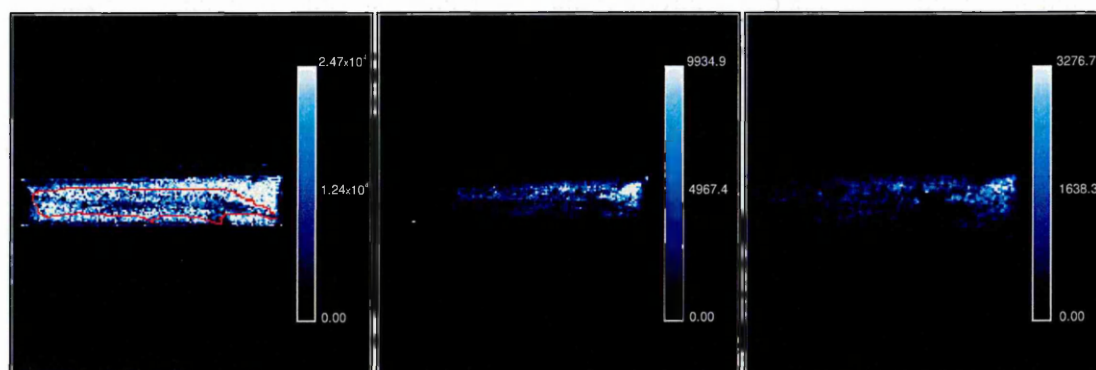
Fig. 21 MALDI-MSI of vein tissue disruption control experiment showing matrix coverage (a. m/z 193.08 red outline indicates plant tissue location), a mesotrione fragment ion (b. m/z 291.03) and the deprotonated molecule of mesotrione (c. m/z 338.03).

The solution was left to dry and the sample was freeze dried before matrix application. The images generated from both the fragment ion mass (Fig. 21 b.) and deprotonated molecule (Fig. 21 c.) were clearly visible in the top right region of the images although they were at a much lower intensity than results for the cell

stripping experiment, indicating there is some suppression occurring from compounds present in the leaf vein tissue.

### 5 Hours following application

Fig. 22 shows MALDI-MS images generated from a leaf midrib vein leaf tissue 5 hours after mesotrione was applied to the apex of the leaf.



(a.)

(b.)

(c.)

Fig. 22 MALDI-MSI of vein tissue disruption experiment showing matrix coverage (a. m/z 193.08 red outline indicates plant tissue location), a mesotrione fragment ion (b. m/z 291.03) and the deprotonated molecule of mesotrione (c. m/z 338.03). 5 hours following application of mesotrione to the leaf tip.

The signals arising from the fragment ion m/z at 291.03 (Fig. 22 b.) and the deprotonated molecule at m/z 338.03 (Fig. 22 c.) appear to be located on the conductive tape rather than in the plant veins tissue (top right of the image) despite the normalisation of this image. This could be due to solvent spreading during matrix application and a suppression effect from other substances within the plant system. The obtained sensitivity was low despite the use of 9-AA and a layer of sputtered gold. These two images, (Fig. 22 b.) and (Fig. 22 c.), suggest that solvent spreading has occurred during the matrix application step and

mesotrione has not remained localised in the tissue. Due to the lack of signal present in the sample the method was repeated with the mesotrione dosed leaf being left on the plant for longer time periods allowing for more mesotrione to become translocated.

## 20 Hours following application

Fig. 23 shows MALDI-MS images generated from a sample which was left for a time period of 20 hours.

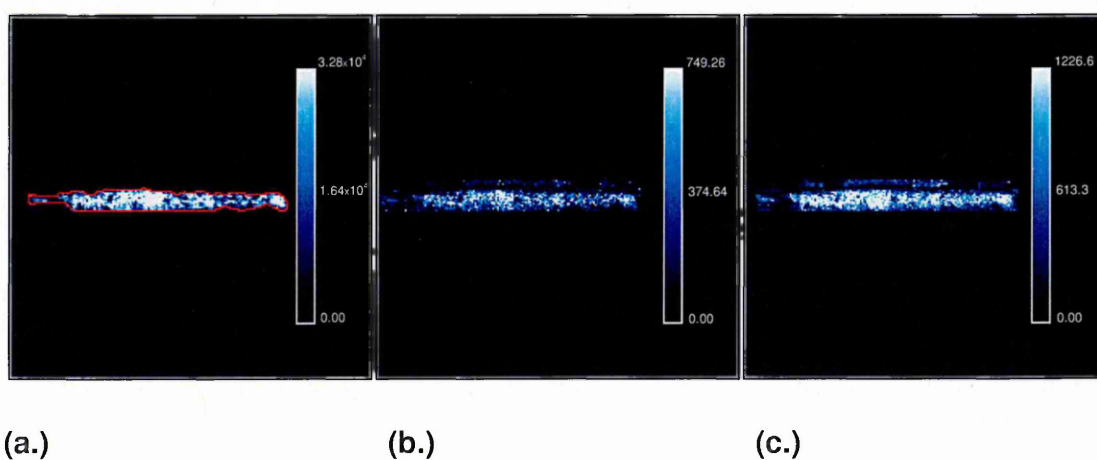
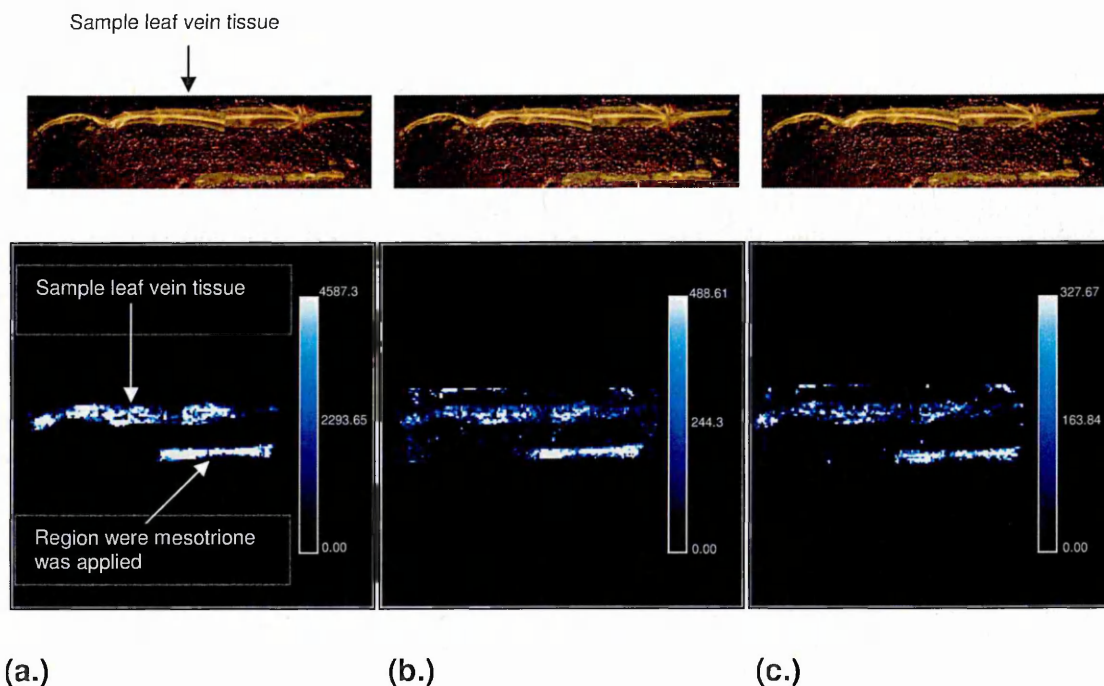


**Fig. 23 MALDI-MSI of vein tissue disruption experiment showing matrix coverage (a.  $m/z$  193.08 red outline indicates plant tissue location), a mesotrione fragment ion (b.  $m/z$  291.03) and the deprotonated molecule of mesotrione (c.  $m/z$  338.03). 20 hours following application of mesotrione to the leaf tip**

Both the fragment ion at  $m/z$  291.03 (Fig. 23 b.) and deprotonated molecule at  $m/z$  338.03 (Fig. 23 c.) are visible within the tissue. These images were again generated from peaks with low signal intensity. For this reason the method was repeated using a more concentrated solution (5.5 mg/mL mesotrione 50:50 acetone:0.1% Tween®).

## 20 Hours following application result with 5.5 mg/mL solution

Fig. 24 shows MALDI-MSI generated from a repeat of the previous method with the more concentrated mesotrione solution.



(a.) (b.) (c.)  
Fig. 24 MALDI-MS image from a vein disruption experiment showing matrix coverage (a.  $m/z$  193.08), a mesotrione fragment ion (b.  $m/z$  291.03) and the deprotonated molecule of mesotrione (c.  $m/z$  338.03). 20 hours following application to the leaf tip. Optical image above to indicate sample orientation.

The images shown are taken from a sample which contains 2 pieces of leaf vein material. The top section corresponds to a region of non-inoculated leaf vein tissue taken from further down the vein of the leaf, away from the inoculation region. The bottom section corresponds to the vein tissue taken directly from the mesotrione inoculated leaf tip. Mesotrione can be seen clearly in both the image of the fragment ion  $m/z$  291.03 (Fig. 24 b.) and the deprotonated molecule  $m/z$  338.03 (Fig. 24 c.). It is distributed evenly throughout the majority of the tissue

and is present in higher abundance in other areas indicated by the darker regions on the sample tissue.

### Improved mesotrione data using image normalization

It has been proposed that normalisation can improve image quality for MALDI-MSI data<sup>7</sup>. This often leads to clearer visualisation of the compound of interest. During the image sample preparation process a number of variables are introduced which if ignored may result in a misleading representation of the sample. One of these variables, over which there is little control, is the homogeneity of matrix coverage using the airspray deposition method. In order to overcome this, tissue images may be normalised against the matrix coverage. The exclusion of this step during image processing may lead to areas which appear to have a low abundance of analyte as a result of poor matrix coverage. Similarly areas which appear to have a particularly high abundance of analyte may be a result of excess matrix coverage in that area.

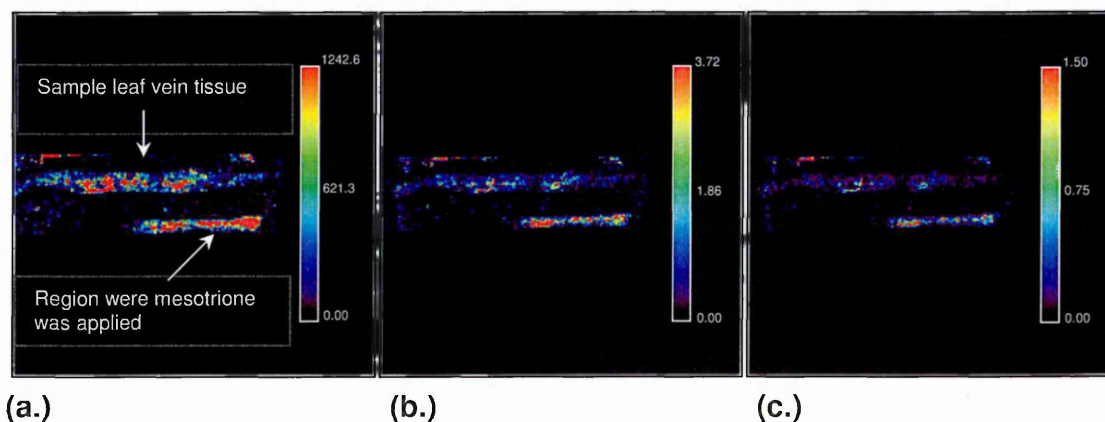


Fig. 25 MALDI-MS image from a vein disruption experiment showing matrix coverage (a. m/z 194.08), the normalised image of a mesotrione fragment ion (b. m/z 291.03) and the

**deprotonated molecule of mesotrione (c. m/z 338.03). 20 hours following application to the leaf tip**

Fig. 25 shows images which display the effects of matrix normalisation of the  $C^{13}$  isotope of 9-AA (m/z 194.08) on the appearance of analyte abundance within samples. Since the intensity of the  $C^{13}$  isotope is still proportional to the presence of 9-AA coverage across the sample but with a lower signal the ratio produced is much larger than the ratio produced from the protonated ion of 9-aminoacridine (m/z 193.08). This gives a better dynamic range across the gamut of colours that indicate the ion intensity with which to identify the distribution of mesotrione above the background noise in the image. From the images of the deprotonated matrix ion at m/z 194.08 (Fig. 25 a.), it can be seen that the matrix ion intensity in the inoculated leaf tip appears to be higher than that of the non-inoculated leaf tip. When the distribution of mesotrione as both the fragment ion and the deprotonated molecule is generated without normalisation, it appears that there is a higher abundance of mesotrione in the vein taken from the leaf tip compared to the vein taken from further down the plant. This is as would be expected, however because the matrix intensity is also elevated in the leaf tip section, we cannot definitively say that the apparent elevated abundance in the leaf tip is not simply an effect of increased matrix abundance and therefore enhanced ionisation of mesotrione in this region. For this reason it is important to verify this result by taking into account the variation in matrix coverage. As can be seen in the normalised images, (Fig. 25 b.) and (Fig. 25 c.), this is not the case. Even after the variability of the matrix coverage is removed through normalisation, the abundance of mesotrione remains elevated in the leaf tip region compared to the section taken from further down the leaf. This form of processing, using  $C^{13}$

isotopes of the matrix ions can also be seen to reduce background interference, leading to the generation of higher quality images as can be seen in images (Fig. 25 b.) and (Fig. 25 c.).

### 2.3.7 Effect of laser fluence for the detection of mesotrione

In order to assess the effect of laser energy on the extent of mesotrione fragmentation a range of standard dilutions was used to generate spectra at two different laser powers. The ion counts recorded, shown in table 1, were used to create graphs of total ion count data against concentration (Fig. 26 and 28) and analyte to matrix ratios against concentration (Fig. 27 and 29).

Laser Power 2603	Conc.	291	338	Matrix	Ratio 291	Ratio 338
	0.5	2106	1457.2	61666.7	0.03416	0.023607
	5	11333.3	11266.7	59000	0.1918	0.192178
	12.5	29000	31000	61666.7	0.47036	0.50246
	25	22666.7	25333.3	54666.7	0.416126	0.4667
	50	24333.3	13000	32666.7	0.6957	0.43809

Laser Power 2728	Conc.	291	338	Matrix	Ratio 291	Ratio 338
	0.5	1301.7	1974.7	43000	0.03027	0.04584
	5	11626.4	6547.7	42000	0.26126	0.133806
	12.5	37000	14333.3	63666.7	0.58065	0.225353
	25	30666.7	16964.5	42333.3	0.70775	0.3752
	50	55000	42666.7	56000	0.97674	0.74127

**Table 1 Ion intensities and ion ratios from analysis of varying concentrations of mesotrione at 2 laser powers.**

The counts observed in table 1 show clear differences in the total number of ions produced and the extent of mesotrione fragmentation between the two laser

powers because the number of ions generated is greatly varied. This becomes more apparent when the analyte/matrix ratio is plotted against mesotrione concentrations.

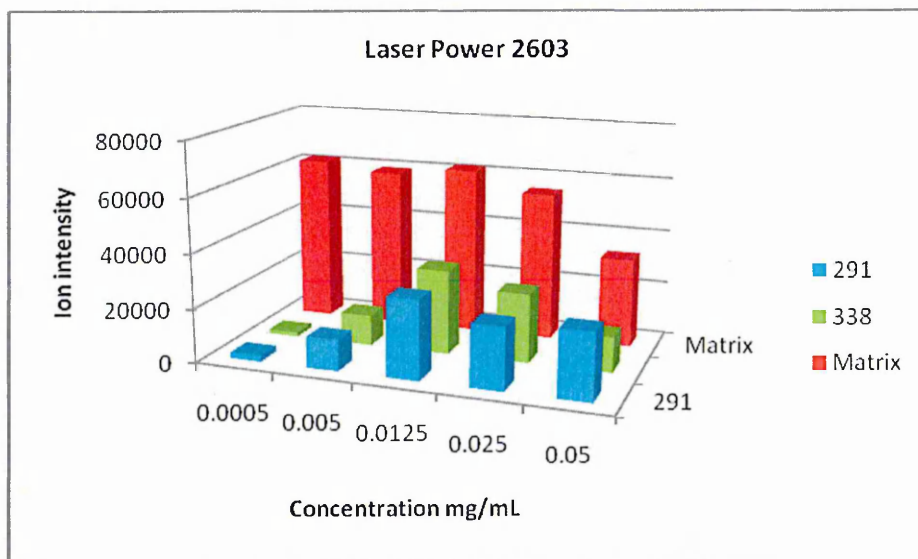


Fig. 26 Ion intensity against concentration of mesotrione for matrix (m/z 193.08), fragment ion (m/z 291.03) and deprotonated molecule (m/z 338.03) at 2603 laser power vs concentration of mesotrione.

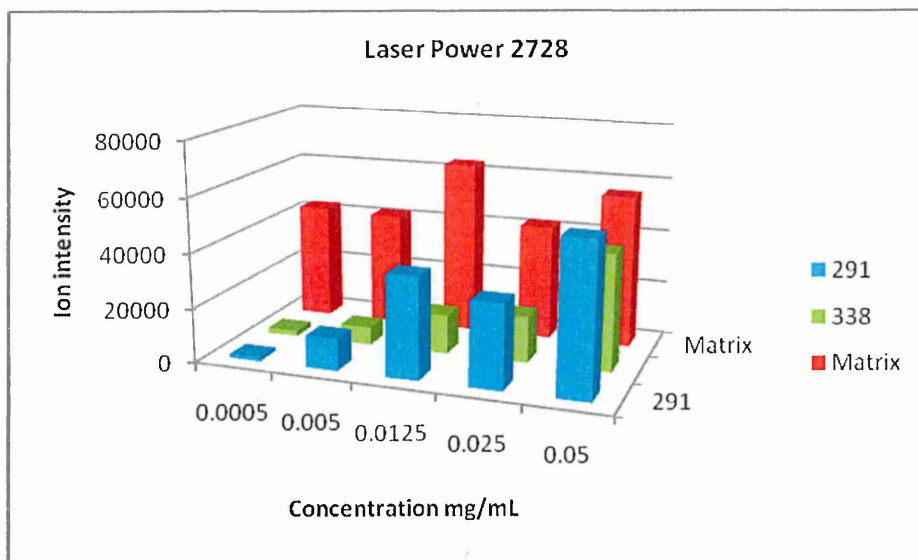


Fig. 27 Ion intensity against concentration of mesotrione for matrix (m/z 193.08), fragment ion (m/z 291.03) and deprotonated molecule (m/z 338.03) at 2728 laser power vs concentration of mesotrione.

The graph in Fig. 26 is of the ion counts for the deprotonated molecule, fragment ion and deprotonated matrix ion plotted against mesotrione concentration in mg/mL at the lower laser power of 2603. At this power we can see that the intensity of the deprotonated molecule is roughly equal to that of the fragment ion. This is as we would expect due to less fragmentation occurring at the lower laser energy. As the concentration of mesotrione increases the signal for the matrix ion ( $m/z$  193.08) decreases, this is evidence of analyte/matrix suppression as the number of matrix primary ions is depleted with the increased concentration of analyte.

The graph in Fig. 27 is of the ion count for the deprotonated molecule, fragment ion and deprotonated matrix ion plotted against mesotrione concentration at the higher laser power of 2728. As the laser fluence is increased the number of primary ions present increases so the analyte/matrix suppression effect is no longer observed with increasing analyte concentration.

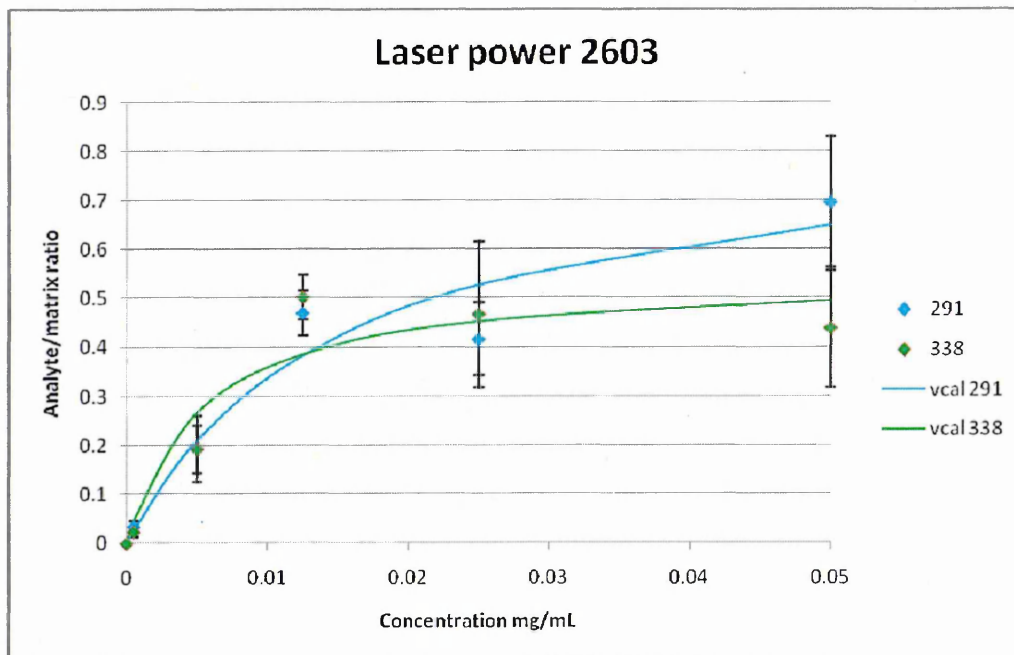


Fig. 28 Analyte to matrix intensity ratio against concentration for the deprotonated molecule (m/z 338.03) in green and fragment ion (m/z 291.03) in blue at 2603 laser power.

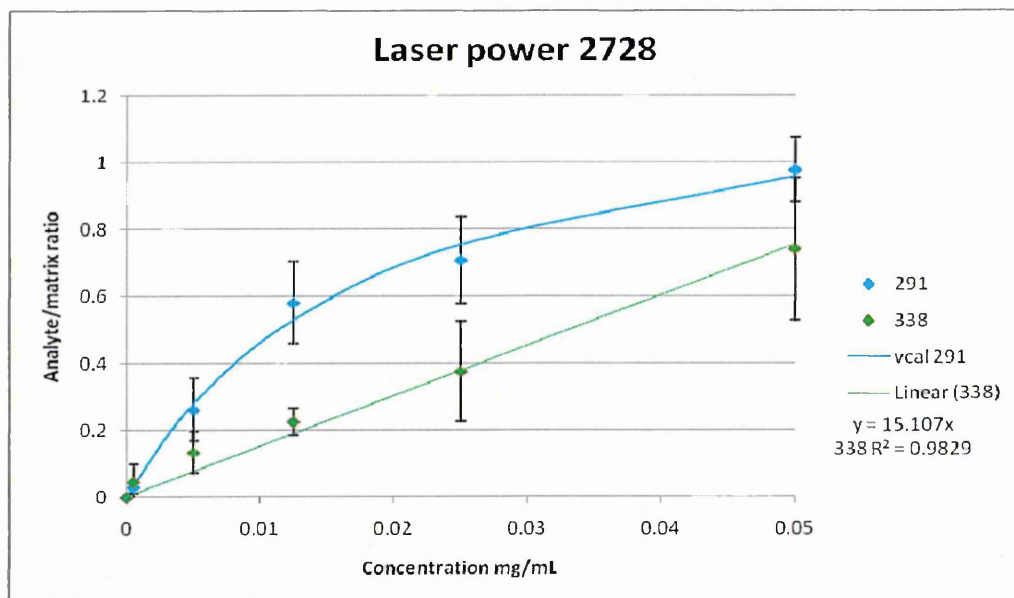


Fig. 29 Analyte to matrix intensity ratio against concentration of mesotrione for the deprotonated molecule (m/z 338.03) in green and fragment ion (m/z 291.03) in blue at 2728 laser power.

The graph in Fig. 28 shows the analyte/matrix intensity ratio of the deprotonated molecule and the fragment ion plotted against the mesotrione concentration at the lower laser power of 2603. The abundance of the deprotonated molecule is slightly higher than that of the fragment ion at lower concentrations of mesotrione (up to 0.0125 mg/mL). At 0.05 mg/mL the abundance of the fragment ion is higher than that of the deprotonated molecule although there are large error bars at this concentration for both points. The data suggests that at higher concentrations there is a saturation effect since a linear line of best fit is not suitable. For this reason a line of best fit has been fitted using the Michaelis-Menten equation to account for the saturation observed. This effect relates to MALDI ionisation theory of primary ion formation as the low laser fluence results in limited number of primary matrix ions discussed in section 1.5.

The graph in Fig. 29 shows the analyte/matrix intensity ratio of the deprotonated molecule and the fragment ion plotted against the mesotrione concentration at the higher laser power of 2728. With the increase in laser power the degree of fragmentation of mesotrione increases as the number of counts observed for the fragment ion mass, which becomes greater than that observed for the deprotonated molecule. The increased level of fragmentation can be clearly seen with the higher abundance of the fragment ion mass at  $m/z$  291.03. The line of best fit for the deprotonated molecule follows a linear response whereas the line of best fit for the fragment ion suggesting a saturation effect is occurring. Therefore the data was subjected to the Michaelis-Menten equation which takes in to account the saturation effect in order to generate the most suitable line of best fit for this data. This effect appears to be more complicated than saturation due

suppression effects or limited number of primary ions due to laser fluence, because the deprotonated molecule still follows a linear curve. This effect may be due to the fragment ion arising as a result of laser desorption ionisation and matrix-assisted laser desorption ionisation.

From the results shown here, it is apparent that the best sensitivity for analysis of mesotrione is obtained at higher laser energy through observation of the fragment ion. The ion intensities are overall much greater than at the lower laser energy because the higher laser fluence provides a higher concentration of matrix primary ions. It would also appear that during the ionisation of mesotrione the deprotonated ion becomes unstable and the internal energy causes the deprotonated molecule to fragment. Since the energy required to cause this fragmentation is relatively low, with regards to the laser power required to produce acceptable sensitivity this fragmentation is unavoidable.

During image analysis many molecules are simultaneously competing for ionization at each acquisition point across the sample. The complex nature of the sample composition may therefore lead to analyte/analyte suppression if the ionisation efficiency of an endogenous compound within the plant tissue is greater than that of the analyte of interest. For this reason concentration levels required to generate signal by conventional MALDI analysis can not necessarily be carried over to direct tissue image analysis. An experiment was carried out to assess how analyte suppression affects the detection for mesotrione (2.2.8). The solutions used in the study of the fragmentation of mesotrione, described above were

employed but with the addition of a plant extract solution, to reflect the complexity of endogenous compounds present within sample tissue.

### 2.3.8 Assessment of suppression effects on the detection of mesotrione using plant extract

Table 2 shows the ion counts for the fragment ion at m/z 291.03, the deprotonated molecule at m/z 338.03 and the matrix at m/z 193.08 for the different concentrations with the addition of the blank solution and addition of a plant extract solution.

Mesotrione with the addition of a blank	Conc.	291	338	Matrix	Ratio 291	Ratio 338
	0.5	2788.23	1084.9	53333.3	0.053358	0.021325
	5	9075.33	7812.4	51000	0.17656	0.14909
	12.5	20666.7	17333.3	50333.33	0.17037	0.1555
	25	34333.3	27000	46666.7	0.73058	0.5766
	50	49666.7	35666.7	38666.7	1.30391	0.9445

Mesotrione with the addition of extract	Conc.	291	338	Matrix	Ratio 291	Ratio 338
	0.5	532.17	428.3	10433.3	0.051539	0.04283
	5	1661.6	1116.4	11232.3	0.14744	0.0997166
	12.5	3249.6	1701.9	10200	0.32034	0.16578
	25	5476.7	2757.4	12000	0.4566	0.22959
	50	6162.73	3806.4	10030	0.6144	0.3795

**Table 2 Ion intensities and ion ratios from analysis of varying concentrations of mesotrione with the addition of a blank solution and a plant extract solution.**

The ion counts and matrix to analyte ratios were plotted against mesotrione concentration to produce a number of graphs demonstrating the effect of the endogenous compound present in the plant tissue on the ionisation of mesotrione.

Fig. 29 shows the ion counts of the deprotonated molecule, fragment ion and deprotonated matrix ion plotted against mesotrione concentration with the addition of a blank to the standards.

The graph in Fig. 30 is of the total ion counts of the deprotonated molecule, fragment ion and deprotonated matrix ion plotted against mesotrione concentration with the addition of the plant extract solution. The signals for the fragment ion, the deprotonated molecule and the matrix have been significantly reduced when compared to Fig. 29.

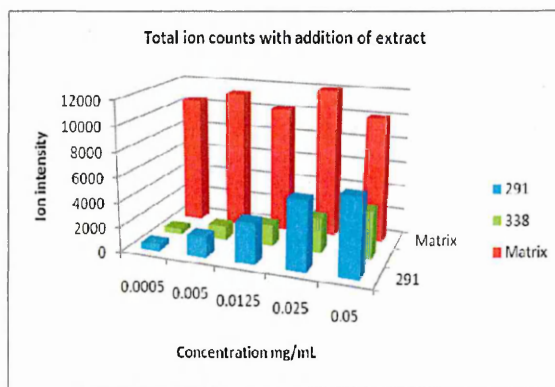
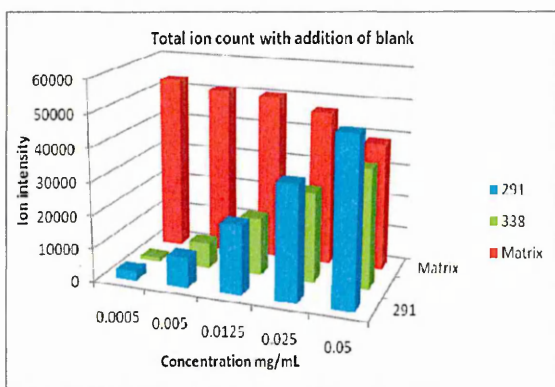


**Fig. 29 Ion intensity against concentration of mesotrione for matrix (m/z 193.08), fragment ion (m/z 291.03) and deprotonated molecule (m/z 338.03) with the addition of the blank solution.**

**Fig. 30 Ion intensity against concentration of mesotrione for matrix (m/z 193.08), fragment ion (m/z 291.03) and deprotonated molecule (m/z 338.03) with the addition of the extract solution.**

The reduced signal could be a result of the plant compounds affecting the crystal formation of the matrix and thus the co-crystallisation of the analyte with the matrix. As this would affect the signal for the matrix proportionally the analyte to matrix ratio would cancel out this effect.

The graph in Fig. 31 shows the analyte/matrix ratio of the fragment ion ( $m/z$  291.03) plotted against the mesotrione standard concentration with the addition of a blank to the solution. The analyte/matrix ratio shows good linear response to the increase in concentration.

The graph in Fig. 32 shows the analyte/matrix ratio of the deprotonated molecule ( $m/z$  338.03) plotted against the mesotrione standard concentration with the addition of a blank to the solution. The analyte/matrix ratio against concentration shows good linear response to the increase in concentration.

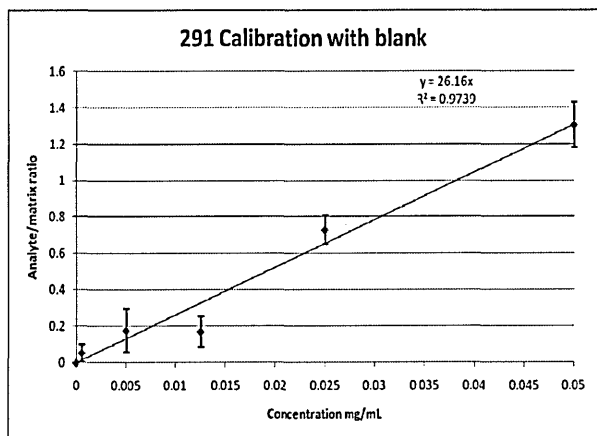


**Fig. 31** Analyte to matrix intensity ratio against concentration of mesotrione for the fragment ion (m/z 291.03) with the addition of the blank solution.

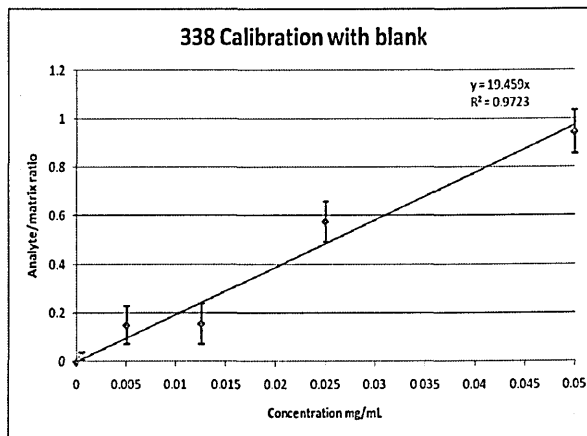


**Fig. 32** Analyte to matrix intensity ratio against concentration of mesotrione for the deprotonated molecule (m/z 338.03) with the addition of the blank solution.

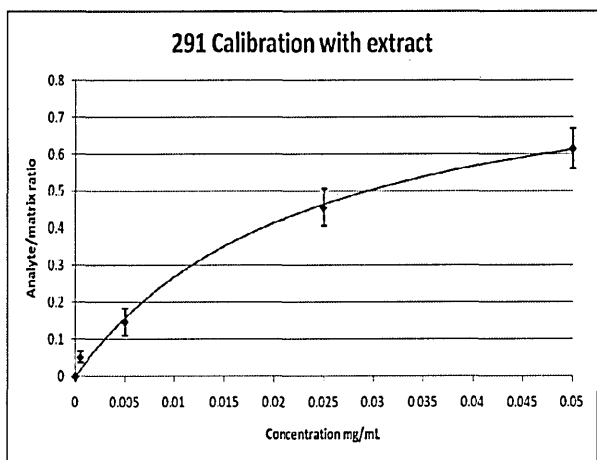


**Fig. 33** Analyte to matrix intensity ratio against concentration of mesotrione for the fragment ion (m/z 291.03) with the addition of the extract solution.

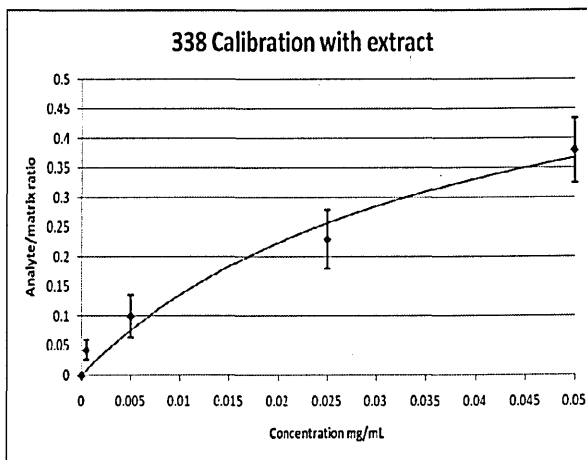


**Fig. 34** Analyte to matrix intensity ratio against concentration of mesotrione for the deprotonated molecule (m/z 338.03) with the addition of the extract solution.

The graph in Fig. 33 shows the matrix/analyte ratio of the fragment ion (m/z 291.03) plotted against the mesotrione concentration with the addition of the plant extract solution. This shows that the signal for the fragment ion has been

significantly reduced compared to Fig. 31 indicating a suppression effect is being observed from endogenous materials within the plant system.

The graph in Fig. 34 shows the analyte/matrix ratio of the deprotonated molecule ( $m/z$  338.03) plotted against the mesotrione concentration with the addition of the plant extract solution. This also shows that the signal has been significantly reduced compared to Fig. 32 and again is displaying indicating a suppression effect is being observed from endogenous materials within the plant system. Both graphs (Fig. 33 and 34) a displaying evidence of analyte-analyte suppression (discussed in section 1.6) because the line of best fit is no longer following a linear response as the concentration of mesotrione increases.

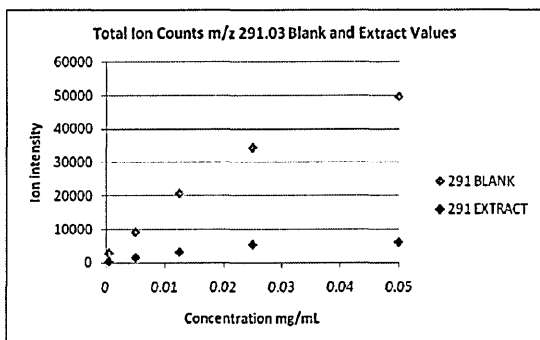


**Fig. 35 Total ion intensities for the fragment ion ( $m/z$  291.03) with the addition of the extract (dark blue points) and the blank solution (light blue points).**

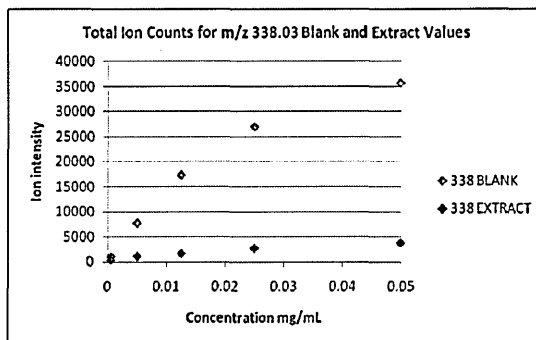


**Fig. 36 Total ion intensities for deprotonated molecule ( $m/z$  338.03) with the addition of the extract (dark green points) and the blank solution (light green points).**

The graph in Fig. 35 shows total ion counts for the mesotrione fragment ion from the results obtained with the addition of a blank compared to the addition of the extract solution. The graph in Fig. 36 shows total ion counts for the mesotrione

deprotonated molecule from the results obtained with the addition of a blank compared to the addition of the extract solution. These graphs clearly show the extent of the effect the addition of endogenous materials has on the ionisation of mesotrione. This graph clearly shows the extent of the effect the addition of endogenous materials has on the ionisation of mesotrione.

## 2.4 Discussion

MALDI-MSI provided us with clear images for the location of mesotrione following application of the compound to the surface of soya bean leaves once the issues of sensitivity and mass resolution had been resolved. Sinapinic acid yields good sensitivity when used as a matrix for the analysis of mesotrione by conventional MALDI-MS. However, due to its large crystalline structure and the nature of plant tissue, a good even and homogenous distribution of sinapinic acid was difficult to achieve using air spray deposition. Therefore co-crystallisation between the matrix and mesotrione was limited, affecting the sensitivity of mesotrione with direct tissue analysis. By following the methodology described in a paper published using 9-aminoacridine as a matrix for negative ion mode MALDI-MS<sup>5</sup> the sensitivity for direct tissue analysis of mesotrione was significantly improved both for the fragment ion mass and the deprotonated molecule mass. This allowed for the visualization of mesotrione penetrating the waxy cuticle layer in the time taken for a 5µL drop to dry, whilst sinapinic acid could not produce enough sensitivity 6 hours following application. This method generated much clearer images than those from direct analysis of mesotrione at 0, 5, 48 and 72 hours on the surface of soya reported by Mullen *et al*<sup>9</sup>.

Eliminating the charging effect observed with the Voyager DE-PRO MALDI-TOF-MS by using gold sputter coating played a crucial part in obtaining good quality images. It significantly improved the mass spectral peak resolution, which in turn improved sensitivity along with decreasing the effect of background noise interfering with the image generated.

The effect of the laser energy on the fragmentation of mesotrione was very clear; the higher the laser energy the greater the fragmentation. Analyte/matrix suppression was also observed because the line of best fit for the analyte against matrix ratio generated by the fragment ion ( $m/z$  291.03) and the deprotonated molecule at the lower laser power was no longer linear with increasing concentration. This saturation effect relates to the MALDI ionisation theory discussed in section 1.5 and 1.6 as the number of primary matrix ions available generated by the laser fluence is limited preventing the formation of analyte ions through secondary reactions. The effect observed with increased laser fluence on mesotrione deprotonated molecule ( $m/z$  338.03) resulted in a linear line of best fit as sufficient primary ions were present. The line of best fit for the fragment ion ( $m/z$  291.03) was generated using the Michaelis Menten equation due to a saturation effect at high concentration. As the line of best fit for the deprotonated molecule was linear the effect observed with the deprotonated molecule maybe arising from laser desorption ionisation and matrix-assisted laser desorption ionisation of mesotrione.

Since the mesotrione experiments required direct tissue analysis, the variation in laser energies was limited because direct tissue analysis required more laser energy to ionise the analyte of interest. This is due to endogenous compounds also absorbing the energy of the laser and analyte-analyte suppression effects revisited below. A low laser power would not produce sufficient sensitivity for analysis of the deprotonated molecule. Using a higher laser power and images generated from the fragment ion mass ( $m/z$  291.03) exhibited the best representation of the mesotrione distribution. The extent to which the laser power could be raised was limited because fragmentation of endogenous compound results in increased background noise interference, which had a significant detrimental effect on the images produced.

Following the results obtained from conventional MALDI analysis of mesotrione with the addition of a plant tissue extract solution. The visual effect the plant extract had on the matrix crystal formation was clearly visible to the human eye and, as would be expected, this affected the total ion counts obtained for both the analyte and the matrix, resulting in a significant reduction in the ion intensities observed. Calculating the analyte to matrix ratio should take this factor into account and it would be expected that a similar ratio between the results would be obtained with the addition of a blank solution as that obtained with the addition of the extract solution. The graphs generated (Fig. 29 compared to Fig. 30 and Fig. 35 compared to Fig. 36) show that this was not the case and compounds present within the plant tissue reduce the sensitivity toward mesotrione. For these reasons, efficient determination of the distribution of mesotrione within the plant transport tissues of the leaf veins cannot be achieved at low concentrations whilst its

presence within the tissue at high concentrations can be determined. Mesotrione cannot be observed in the plant's transport system from direct tissue analysis due to analyte-analyte suppression effects (discussed in section 1.6) caused by endogenous compounds present within the plant tissue having higher deprotonation efficiency than mesotrione.

## 2.5 Conclusions

Initial experiments for the analysis of azoxystrobin using an indirect MALDI-MSI method by blotting the compound onto a cellulose membrane provided data with excellent sensitivity with spatial distribution of the compound's location being preserved. The direct tissue MALDI-MSI method data show that detection of agrochemicals from the upper epidermis layer following removal of the cuticle was achievable with adequate sensitivity once a more suitable matrix was obtained and the problem of sample charging was prevented with gold sputter coating. Attempts to observe translocation of mesotrione in the midrib vein of a leaf following application to the leaf tip resulted in low signal for both the fragment ion ( $m/z$  291.03) and the deprotonated molecule ( $m/z$  338.03). This signal suppression was attributed to fragmentation of mesotrione reducing the sensitivity towards individual ions, analyte-matrix and analyte-analyte suppression effects preventing suitable sensitivity towards mesotrione in order to observe translocation within the plant transport systems following foliar application. For these reasons it was decided to introduce nicosulfuron and fluazifop-p butyl to translocation experiments and assess IR lasers as an alternative ionisation method.

## 2.6 References

1. Taiz L. Zeiger E. Plant Physiology fourth edition Sinauer Associations Inc.
2. Terashima, I. and Hikosaka, K. (1995) Comparative ecophysiology of leaf and canopy photosynthesis. *Plant Cell and Environment*. **18**:1111-1128.
3. Kock, K., Neinhuis, C., Ensikat H,J. and Barthlott, W. (2004) Self assembly of epicuticular waxes on living plant surfaces imaged by atomic force microscopy (AFM). *Journal of Experimental Botany*. **397**: 711-718.
4. Audus L. J. (1976) Herbicides Volume 2. Academic Press Inc. UK.
5. Altelaar M. A. F., Klinkert I., Jalink K., Lange R. P. J., Adan R. A., Heeren R. M. A. and Piersma S. R. (2006) Gold-Enhanced Biomolecular Surface Imaging of Cells and Tissues by SIMS and MALDI Mass Spectrometry. *Analytical Chemistry*. **78**: 734-742
6. Vermillion-Salsbury R. L. and Hercules D. M. (2002) 9-Aminoacridine as a matrix for negative mode matrix-assisted laser desorption/ionization. *Rapid Communications in Mass Spectrometry*. **16**: 1575-1581.
7. Prideaux B., Atkinson S., Carolan V., Morton J. and Clench M. R. (2007) Sample preparation and data interpretation procedures for the examination of xenobiotic compounds in skin by indirect imaging MALDI-MS. *International Journal of Mass Spectrometry*. **260**: 243-251.

8. Miller J. C. and Miller J. N. (1993) *Statistics for Analytical Chemistry*. Ellis Horwood Ltd. Great Britain.

9. Mullen A. K., Clench M. R., Crosland S. and Sharples K. R. (2005) Determination of agrochemical compounds in soya plants by imaging matrix-assisted laser desorption/ionisation mass spectrometry. *Rapid Communications in Mass Spectrometry* 19: 2507-2516.

## **Chapter Three: Detection of Translocated Agrochemicals in Plant Stems**

## 3.1 Introduction

### 3.1.1 Translocation in the xylem and phloem

There are two transport systems in vascular plants, the xylem and phloem. The xylem is largely comprised of non living cells which have a specialized anatomy. This enables them to transport large quantities of water with great efficiency. The two types of tracheary elements in the xylem are tracheids and vessel elements. As these cell types mature, production of thick lignified cell walls and subsequent cell death results in the loss of the cytoplasm and all of its contents. This results in hollow tubes through which water can flow with relatively little resistance been left behind <sup>1</sup>.

The phloem is the principal food conducting tissue of vascular tissue and is usually spatially associated with the xylem. The basic components of the phloem are the sieve tubes or sieve elements and companion cells. Sieve tubes are made of sieve cells joined end to end in the same way that xylem cells join to make xylem vessels. The sieve tubes are partially closed at intervals by crossed walled regions called sieve plates which contain many holes allowing the contents of the sieve tubes to pass through <sup>2</sup>.

Each sieve element is associated with a companion cell (Fig. 1). The function of the companion cell is not clear but as the cell possesses a dense cytosol and numerous mitochondria it is assumed they play a metabolic role in maintaining phloem transport.

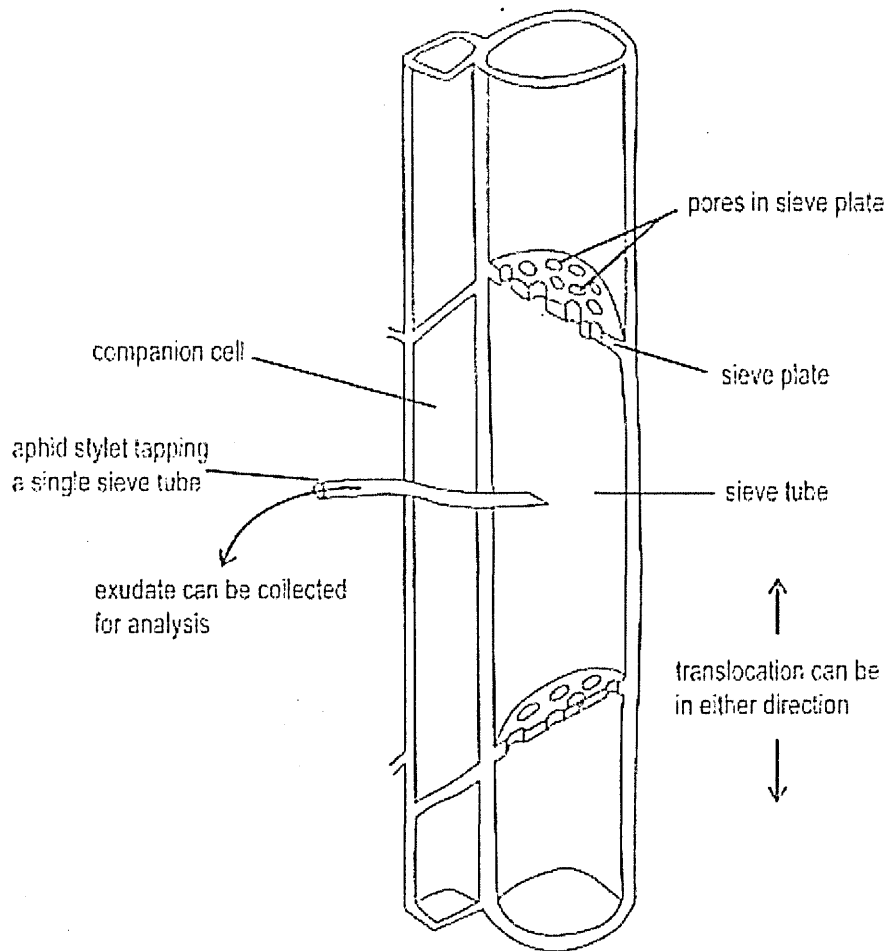


**Fig. 1 Phloem structure<sup>2</sup>.**

Water is the most abundant substance in the phloem acting as a solvent for translocated solutes including carbohydrates, proteins, amino acids, hormones and some inorganic ions. Sucrose carbohydrates are the most concentrated and significant solutes in the phloem sap, reaching concentrations of 0.3 to 0.9 M<sup>3</sup>. Results from analysis of the phloem sap indicate that sugars are translocated in the non-reducing form because reducing sugars such as glucose and fructose with exposed aldehyde or ketone groups are more reactive than non-reducing sugars such as sucrose<sup>3</sup>. Nitrogen is found in the phloem mainly as amides, amino acids and, glutamine and asparagine and their respective amides. The concentrations

of amino acids and organic acids reported varies widely even for the same species, however their concentrations are usually low compared to carbohydrate concentrations. Inorganic solutes which move within the phloem include potassium, magnesium, phosphate and chloride.

The mechanism of phloem translocation is best explained by the pressure-flow model which agrees with most of the structural and experimental data available. The pressure flow model was first put forward by E. Munch in 1926. The theory involves a mass flow or bulk flow of the phloem sieve tube contents been pushed along by pressure difference. The pressure difference is created by loading and unloading of the phloem sieve tubes <sup>2</sup>. The minor veins in the leaf generally contain two to three times more sucrose than surrounding mesophyll tissue suggesting sucrose is actively pumped against its concentration gradient. This phloem loading requires metabolic energy because sucrose is moved against its concentration gradient, this movement is also selective because sucrose is loaded and glucose and fructose are not. Unloading of the phloem occurs actively in regions of metabolic activity or storage. Since the regions are usually the growing tips of the leaves or roots where the solutes are unloaded, this unloading reduces local pressure in the phloem so phloem sap flows in that direction explaining why the direction of the flow can change or flow can occur in two directions simultaneously. Since diffusion is far too slow to account for the velocities of the phloem movement the movement is due to pressure gradients created by phloem loading which leads to a low (negative) solute potential ( $\Psi_s$ ) resulting in a steep drop in the water potential ( $\Psi_w$ ) in response water enters the sieve elements and increases the turgor pressure ( $\Psi_p$ ). As the contents of the phloem are unloaded in

areas of storage or metabolic activity the lower sugar concentration results in a higher solute potential, because the water potential rises above that of the xylem, water leaves the phloem, reducing the turgor pressure in this region thus creating the pressure gradient <sup>3</sup>.

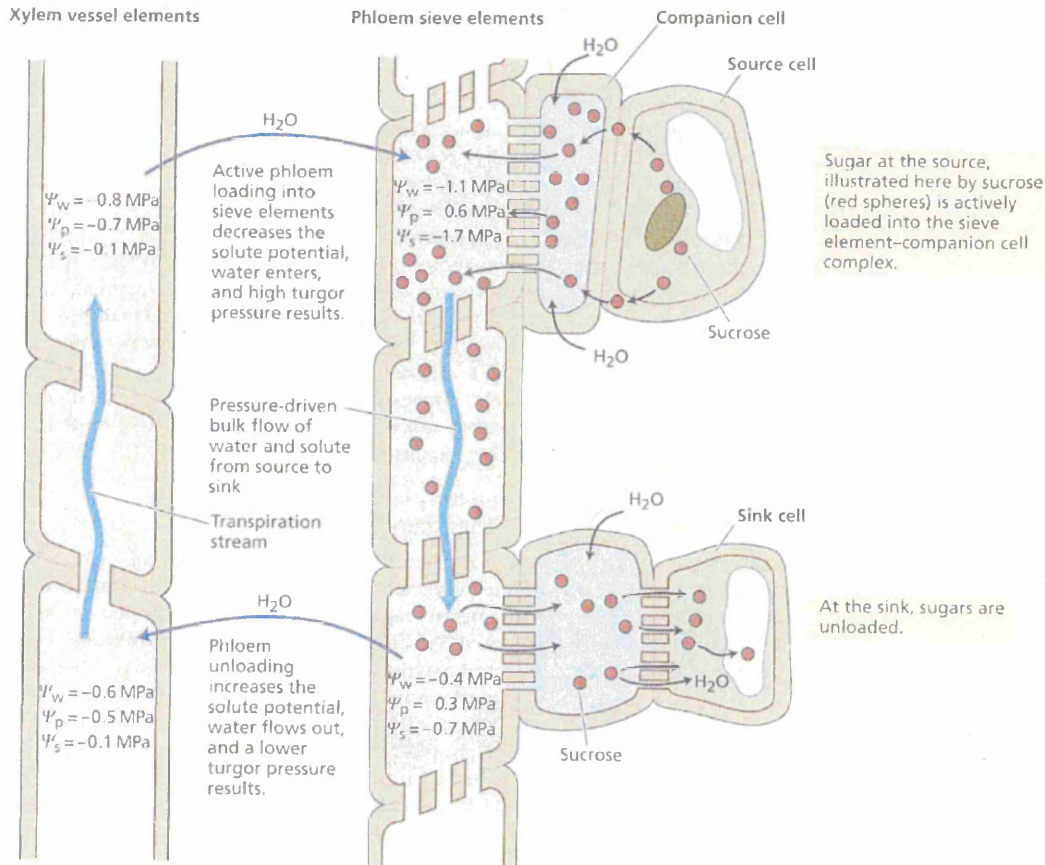


**Fig. 2 Translocation in the phloem pressure-flow model, possible values for solute potential ( $\Psi_s$ ), water potential ( $\Psi_w$ ) and turgor pressure ( $\Psi_p$ ) in the xylem and phloem. <sup>3</sup>**

If the sieve plates were not present (Fig. 1) in the sieve elements the pressure variation between the loading and unloading regions would quickly equilibrate (Fig. 2). The presence of the sieve plates greatly increases the resistance along the translocation pathway allowing the pressure difference to occur.

### 3.1.2 IR-LDI and IR-MALDI with water as a matrix

Following the introduction of MALDI-MS in the mid 1980's<sup>4</sup>, the technique has almost exclusively been associated with pulsed UV-lasers and, after rapid methodological and instrumental development, UV-MALDI-MS has become a well established method for the analysis of a wide range of biomolecules, technical polymers<sup>5</sup> and large nucleic acids<sup>6</sup>. As an alternative to UV-MALDI, infra-red matrix-assisted laser desorption/ionisation (IR-MALDI) or infra-red laser desorption ionisation (IR-LDI) has been used in the study of small molecules, carbohydrates, flavonoids, nucleic acids and proteins<sup>5-12</sup>.

The desorption and ionisation process in IR-MALDI-MS is a result of the transfer of energy to a solid sample using IR wavelengths through vibrational energy absorption<sup>7</sup>, either O-H or N-H stretch vibrations of the molecules are excited at wavelengths around 3  $\mu\text{m}$  allowing for ice to be used as a matrix<sup>8</sup>. Typically pulsed erbium solid-state lasers, Er:YAG (wavelength = 2.94  $\mu\text{m}$ ), or Er:YSGG (wavelength = 2.79  $\mu\text{m}$ ), with pulse durations between 50 and 100 ns, or wavelength tuneable optical parametric oscillator (OPO) laser systems with pulse durations of 5-10 ns can commonly used for IR-MALDI<sup>9</sup>. The first results for IR-MALDI were reported in 1990 by Overberg *et al.* using an Er:YAG laser, emission wavelength of 2.94  $\mu\text{m}$  and a pulse duration of 200 ns for the analysis of large biomolecules<sup>10</sup>. IR-MALDI has been demonstrated to be advantageous whenever particularly large and/or labile compounds have been analysed which are not amenable to UV-MALDI because IR-MALDI is regarded as a softer ionisation technique resulting in a low degree of metastable ion fragmentation. Therefore

intact proteins ions with molecular weights exceeding 500kDa have been observed

11

Results for the analysis of plant material with IR-MALDI previously reported have been concerned with the detection of endogenous metabolites. Dreisewerd *et al*<sup>12</sup> reported various small molecules including carbohydrates, phospholipids, triglycerides and flavonoids from a range of sample material including, seeds, coconuts and strawberries. Atmospheric pressure IR-MALDI has also been used for plant metabolomics studies by Li *et al*<sup>13</sup>. Analysis of plant organs including flowers, ovaries, aggregate fruits, fruits, leaves, tubers, bulbs and seeds from various species yielded metabolomic profiles of amino acids, sugars, lipids, reactants and products of nucleotide, oligosaccharide and flavonoid biosynthesis. Since IR-MALDI and IR-LDI produce ions via different mechanisms to UV-MALDI the potential to observe ions relating to the agrochemical of interest which cannot be observed with UV-MALDI is a possibility. Sensitivity toward the protonated molecules may also be improved due to IR lasers providing a softer ionisation mechanism.

The aims of the work reported in this chapter are to obtain MALDI-MSI data to determine the distribution of agrochemicals in the plant's transport systems following uptake via the roots and following foliar absorption.

## **3.2 Methods**

### **3.2.1 Uptake of azoxystrobin via the roots in soya bean plants**

Soya bean plants were germinated and grown in potting compost (B&Q, Sheffield, UK) at room temperature on the laboratory bench until the first tri-lobate leaf was

visible. Each plant was then removed from the soil and washed before being introduced to glass vials containing 1/2 strength Hogland's N<sup>o</sup>2 Basel salt solution (Sigma Aldrich, Dorset, UK). The solution was then spiked with azoxystrobin to give a concentration of 20 ppm, and the plants were left for 24 hours before a further addition of azoxystrobin was made to give a final concentration of 40 ppm. The plant was left for another 24 hours before being removed and prepared for cryostat (Leica, Milton Keynes, UK) sectioning along the longitudinal axes of the root bundle region of the plant and the stem above. Samples were arranged on a target plate and imaging analysis was performed using an Applied Biosystems/MDS Sciex Q-Star Pulsar / mass spectrometer (Concord, Ontario, Canada) fitted with an orthogonal MALDI source and an Nd:YAG laser ( $\lambda = 355 \text{ nm}$ ) at a laser power of  $3.2 \mu\text{J}$  and a laser repetition rate of 1000 Hz. Images were acquired at  $150 \mu\text{m} \times 150 \mu\text{m}$  increments.

### **3.2.2 Method for encasing stem sections in ice**

In order to obtain horizontal sections from the plant stem samples the sample had to be encased in a solid support so the sample could be passed over the stationary blade and a  $30 \mu\text{m}$  section could be taken within the cryostat instrument, without the stem sample becoming dislodged or damaged during this process. To prevent any signal suppression deionised water was rapidly frozen around the sample via the following method.

The foliage and roots were removed from the plant samples and the stem was secured ensuring it was as straight as possible to the bench surface with masking

tape. The stem length was measured and a desired section cut, approx 1-2 cm in length. The ends of the cut section were sealed using 10% cellulose acetate (Sigma Aldrich, Dorset, UK) in acetone solution.

The cut stem section was placed in trough made from parafilm, along with a small amount of deionised water (2-3 mL), ensuring the stem was submerged in a horizontal orientation. The sample in water was then placed into a polystyrene box filled with liquid nitrogen. (The sample was orientated to be upright in a floatation device (a weighing boat) to avoid losing the sample or the deionised water and to allow for slower freezing.) The sample once frozen was placed into a petri dish and labelled, then placed in a -80 °C freezer until required.

Desired stem sections (1-2 cm) were taken from regions along the plant stem and the freezing process was repeated.

Ice stem samples were trimmed to form a flat edge perpendicular to the orientation of the plant stem so that they could be secured to the cryostat (Leica, Milton Keynes, UK) stage successfully using Cryo-m-bed embedding compound (Bright Instrument Company Ltd, Cambridge, UK).

Once a suitable section was obtained it was attached to pre-frozen double sided carbon tape by lightly pressing the tape onto the tissue. The tape had to remain frozen to prevent the sample defrosting. Once all desired sections were obtained they were transferred to a pre-cooled freeze drier, again ensuring samples remain frozen during this step.

Once samples had been freeze dried they were arranged on a target plate as desired before the appropriate matrix was applied using the gravity feed airgun (Iwata Media Inc., Portland, OR, USA).

### Method for encasing stems in ice before sectioning



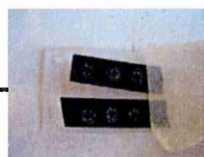
Specified sections of the stem were cut away from the stem and the end sealed with cellulose acetate. The stem was then suspended in water in a fashioned piece of parafilm before being floated in a weighing boat on liquid nitrogen.



The ice encased stem can then be trimmed down to a manageable size and a flat edge perpendicular to the stem can be shaved off in order to attach the stem to the sample stage



The freeze dried sections can then be attached to a MALDI target and matrix applied using airspray.



The carbon tape was then attached glass sides and placed inside a pre-frozen glass jar before being freeze dried.



30µm section of the stem were taken and attached to pre-frozen double sided carbon tape

### 3.2.3 Uptake of azoxystrobin via the roots in sunflower plants

A sunflower plant was germinated and grown in potting compost (B&Q, Sheffield, UK) until it had reached a height of 140 mm. The plant was then removed from the soil and washed before being introduced into a conical flask containing 1/2 strength Hogland's N<sup>o</sup>2 Basel salt solution (Sigma Aldrich, Dorset, UK). The solutions were then spiked with azoxystrobin to give a concentration of 20 ppm, and the plants were left for 24 hours (on lab bench) before a further addition of azoxystrobin was made to give a final concentration of 40 ppm. The plant was left

for another 24 h before being removed and prepared for cryostat (Leica, Milton Keynes, UK) sectioning along the horizontal axes at 10, 50, 90 and 130 mm from the root bundle region, using the method for encasing stem sections as described in section 3.2.2. Control sections were taken from an undosed plant to be used as positive and negative controls. Positive controls were spiked with 1  $\mu$ L of a 1 mg/mL solution of azoxystrobin in acetonitrile. Samples were arranged on a target plate and the matrix (10 mg/mL  $\alpha$ -CHCA 0.1% TFA) was applied using an Iwata gravity-fed pneumatic air spray gun (Iwata Media Inc., Portland, OR, USA) by passing the compressed air gun over the sample 15 times ensuring the sample tissue did not get saturated and even coverage had been achieved.

Analysis was performed using an Applied Biosystems/MDS Sciex Q-Star Pulsar / (Concord, Ontario, Canada) fitted with an orthogonal MALDI source and an Nd:YAG laser ( $\lambda = 355$  nm) at a laser power of 3.2  $\mu$ J and a laser repetition rate of 1000 Hz . Images were acquired with a spatial resolution of 250  $\mu$ m x 250  $\mu$ m.

#### **3.2.4 Uptake of nicosulfuron via the roots (hydroponics experiment)**

A Sunflower plant was germinated and grown in multipurpose potting compost (B&Q, Sheffield, UK) until it had reached a height of 150 mm. The plant was then removed from the soil and washed before being introduced to a conical flask containing 1/2 strength Hogland's N<sup>o</sup>2 Basel salt solution (Sigma Aldrich, Dorset, UK). This solution was then spiked with nicosulfuron to give a concentration of 20 ppm, and the plant was left for 24 hours (on lab bench) before a further addition of nicosulfuron was made to give a final concentration of 40 ppm. The plant was left

for another 24 hours (on lab bench) before being removed and prepared for cryostat (Leica, Milton Keynes, UK) sectioning along the horizontal axes at 10 mm, 30 mm, 50 mm and 140 mm from the root bundle region. Control sections were taken from an undosed plant to be used as positive and negative controls, positive controls were spiked with 1  $\mu\text{L}$  of a 1 mg/mL solution of nicosulfuron in acetonitrile. Samples were arranged on a target plate and the matrix (10 mg/mL  $\alpha$ -CHCA 1.0% TFA (Sigma Aldrich, Dorset, UK)) was applied using an Iwata gravity-fed pneumatic air spray gun (Iwata Media Inc., Portland, OR, USA) by passing the compressed air gun over the sample 15 times, ensuring the sample tissue did not get saturated and even coverage had been achieved. The appropriate areas were then imaged using an Applied Biosystems/MDS Sciex Q-star pulsar / mass spectrometer (Concord, Ontario, Canada) fitted with an orthogonal MALDI source and an Nd:YAG laser ( $\lambda = 355 \text{ nm}$ ) at a laser power of 3.2  $\mu\text{J}$  and a laser repetition rate of 1000 Hz. Images were acquired with a spatial resolution of 200  $\mu\text{m} \times 200 \mu\text{m}$ .

### **3.2.5 Absorption of nicosulfuron via foliar application**

A sunflower plant was germinated and grown in potting compost (B&Q, Sheffield, UK) until it had reached a height of 135 mm for the 24 hour experiment and 200 mm for the 48 hour experiment. 50x1  $\mu\text{L}$  of a 1.25 mg/mL solution of nicosulfuron in 50:50 acetonitrile: 0.1% Tween® (Sigma Aldrich, Dorset, UK) was applied to the tissue either side of the midrib vein to a leaf 125 mm along the stem of the 24 hour experiment plant and 145 mm along the stem of the 48 hour experiment plant. The plants were then left for 24 and 48 hours at 21  $^{\circ}\text{C}$  with a relative humidity of

55% (Sanyo, Versatile environmental test chamber, Hertfordshire, UK) before being removed and prepared for cryostat (Leica, Milton Keynes, UK) sectioning along the horizontal axes at varying distances from the root bundle region. Control sections were taken from an undosed plant to be used as positive and negative controls. Positive controls were spiked with 2  $\mu\text{L}$  of a 2.5 mg/mL solution of nicosulfuron in acetonitrile. Samples were arranged on target plate and the matrix (25 mg/mL  $\alpha$ -CHCA 0.1% TFA) was applied using an Iwata gravity-fed pneumatic air spray gun (Iwata Media Inc., Portland, OR, USA) by passing the compressed air gun over the sample 15 times, ensuring the sample tissue did not get saturated and even coverage had been achieved.

The appropriate areas were then imaged using an Applied Biosystems/MDS Sciex Q-star pulsar / mass spectrometer (Concord, Ontario, Canada) fitted with an orthogonal MALDI source and a nitrogen laser ( $\lambda = 337 \text{ nm}$ ) at a laser power of 35  $\mu\text{J}$  and a laser repetition rate of 20 Hz. Images were obtained with a spatial resolution of 200  $\mu\text{m} \times 200 \mu\text{m}$ .

### **Processing of MALDI-MSI data**

All images were created using Applied Biosystems oMALDI Server 5.0 tissue imaging software. All images presented are normalised against a matrix fragment ion to reduce effects caused by matrix inhomogeneity. In all cases other than the 24 hour foliar absorption experiment the ion chosen to act as the "internal standard" for normalisation was  $m/z$  172.04. For the 24 hour foliar absorption experiment the signals generated from the cyclised pyridylsulfonamide at  $m/z$  185.00 were of very low intensity and dividing this intensity by the intensity of the

ion at  $m/z$  172.04 resulted in images of low numbers of counts that were difficult to manipulate. In this case the ion chosen for normalisation was  $m/z$  147.06, the  $C^{13}$  isotope of the  $\alpha$ -CHCA fragment ion peak at  $m/z$  146.06. This increased the intensity of the pixels in the resulting image making presentation clearer.

### **3.2.6 Nicosulfuron and azoxystrobin uptake following stem application experiment**

A sunflower plant was germinated and grown in multipurpose potting compost (B&Q, Sheffield, UK) the specimen used in this instance had reached a height of 270 mm. 25  $\mu$ L of a 5 mg/mL solution of nicosulfuron in acetonitrile was combined with 25  $\mu$ L of a 5mg/mL solution of azoxystrobin in acetone. 50  $\mu$ L of 0.1% Tween® (Sigma Aldrich, Dorset, UK) was then added, resulting in 100  $\mu$ L of a 1.25 mg/mL nicosulfuron/azoxystrobin in 25:25:50 acetonitrile:acetone:0.1% Tween® (Sigma Aldrich, Dorset, UK) solution. 50  $\mu$ L of this solution was added into a well of parafilm fashioned around the plant stem (see Fig. 3).

The plant was then left for 24 hours at 21 °C with a relative humidity of 55% (Sanyo, Versatile environmental test chamber, Hertfordshire, UK) before being removed and prepared for cryostat (Leica, Milton Keynes, UK) sectioning along the horizontal axes at varying distances from the root bundle region. Control sections were taken from an undosed plant to be used as positive and negative controls. Positive controls were spiked with 2  $\mu$ L of a 2.5 mg/mL solution of nicosulfuron in acetonitrile on the left side of the control section and with 2  $\mu$ L of a 2.5 mg/mL solution of azoxystrobin in acetone on the right side of the control section. Sectioned samples were then mounted onto a MALDI target using conductive tape.

Samples were arranged on the target plate and the matrix (25 mg/mL  $\alpha$ -CHCA 0.1% TFA) was applied using an Iwata gravity-fed pneumatic air spray gun (Iwata Media Inc., Portland, OR, USA) by passing the compressed air gun over the sample 15 times, ensuring the sample tissue did not get saturated and even coverage had been achieved.

The appropriate areas were then imaged using an Applied Biosystems/MDS Sciex Q-star pulsar / mass spectrometer (Concord, Ontario, Canada) fitted with an orthogonal MALDI source and a nitrogen laser ( $\lambda = 337$  nm) at a laser power of 28  $\mu$ J and a laser repetition rate of 20 Hz. Images were obtained with a spatial resolution of 500  $\mu$ m x 500  $\mu$ m.



**Fig. 3 Optical image of parafilm fashioned around the plant stem to contain the azoxystrobin nicosulfuron solution.**

### **3.2.7 Nicosulfuron and azoxystrobin uptake following stem application experiment, using Labcyte Portrait 630 matrix applicator**

The top section (260 mm along the stem) of the sample tissue prepared as described in 3.2.6 was attached to a MALDI target plate using carbon tape, along with a negative control section taken from an undosed plant. The matrix was applied using a Labcyte portrait 630 automatic matrix spotter (Sunnyvale, California, USA) using a 25 mg/mL solution of  $\alpha$ -CHCA (Sigma Aldrich, Dorset, UK) with 5 drops per point per pass and 15 passes. The appropriate areas were then imaged using an Applied Biosystems/MDS Sciex Q-star pulsar I mass spectrometer (Concord, Ontario, Canada) fitted with an orthogonal MALDI source and a nitrogen laser ( $\lambda = 337$  nm) at a laser power of 28  $\mu$ J and a laser repetition rate of 20 Hz. Images were obtained with a spatial resolution of 150  $\mu$ m x 150  $\mu$ m.

### **3.2.8 IR-LDI analysis of mesotrione and fluaziflop-p-butyl**

A small rose bush was purchased from a shop near the University of Münster, Germany, both mesotrione and fluaziflop-p-butyl was applied to leaves on stems just below rose buds. 30  $\mu$ L of a 5.4 mg/mL solution (50:50 acetone:0.1% Tween® (Sigma Aldrich, Dorset, UK)) of mesotrione solution and 30  $\mu$ L of a 20 mg/mL solution of fluaziflop-p butyl were applied to the leaves and spread across the surface using the pipette tip. The plant was then left for 24 hours before horizontal stem section samples were taken from the stem adjacent to the application point, 1 cm above that and from tissue just below the rose bud. Samples were then secured to a glass slide using an adhesive pad, this slide was then secured to the target plate. IR-LDI-MS spectra were acquired using a prototype orthogonal TOF equipped with an Er:YAG infrared laser (Speser,

Spectrum GmbH, Berlin, Germany) that operates at a wavelength of 2.94  $\mu\text{m}$ . The pulse duration of this laser is  $\approx 100$  ms. The data was displayed using the freeware software package "Moverz".

### **3.2.9 IR-MALDI Analysis of uptake of nicosulfuron following foliar application**

A sunflower plant was germinated and grown in potting compost (B&Q, Sheffield, UK) (B&Q Sheffield, UK). The specimen used in this instance had reached a height of 60 cm. 40x1  $\mu\text{L}$  of a 0.5 mg/mL solution of nicosulfuron in 50:50 acetonitrile: 0.1% Tween® (Sigma Aldrich, Dorset, UK) was applied to the tissue either side of the midrib vein of a leaf 410 mm from the root tip. The plant was then left for 24 hours at room temperature before being removed and prepared for cryostat (Leica, Milton Keynes, UK) sectioning along the horizontal axes at 5mm, 205 mm, 405 mm, and 585 mm from the root bundle region. Sectioned samples were then mounted on conductive tape and stored at -80 °C. Control sections were taken from an undosed plant to be used as positive and negative controls. Positive controls were spiked with 1  $\mu\text{L}$  of a 1 mg/mL solution of nicosulfuron in acetonitrile, then refrozen before transportation. Sections were packed into a polystyrene container with dry ice to ensure they remained frozen and posted to the University of Münster. IR-LDI-MS spectra were acquired using a prototype orthogonal TOF equipped with an Er:YAG infrared laser (Speser, Spectrum GmbH, Berlin, Germany) that operates at a wavelength of 2.94  $\mu\text{m}$ . The pulse duration of this laser is  $\approx 100$  ms. The data were displayed using the freeware software package "Moverz".

### **3.2.10 IR-MALDI analysis of uptake of nicosulfuron via the roots (hydroponics experiment)**

A sunflower plant was germinated and grown in multipurpose potting compost (B&Q, Sheffield, UK) until it had reached a height of 150 mm. The plants were then removed from the soil and washed before being introduced to a conical flask containing 1/2 strength Hogland's N<sup>o</sup>2 Basel salt solution (Sigma Aldrich, Dorset, UK). The solutions were then spiked with nicosulfuron to give a concentration of 20 ppm, and the plants were left for 24 hours before a further addition of nicosulfuron was made to give a final concentration of 40 ppm. The plants were left for another 24 hours before being removed and prepared for cryostat (Leica, Milton Keynes, UK) sectioning along the horizontal axes at 10 mm, 30 mm, 50 mm and 140 mm from the root bundle region using the method for encasing stem sections (3.2.1). Control sections were taken from an undosed plant to be used as positive and negative controls. Positive controls were spiked with 1  $\mu$ L of a 1 mg/mL solution of nicosulfuron in acetonitrile then refrozen before transportation. Sections were packed into a polystyrene container with dry ice to ensure they remained frozen and posted to the University of Münster. IR-LDI-MS spectra were acquired using a prototype orthogonal TOF equipped with an Er:YAG infrared laser (Speser, Spectrum GmbH, Berlin, Germany) that operates at a wavelength of 2.94  $\mu$ m. The pulse duration of this laser is  $\approx$  100 ms. The data were displayed using the freeware software package "Moverz".

### **3.2.11 IR-MALDI analysis of uptake of azoxystrobin via the roots (hydroponics experiment) for IR method**

Sunflower plants were germinated and grown in potting compost (B&Q, Sheffield, UK). The specimen used in this instance had reached a height of 140 mm. The plant was then removed from the soil and washed before being introduced to conical flask containing 1/2 strength Hogland's N<sup>o</sup>2 Basel salt solution (Sigma Aldrich, Dorset, UK). The solutions were then spiked with azoxystrobin to give a concentration of 20 ppm, and the plants were left for 24 hours before a further addition of azoxystrobin was made to give a final concentration of 40 ppm. The plants were left for another 24 hours before being removed and prepared for cryostat (Leica, Milton Keynes, UK) sectioning along the horizontal axes at 50 mm and 130 mm from the root bundle region. Control sections were taken from an undosed plant to be used as positive and negative controls. Positive controls were spiked with 1 µL of a 1 mg/mL solution of azoxystrobin in acetonitrile. Sections were packed into a polystyrene container with dry ice to ensure they remained frozen and posted to the University of Münster. IR LDI MS spectra were acquired using a prototype orthogonal TOF equipped with an Er:YAG infrared laser (Speser, Spectrum GmbH, Berlin, Germany) that operates at a wavelength of 2.94 µm. The pulse duration of this laser is ≈ 100 ms. The data were displayed using the freeware software package "Moverz".

### 3.3 Results

#### 3.3.1 Uptake of azoxystrobin via the roots in soya bean plants

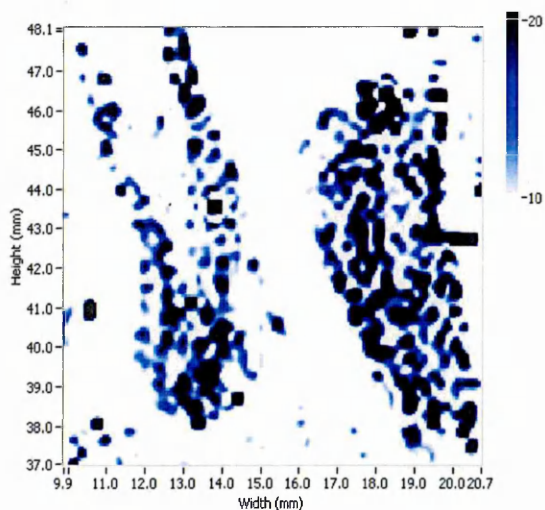


Fig. 4 MALDI-MS image of the distribution of the azoxystrobin's fragment ion at  $m/z$  372.09 in longitudinal cross sections of soya bean root bundle tissue.

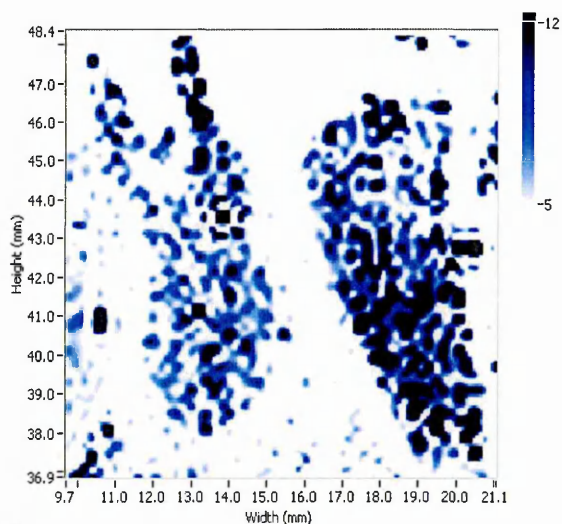
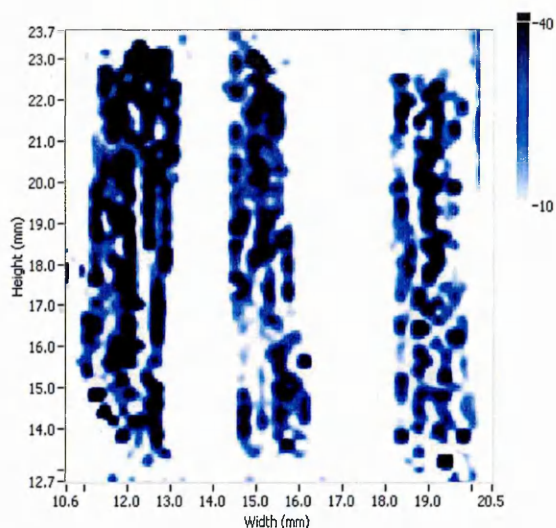


Fig. 5 MALDI-MS image of the distribution of the azoxystrobin sodium adduct of the molecular ion at  $m/z$  426.11 in longitudinal cross section of soya bean root bundle tissue.

Fig. 4 shows the distribution of the azoxystrobin fragment ion at  $m/z$  372.09 in longitudinal cross sections of soya bean root bundle tissue. Figure 4 shows that azoxystrobin is distributed evenly throughout the root bundle tissue in the two

adjacent sections. The signal observed within the tissue is present with high intensity indicated by the intensity scale on the right of the image, although an element of background interference is present as the lower value of this scale has been increased to remove background noise in the image.

Fig. 5 shows the distribution of the azoxystrobin sodium adduct at  $m/z$  426.11 in longitudinal cross sections of soya bean root bundle tissue. Figure 5 clearly shows the distribution of azoxystrobin present within the 2 adjacent longitudinal root bundle sections. The intensity of the analyte to matrix ratio for this ion is not as high as observed with the azoxystrobin fragment ion but less background interference is present at this  $m/z$ .



**Fig. 6 MALDI-MS image of the distribution of the azoxystrobin fragment ion at  $m/z$  372.09 in longitudinal cross section of soya bean stem tissue above the root bundle.**

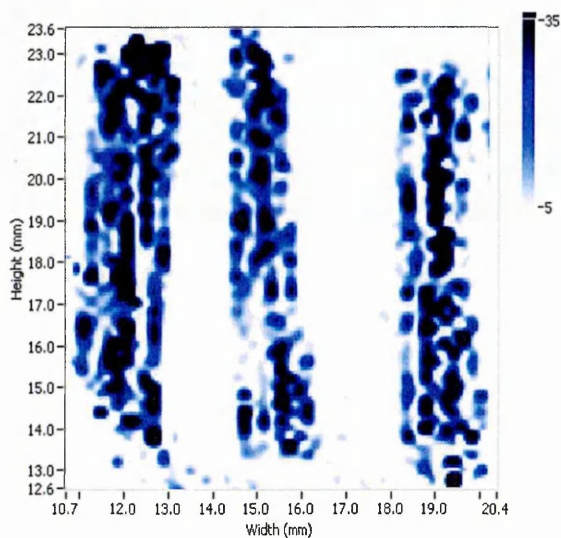


**Fig. 7 MALDI-MS image of the distribution of the azoxystrobin sodium adduct of the molecular ion at  $m/z$  426.11 in longitudinal cross section of soya bean stem tissue above root bundle.**

Fig. 6 shows the distribution of the azoxystrobin fragment ion at  $m/z$  372.09 in longitudinal cross section of soya bean stem tissue above the root bundle.

It shows the even distribution of azoxystrobin in 3 adjacent longitudinal sections of the stem tissue above the root bundle region. The ion is present in high

abundance within the tissue samples indicated by the intensity scale on the right hand side of the image.

Fig. 7 shows the distribution of the azoxystrobin sodium adduct at  $m/z$  426.11 in longitudinal cross section of soya bean stem tissue above the root bundle. It clearly shows the distribution of azoxystrobin in the 3 adjacent longitudinal sections of the stem tissue above the root bundle. The presence of this ion in these sections is observed with a high signal indicated by the intensity scale on the right.

### **3.3.3 Uptake azoxystrobin via the roots in sunflowers plants**

Fig. 8 (a) shows the distribution of the azoxystrobin fragment ion at  $m/z$  372.09 in horizontal sections taken at varying distances from the root bundle. The compound is clearly visible in the positive control, confirming the ion originates from azoxystrobin. There is a low signal present in the negative control section taken from an undosed plant so slight interference from an endogenous compound is observed at this  $m/z$ . There is signal present in the sections 10, 50, 90 and 130 mm away from the root tip in the sunflower plant horizontal sample sections with the highest abundance observed in the sample section 50mm from the root tip.

Fig. 9 (a) shows the distribution of the azoxystrobin protonated molecule at  $m/z$  404.12 in horizontal sections taken at varying distances from the root bundle. The compound is clearly visible in the positive control, confirming the ion originates from azoxystrobin. There is no signal present in the negative control section taken from an undosed plant so no interference from an endogenous compound is observed at this  $m/z$ . There is signal present in the section 10 mm away from the

root tip in the sunflower plant horizontal sample sections despite the highest abundance of azoxystrobin being observed in the section 50mm from the root tip in Fig. 8. The signal for the protonated molecule shows a high abundance allowing for the distribution to be observed in this section. Slight signal can be seen in the sections 50, 90, and 130 mm away from the root tip at this m/z which can be attributed to background noise.

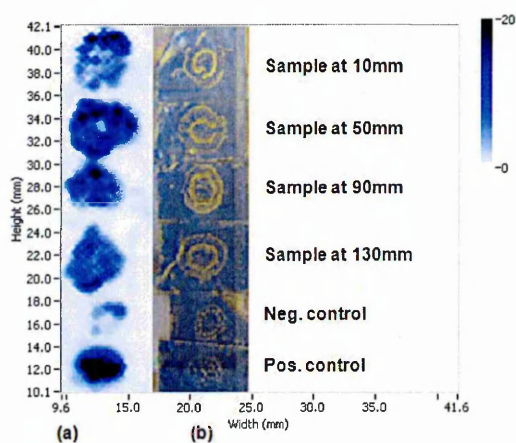


Fig. 8 (a) MALDI-MS image of the distribution of the azoxystrobin fragment ion at m/z 372.09 in horizontal sections taken at varying distances from the root bundle. (b) Optical image of horizontal sections taken at varying distances from the root bundle.

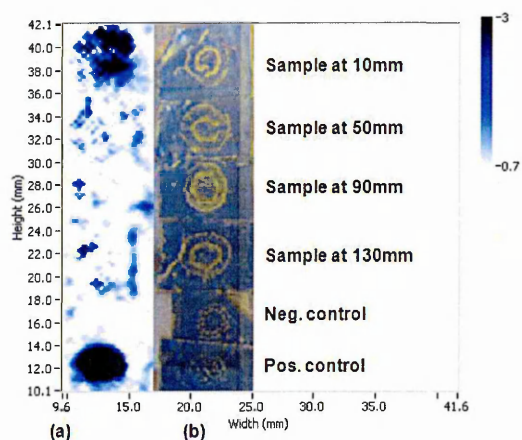


Fig. 9 (a) MALDI-MS image of the distribution of the azoxystrobin protonated molecule at m/z 404.12 in horizontal sections taken at varying distances from the root bundle. (b) Optical image of horizontal sections taken at varying distances from the root bundle.

Due to unsuccessful attempts to image the distribution of mesotrione and fluzifop-p-butyl following foliar application, experiments were performed using nicosulfuron with both the hydroponics method and the foliar application method (3.2.4 and 3.2.5).

### 3.3.4 Uptake of nicosulfuron via the roots (hydroponics experiment)

The positive ion MALDI mass spectrum of nicosulfuron (Fig.10) exhibits a number of ions which can potentially be used to generate images *i.e.* the  $[M+H]^+$  ion at  $m/z$  411.10,  $Na^+$  adduct at  $m/z$  433.06 the  $K^+$  adduct at  $m/z$  449.04 and fragment ions at  $m/z$  182.06 and  $m/z$  156.07.

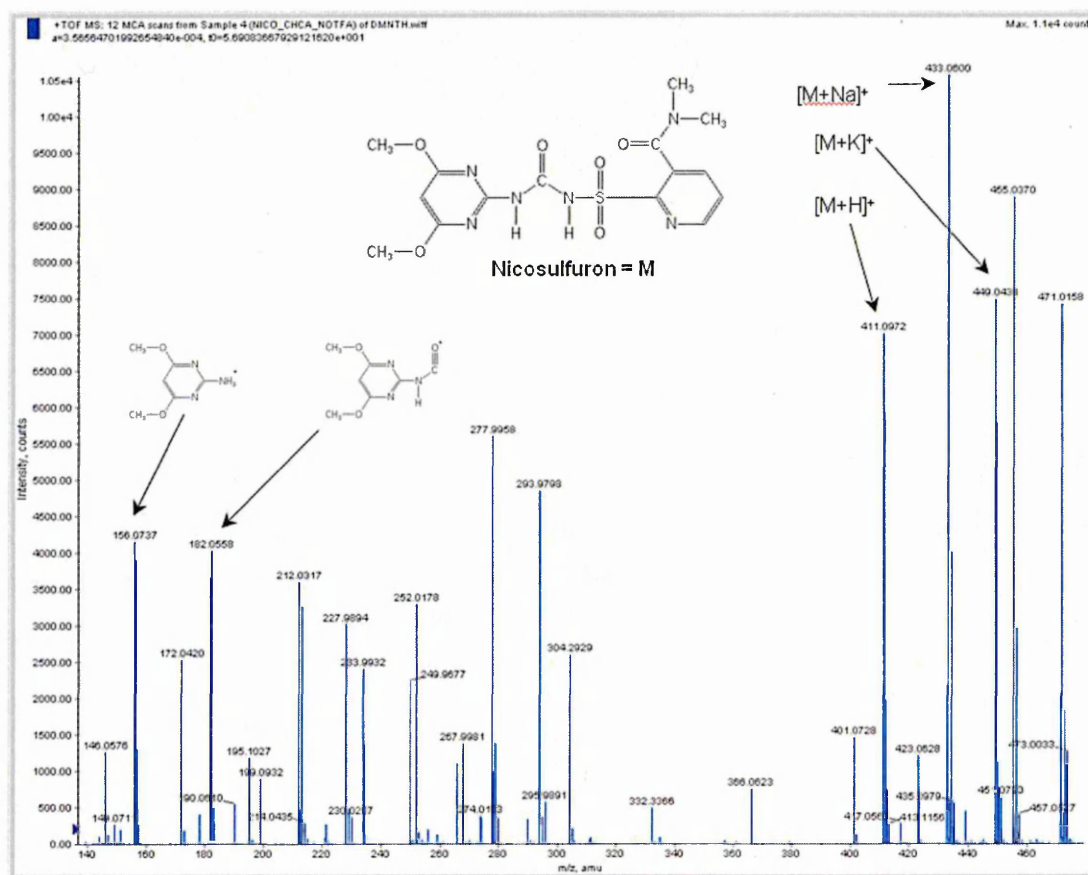
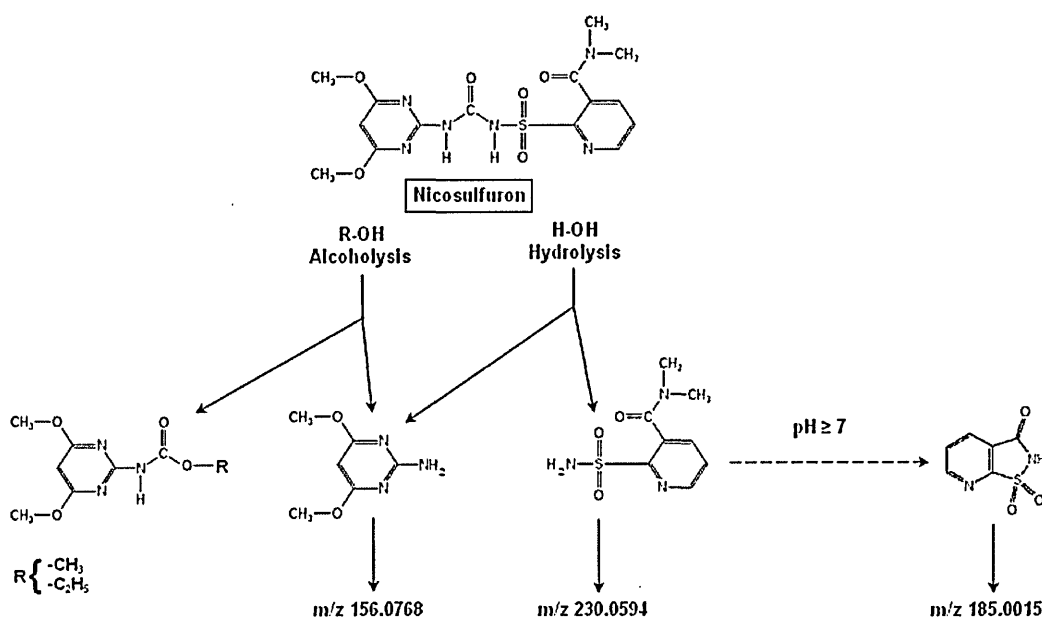


Fig. 10 Positive ion MALDI mass spectrum of nicosulfuron (1.0mg/mL) with CHCA (10mg/mL in acetone) 50:50. Showing the  $[M+H]^+$  ion at  $m/z$  411.10,  $Na^+$  adduct at  $m/z$  433.06, the  $K^+$  adduct at  $m/z$  449.04 and fragment ions at  $m/z$  182.06 and  $m/z$  156.07.

The fragment ion at  $m/z$  156.08 is clearly observed not only in conventional MALDI samples but also in tissue samples, therefore it potentially allows the generation of clear MALDI-MS images for the distribution of nicosulfuron following either uptake via the roots or absorption following foliar application.

A previous study by Sabadie<sup>14</sup> described the formation of breakdown products of nicosulfuron via alcoholysis and hydrolysis.



**Fig. 11** Alcoholysis and hydrolysis products of nicosulfuron and resulting protonated  $m/z$  values<sup>14</sup>.

This would potentially lead to a species of aminopyrimidal structure (Figure 11) of RMM 155 and is a possible source of the ion at  $m/z$  156.08 in Fig. 10 and Fig. 11. In a previous study conducted by electrospray tandem mass spectrometry, Li *et al*<sup>15</sup> reported that the major product ion observed under CID for nicosulfuron was  $m/z$  182.06. This may have been evidence that the ion observed at  $m/z$  156.08 in

the work reported here was arising as a result of hydrolysis of the urea bond rather than by "in source" fragmentation. To investigate if this was an ion being produced as a result of in source fragmentation or from a compound formed by alcoholysis by the matrix solution or hydrolysis by water or TFA, nicosulfuron was analyzed using just acetonitrile as a solvent. The nicosulfuron was dissolved in acetonitrile (2.5mg/mL) and a saturated solution of  $\alpha$ -CHCA in acetonitrile was employed as the matrix.

The spectrum obtained (Fig. 12) shows the aminopyrimidine species as the base peak along with the  $[M+H]^+$ ,  $[M+Na]^+$  and  $[M+K]^+$  ions of nicosulfuron.

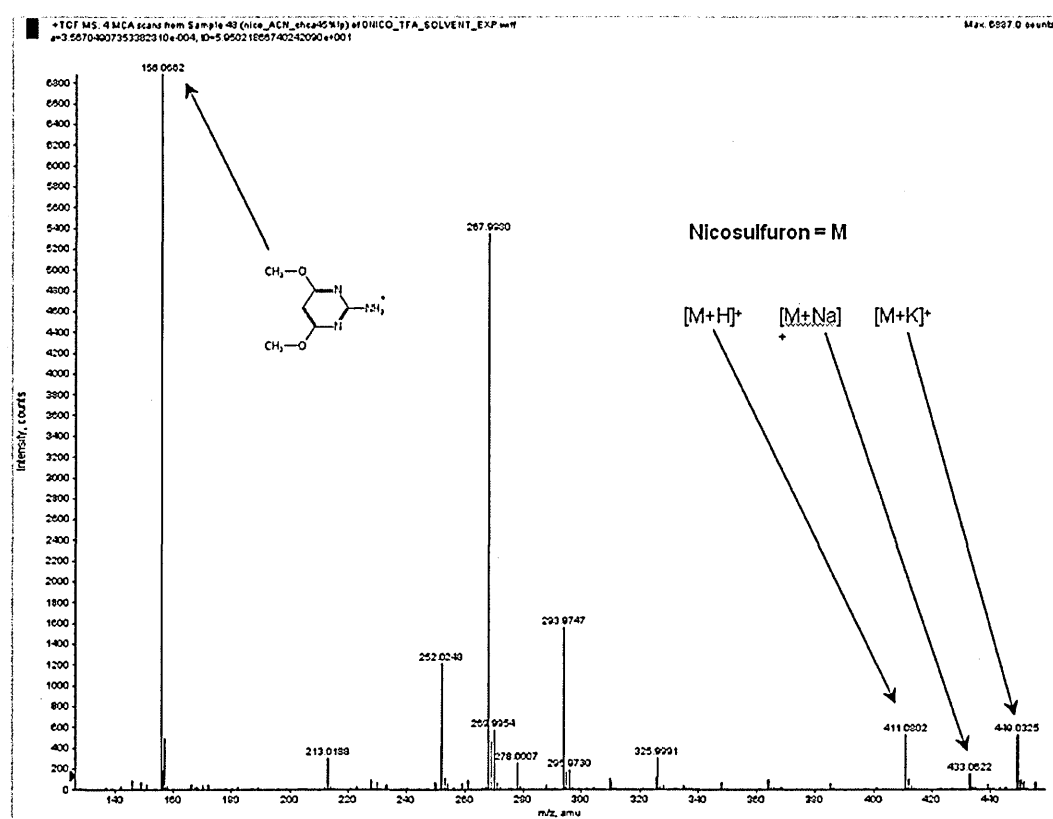
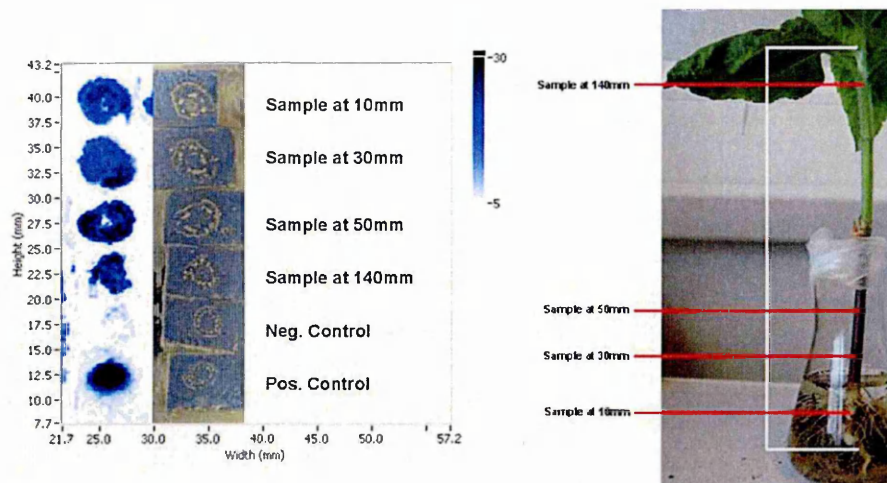


Fig. 12 Positive ion MALDI mass spectrum of nicosulfuron (2.5mg/mL in acetonitrile) with  $\alpha$ -CHCA (saturated solution in acetonitrile) 50:50. Showing the  $[M+H]^+$  ion at m/z 411.08, Na<sup>+</sup> adduct at m/z 433.06 the K<sup>+</sup> adduct at m/z 449.03 and fragment ion m/z 156.07.

Another potential source of the ion at  $m/z$  156.08 in plants is histidine. This has the same molecular formula as 2-amino-4,6-dimethoxypyrimidine ( $C_6H_9N_3O_2$ ) and is present as an endogenous metabolite as part of the histidine biosynthesis and methionine salvage pathway<sup>13</sup>; here it is assumed that by dissolving the matrix compound in acetone co-crystallization of the matrix with histidine is minimized hence limiting ionisation of histidine, indicated by the low signal in the negative control in the images.

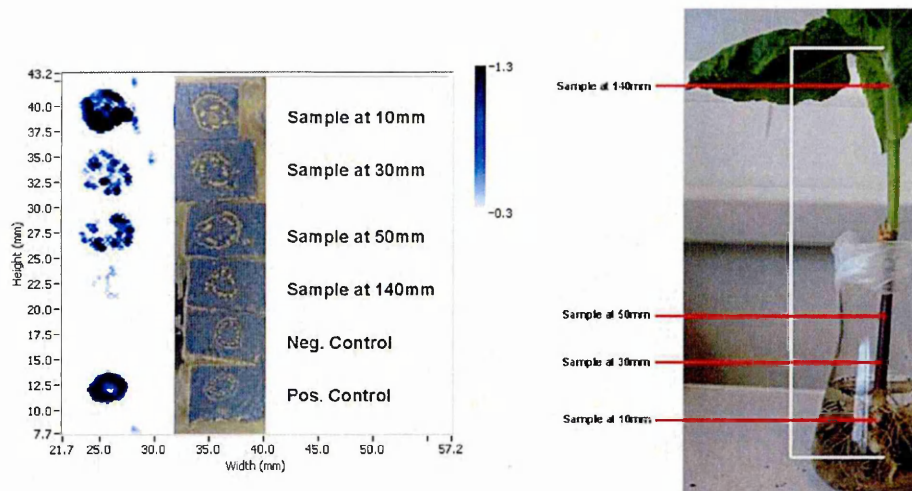
Whilst the use of SRM techniques adds specificity to MALDI-MSI experiments, for the work reported here it was found that because the  $[M+H]^+$  ion of nicosulfuron was of relatively low abundance the sensitivity obtainable was not adequate to allow SRM experiments to be performed. Experiments were therefore conducted in full scan mode and a very narrow mass window (0.013 Da) around the fragment ion of interest ( $m/z$  156.08) was used to ensure a degree of specificity. The inclusion of positive and negative controls also highlighted potential interferences.

Alcoholysis and hydrolysis of nicosulfuron causes breakdown of the urea part of the molecule and in fact results in the production of 4 products; a pyridylsulfonyl-carbamate (the exact molecular mass of which depends on the alcohol), the aminopyrimidine (RMM 155.08), as previously discussed, a pyridylsulfonamide (RMM 229.06) and a cyclized pyridylsulfonamide (RMM 184.00)<sup>14</sup>.



(a) (b) (c)

**Fig. 13** Image of a sunflower plant stem following uptake via the roots after a 48 hour hydroponics experiment. (a) MALDI-MS Image of nicosulfuron fragment ion at  $m/z$  156.08 (image range  $m/z$  156.068-156.081 and normalised against  $\alpha$ -CHCA  $m/z$  172.04 peak). (b) Optical image of horizontal sections taken at varying distances from the root bundle. (c) Optical image indicating region where horizontal sections were taken from in the hydroponics experiment.



(a) (b) (c)

**Fig. 14** Images of a sunflower plant stem following uptake via the roots after a 48 hour hydroponics experiment. (a) MALDI-MSI Image of nicosulfuron potassium adduct ion at  $m/z$  449.06 (image range  $m/z$  449.042-449.076 and normalised against  $\alpha$ -CHCA  $m/z$  172.04 peak).

**(b) Optical image of horizontal sections taken at varying distances from the root bundle. (c) Optical image indicating region where horizontal sections were taken from in the hydroponics experiment.**

Fig. 13 (a) shows the presence of 2-amino-4,6-dimethoxypyrimidine ( $m/z$  156.08) in all of the sample sections and the positive control. Low signal from endogenous compounds can be seen in the negative control. These data show that nicosulfuron has translocated around all of the plant tissue following uptake via the roots after 48 hours. Confirmation of these findings is given in Fig. 14. This is generated from the potassium adduct at  $m/z$  449.06 using the matrix peak at  $m/z$  172.04 as an internal standard.

Fig. 14 (a) shows the distribution of nicosulfuron potassium adduct at  $m/z$  449.06. The presence of nicosulfuron is clearly indicated in the positive control and samples taken 10, 30 and 50 mm from the root tip, with a weak signal being also observed in the sample taken at 140 mm.

Fig. 15 (a) shows the distribution of the phase I cyclized pyridylsulfonamide metabolite at  $m/z$  185.00 (Fig. 11).

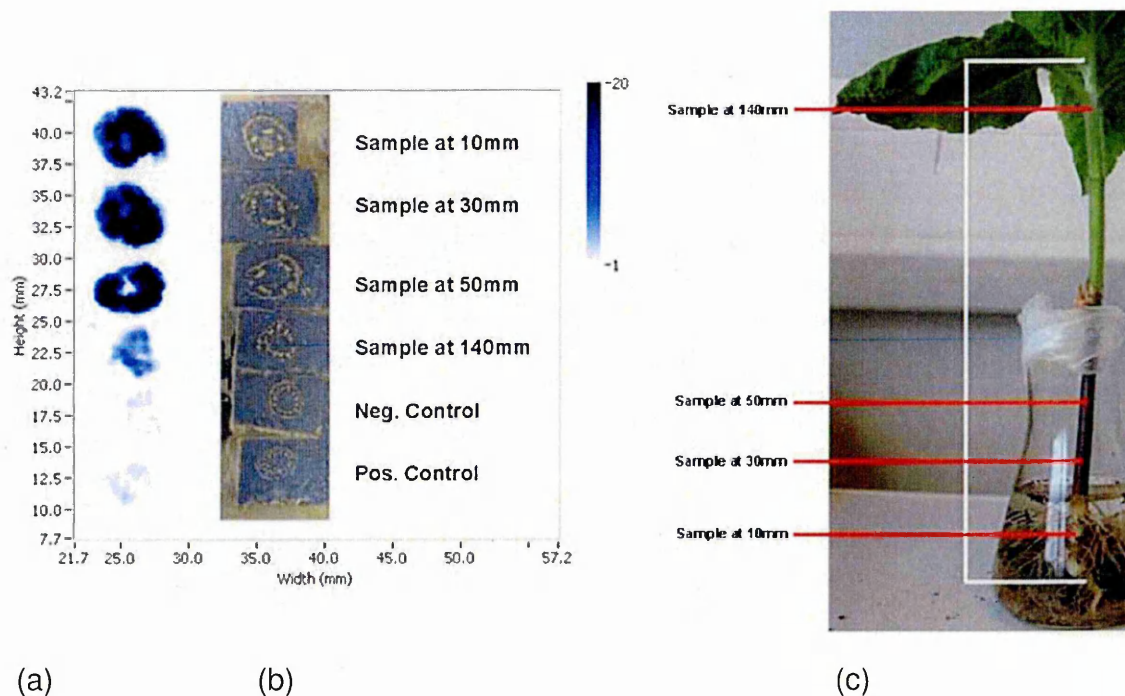


**Fig. 15 Images of a sunflower plant stem following uptake via the roots after a 48 hour hydroponics experiment. (a) MALDI-MS Image of cyclised pyridylsulfonamide at  $m/z$  185.00 (image range  $m/z$  185.001-185.009 and normalised against  $\alpha$ -CHCA  $m/z$  172.04 peak). (b) Optical image of horizontal sections taken at varying distances from the root bundle. (c) Optical image indicating region where horizontal sections were taken from in the hydroponics experiment.**

This compound can be seen in the samples at 10, 30 and 50 mm and some signal can be seen clearly in the sample 140 mm from the root tip. The compound is not present in either the positive or the negative control indicating that there is no endogenous compound at this mass and production of this compound is a result of the hydrolysis reaction of nicosulfuron in the plant's transport system.

### 3.3.5 Absorption of nicosulfuron following foliar application

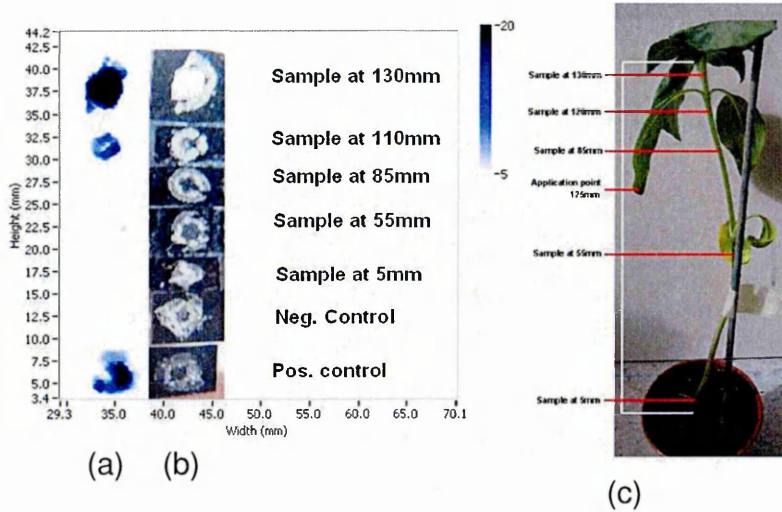


Fig. 16 Images of a sunflower plant stem following uptake via the leaves after a 24 hour foliar application experiment. (a) MALDI-MS Image of nicosulfuron fragment ion at m/z 156.08 (image range m/z 156.068-156.081 and normalised against  $\alpha$ -CHCA m/z 172.04 peak). (b) Optical image of horizontal sections taken at varying distances from the root bundle. (c) Optical image indicating region where horizontal sections were taken from in the 24 hour foliar application experiment.

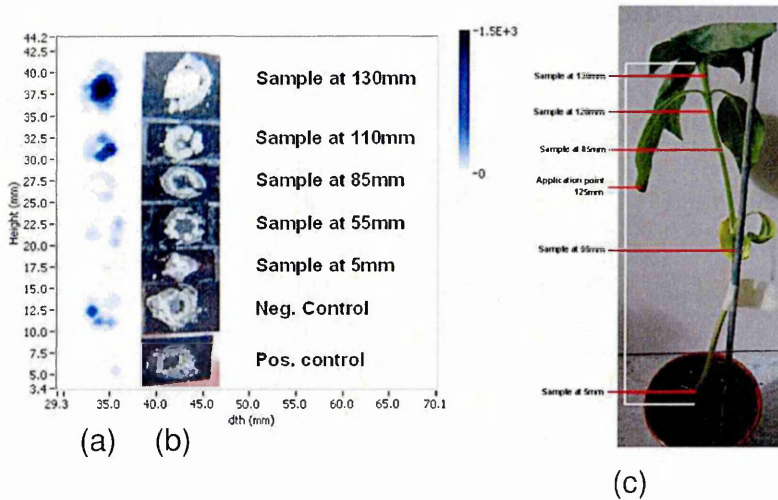


Fig. 17 Images of a sunflower plant stem following uptake via the leaves after a 24 hour foliar application experiment. (a) MALDI-MS Image of cyclised pyridylsulfonamide at m/z 185.00 (image range m/z 185.001-185.009 and normalised against  $\alpha$ -CHCA m/z 147.06 C<sup>13</sup> fragment ion peak increasing the dynamic range for the intensity of the image.). (b) Optical

image of horizontal sections taken at varying distances from the root bundle. (c) Optical image indicating region where horizontal sections were taken from in the 24 hour foliar application experiment.

Fig. 16 shows the aminopyrimidine compound 24 hours after nicosulfuron foliar application. These data indicate that nicosulfuron has been absorbed and translocated to stem tissue above and slightly below the application point at 125 mm. The image generated from the peak at  $m/z$  156.08 shows that the aminopyrimidine structure is present in the sample at 130 mm and the positive control with high intensity and also in the sample at 110 mm. Nicosulfuron can not be identified in any of the other stem sections at this  $m/z$ .

Fig. 17, the image generated from the ion at  $m/z$  185.00, indicates that nicosulfuron has been hydrolysed and is present in the same area as the fragment ion at  $m/z$  156.08 (see Fig. 16).

An image for the potassium adduct in these samples could not be generated. This could be due to the plant not having excess potassium present, which was provided by the nutrient solution in the hydroponics experiment.

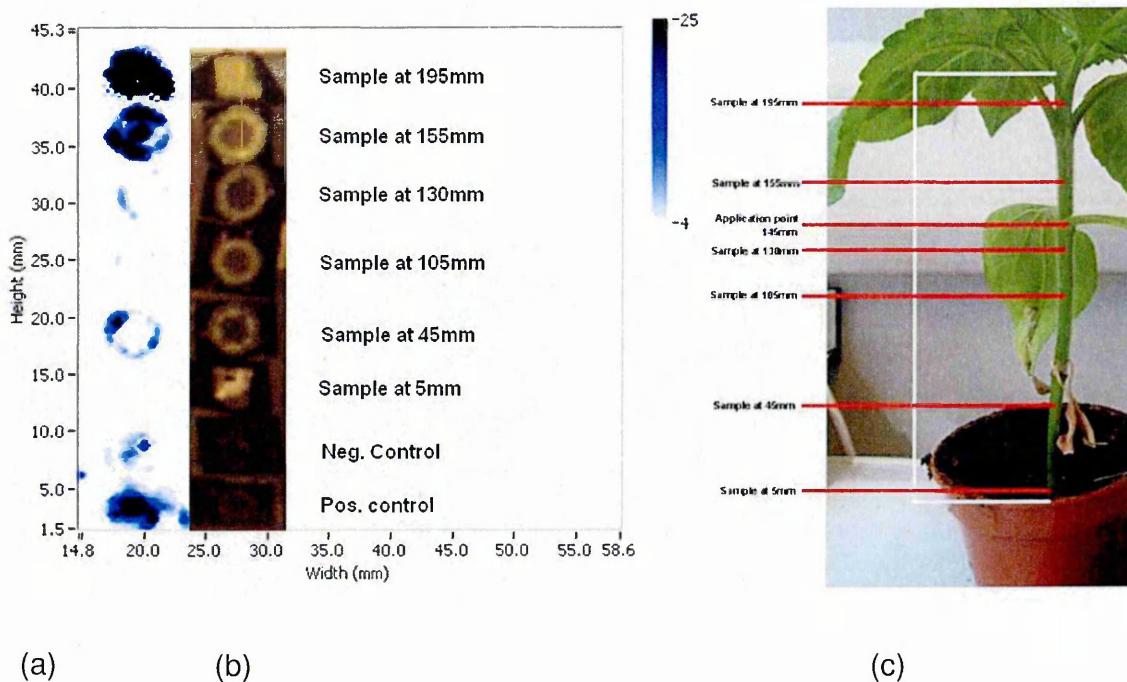


Fig. 18 Images of a sunflower plant stem following uptake via the leaves after a 48 hour foliar application experiment. (a) MALDI-MS Image of nicosulfuron fragment ion at  $m/z$  156.08 (image range  $m/z$  156.068-156.08 and normalised against  $\alpha$ -CHCA  $m/z$  172.04 peak). (b) Optical image of horizontal sections taken at varying distances from the root bundle. (c) Optical image indicating region where horizontal sections were taken from in the 48 hour foliar application experiment.

The image generated from the peak at  $m/z$  156.08 (Fig. 18) 48 hours following foliar application shows that the aminopyrimidine structure is present in the positive control and the samples at 155 mm and 195 mm. This indicates that nicosulfuron has translocated towards the growing tips of the plant. Signal is also observed in the sample 45 mm along the stem due to translocation towards the growing tips of the roots.

### 3.3.6 Nicosulfuron and azoxystrobin uptake following stem application experiment

Nicosulfuron is both xylem and phloem mobile so has the ability to travel both up and down the transport vessels towards the growing tips of the plant. Since azoxystrobin is only mobile within the xylem, azoxystrobin can only travel upwards in the transpiration stream of the xylem. If azoxystrobin was applied to a leaf it would be absorbed into the leaf tissue into the xylem and translocated to the tip of the leaf away from the petiole and plant stem. For this reason in order to assess translocation of both nicosulfuron and azoxystrobin within the same plant transport system a mixture of the compounds was applied to the stem by pipetting the solution into a well of parafilm fashioned around the plant stem 140 mm from the root tip. Sections were taken on, above and below this application point 24 hours following application to assess the translocation of the compounds.

The image in Fig. 19 (a) shows the presence of 2-amino-4, 6-dimethoxypyrimidine ( $m/z$  156.08) in the sample section 260 mm along the plant stem and the positive control. Low signal from endogenous compounds can be seen in the negative control. These data show that nicosulfuron has translocated in either the xylem or the phloem towards the growing tips of the plant stem following absorption into the stem tissue 24 hours following application.

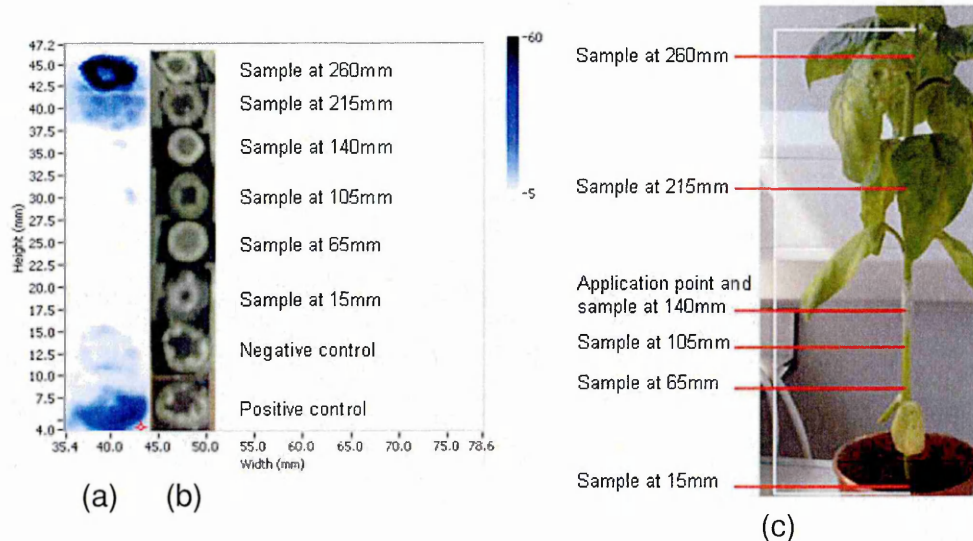


**Fig. 19** Images of a sunflower plant stem following uptake via the stem 24 hours after application of the azoxystrobin and nicosulfuron. (a) MALDI-MS Image of nicosulfuron fragment ion at  $m/z$  156.08 (image range  $m/z$  156.068-156.081 and normalised against  $\alpha$ -CHCA  $m/z$  172.04 peak). (b) Optical image of horizontal sections taken at varying distances from the root bundle. (c) Optical image indicating region where horizontal sections were taken from in the 24 hour foliar applied experiment.

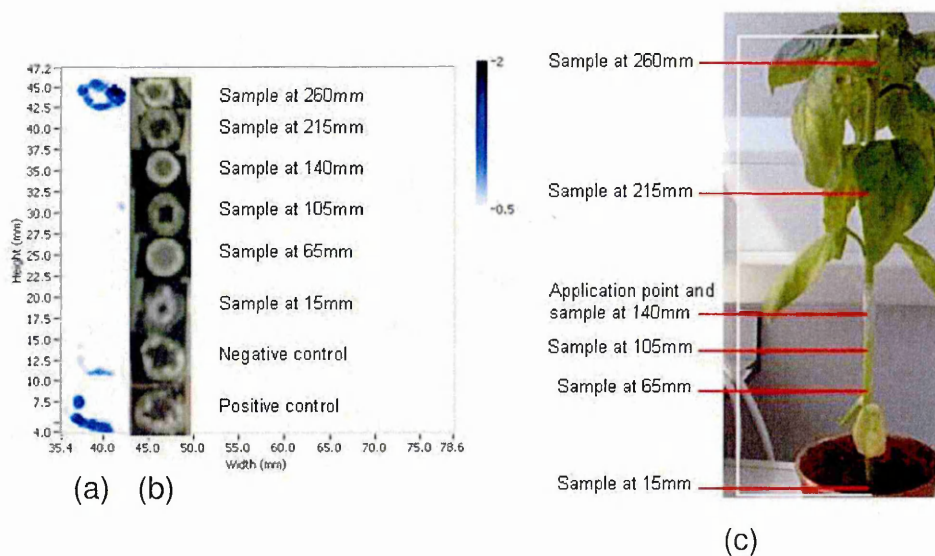


**Fig. 20** Images of a sunflower plant stem following uptake via the stem 24 hours after application of the azoxystrobin and nicosulfuron. (a) MALDI-MS Image of azoxystrobin fragment ion at  $m/z$  372.10 (image range  $m/z$  372.080 to 372.120) and normalised against  $\alpha$ -CHCA  $m/z$  172.04 peak). (b) Optical image of horizontal sections taken at varying distances

from the root bundle. (c) Optical image indicating region where horizontal sections were taken from in the 24 hour foliar applied experiment.

The image in Fig. 20 (a) shows the presence of azoxystrobin's fragment ion ( $m/z$  372.10) in the sample section 260 mm along the plant stem and the positive control. Low signal from endogenous compounds can be seen in the negative control. These data show that azoxystrobin has translocated in the xylem transpiration stream towards the growing tips of the plant stem following absorption into the stem tissue 24 hours following application.

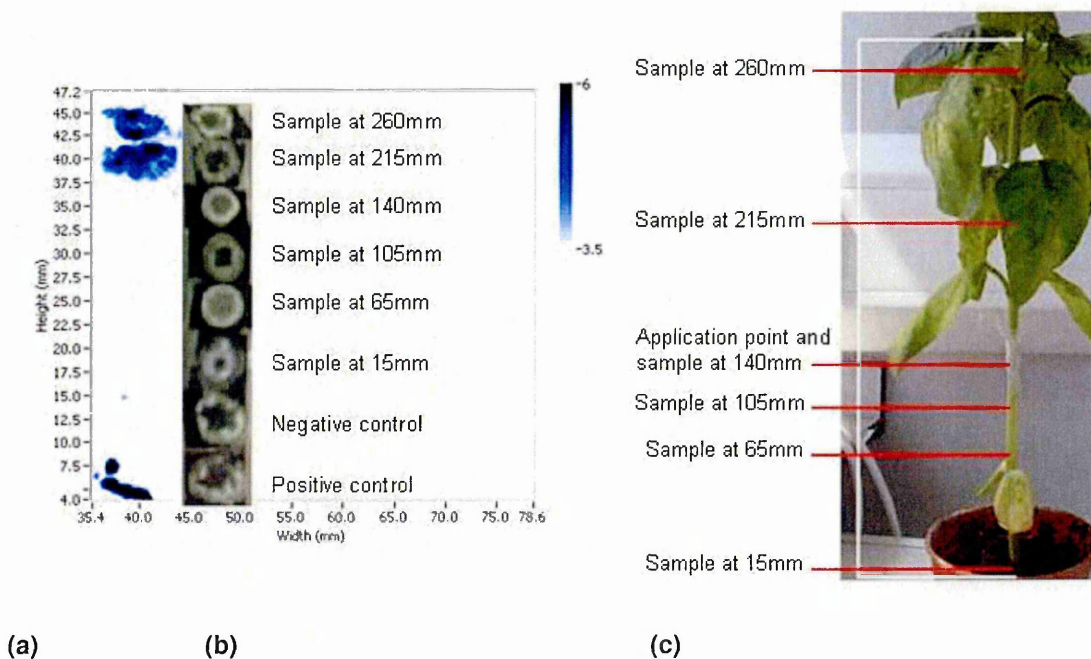


**Fig. 21** Image of a sunflower plant stem following uptake via the stem 24 hours after application of the azoxystrobin and nicosulfuron. (a) MALDI-MS Image of azoxystrobin protonated molecule at  $m/z$  404.12 (image range  $m/z$  404.100 to 404.150) and normalised against  $\alpha$ -CHCA  $m/z$  190.05 peak). (b) Optical image of horizontal sections taken at varying distances from the root bundle. (c) Optical image indicating region where horizontal sections were taken from in the 24 hour foliar applied experiment.

### 3.3.7 Nicosulfuron and azoxystrobin uptake following stem application experiment, using Labcyte Portrait 630 matrix applicator

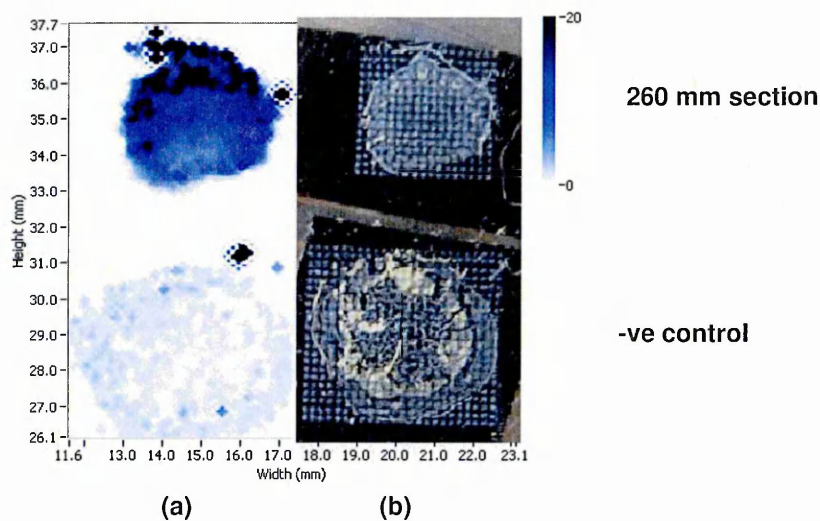


Fig. 22 Images of a sunflower plant stem following uptake via the stem 24 hours after application of the azoxystrobin and nicosulfuron. (a) MALDI-MS Image of nicosulfuron fragment ion at m/z 156.08 (image range m/z 156.068-156.081). (b) Optical image of horizontal sections taken 260mm along the stem in the 24 hour stem application experiment and a negative control section.

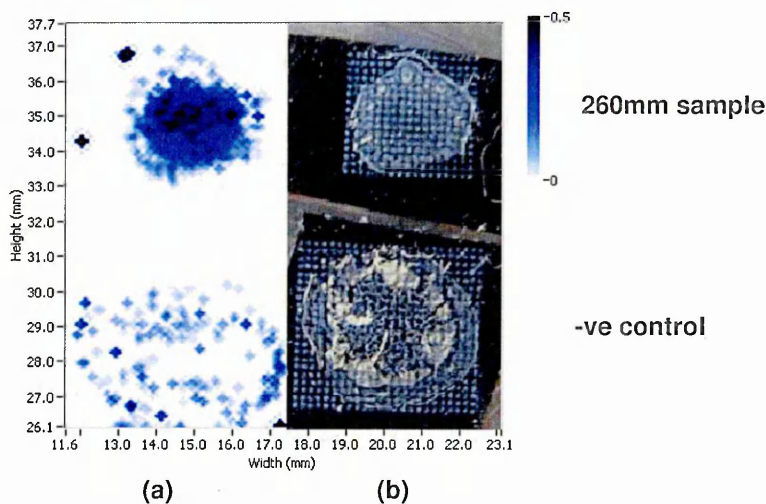


Fig. 23 Images of a sunflower plant stem following uptake via the stem 24 hours after application of the azoxystrobin and nicosulfuron. (a) MALDI-MS Image of azoxystrobin fragment ion at m/z 372.10 (image range m/z 372.080 to 372.120). (b) Optical image of

**horizontal sections taken 260mm along the stem taken in the 24 hour stem application experiment and a negative control section.**

Fig. 22 (a) shows the MALDI-MSI and the distribution of 2-amino-4, 6-dimethoxypyrimidine, nicosulfuron fragment ion at  $m/z$  156.08 in the sample section 260 mm along the plant stem. Low signal from endogenous compounds can be seen in the negative control. The response for this ion and ions relating to azoxystrobin appears to have not been greatly improved by applying the matrix with the Labcyte automatic spotter compared to the sections prepared using airspray deposition. This is indicated by the intensity ratios observed on the right of the images in Fig. 19 and 22 ( $m/z$  156.08), 20 and 23 ( $m/z$  372.10), 21 and 24 ( $m/z$  404.12). Automatic spotters are reported to enhance sensitivity due to an increased amount of analyte being drawn out of the tissue and co-crystallization between the analyte and matrix being enhanced by the number of passes being increased and the instrument's ability to apply a volume which does not spread across the sample section <sup>16</sup>. Since the effect of solvent spreading has been removed in this experiment the spatial distribution of the compound observed in this MALDI-MSI is accurate to the original distribution of the translocated compound. That is, the MALDI-MSI shows the nicosulfuron is present in a greater concentration in the outside of the stem where the vascular bundles are located as indicated by the darker region.

The image in Fig. 23 (a) shows the presence of the azoxystrobin fragment ion ( $m/z$  372.10) in the sample section 260 mm along the plant stem. Low signal from endogenous compounds can be seen in the negative control. These data show that azoxystrobin has translocated in the xylem transpiration stream towards the

growing tips of the plant stem following absorption into the stem tissue 24 hours following application. Azoxystrobin appears to be present in the highest concentration in the centre of the section, indicated by the darker region.

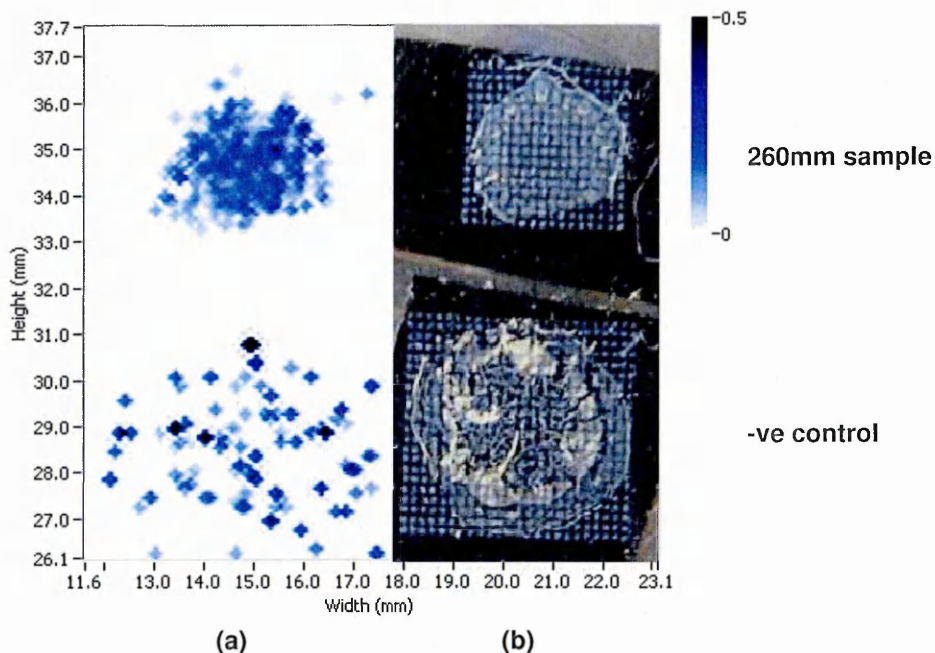


**Fig. 24** Images of a sunflower plant stem section following uptake via the stem 24 hours after application of the azoxystrobin and nicosulfuron. (a) MALDI-MSI Image of azoxystrobin fragment ion at  $m/z$  404.12 (image range  $m/z$  404.010 to 404.150). (b) Optical image of horizontal sections taken 260mm along the stem taken in the 24 hour stem application experiment and a negative control section.

The image in Fig. 24 (a) shows the presence of azoxystrobin's protonated molecule ( $m/z$  404.12) in the sample section 260 mm along the plant stem. Slight interference from endogenous compounds can be seen in the negative control. These data show that azoxystrobin has translocated in the xylem transpiration stream towards the growing tips of the plant stem following absorption into the stem tissue 24 hours following application.

### 3.3.8 IR-LDI from analysis of fluazifop-p-butyl

IR lasers provides an alternative ionisation method to UV lasers as water or ice present within the sample acts as the matrix, this removes the problem of matrix ions at low mass interfering with ions of interest.

Fig. 25 shows the positive IR-LDI mass spectrum of a fluazifop-b butyl horizontal control stem section from an undosed region, mass region  $m/z$  0-500.

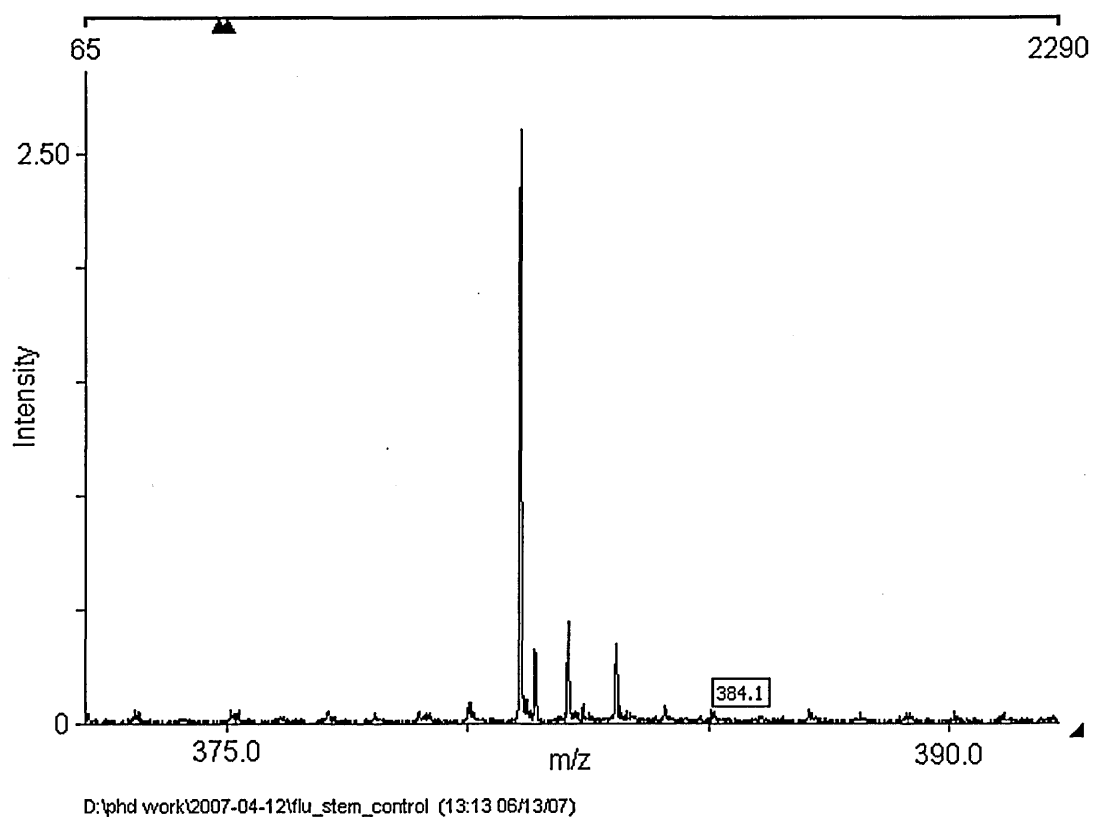


Fig. 25 Positive IR-LDI mass spectrum of Fluazifop-p butyl on stem tissue control

The spectrum in Fig. 25 is from fluazifop-p butyl solution pipetted onto a control stem section. The spectrum does not show any peaks at either the protonated molecule mass or potential fragment masses. This is probably due to the poor

ionisation observed with fluazifop-p butyl. As the fluazifop acid control was unavailable a true control spectrum could not be obtained.

Fig. 26 shows the positive IR-LDI mass spectrum of a fluazifop-b butyl horizontal stem section at the application point, mass region  $m/z$  0-500.

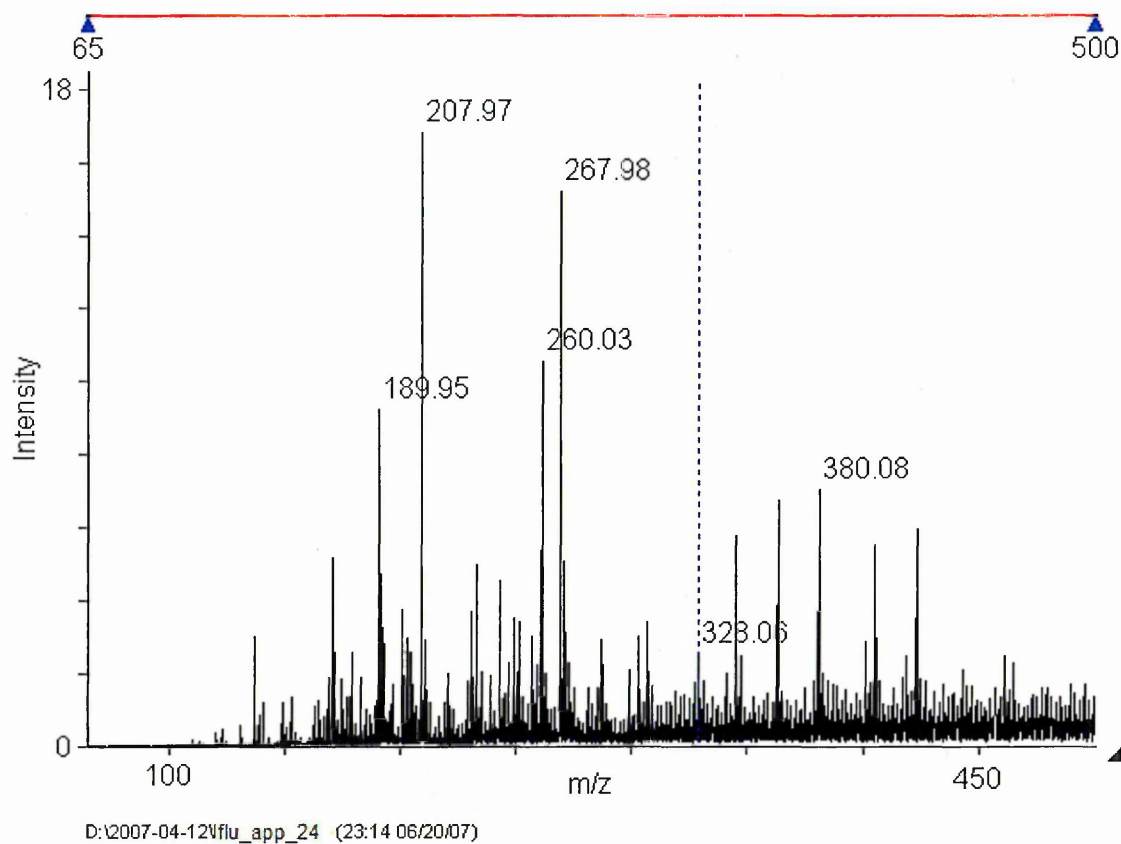
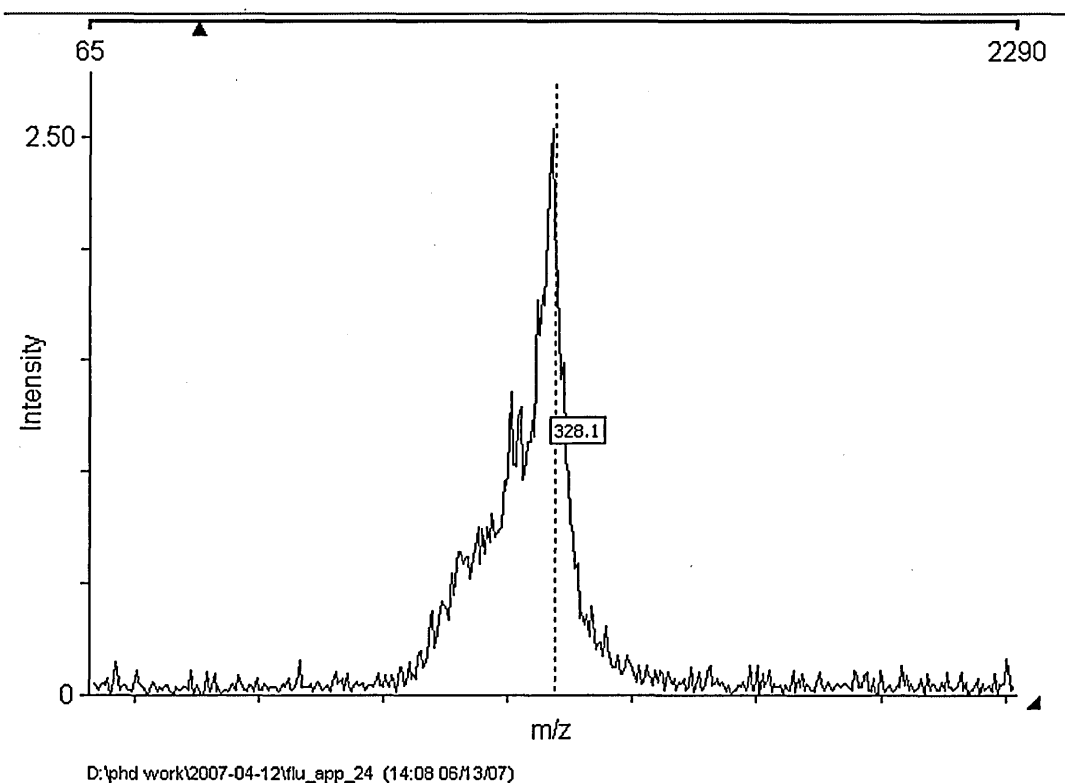


Fig. 26 Positive IR-LDI mass spectrum from fluazifop-p butyl application point indicating peak at  $m/z$  328.06 (mass region  $m/z$  0-500).

The peak at  $m/z$  328.06 for protonated fluazifop acid can be distinguished from the baseline noise. This can be more clearly seen in Fig. 27 (peak located at the dashed line).

Fig. 27 shows the positive IR-LDI mass spectrum of a fluazifop-b butyl horizontal stem section from the application point.



**Fig. 27 Positive IR-LDI mass spectrum from fluazifop horizontal stem section at application point showing peak at m/z 328.1**

The spectrum shows a clear peak at m/z 328.1, which is the protonated mass for fluazifop acid, in a section taken where fluazifop-p-butyl was applied. This indicates that fluazifop-p-butyl has absorbed and converted to fluazifop acid.

Fig. 28 shows the positive IR-LDI mass spectrum of a fluazifop-b butyl horizontal stem section from the application point, mass region  $m/z$  360-420.

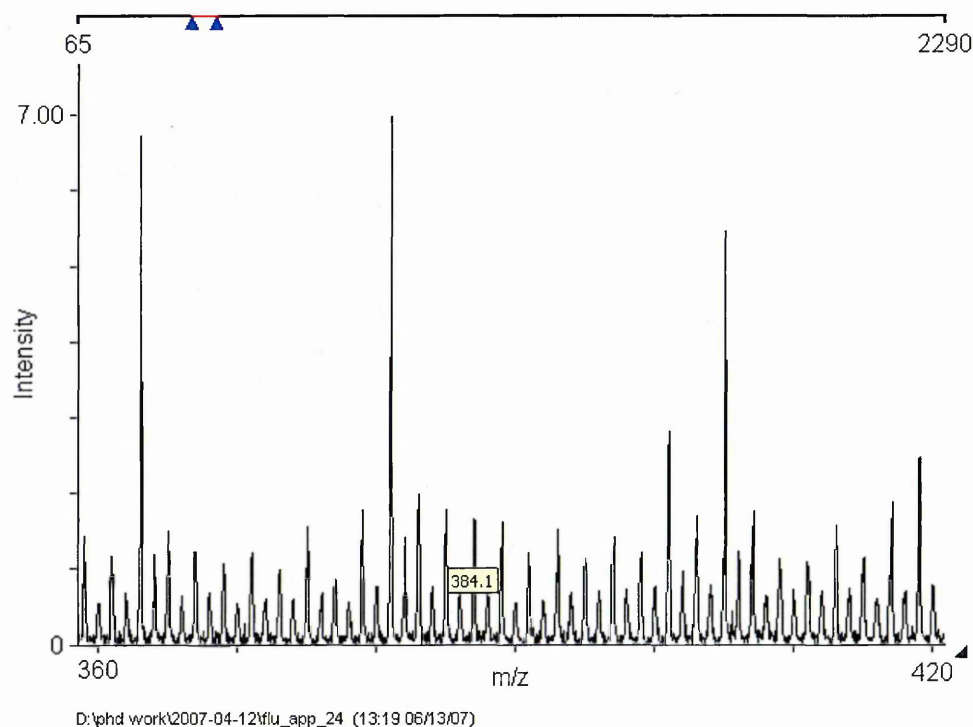


**Fig. 28 Positive IR-LDI mass spectrum from fluazifop horizontal stem section at application point showing peak at  $m/z$  384.1, (mass region  $m/z$  360 to 420).**

The spectrum shows the  $m/z$  region at 384.1 from the same sample section where fluazifop-p butyl was applied, (see Fig. 26 and 27). This shows that none of the fluazifop-p butyl has been identified in this sample. This would be expected as fluazifop-p butyl could not be identified in the control sample and following absorption fluazifop-p butyl is converted to fluazifop acid. No peak could be found for the potassium adduct of fluazifop acid at  $m/z$  366 in this spectrum.

Following the observation of a peak in the spectra shown in Fig. 26 and 27 from the sample taken at the application point, a spectrum from a horizontal sample

section taken 1 cm away from the application point was interpreted to see if fluazifop-p butyl had translocated to this region.

Fig. 29 shows the positive IR-LDI mass spectrum of a fluazifop-b butyl horizontal stem section 1cm from the application point, mass region m/z 0-500.

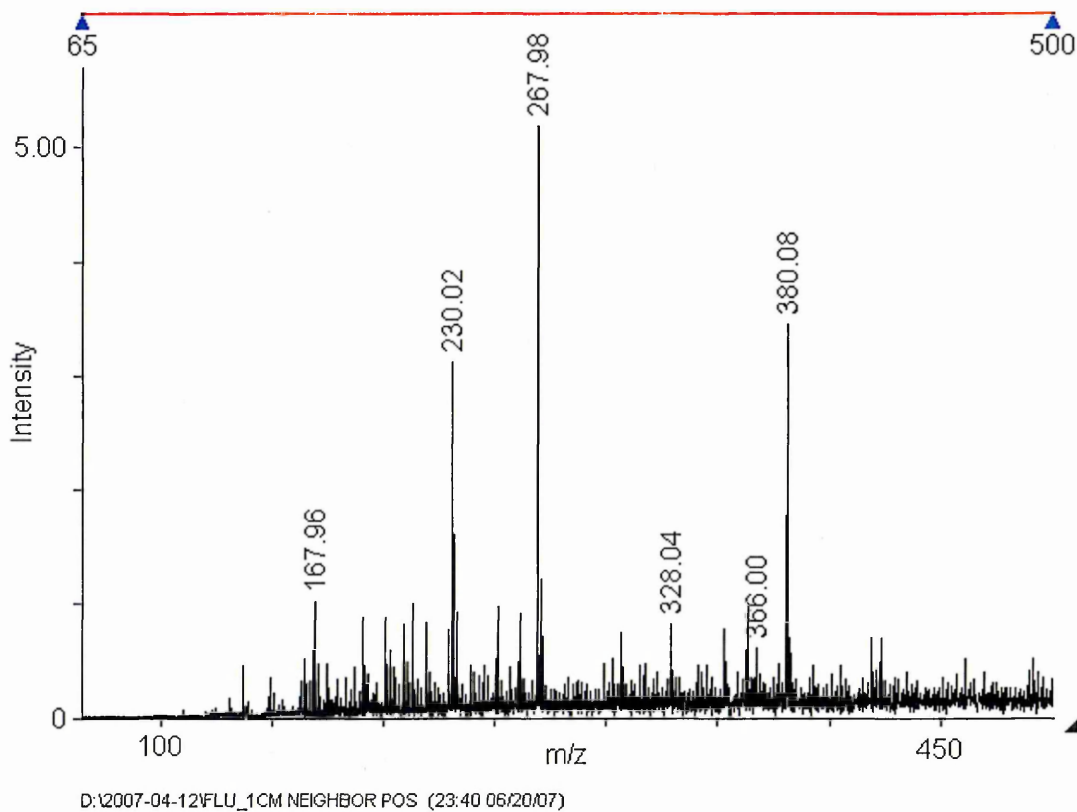


**Fig. 29 Positive IR-LDI mass spectrum from fluazifop-p butyl 1 cm from the application point indicating peaks at m/z 328.04 and 366.00 (mass region m/z 0-500).**

Two peaks relating to fluazifop-p butyl can be seen in the spectrum at m/z 328.04 (protonated fluazifop acid) and m/z 366.00 (potassium adduct of fluazifop acid).

Fig. 30 shows the positive IR-LDI mass spectrum of a fluazifop-p butyl horizontal stem section 1 cm from the application point, mass region  $m/z$  320-345.

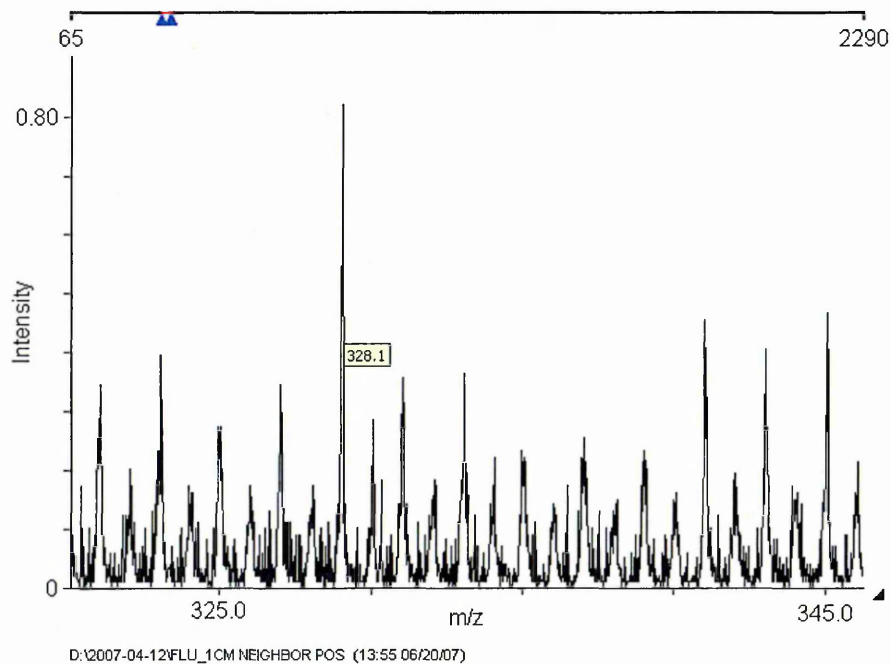


**Fig. 30 Positive IR-LDI mass spectrum of fluazifop horizontal stem section 1cm from the application point showing peak at  $m/z$  328.1, the molecular ion for fluazifop acid.**

The peak for fluazifop acid positive molecular ion ( $m/z$  328.1) is clearly visible above the background noise in this spectrum. This indicates that the fluazifop acid has been translocated to a region 1 cm away from the original application point.

Fig. 31 shows the positive IR-LDI mass spectrum of a fluazifop-b butyl horizontal stem section 1 cm from the application point, mass region  $m/z$  345-375.

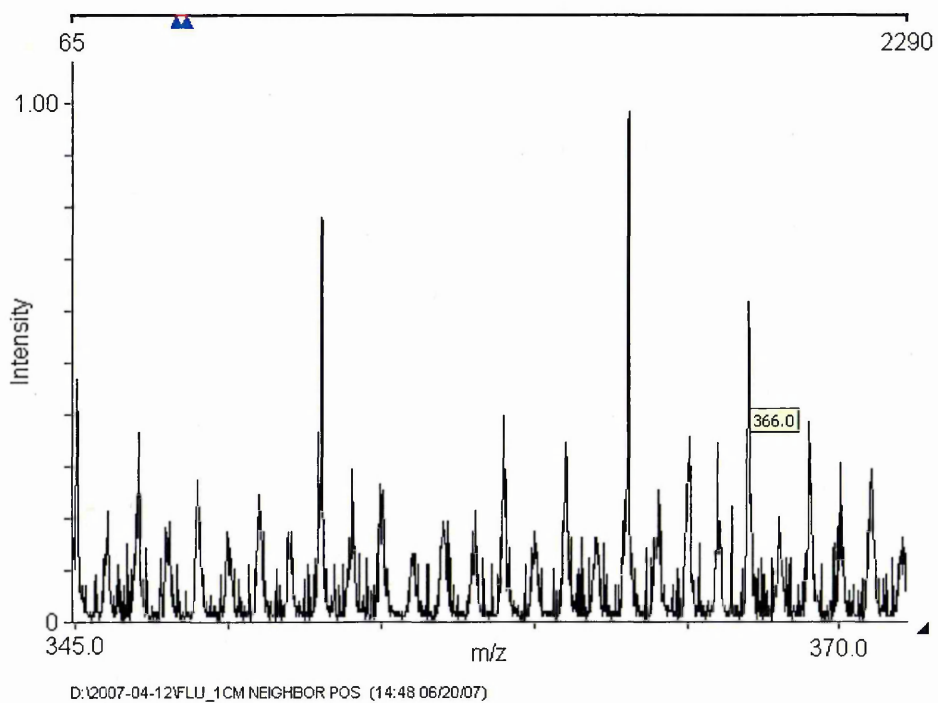


**Fig. 31 Positive IR-LDI mass spectrum of fluazifop horizontal stem section 1 cm from the application point showing peak at  $m/z$  366, potassium adduct for fluazifop acid.**

The spectrum shows the positive potassium adduct of fluazifop acid ( $m/z$  366.0), which is identifiable above the background noise.

Fig. 32 shows the positive IR-LDI mass spectrum of a fluazifop-b butyl horizontal stem section 2 cm from the application point, mass region  $m/z$  315-345.

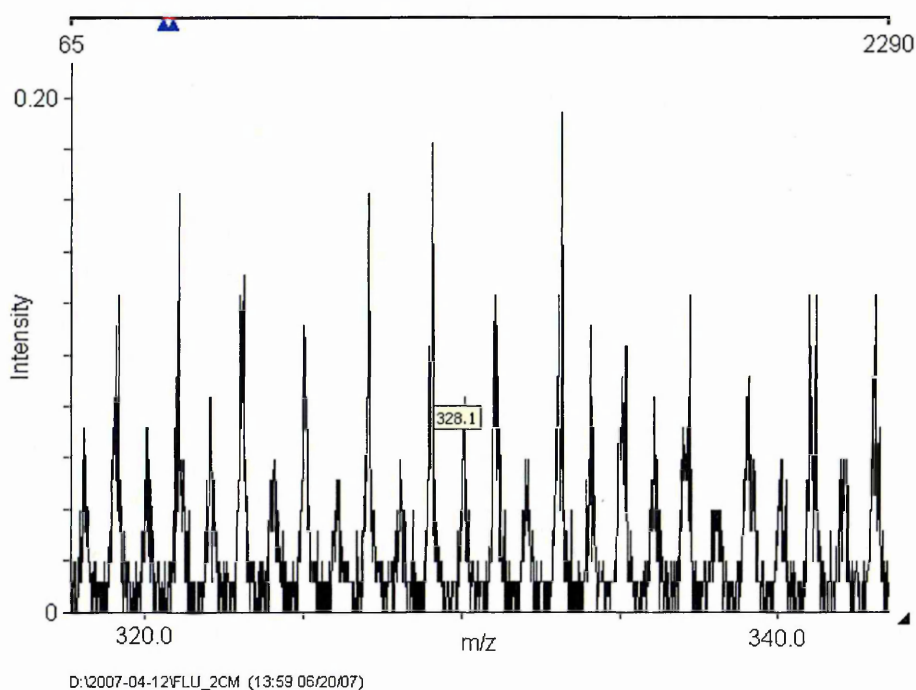


**Fig. 32 Positive IR-LDI mass spectrum of fluazifop-b butyl horizontal stem section 2cm from the application point showing peak at  $m/z$  328.1.**

The peak at  $m/z$  328.1 is present with the same intensity as the background noise and does not give sufficient evidence to say fluazifop-b butyl is present in this sample. Further analysis of this sample could reveal a significant peak at  $m/z$  328.1 and 366.0 if the right area was targeted, however due to limited time only one spectrum was obtained for this sample.

The spectrum obtained for the sample taken from the base of the rose bud also did not reveal any peaks relating to ions of fluazifop-p-butyl or fluazifop acid.

### 3.3.9 IR-MALDI analysis from nicosulfuron following uptake via the roots and foliar application

Fig. 33 shows positive IR-MALDI mass spectra from negative control samples at varying regions of the sample pith and vascular bundle (VB), with varying ion source gas pressures (1 mB or 4 mB).

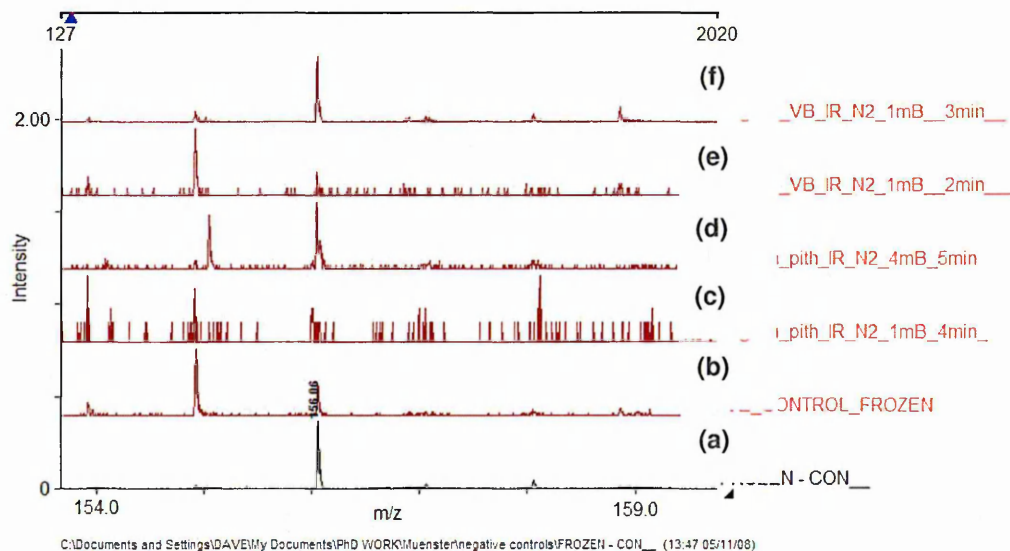


**Fig. 33 Positive IR-MALDI mass spectra showing peak at  $m/z$  156.06 on frozen and freeze dried (FD) negative control sections of a sunflower stem. Spectrum from (a) Frozen negative control. (b) Frozen negative control. (c) FD negative control from pith region. (d) FD negative control pith region. (e) FD negative control vascular bundle region. (f) FD negative control vascular bundle region.**

Two of the spectra are from the frozen sample section and 4 spectra are from the dried section; these are overlaid to show a peak present at  $m/z$  156.06. This peak corresponds to protonated histidine, which is involved in histidine biosynthesis and the methionine salvage pathway and present as an endogenous metabolite. Since histidine has the same molecular formula as nicosulfuron's fragment ion it is not possible to confirm that a peak present at this mass is due to the nicosulfuron or

the endogenous histidine unless there is a significant variation in the intensities observed.

Fig. 34 shows positive IR-MALDI mass spectra from the frozen negative control, with nicosulfuron standard spot solution with 2% TFA, frozen positive and dried positive control sections overlaid.

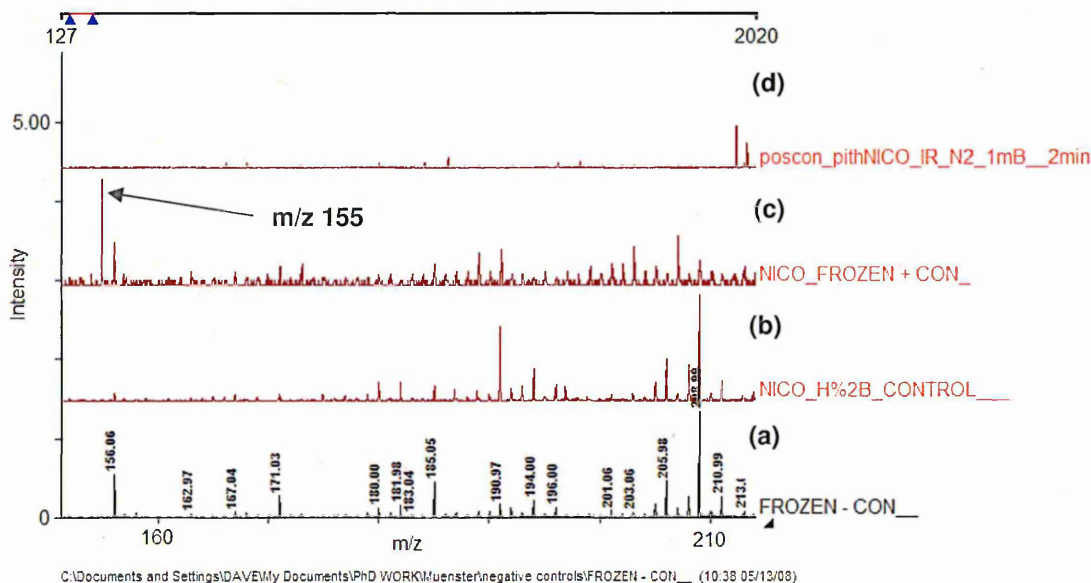


**Fig. 34 Positive IR-MALDI mass spectra showing (a) frozen negative control. (b) Nicosulfuron spot sample (2% TFA). (c) Nicosulfuron frozen positive control and (d) freeze dried nicosulfuron positive control.**

A small peak can be seen at m/z 156 in the frozen positive control (a), but not in the dried section (d) and there is no significant increase in intensity between the positive (b) and the negative (a). There is a peak present at 155 (indicated on the spectra) in the frozen positive control (c) which could be due to an unprotonated  $[M^+]$  aminopyrimidine fragment ion usually observed in its protonated form at m/z

156. But as this structure contains a primary amine we would expect this to become protonated.

Fig. 35 shows positive IR-MALDI mass spectra at m/z 156 region of the frozen negative, positive, 10 mm, 55 mm and 135 mm frozen hydroponics experiment sections in ascending order.

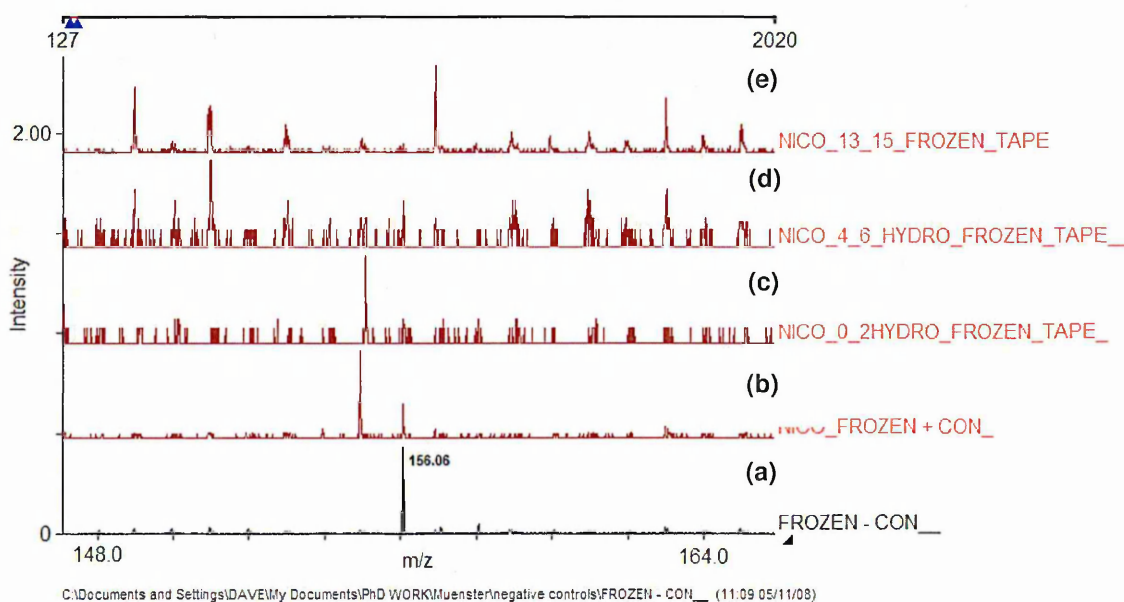


**Fig. 35 Positive IR-MALDI mass spectra showing a peak at m/z 156 on (a) frozen negative control. (b) frozen positive control. (c) Frozen section 10mm from root tip (d) Frozen section 55mm from root tip (e) Frozen section 135mm from root tip frozen. From the nicosulfuron hydroponics experiment.**

There are no visible peaks present in any of the nicosulfuron hydroponics samples at m/z values relating to nicosulfuron. This could be due to the samples dehydrating in the ion source because they are under vacuum, causing a loss in sensitivity.

Fig. 36 shows positive IR-MALDI mass spectra from the frozen positive, negative, root (5 mm), 205 mm, 405 mm and 585 mm sections in ascending order from the foliar applied experiment.

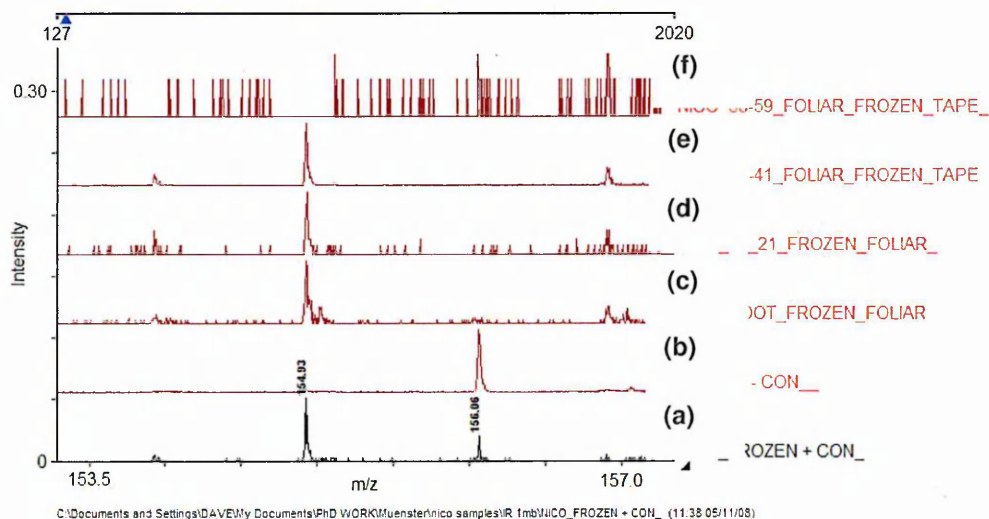


**Fig. 36 Positive IR-MALDI mass spectra showing a peak at  $m/z$  156 region on (a) frozen positive control, (b) frozen negative control (c) Root tip section. (d) Frozen section 205mm from root tip, (e) frozen section 405mm from root tip, (f) frozen section 585mm from root tip from the nicosulfuron foliar experiment in ascending order.**

There are no significant peaks present in the sample sections at  $m/z$  156. There is possible evidence in (a), (c), (d), and (e) of the unprotonated  $[M^+]$  aminopyrimidine fragment ion at  $m/z$  155 although due to the primary amine present in this structure, which we would expect to become protonated and the lack of evidence present from the hydroponics samples, this peak can be disregarded.

Fig. 37 shows positive IR-MALDI mass spectra acquired from the frozen negative control sections ascending to freeze dried samples, analyzing the pith region at 1 mB and 4 mB ion source pressure followed by analysis of the vascular bundle (VB) regions at the two ion source pressures.

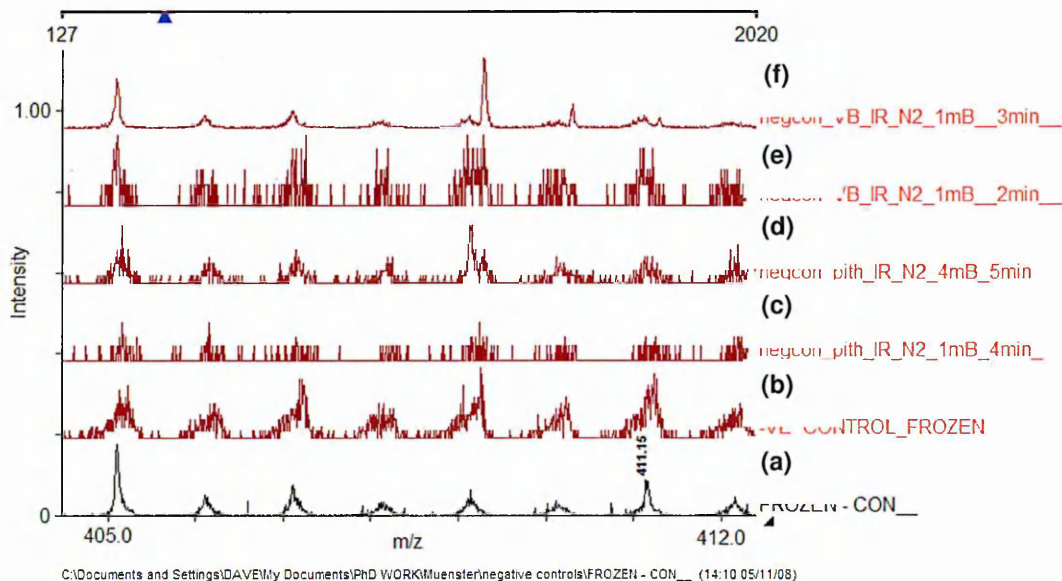


**Fig. 37 Positive IR-MALDI mass spectra showing two frozen negative control sections, mass region m/z 405-412 from a sunflower stem. Spectrum from (a) Frozen negative control. (b) Frozen negative control. (c) FD negative control from pith region. (d) FD negative control pith region. (e) FD negative control vascular bundle region. (f) FD negative control vascular bundle region.**

A small peak can be seen at m/z 411.15 in the negative control sections which is most apparent in the frozen sample sections. As the nicosulfuron protonated molecule has a m/z of 411.1081 and there is an endogenous metabolite present at m/z 411.15 it may not be possible to distinguish between the metabolite and nicosulfuron unless there is a significant difference in intensity. This endogenous peak could be due to sesamololol potassium adduct which has an exact m/z of

411.0846 and is involved in lignan biosynthesis. This peak is more apparent in the frozen than in the dried sections.

Fig. 38 shows positive IR-MALDI mass spectra from frozen sections with the negative control, nicosulfuron positive control, root section at 5 mm, section at 50 mm and section at 140 mm along the plant stem, in ascending order, from the nicosulfuron uptake via the roots method (3.2.4).

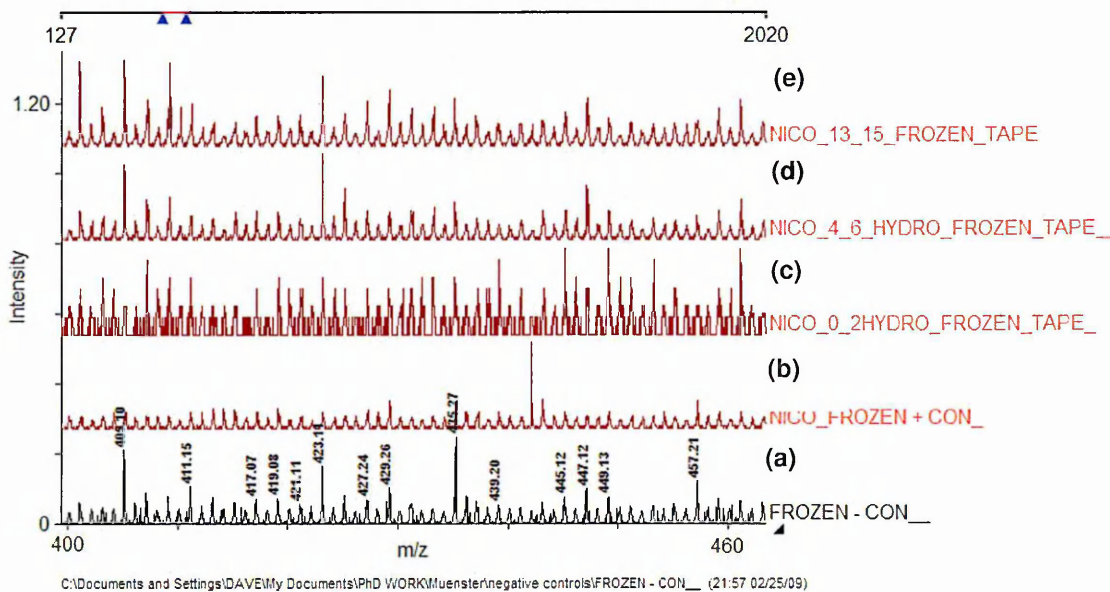
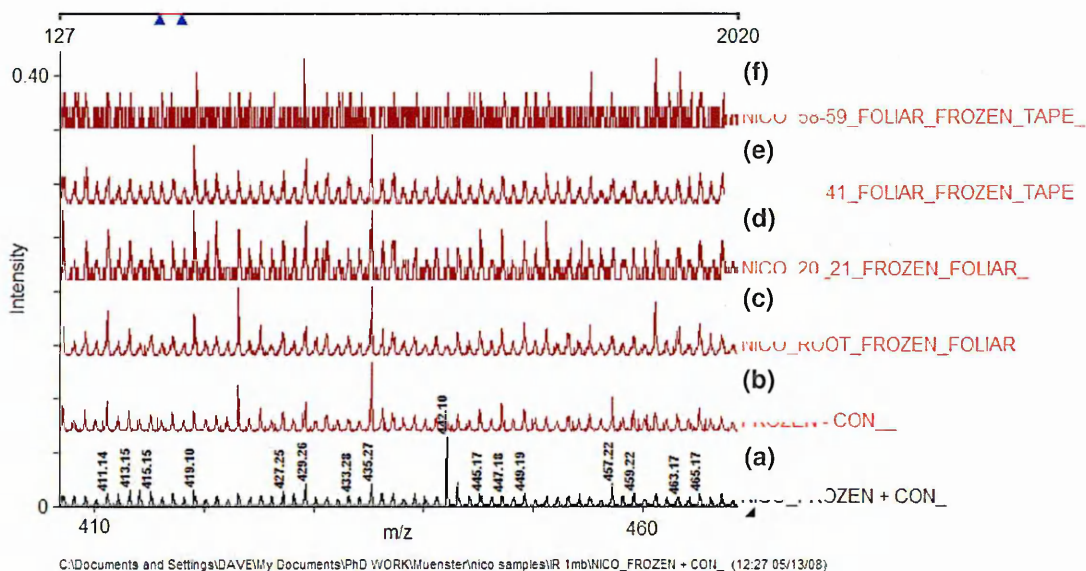


Fig. 38 Positive IR-MALDI mass spectra showing (a) frozen negative control. (b) frozen positive control. (c) Frozen section 10mm from root tip (d) Frozen section 55mm from root tip (e) Frozen section 135mm from root tip frozen. From the nicosulfuron hydroponics experiment.

There is no significant peak present at m/z 411 or 449 (mass of nicosulfuron protonated molecule, exact mass m/z 411.10 and nicosulfuron's potassium adduct, exact mass m/z 449.0646) in the nicosulfuron hydroponics sections compared to

the frozen negative control section. There is an unidentified endogenous metabolite present at  $m/z$  449.13 indicated in the frozen negative section.

Fig. 39 shows positive IR-MALDI mass spectra from frozen sections from nicosulfuron positive control, negative control, root section 5 mm, 205 mm, 405 mm and 585 mm along the plant stem, in ascending order, from the foliar applied nicosulfuron experiment (3.2.5).



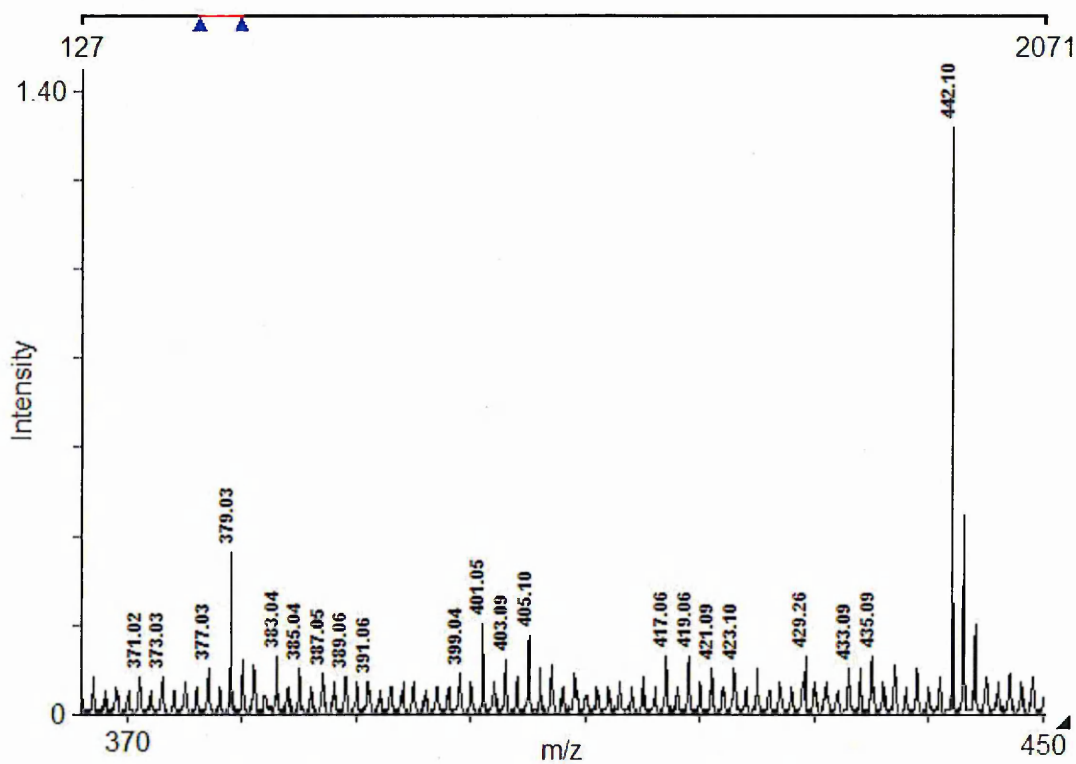
**Fig. 39** Positive IR-MALDI mass spectra showing (a) frozen positive control, (b) frozen negative control (c) Root tip section. (d) Frozen section 205mm from root tip, (e) frozen section 405mm from root tip, (f) frozen section 585mm from root tip from the nicosulfuron foliar experiment in ascending order.

Again there is no significant peaks present at  $m/z$  411 or 449 (mass of nicosulfuron protonated molecule, exact mass  $m/z$  411.10 and nicosulfuron's potassium adduct, exact mass  $m/z$  449.06) in the nicosulfuron foliar sections

compared to the frozen negative control section. There is an unidentified endogenous metabolite present at  $m/z$  449.13 indicated in the frozen negative section.

### 3.3.10 IR-MALDI analysis from azoxystrobin uptake

Fig. 40 shows the positive ion IR-MALDI mass spectrum from a spot sample of azoxystrobin dosed with potassium acetate.



C:\Documents and Settings\DAVE\My Documents\PhD WORK\Muenster\AZ\_K\_CONTROL\_ (13:11 05/13/08)

Fig. 40 Positive IR-MALDI mass spectrum showing a peak at  $m/z$  442.10 from azoxystrobin spot sample with potassium acetate.

The potassium adduct ( $m/z$  442.10) is clearly visible.

Fig. 41 shows a positive IR-MALDI mass spectrum of azoxystrobin with the addition of TFA (10  $\mu$ L of a 1% TFA to 10  $\mu$ L of 1 mg/mL solution of azoxystrobin in acetone).

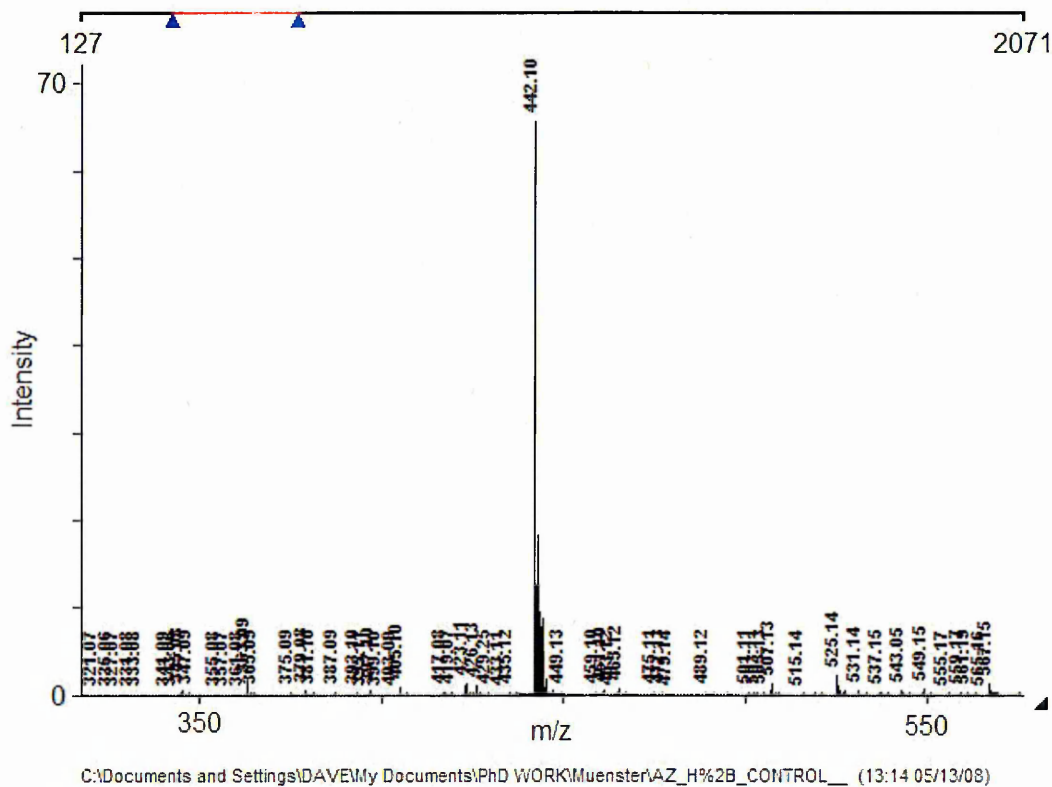
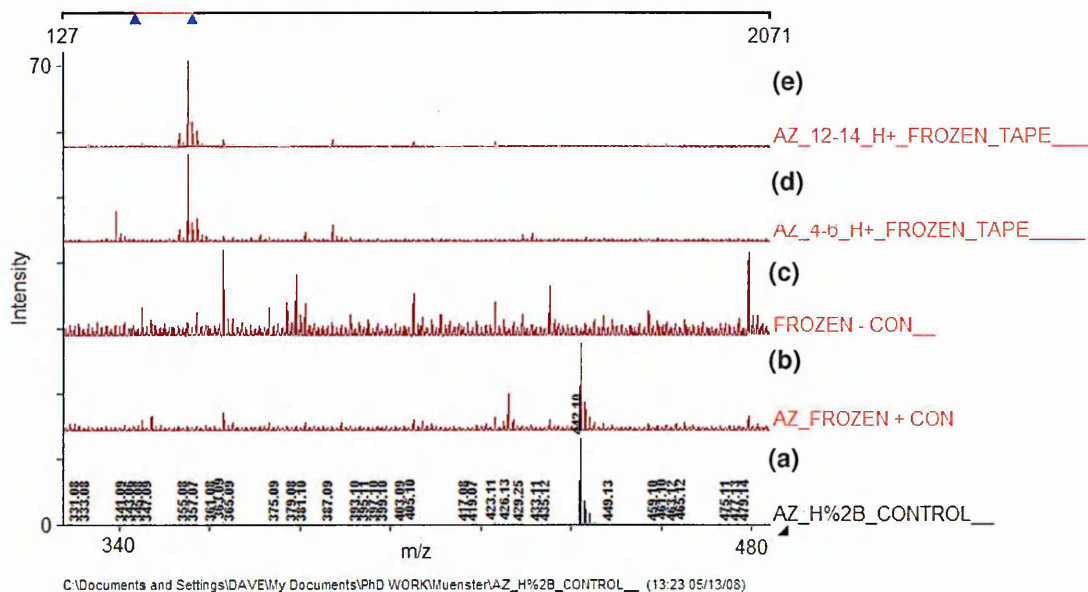


Fig. 41 Positive IR-MALDI mass spectrum showing a peak at m/z 442.10 from azoxystrobin spot sample with 0.5% TFA.

The intensity of the potassium adduct is greatly enhanced compared to the spectrum in Fig.40.

Fig. 42 shows positive IR-MALDI mass spectra from the frozen sections with the addition of 1  $\mu$ L of a 2% TFA solution from azoxystrobin acidified positive control spot sample (Fig. 41), frozen positive, negative control, sample 50 mm and sample 130 mm along the plant stem from the uptake of azoxystrobin via the root experiment (3.2.3).



**Fig. 42 Positive IR-MALDI mass spectra showing azoxystrobin (a) positive spot control, (b) azoxystrobin frozen positive control section, (c) frozen negative control section (d) frozen sections 50 mm, and (e) 130 mm, from azoxystrobin hydroponics experiment.**

The spectra above show a peak present in the control spot and the frozen azoxystrobin control section at m/z 442.10. The spectra from the sample sections did not show any peaks related to azoxystrobin. There is no endogenous peak present in the negative control at m/z 442.10. There are no peaks at m/z relating to azoxystrobin in the azoxystrobin sample sections.

### 3.4 Discussion

In this chapter MALDI-MSI has been used to assess translocation of agrochemicals in plant stem tissue. Azoxystrobin distribution has been successfully imaged in two plant species soya bean and sunflowers, in both the root and stem tissue, using a number of  $m/z$  values. Nicosulfuron translocation has been determined in sunflowers following uptake via the roots after 48 hour time periods and absorption following foliar application after 24 and 48 hour time periods. A nicosulfuron phase 1 metabolite, formed as a result of hydrolysis within the plant system, has also been identified. Translocation of azoxystrobin and nicosulfuron within the same plant system, 24 hours following application to the plant stem, was also detected. These findings indicate that determination of the translocation of agrochemicals using MALDI-MSI is compound dependant as the distribution of mesotrione and fluazifop-p butyl following foliar application was unsuccessful using the same methods. It has also been found that there is potential for alternative ionisation methods with IR-LDI-MS as ions relating to fluazifop-p butyl from sample tissue were identified. Positive controls from azoxystrobin also yielded results, although the sensitivity was not high enough to acquire results from sample tissue. Once a suitably cooled sample stage, to ensure the sample tissue remains frozen within the ion source vacuum, has been developed, the sensitivity of the method may be able to detect azoxystrobin and nicosulfuron in sample tissue.

The urea bond present in nicosulfuron fragments to form an aminopyrimidine ion species which has a very high ionisation efficiency, giving very good sensitivity from spiked tissue control sections and sample tissue. Since other herbicides in

the sulfonylurea group possess the same urea bond, this will be susceptible to hydrolysis in the same way as nicosulfuron<sup>17</sup>. We can assume therefore that they will fragment with a similar mechanism as nicosulfuron, to produce ion species with similar ionisation efficiencies as the aminopyrimidine species observed with nicosulfuron<sup>14</sup>.

### **3.5 Conclusion**

MALDI-MSI of the distribution of azoxystrobin in the root bundle tissue and stem tissue by direct analysis of sectioned tissue, following uptake via the roots, was successful. Using sunflower plants instead of soya bean allowed for sections from the whole plant stem to be obtained so data for the extent of translocation throughout the whole plant system was acquired. Applying these methods to try and observe translocation of mesotrione and fluazifop-p butyl following foliar application was unsuccessful, which was attributed to poor ionisation efficiencies of the compounds in relation to endogenous compounds present within the plant, analyte-analyte suppression. Repeating the methods with nicosulfuron, which is both phloem and xylem mobile, produced results from both uptake and translocation via the roots, translocation following foliar application and uptake of both nicosulfuron and azoxystrobin via the stem tissue. Following the results obtained with nicosulfuron the absorption following foliar application method for the 24 hours time point was repeated with a 4 other sulfonylurea herbicides.

### 3.6 References

1. Esau K. (1965) Plant anatomy. John Wiley & Sons Inc. Japan.
2. Oxalde E. (2007) Plant Physiology. Studymates LTD. UK.
3. Taiz L. Zeiger E. Plant Physiology fourth edition Sinauer Associations Inc.
4. M. Karas, D. Bachmann, U. Bahr, F. Hillenkamp. (1987) Matrix-Assisted Ultraviolet-Laser Desorption of Nonvolatile Compounds. *International Journal of Mass Spectrometry and Ion Processes*. **78**: 53-68.
5. K. Dreisewerd, S. Berkenkamp, A. Leisner, A. Rohlfing, C. Menzel. (2003) Fundamentals of matrix-assisted laser desorption/ionization mass spectrometry with pulsed infrared lasers. *International Journal of Mass Spectrometry*. **226**: 189-209.
6. Berkenkamp, S., Kirpekar F. and Hillenkamp F. (1998). Infrared MALDI Mass Spectrometry of Large Nucleic Acids. *Science*. **281**: 260-262.
7. M. W. Little, J. Laboy and K. K. Murray. ( 2007) Wavelength Dependence of Soft Infrared Laser Desorption and Ionization. *Journal of Physical Chemistry*. **111**: 1412-1416.
8. Berkenkamp S., Karas M. and Hillenkamp F. (1996) Ice as a matrix for IR-matrix-assisted laser desorption/ionisation: Mass spectra from a protein single

crystal. *Proceedings of the National Academy of Sciences of the United States of America*. **93**: 7003-7007.

9. K. Dreisewerd. (2003) The Desorption Process in MALDI. *Chemical Reviews*. **103**: 395-425.

10. Overberg A., Karas M., Bahr U., Kaufmann R. and Hillenkamp F. (2005) Matrix-assisted infrared-laser (2.94  $\mu\text{m}$ ) desorption/ionization mass spectrometry of large biomolecules. *Rapid Communications in Mass Spectrometry*. **8**: 293-296.

11. S. Berkenkamp, C. Menzel, M. Karas, F. Hillenkamp. (1997) Performance of Infrared Matrix-assisted Laser Desorption/Ionization Mass Spectrometry with Lasers Emitting in the 3  $\mu\text{m}$  Wavelength Range *Rapid Communications in Mass Spectrometry*. **11**: 13: 1399-1406.

12. Dreisewerd K., Draude F., Kruppe S., Rohlfing A., Berkenkamp S. and Pohlentz G. (2007) Molecular Analysis of Native Tissue and Whole Oils by Infrared Laser Mass Spectrometry. *Analytical Chemistry*. **79**: 4514-4520.

13. Li, Y. Shrestha, B. and Vertes A. (2008) Atmospheric pressure infrared MALDI imaging mass spectrometry for plant metabolomics. *Analytical Chemistry*. **80**: 407-420.

14. Sabadie, J. (2002) Nicosulfuron: Alcoholysis, Chemical Hydrolysis, and Degradation on Various Minerals. *Journal of Agricultural and Food Chemistry*. **50**: 526-531.

15. Li L. Y. T., Campbell D. A., Bennett P. K. and Henion J. (1996) Acceptance criteria for ultratrace HPLC-tandem mass spectrometry: Quantitative and qualitative determination of sulfonylurea herbicides in soil. *Analytical Chemistry*. **68**: 19: 3397-3404.

16. Aerni H-R., Cornett D. S., Caprioli R. M. (2006) Automated Acoustic Matrix Deposition for MALDI Sample Preparation. *Analytical Chemistry*. (2006) **78**: 827-834.

17. Sarmah A. and Sabadie J. (2002) Hydrolysis of Sulfonylurea Herbicides in Soils and Aqueous Solutions: a Review. *Journal of Agricultural and Food Chemistry*. **50**: 6253-6265.

## **Chapter Four: Detection of Sulfonylurea Herbicide**

### **Translocation**

## 4.1 Introduction

For the final chapter, herbicides from the sulfonylurea group will be evaluated and limits of detection will be determined from spot sample analysis and from spiked tissue controls to decide if a quick preliminary method can be applied to determine whether MALDI-MSI can be used to assess translocation. The distribution of the herbicides following foliar absorption and translocation will be assessed 24 hours after application to sunflower species.

Sulfonylurea herbicides are a unique group of herbicides. Due to their low toxicity in mammals and unprecedented herbicidal activity, they have become very popular worldwide. They can be used to control a range of weeds and some grasses in a variety of crops and vegetables i.e. barley, wheat, oats, rice, soya beans, potatoes and more. Sulfonylurea herbicides are potent inhibitors of the enzyme acetolactate synthase (ALS) which is involved in branched chain amino acid biosynthesis in plants. ALS is a thiamine pyrophosphate (TPP)-dependent enzyme which catalyses in the condensation of pyruvate,  $\alpha$ -aceto-  $\alpha$ -hydroxybutyrate and carbon dioxide in isoleucine biosynthesis or the condensation of pyruvate molecules to form acetolactate and carbon dioxide in leucine and valine biosynthesis <sup>1</sup>. ALS inhibitors are regarded as the most active group of herbicidal compounds found to date and display very high herbicidal activity in soil and following foliar application <sup>2</sup>.

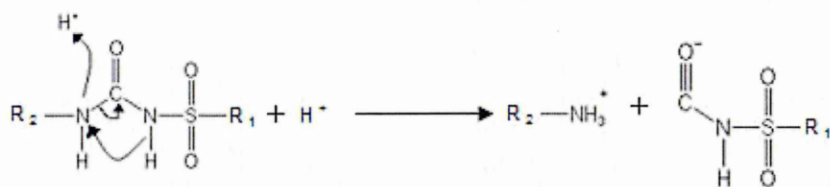


Fig. 1 Mechanism of sulfonamide fragmentation observed with MALDI-MS.

Fig. 1 shows the proton transfer which occurs at the urea bond of sulfonamide herbicides during ionisation. Sulfonamide herbicides have a general structure based on the  $R_1$  moiety being either an aliphatic, aromatic or heterocyclic group connected by the sulfonamide bridge to the  $R_2$  moiety, which can either be a substituted triazine or pyrimidine system<sup>2</sup>. As we have observed with nicosulfuron, the sulfonamide bridge fragments to leave the  $R_2$  moiety with a positive charge, which can be detected with good sensitivity from tissue sections, allowing the distribution of the sulfonamide herbicide to be imaged.

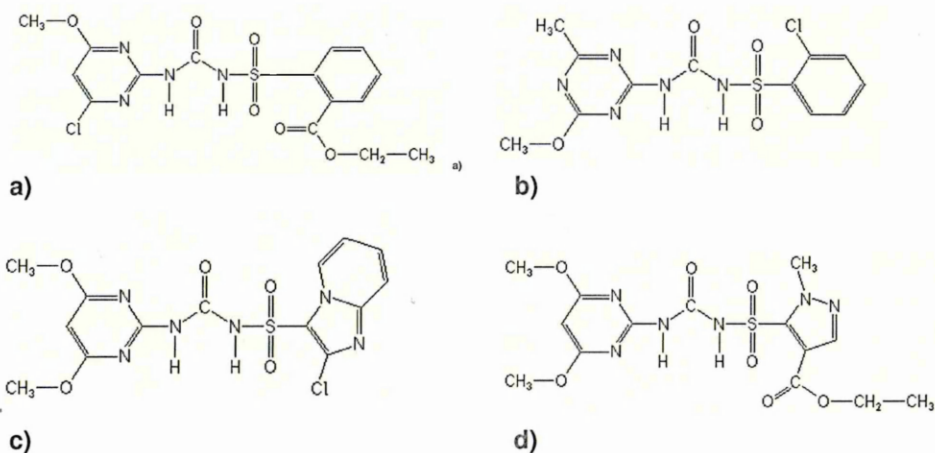


Fig. 2 Structures of sulfonamide herbicides. a) chlorimuron-ethyl, b) chlorsulfuron, c) imazosulfuron and d) pyrazosulfuron-ethyl.

Fig. 2 shows the structures of the sulfonylurea herbicides examined in this chapter. Fig. 2a) shows the structure of chlorimuron-ethyl, Fig. 2b) shows the structure of chlorsulfuron, Fig. 2c) shows the structure of pyrazosulfuron and Fig. 2d) shows the structure of imazosulfuron. The R<sub>2</sub> moiety resulting from fragmentation can be seen on the left side of the urea bond.

The aims of this chapter are to apply the methods developed from the analysis of azoxystrobin, mesotrione and nicosulfuron to a range of sulfonylurea herbicides and determine the extent of the translocation 24 hours following foliar application to sunflower plants. Also, to design a method to determine if MALDI-MSI can be applied to assess agrochemical translocation through a preliminary method such as limit of detection from conventional MALDI analysis and relate this to spiked control tissue sections.

## 4.2 Methods

### 4.2.1 Sulfonylurea herbicides analysis by conventional MALDI analysis

Conventional MALDI analysis was performed on solutions prepared from four sulfonylurea herbicides, (chlorimuron-ethyl, chlorsulfuron, imazosulfuron and pyrazosulfuron-ethyl) using standard stock solutions of 1.0 mg/mL in acetonitrile.

1 µL of each of the above solutions were combined with 1 µL of α-CHCA (Sigma Aldrich, Dorset, UK) (10 mg/mL 1% TFA). Solutions were mixed and 1 µL was pipetted onto a well of a conventional stainless steel MALDI target. Positive MALDI-MS spectra were acquired at a laser power of 25 µJ.

#### **4.2.2 Limit of detection for sulfonylurea herbicides by conventional MALDI analysis**

A range of solutions of each of the sulfonylurea herbicides was prepared from a stock solution of 1.0 mg/mL in acetonitrile. The concentration range was 0.001, 0.01, 0.025, 0.05 and 0.1 mg/mL. 10  $\mu$ L of these solutions were combined with 10  $\mu$ L of the matrix solution  $\alpha$ -CHCA (Sigma Aldrich, Dorset, UK) (10 mg/mL 1.0% TFA). 1  $\mu$ L of these analyte:matrix solutions were pipetted on to the spot target plate in triplicate. Spectra were then acquired using oMALDI server 5.1 automatic acquisition method with a random solid pattern of laser movement across the spot (fast pattern speed, dwell time 0.2 second, period duration time 0.333 minutes and accumulation time of 5.0 seconds). Positive MALDI-MS spectra were acquired in triplicate at a laser power of 25  $\mu$ J. The intensities of the substituted triazine or pyrimidine fragment ions and  $\alpha$ -CHCA fragment ion at  $m/z$  172.04 generated were used to calculate analyte to matrix ratios, which were averaged. The ratios were plotted against concentration with +/- error bars using Excel.

#### **4.2.2 Limit of detection of sulfonylurea herbicides on control plant stem tissue sections**

Five 30 micron control sections were taken from an undosed plant stem and attached to double sided carbon tape using the method described previously in chapter 3 (section 3.2.2.). The sections were then spiked with 2  $\mu$ L of 0.625, 1.25, 2.5 and 5.0 mg/mL solutions of the desired sulfonylurea herbicide, leaving the fifth section to act as a negative control. Samples were arranged on a target plate and the matrix (10 mg/mL  $\alpha$ -CHCA (Sigma Aldrich, Dorset, UK) 0.1% TFA) was

applied using an Iwata gravity-fed pneumatic air spray gun (Iwata Media Inc., Portland, OR, USA) by passing the compressed air gun over the sample 15 times, ensuring the sample tissue did not get saturated and even coverage had been achieved. The appropriate areas were then imaged using an Applied Biosystems/MDS Sciex Q-star pulsar I mass spectrometer (Concord, Ontario, Canada) fitted with an orthogonal MALDI source and a nitrogen laser, at a laser power of 25  $\mu$ J for chlorsulfuron and chlorimuron-ethyl and 35  $\mu$ J for imazosulfuron and pyrazosulfuron-ethyl with a laser repetition rate of 20 Hz. Images were obtained with a spatial resolution of 500  $\mu$ m x 500  $\mu$ m.

#### **4.2.3 Absorption of sulfonylurea herbicides via foliar application**

Sunflower plants were germinated and grown in potting compost (B&Q, Sheffield, UK). 50x1  $\mu$ L of a 1.0 mg/mL solution of the desired sulfonylurea herbicide in 50:50 acetonitrile: 0.1% Tween® (Sigma Aldrich, Dorset, UK) was applied to the tissue either side of the midrib vein of a leaf. The plants were then left for 24 hours at 21 °C with a relative humidity of 55% (Sanyo, Versatile environmental test chamber, Hertfordshire, UK) before being removed and prepared for cryostat (Leica, Milton Keynes, UK) sectioning along the horizontal axes at varying distances from the root bundle region. Control sections were taken from an undosed plant to be used as positive and negative controls. Positive controls were spiked with 2  $\mu$ L of a 1.0 mg/mL solution for chlorsulfuron and chlorimuron-ethyl and 2  $\mu$ L of a 5.0 mg/mL solution for imazosulfuron and pyrazosulfuron-ethyl. Sections were coated in  $\alpha$ -CHCA (Sigma Aldrich, Dorset, UK) (10 mg/mL 1.0% TFA) by passing the compressed air gun over the sample for 15 times, ensuring the sample tissue did not get saturated and even coverage had been achieved.

Sectioned samples were then mounted onto a MALDI target using conductive tape. The appropriate areas were then imaged using an Applied Biosystems/MDS Sciex Q-star pulsar / mass spectrometer (Concord, Ontario, Canada) fitted with an orthogonal MALDI source and a nitrogen laser, at a laser power of 25  $\mu\text{J}$  for chlorsulfuron and chlorimuron-ethyl and 35  $\mu\text{J}$  for imazosulfuron and pyrazosulfuron-ethyl, with a laser repetition rate of 20 Hz. Images were obtained with a spatial resolution of 500  $\mu\text{m}$  x 500  $\mu\text{m}$ .

## 4.3 Results

### 4.3.1 Positive ion MALDI-MS spectra and limit of detection of sulfonylurea herbicides

#### 4.3.1.1 Chlorsulfuron positive MALDI-MS

Fig. 3 shows the positive ion MALDI mass spectrum of chlorsulfuron.

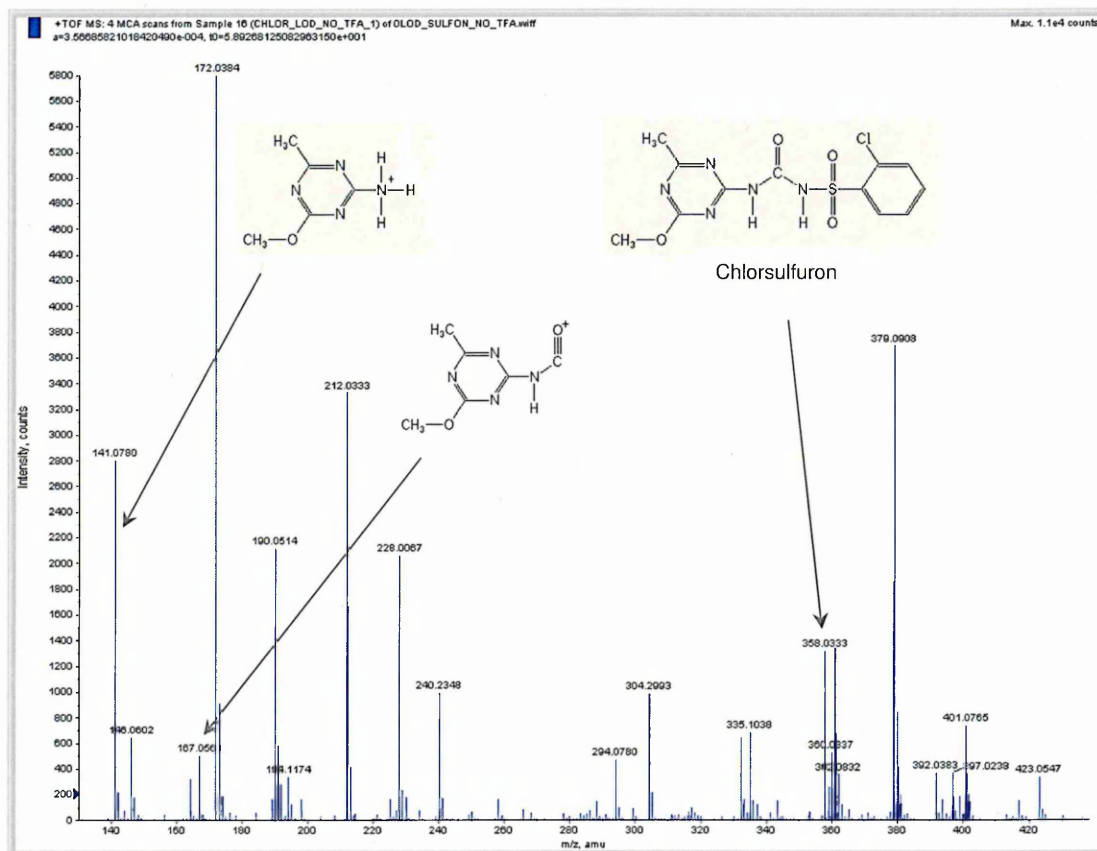
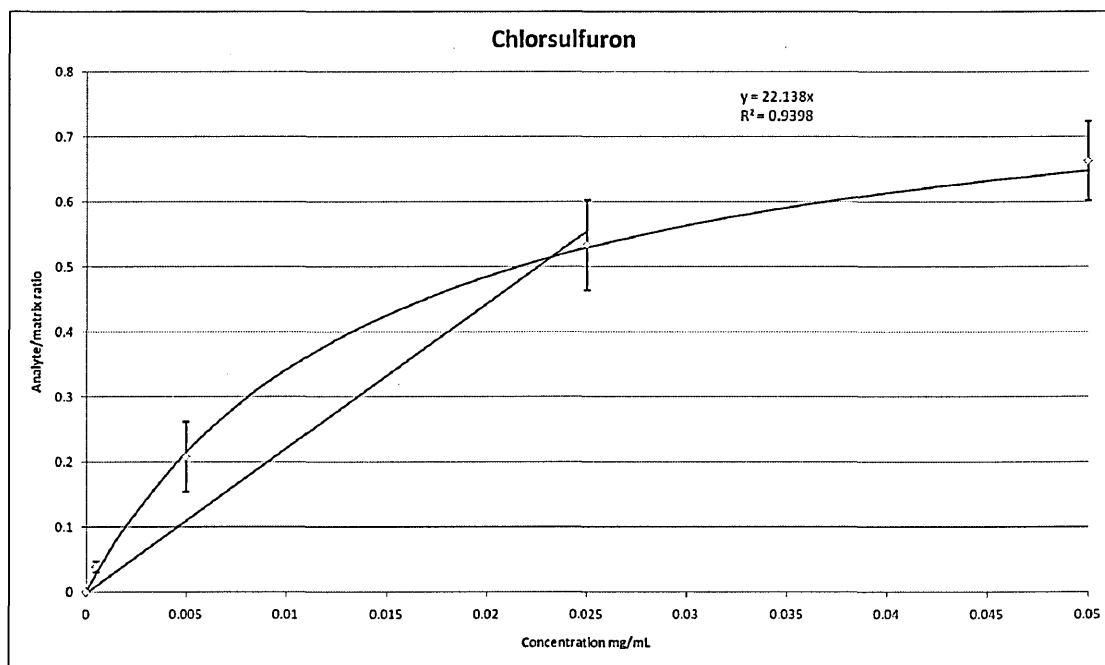


Fig. 3 Positive ion MALDI mass spectrum of chlorsulfuron (1.0mg/mL) with  $\alpha$ -CHCA (10mg/mL 1% TFA in acetone) 50:50. Showing the  $[M+H]^+$  ion at m/z 358.03 and aminotriazine fragment ions at m/z 167.06 and m/z 141.08.

The spectrum exhibits a number of ions which can potentially be used to generate images *i.e.* the  $[M+H]^+$  ion at m/z 358.03 and aminotriazine fragment ions at m/z 167.06 and m/z 141.08. The fragment ion at m/z 141.08 is clearly observed in spot

samples and is present as the most abundant ion relating to imazosulfuron. For this reason this ion's intensity will be used for the limit of detection experiment.



**Fig. 4 Calibration curve for analyte to matrix ratio against chlorosulfuron concentration for the chlorsulfuron fragment ion (m/z 141.08). Matrix ion (m/z 172.04).**

Fig. 4 shows the calibration graph from the chlorsulfuron fragment ion (m/z 141.08) against the  $\alpha$ -CHCA matrix ion (m/z 172.04). The limit of detection calculated from this graph was 10.34  $\mu\text{g/mL}$  using linear regression through the first three data points<sup>3</sup>. Previously reported data for the limit of detection of chlorsulfuron using solid phase extraction followed by high performance liquid chromatography electrospray ionisation mass spectrometry is 1.5  $\mu\text{g/mL}$ <sup>4</sup>.

### 4.3.1.2 Chlorimuron-ethyl positive MALDI-MS

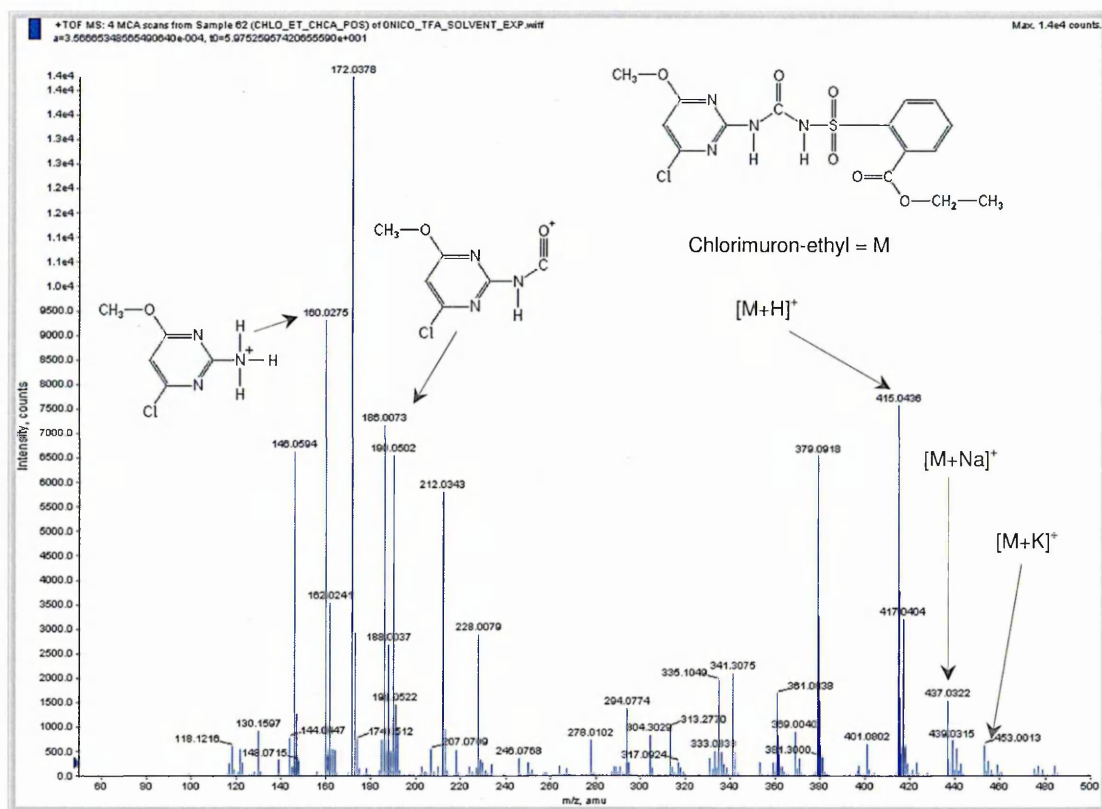
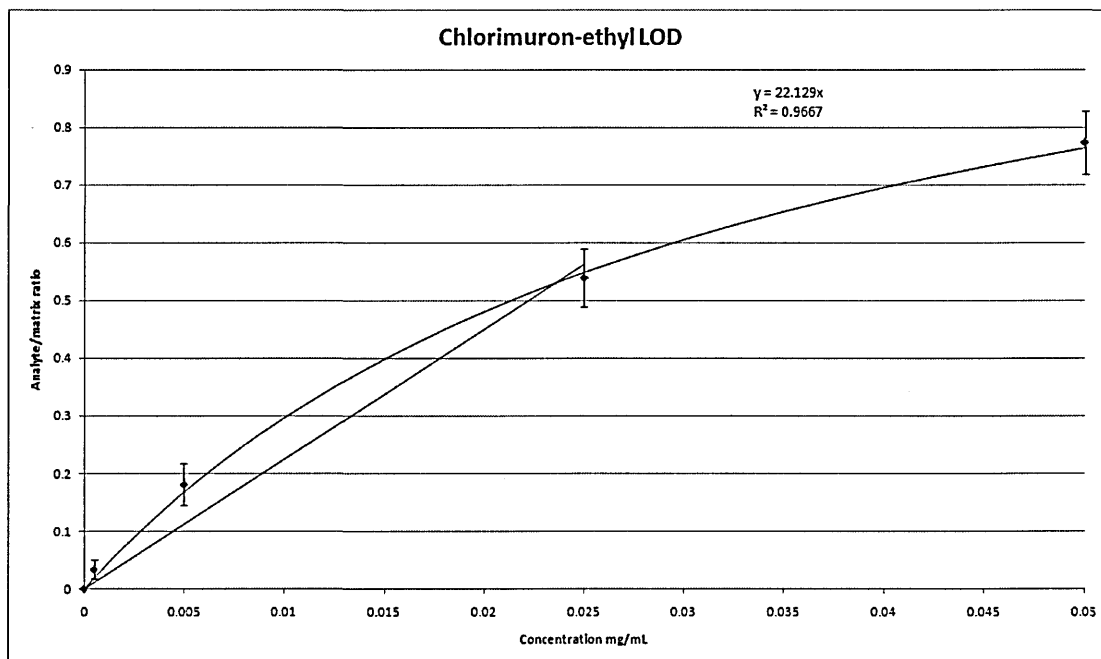


Fig. 5 Positive ion MALDI mass spectrum of chlorimuron-ethyl (1.0mg/mL) with  $\alpha$ -CHCA (10mg/mL 1% TFA in acetone) 50:50. Showing the  $[M+H]^+$  ion at m/z 415.04,  $Na^+$  adduct at m/z 437.03, the  $K^+$  adduct at m/z 453.00 and fragment ions at m/z 186.01 and m/z 160.03.

Fig. 5 shows the positive ion MALDI mass spectrum of chlorimuron-ethyl. The spectrum exhibits a number of ions which can potentially be used to generate images *i.e.* the  $[M+H]^+$  ion at m/z 415.04,  $Na^+$  adduct at m/z 437.03 the  $K^+$  adduct at m/z 453.00 and fragment ions at m/z 186.01 and m/z 160.03. The fragment ion at m/z 160.03 is clearly observed in spot samples and is present as the most abundant ion relating to chlorimuron-ethyl. For this reason, this ion's intensity will be used for the limit of detection experiment.



**Fig. 6 Calibration curve for analyte to matrix ratio against chlorimuron- ethyl concentration for the chlorimuron- ethyl fragment ion (m/z 160.03). Matrix ion (m/z 172.04).**

Fig. 6 shows the calibration graph for the chlorimuron- ethyl fragment ion (m/z 160.03) against the  $\alpha$ -CHCA matrix ion (m/z 172.04). The limit of detection calculated from this graph was 0.52  $\mu\text{g/mL}$  using linear regression through the first three data points <sup>3</sup>. Previously reported data for the limit of detection of chlorimuron-ethyl using solid phase extraction followed by high performance liquid chromatography electrospray ionisation mass spectrometry is 2.5  $\mu\text{g/mL}$  <sup>4</sup>.

### 4.3.1.3 Imazosulfuron positive MALDI-MS

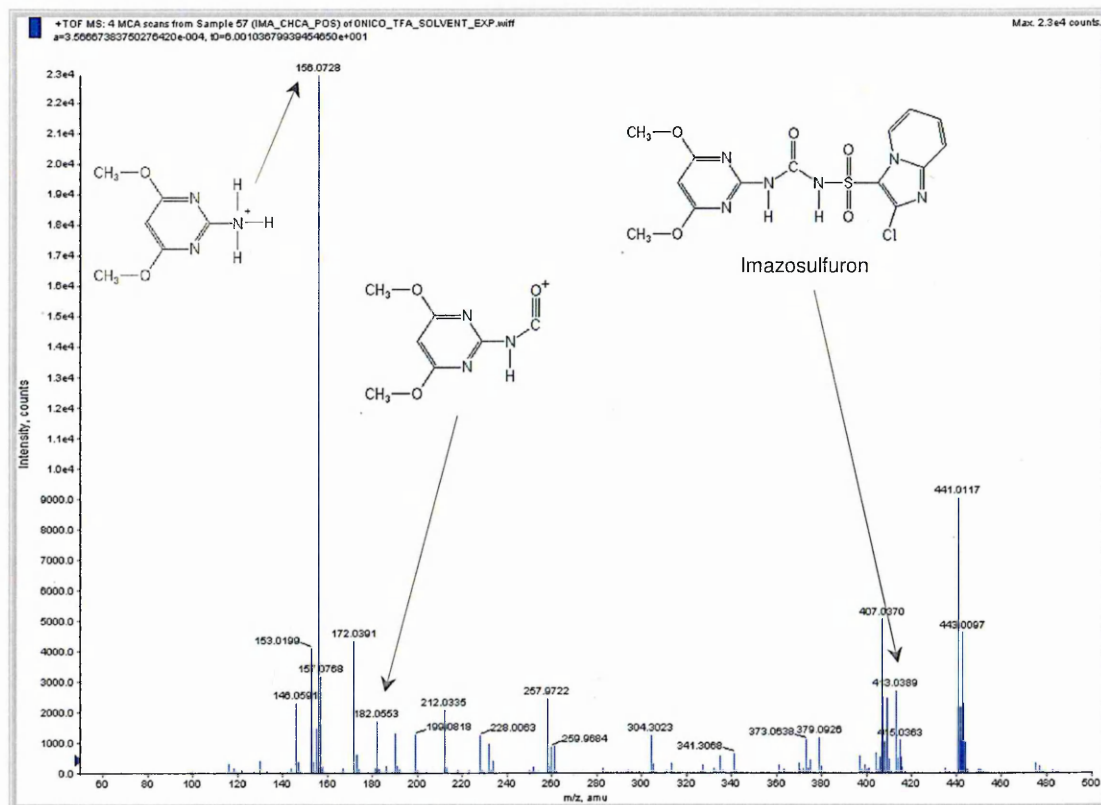
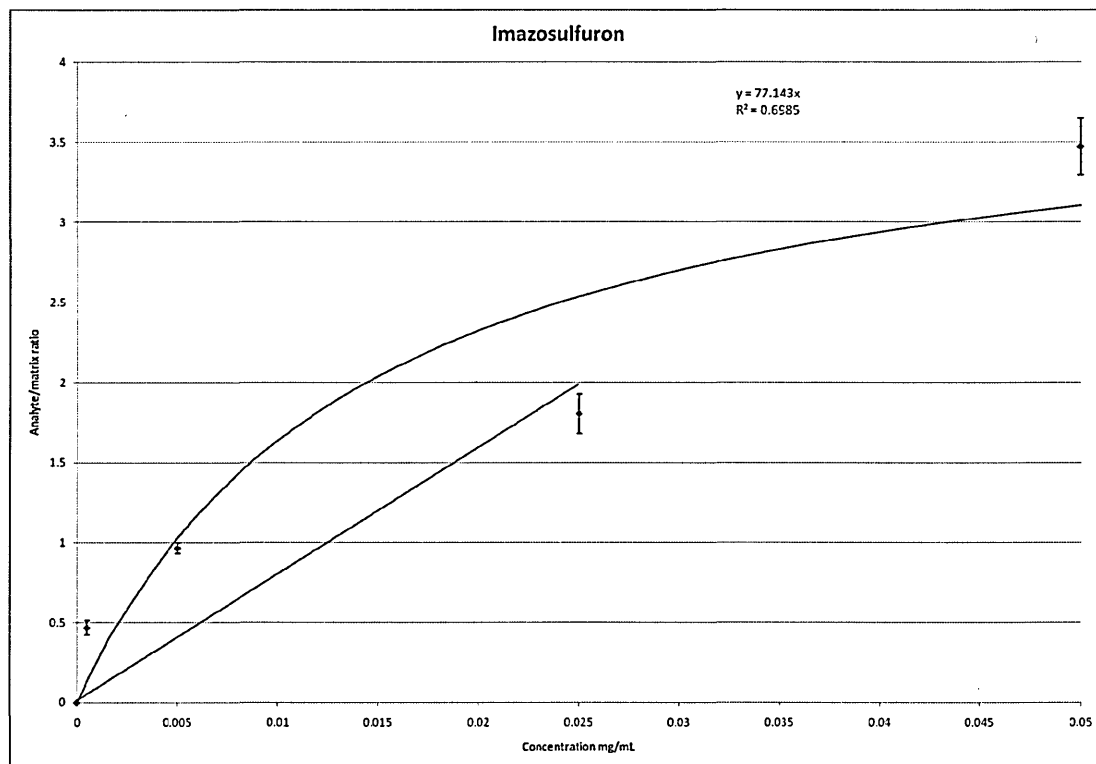


Fig. 7 Positive ion MALDI mass spectrum of imazosulfuron (1.0mg/mL) with  $\alpha$ -CHCA (10mg/mL 1% TFA in acetone) 50:50. Showing the  $[M+H]^+$  ion at m/z 413.04 and fragment ions at m/z 182.06 and m/z 156.07.

Fig. 7 shows the positive ion MALDI mass spectrum of imazosulfuron. It exhibits a number of ions which can potentially be used to generate images *i.e.* the  $[M+H]^+$  ion at m/z 413.04 and fragment ions at m/z 182.04 and m/z 156.07. The fragment ion at m/z 156.07 is clearly observed in spot samples and is present as the most abundant ion relating to imazosulfuron. For this reason, this ion's intensity will be used for the limit of detection experiment.



**Fig. 8 Calibration curve for analyte to matrix ratio against imazosulfuron concentration for the imazosulfuron fragment ion (m/z 156.08). Matrix ion (m/z 172.04).**

Fig. 8 shows the calibration graph from the imazosulfuron fragment ion (m/z 156.08) against the  $\alpha$ -CHCA matrix ion (m/z 172.04). The limit of detection calculated from this graph was 14.35  $\mu\text{g/mL}$  using linear regression through the first three data points<sup>3</sup>. No previously reported data for a limit of detection could be found for imazosulfuron.

### 4.3.1.4 Pyrazosulfuron-ethyl positive MALDI-MS

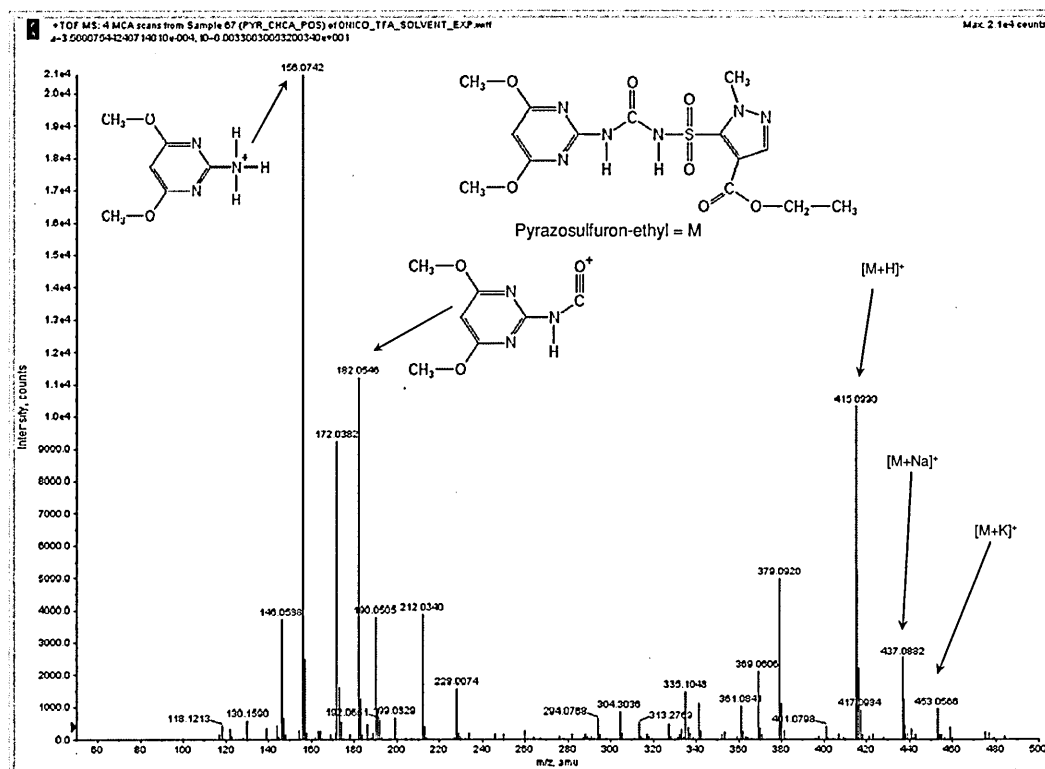
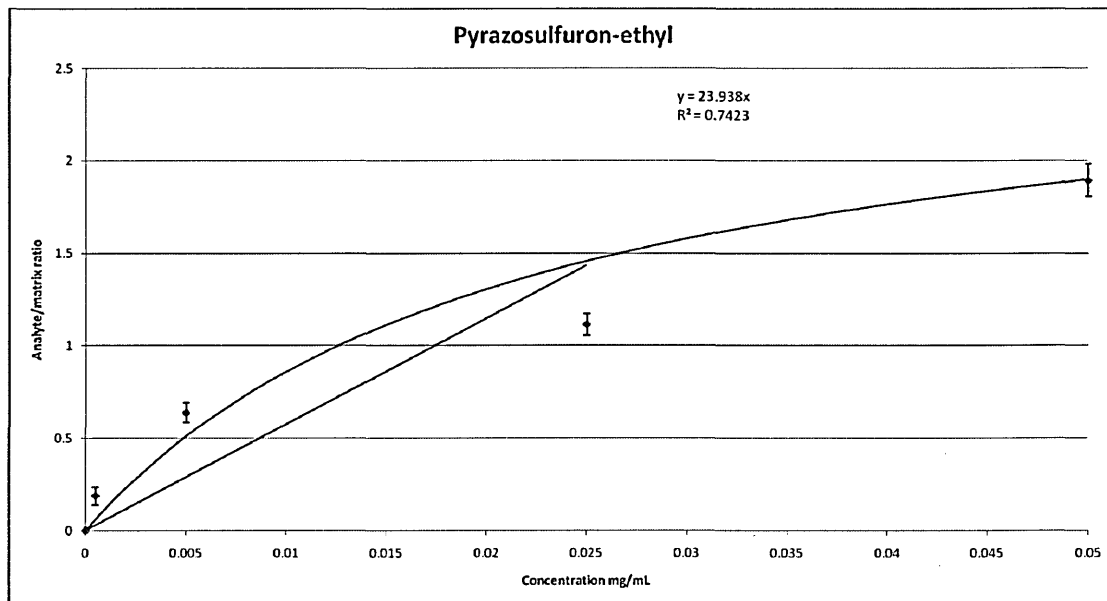


Fig. 9 Positive ion MALDI mass spectrum of pyrazosulfuron-ethyl (1.0mg/mL) with  $\alpha$ -CHCA (10mg/mL 1% TFA in acetone) 50:50. Showing the  $[M+H]^+$  ion at m/z 415.10, the  $Na^+$  adduct at m/z 437.09, the  $K^+$  adduct at m/z 453.06 and fragment ions at m/z 182.06 and m/z 156.07.

Fig. 9 shows the positive ion MALDI mass spectrum of pyrazosulfuron-ethyl. The spectrum exhibits a number of ions which can potentially be used to generate images *i.e.* the  $[M+H]^+$  ion at m/z 415.10, the  $Na^+$  adduct at m/z 437.09, the  $K^+$  adduct at m/z 453.06 and fragment ions at m/z 182.06 and m/z 156.07. The fragment ion at m/z 156.07 is clearly observed in spot samples and is present as the most abundant ion relating to pyrazosulfuron-ethyl. For this reason, this ion's intensity will be used in the limit of detection experiment.



**Fig. 10 Calibration curve for analyte to matrix ratio against pyrazosulfuron-ethyl concentration for the pyrazosulfuron-ethyl fragment ion (m/z 156.08). Matrix ion (m/z 172.04).**

Fig. 10 shows the calibration graph from pyrazosulfuron-ethyl fragment ion (m/z 156.08) against the  $\alpha$ -CHCA matrix ion (m/z 172.04). The limit of detection calculated from this graph was 18.18  $\mu\text{g/mL}$  using linear regression through the first three data points<sup>3</sup>. Previously reported data for the limit of detection of pyrazosulfuron-ethyl using solid phase extraction followed by high performance liquid chromatography electrospray ionisation mass spectrometry is 3.0  $\mu\text{g/mL}$ <sup>4</sup>.

## 4.3.2 MALDI-MSI of spiked control sections

### 4.3.2.1 MALDI-MSI of chlorimuron-ethyl spiked sections

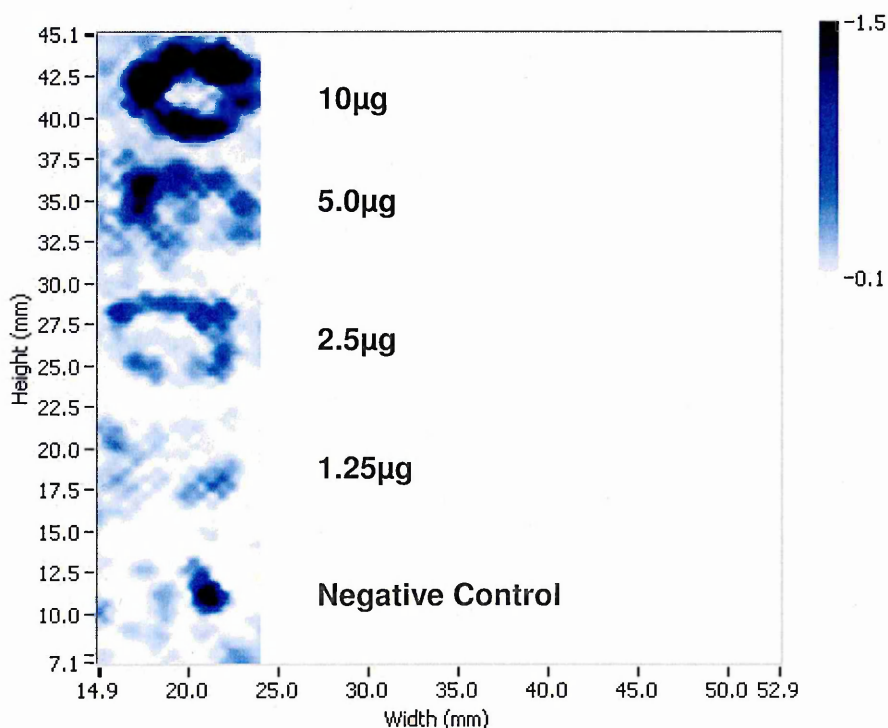


**Fig. 11 MALDI-MS image of control cross section and spiked control sections. Image of chlorimuron-ethyl fragment ion at  $m/z$  160.03 (image range  $m/z$  160.004-160.051 and normalised against  $\alpha$ -CHCA  $m/z$  172.04 peak). Values are equivalent  $\mu\text{g}$  spiked onto tissue.**

Fig. 11 shows the distribution of the chlorimuron-ethyl fragment ion at  $m/z$  160.03 in spiked control stem sections. The image shows the compound is clearly present on the 10  $\mu\text{g}$  spiked section, around the outside edge of the tissue. Signal is present on the tissue sections spiked with 5.0 and 2.5  $\mu\text{g}$ , around the outside edge of the section where the solution has soaked into the tissue. No signal has been observed in the sections spiked with 1.25  $\mu\text{g}$  and a small area of contamination can be seen in the negative control.

### 4.3.2.2 MALDI-MSI of chlorsulfuron spiked sections

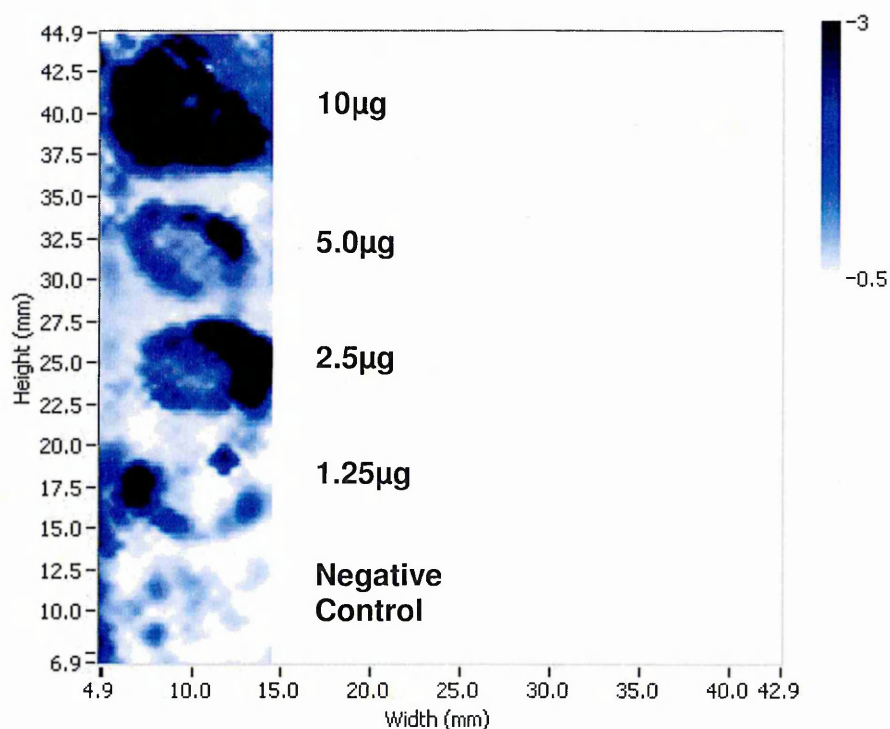


Fig. 12 MALDI-MS image of control cross section and spiked control sections. Image of chlorsulfuron fragment ion at m/z 141.08 (image range m/z 141.060-141.081 and normalised against  $\alpha$ -CHCA m/z 172.04 peak). Values are equivalent  $\mu\text{g}$  spiked onto tissue.

Fig. 12 shows the distribution of the chlorsulfuron fragment ion at m/z 141.08 in spiked control stem sections. The image shows that the compound is clearly present on the 10  $\mu\text{g}$  spiked section, across all of the tissue. Signal is present in the tissue sections spiked with 5.0, 2.5 and 1.25  $\mu\text{g}$  around the outside edges of the sections where the solution has soaked into the tissue.

No satisfactory results were obtained for imazosulfuron or pyrazosulfuron using this method.

### 4.3.3 MALDI-MSI of sulfonylurea herbicides 24 hour following foliar application

#### 4.3.3.1 MALDI-MSI of chlorsulfuron

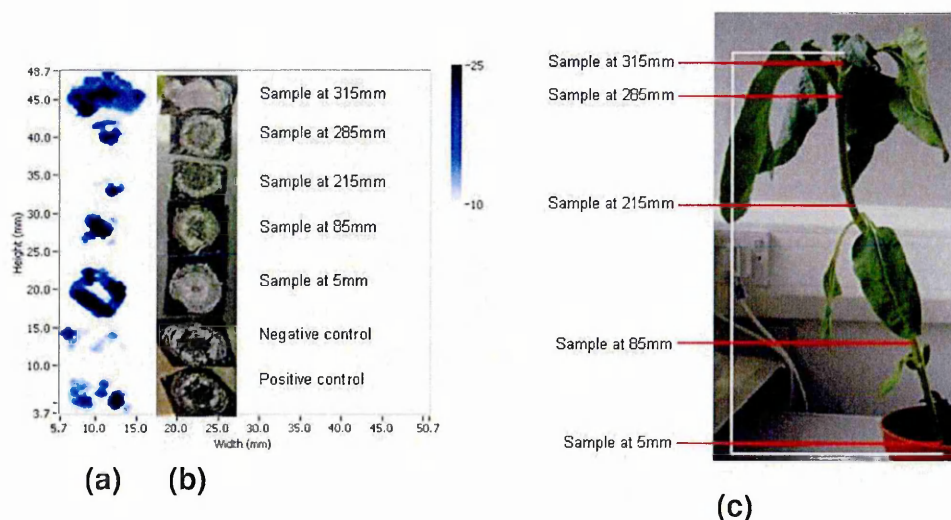


Fig. 13 Cross sections of a stem of a sunflower plant following uptake of chlorsulfuron via the leaves after a 24 hour foliar application experiment. (a) MALDI-MS image of chlorsulfuron fragment ion at  $m/z$  141.08 (image range  $m/z$  141.060-141.081 and normalised against  $\alpha$ -CHCA  $m/z$  172.04 peak). (b) Optical image of horizontal sections. (c) Optical image indicating region where horizontal sections were taken from in the 24 hour foliar application experiment.

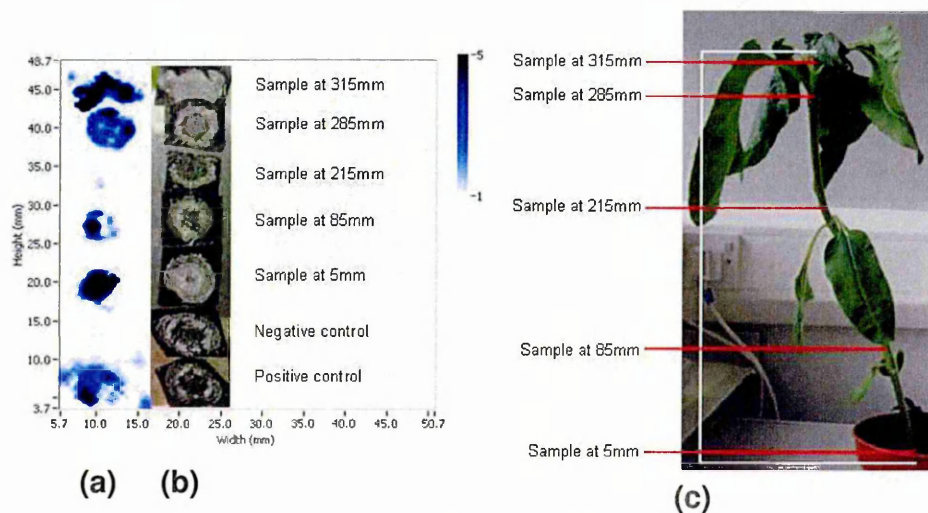


Fig. 14 Cross sections of a stem of a sunflower plant following uptake of chlorsulfuron via the leaves after a 24 hour foliar application experiment. (a) MALDI-MS image of

chlorsulfuron  $[M+H]^+$  ion at  $m/z$  358.04 (image range  $m/z$  357.995-358.051 and normalised against  $\alpha$ -CHCA  $m/z$  190.05 peak). (b) Optical image of horizontal sections. (c) Optical image indicating region where horizontal sections were taken from in the 24 hour foliar application experiment.

Fig. 13 (a) shows the MALDI-MS image of the distribution of the chlorsulfuron aminotrizine fragment ion at  $m/z$  141.08, 24 hours after foliar application.

These data indicate that chlorsulfuron has been absorbed and translocated throughout all of the stem tissue sections from the application point at 205 mm. The image generated from the peak at  $m/z$  141.08 shows that the aminotrizine fragment ion is present in the highest concentrations (indicated by the high signal) in the sections 315 mm and 5 mm along the plant stem i.e. the growing tip at the top of the plant. High signal is also observed in the positive control, confirming the ion originates from chlorsulfuron. Only slight interference is observed in the negative control, due to endogenous compounds present at  $m/z$  141.08.

Fig. 14 (a) shows the MALDI-MS image of the distribution of the chlorsulfuron protonated molecule at  $m/z$  358.04, 24 hours after foliar application. These data indicate that chlorsulfuron has been absorbed and translocated throughout all of the stem tissue sections from the application point at 205 mm, supporting the data seen in Fig. 13 of the chlorsulfuron fragment ion at  $m/z$  141.08. The image generated from the peak at  $m/z$  358.04 shows that the chlorsulfuron protonated molecule is present in the highest concentrations (indicated by the high signal) in the sections 315 mm and 5 mm along the plant stem i.e. the growing tip at the top of the plant. High signal is also observed in the positive control, confirming that the ion originates from chlorsulfuron. As no interference is observed in the

negative control there are no endogenous compounds present at this  $m/z$  ratio. As this image was acquired at a lower laser power of 28  $\mu\text{J}$  compared to 35  $\mu\text{J}$  (used to acquire the images for pyrazosulfuron and imazosulfuron) not all of the chlorsulfuron has fragmented, although a higher signal was observed for the aminotrizine fragment ion at  $m/z$  141.08 24 (Fig. 13) indicated by the scale on the right side of the MALDI-MS images.

#### **4.3.3.2 MALDI-MSI of chlorimuron-ethyl**

Fig. 15 (a) shows the MALDI-MS image of the distribution of the chlorimuron-ethyl aminopyrimidine fragment ion 24 hours after chlorimuron-ethyl foliar application.

These data indicate that chlorimuron-ethyl has been absorbed and translocated to stem tissue above the application point at 210 mm. The image generated from the peak at  $m/z$  160.03 shows that the aminopyrimidine structure is present in the sample at 295 mm and 275 mm from the root tip and the positive control with high intensity. Chlorimuron-ethyl can not be identified in any other of the stem sections at this  $m/z$ .

Fig. 16 (a) shows the MALDI-MS image of the distribution of the chlorimuron-ethyl protonated molecule, 24 hours after foliar application. These data indicate that chlorimuron-ethyl has been absorbed and translocated to stem tissue above the application point at 210 mm. The image generated from the peak at  $m/z$  415.05 shows that the aminopyrimidine structure is present in the sample at 295 mm, 275 mm and 5 mm from the root tip and the positive control with high intensity. Chlorimuron-ethyl can not be identified in any of the other of the stem sections at

this m/z. As this image was acquired at a lower laser power of 28  $\mu$ J compared to 35  $\mu$ J (used to acquire the images for pyrazosulfuron and imazosulfuron) not all of the chlorimuron-ethyl has fragmented, and a higher signal was observed for the chlorimuron protonated molecule at m/z 415.05 (Fig. 15) indicated by the scale on the right side of the MALDI-MS images. This higher signal observed with the chlorimuron-ethyl protonated molecule at m/z 415.05 has provided enough sensitivity to indicate the chlorimuron-ethyl has translocated towards the growing tips of the roots.

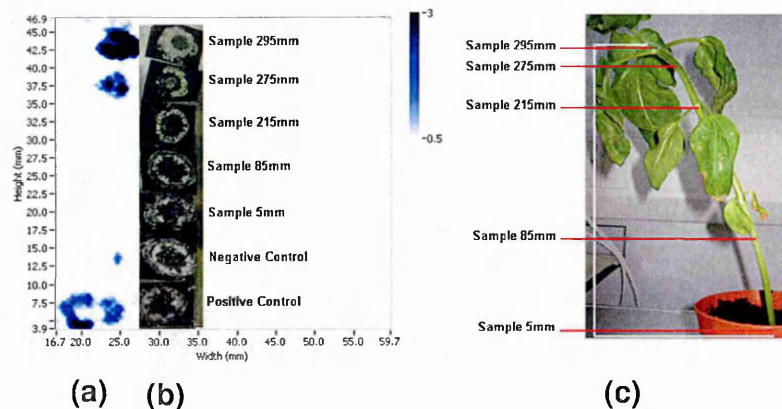


Fig. 15 Cross sections of a stem of a sunflower plant following uptake of chlorimuron-ethyl via the leaves after a 24 hour foliar application experiment. (a) MALDI-MS image of chlorimuron-ethyl fragment ion at  $m/z$  160.03 (image range  $m/z$  160.004-160.051 and normalised against  $\alpha$ -CHCA  $m/z$  172.04 peak). (b) Optical image of horizontal sections. (c) Optical image indicating region where horizontal sections were taken from in the 24 hour foliar application experiment.

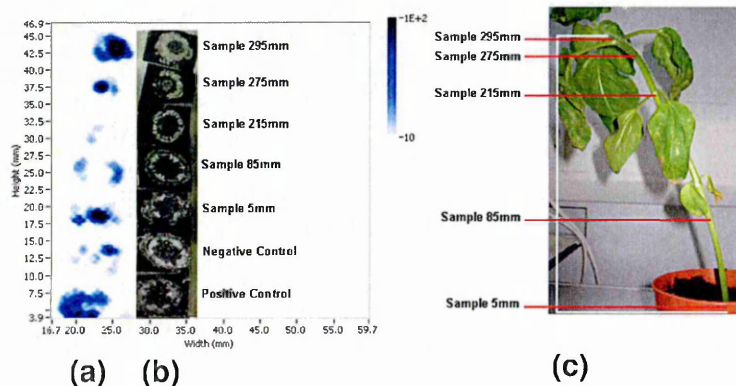


Fig. 16 Cross sections of a stem of a sunflower plant following uptake of chlorimuron-ethyl via the leaves after a 24 hour foliar application experiment. (a) MALDI-MS image of chlorimuron-ethyl  $[M+H]^+$  ion at  $m/z$  415.05 (image range  $m/z$  415.021-415.082 and normalised against  $\alpha$ -CHCA  $m/z$  190.05 peak). (b) Optical image of horizontal sections. (c) Optical image indicating region where horizontal sections were taken from in the 24 hour foliar application experiment.

#### 4.3.3.3 MALDI-MSI of imazosulfuron

Fig. 17 (a) shows the MALDI-MS image of the distribution of the imazosulfuron aminopyrimidine compound at  $m/z$  156.08, 24 hours after foliar application. These data indicate that imazosulfuron has been absorbed and translocated to stem tissue above the application point at 270 mm. The image generated from the peak at  $m/z$  156.08 shows that the aminopyrimidine structure is present in the sample at 405 mm, 385 mm and the positive control with high intensity and a low signal at 275 mm. Imazosulfuron can not be identified in any of the other of the stem sections at this  $m/z$ .

Fig. 18 (a) shows the MALDI-MS image of the distribution of the imazosulfuron aminopyrimidine compound at  $m/z$  182.06, 24 hours after foliar application. These data indicate that imazosulfuron has been absorbed and translocated to stem tissue above the application point at 270 mm. The image generated from the peak at  $m/z$  182.06 shows that the aminopyrimidine structure is present in the sample at 405 mm, 385 mm and the positive control with high intensity and a low signal at 275 mm. This confirms the image generated from imazosulfuron aminopyrimidine compound at  $m/z$  156.08, in Fig. 17. Imazosulfuron can not be identified in any other of the stem sections at this  $m/z$ . Although the signal for this ion is higher than the signal observed for imazosulfuron aminopyrimidine compound at  $m/z$  156.08 the interference from background noise is also more apparent due to the high laser power used in the acquisition of the image.

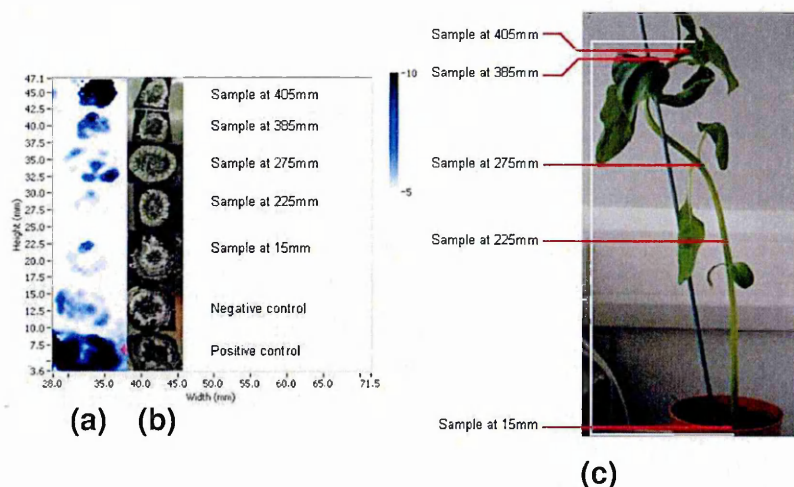


Fig. 17 Cross sections of a stem of a sunflower plant following uptake of imazosulfuron via the leaves after a 24 hour foliar application experiment. (a) MALDI-MS image of imazosulfuron fragment ion at  $m/z$  156.08 (image range  $m/z$  156.033-156.090 and normalised against  $\alpha$ -CHCA  $m/z$  172.04 peak). (b) Optical image of horizontal sections. (c) Optical image indicating region where horizontal sections were taken from in the 24 hour foliar application experiment.

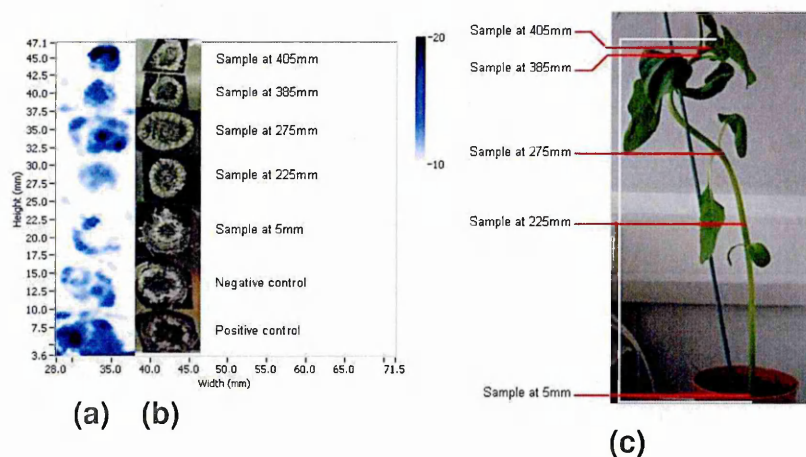
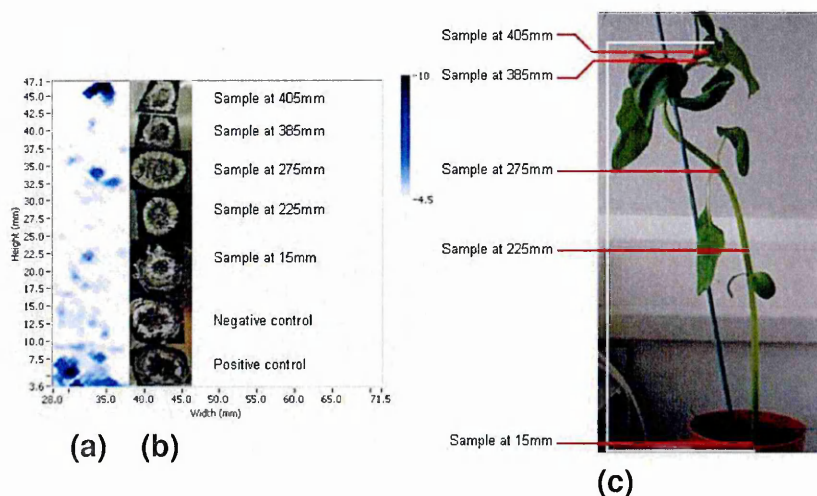


Fig. 18 Cross sections of a stem of a sunflower plant following uptake of imazosulfuron via the leaves after a 24 hour foliar application experiment. (a) MALDI-MS image of imazosulfuron fragment ion at  $m/z$  182.06 (image range  $m/z$  182.032-182.096 and normalised against  $\alpha$ -CHCA  $m/z$  172.04 peak). (b) Optical image of horizontal sections. (c) Optical image indicating region where horizontal sections were taken from in the 24 hour foliar application experiment.



**Fig. 19** Cross sections of a stem of a sunflower plant following uptake of imazosulfuron via the leaves after a 24 hour foliar application experiment. (a) MALDI-MS image of imazosulfuron  $[M+H]^+$  ion at  $m/z$  413.04 (image range  $m/z$  413.016-413.062 and normalised against  $\alpha$ -CHCA  $m/z$  172.04 peak). (b) Optical image of horizontal sections. (c) Optical image indicating region where horizontal sections were taken from in the 24 hour foliar application experiment.

Fig. 19 (a) shows the MALDI-MS image of the distribution of the imazosulfuron protonated molecule, 24 hours after foliar application. These data indicate that imazosulfuron has been absorbed and translocated to stem tissue above the application point at 270 mm. The image generated from the peak at  $m/z$  413.04 shows that the aminopyrimidine structure is present in the sample at 405 mm and the positive control with high intensity with weak signal observed in the section at 275 mm. Imazosulfuron can not be identified in any of the other of the stem sections at this  $m/z$ .

#### 4.3.3.4 MALDI-MSI of pyrazosulfuron

Fig. 20 (a) shows the MALDI-MS image of the distribution of the pyrazosulfuron aminopyrimidine compound at  $m/z$  156.08, 24 hours after foliar application.

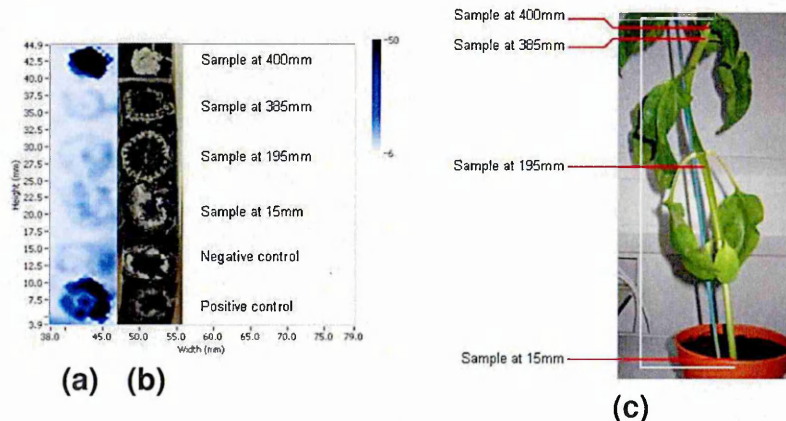


**Fig. 20** Cross sections of a stem of a sunflower plant following uptake of pyrazosulfuron via the leaves after a 24 hour foliar application experiment. (a) MALDI-MS image of pyrazosulfuron fragment ion at  $m/z$  156.08 (image range  $m/z$  156.033-156.096 and normalised against  $\alpha$ -CHCA  $m/z$  172.04 peak). (b) Optical image of horizontal sections. (c) Optical image indicating region where horizontal sections were taken from in the 24 hour foliar application experiment.

These data indicate that pyrazosulfuron has been absorbed and translocated to stem tissue above the application point at 230 mm. The image generated from the peak at  $m/z$  156.08 shows that the aminopyrimidine structure is present in the sample at 400 mm and the positive control with high intensity. Pyrazosulfuron can not be identified in any of the other of the stem sections at this  $m/z$ .

## 4.4 Discussion

The positive MALDI-MS spectra exhibited a number of peaks relating to the compounds in all instances. The limit of detection spot sample results show that

chlorimuron-ethyl has the lowest value at 0.523 µg/mL. Whilst the chlorsulfuron limit of detection was 10.34 µg/mL when observing the respective aminotrizine and aminopyrimidine fragment ions at m/z 141.08 2 and 160.03. These results did not correspond to the values observed for the limit of detection on spiked control section results, since a greater sensitivity was observed with chlorsulfuron.

The results from sulfonylurea herbicides, 24 hours following foliar application, show that in all cases it was possible to detect the R<sub>2</sub> species (Fig.1 and 2) resulting from in source fragmentation of the sulfonylurea compound urea bond. It was found that a higher laser energy was required to cause the fragmentation of pyrazosulfuron-ethyl and imazosulfuron than chlorsulfuron and chlorimuron-ethyl. Data could be obtained from the protonated molecules of chlorsulfuron, chlorimuron-ethyl and imazosulfuron, in some cases indicating better sensitivity and identifying compounds in tissue sections where the R<sub>2</sub> fragment ion had not been observed.

## 4.5 Conclusion

The limit of detection values from spot sample analysis of the sulfonylurea herbicides yielded varying results with the lowest value observed with chlorimuron-ethyl at 0.523 µg/mL. This did not concur with the findings from the spiked control sections method, where the best sensitivity was observed with chlorsulfuron where the distribution of the fragment ion was clearly observed with 1.25µg spiked onto the tissue. Images for the spiked imazosulfuron pyrazosulfuron-ethyl were unsuccessful due to background inference caused by the laser energy being too high during acquisition.

The extent of translocation of the four sulfonylurea compounds, 24 hours following foliar application, was successfully obtained using MALDI-MSI. The extent of translocation varies with chlorsulfuron showing the greatest extent with movement towards both growing tips of the leaves and the roots. The pyrazosulfuron fragment ion was only observed in one sample section, at the growing tips of the leaves.

## 4.6 References

1. Ren T-R., Yang H-W., Gao X., Yang X-L., Zhou J-J. and Cheng F-H. (2000) Design, synthesis and structure-activity relationships of novel ALS inhibitors *Pesticide Management Science*. **56**: 218-226.
2. Sarmah A. J. and Sabadie J. (2002) Hydrolysis of sulfonylurea herbicides in soils and aqueous solutions : a review. *Journal of Agricultural and Food Chemistry* **50**: 6253-6265.
3. Miller J. C. and Miller J. N. (1993) *Statistics for Analytical Chemistry*. Ellis Horwood Ltd. Great Britain.
4. Guibiao Y., Wei Z., Xin C., Canping P. and Shuren J. (2006) Determination and Quantitation of Ten Sulfonylurea Herbicides in Soil Samples Using Liquid Chromatography with Electrospray Ionization Mass Spectrometric Detection. *Chinese Journal of Analytical Chemistry* **34**: 1207-1212.
5. Perreau F., Bados P., Kerhoas L., Nélieu S. and Einhorn J. (2007) Trace analysis of sulfonylurea herbicides and their metabolites in water using a combination of off-line or on-line solid-phase extraction and liquid chromatography-tandem mass spectrometry. *Analytical and Bioanalytical Chemistry* **338**: 1265-1273.

## 5.1 Conclusions

MALDI-MSI has become an established technique for determining the distribution of xenobiotics and endogenous compounds in biological tissues. The data presented in this thesis show that MALDI-MSI can be used to determine the distribution of agrochemicals from plant leaf surfaces and within the plant transport systems following uptake via the roots (translocation in the roots) and absorption following foliar application (translocation in the phloem).

As conventional MALDI analysis can confirm the location of a xenobiotic within a tissue sample provided the laser is fired at the correct location. MALDI-MSI can provide data to show the localisation of the xenobiotic across the whole sample and show regions of high abundance compared to regions of lower abundance with the same sample of different samples within the same image.

The study was started by performing initial experiments for the analysis of azoxystrobin using an indirect MALDI-MSI method by blotting the compound onto a cellulose membrane. This led onto the direct tissue MALDI-MSI analysis of mesotrione from the upper epidermis layer following removal of the cuticle. These experiments were successful and further developed into a more sensitive method, with a higher degree of spatial resolution once a more suitable matrix was obtained and the problem of sample charging was prevented with gold sputter coating. Attempts to observe translocation of mesotrione following foliar uptake were hindered by signal suppression. Although the mesotrione was observed in tissue leading towards the petiole and stem of the plant, low signals for both the fragment ion ( $m/z$  291.03) and the deprotonated molecule ( $m/z$  338.03) were

observed. This low signal was attributed to fragmentation of mesotrione because the deprotonated molecule is unstable, resulting in the formation of a fragment ion at  $m/z$  291.03, along with the deprotonated molecule at  $m/z$  338.03 observed in the mass spectrum (section 2.3.1). This fragmentation reduces the sensitivity towards the overall amount of mesotrione present within the sample tissue. The effect of laser energy was assessed in section 2.3.7. These data show that the higher laser energy (2728) yielded a much higher signal for the fragment ion at  $m/z$  291.03. It is proposed that in the method to assess the translocation of mesotrione following foliar application (section 2.2.6) were experiments performed by direct tissue analysis, the laser energy required to produce adequate sensitivity was high, due to an endogenous compound absorbing the energy of the laser. This high laser energy also resulted in fragmentation. The laser energy could not be increased substantially to a value where all the mesotrione was fragmented due to background noise generated from compounds within the tissue having a detrimental effect on the images generated.

The effect of compounds present within the plant tissue on the ionisation efficiency of mesotrione was assessed in section 2.3.8. This clearly demonstrated the effect of the endogenous compounds suppressing mesotrione due to analyte/analyte suppression effects observed with a mixture of analytes.

The use of MALDI-MSI to determine the distribution of azoxystrobin in the root bundle tissue and stem tissue by direct analysis of sectioned tissue following uptake via the roots had been shown to be successful previously<sup>1</sup>. In this work the extent of translocation along a whole plant stem was studied using sunflower

plants since the sunflower species has a larger stem than soya bean and horizontal sections could be taken easily from the whole of the plant stem length. This process was made much quicker and simpler by incorporating an ice support, rapidly frozen around the stem section (section 3.2.2). Applying these methods in an attempt to observe translocation of mesotrione and fluazifop-p butyl following foliar application was unsuccessful. This was attributed to poor ionisation efficiencies of the compounds in comparison to endogenous compounds present within the plant.

Applying the methods developed here to a study of nicosulfuron (which is both phloem and xylem mobile), produced results from both uptake and translocation via the roots and translocation following foliar application at two time points (24 and 48 hours). Images were generated from fragment ions, a metal adduct and a product of phase I metabolism (hydrolysis).

The uptake of two agrochemicals (nicosulfuron and azoxystrobin) within the same plant was observed by MALDI-MSI, following co-application to the plant stem via the stem tissue.

Data obtained from the University of Münster for the IR-LDI of fluazifop-p butyl were promising although further investigation into the technique is required.

The findings of Chapter 3 lead onto the work presented in the Chapter 4 where the methods developed were applied to herbicides from the sulfonylurea group. Limit of detection experiments were performed using spot sample analysis followed by

spiked tissue controls to decide if a quick preliminary method can be applied to determine whether MALDI-MSI can be used to assess translocation.

The limit of detection values from spot sample analysis of the sulfonylurea herbicides yielded varying results, with the lowest value observed with chlorimuron-ethyl at 0.523 µg/mL. This did not agree with the findings from the spiked control sections method, where the best sensitivity was observed with chlorsulfuron with the distribution of the fragment ion being clearly observed with 1.25 µg spiked onto the tissue. Images for the spiked imazosulfuron and pyrazosulfuron-ethyl sections were unsuccessful due to background interference caused by the laser energy being too high during acquisition.

The translocation of the four sulfonylurea compounds 24 hours following foliar application was successfully studied by MALDI-MSI. The extent of translocation varied, with chlorsulfuron exhibiting the greatest movement. Translocation towards both growing tips of the leaves and the roots was observed. The spiked control section experiment had shown the best sensitivity towards chlorsulfuron which gave the best MALDI response of all the compounds and hence the observed extent of translocation may relate to sufficient compound being present in the sections, allowing for images within the sample section to be generated.

Although many experiments carried out during this study were successful, MALDI-MSI clearly has limitations when applied to the detection of agrochemical translocation. These relate to the ionisation efficiencies of the analyte compared to the endogenous compounds within the plant. These endogenous compounds

severely affected the method's sensitivity towards mesotrione and fluazifop-p butyl. Another factor which has affected the sensitivity of the technique has been extensive fragmentation of the agrochemicals and metal adduct formation reducing the intensity of individual ions.

The problem of compound dependent suppression may be overcome by derivatisation which is commonly used with electrospray ionisation<sup>2</sup>. Compounds such as tris(2,4,6-trimethoxyphenyl)phosphonium propylamine bromide (TMPP), *S*-pentafluorophenyl tris(2,4,6-trimethoxyphenyl)phosphonium acetate bromide (TMPP-AcPFP) and (4-hydrazino-4-oxobutyl) tris(2,4,6-trimethoxyphenyl) bromide (TMPP-PgG) have been successfully used to increase the mass of the analyte and move its position to an area of the mass spectrum with low noise and to assist the detection of non-ionisable compounds<sup>2,3</sup>. These derivatizing agents require solution based reactions with conditions possibly unsuitable for MALDI-MSI as they may cause delocalisation of the analyte on the sample surface. A study performed by Mugo *et al*<sup>4</sup> using 4-dimethylamino-6-(4-methoxy-1-naphthyl)-1,3,5-triazine-2-hydrazine (DMNTH) for the derivatisation of small carbonyl compounds with a rapid on plate and one pot reaction presents a reactive matrix which would be suitable for MALDI-MSI.

The method used to detect agrochemicals spiked onto control tissue gives a good indication as to whether MALDI-MSI can be used to detect its translocation and allows ions observed in MALDI-MS spectra to be identified in tissue. Since this method includes negative controls interferences from endogenous compounds at *m/z* values relating to the agrochemical can be assessed. A range of standard

dilutions can be employed to give an indication of the compound dependent suppression effect. With the advent of automated spotting instruments<sup>5</sup> known concentrations of compounds can be applied to defined regions of tissue creating an array of standards with addition of an internal standard or use of the matrix intensities as an internal standard. Recent development in laser technology with respect to MALDI-MSI has seen the utilisation of high repetition lasers up to 2 KHz<sup>6</sup> which decreases acquisition time and can cause complete ablation of all matrix and co-crystallised analyte present in the pixel area. These advances should lead to MALDI-MSI becoming a semi quantitative technique.

This results reported in this thesis demonstrate that MALDI-MSI is a feasible method to determine the translocation of agrochemicals in plants without the requirement of radiolabels.

## 5.2 References

1. Mullen A. K., Clench M. R., Crosland S. and Sharples K. R. (2005) Determination of Agrochemical Compounds in Soya Plants by Imaging Matrix Assisted Laser Desorption/Ionisation Mass Spectrometry. *Rapid Communications in Mass Spectrometry* **19**: 2507-2516.
2. Cartwright A. J., Jones P., Wolff J-C. and Evans E. J. (2005) Derivatisation of carboxylic acid groups in pharmaceuticals for enhanced detection using liquid chromatography with electrospray ionisation tandem mass spectrometry. *Rapid Communications in Mass Spectrometry* **19**: 1058-1062.

3. Barry S. J., Carr R. M., Lane S. J., Leavens W. J., Manning C. O., Monté S. and Waterhouse I. (2003) Use of S-pentafluorophenyl tris(2,4,6-trimethoxyphenyl)phosphonium acetate bromide (TMPP-AcPFP) and (4-hydrazino-4-oxobutyl) tris(2,4,6-trimethoxyphenyl) bromide for the derivatization of alcohols, aldehydes and ketones for the detection by liquid chromatography/electrospray mass spectrometry. *Rapid Communications in Mass Spectrometry* **17**: 484-497.

4. Mugo S. M. and Bottaro C. S. (2007) Rapid on-plate and one pot derivatization of carbonyl compounds for enhanced detection by reactive matrix LDI-TOF MS using the tailor-made reactive matrix 4-dimethylamino-6-(4-methoxy-1-naphthyl)-1,3,5-triazine-2-hydrazine (DMNTH) *Journal of Mass Spectrometry* **42**: 206-217.

5. Aerni H-R., Cornett D. S. and Caprioli R. M. (2006) Automated Acoustic Matrix Deposition for MALDI Sample Preparation *Analytical Chemistry* **78**: 827-834.

6. Moskovets E., Preisler J., Chen H. S., Rejtar T., Andreev V. and Karger B. L. (2006) High-Throughput Axial MALDI-TOF MS Using a 2-kHz Repetition Rate Laser. *Analytical Chemistry* **78**: 912-918.

## Appendix 1: Publications arising from this thesis

### Papers

- 2009 Anderson D. M. G., Carolan V. A., Crosland S., Sharples K. R. and Clench M. R. (2009) Examination of the Distribution of Nicosulfuron in sunflower Plants by MALDI-MSI. *Rapid Communications in Mass Spectrometry*, Article in press.

### Oral Presentations

- 2008 Anderson D. M. G., Carolan V. A., Crosland S., Sharples K. R. and Clench M. R. (2008) Imaging the Distribution of Agrochemicals in Plants by MALDI-MSI. BMSS (British Mass Spectrometry Society) York, UK.
- 2007 Anderson D. M. G., Carolan V. A., Crosland S., Sharples K. R. and Clench M. R. (2008) Imaging the Distribution of Agrochemicals in Plants by MALDI-MSI. Syngenta CASE Students Showcase, Jealotts Hill International Research Center, Bracknell, UK.

### Poster Presentations

- 2008 Anderson D. M. G., Carolan V. A., Crosland S., Sharples K. R. and Clench M. R. (2008) Examination of the Distribution of Nicosulfuron in Plants by MALDI-MSI. RSC (Royal Society of Chemistry), Hull, UK.
- Anderson D. M. G., Carolan V. A., Crosland S., Sharples K. R. and Clench M. R. (2008) Examination of the Distribution of Nicosulfuron in Sunflower Plants by MALDI-MSI. ASMS (American Society for Mass Spectrometry), Denver, USA.

- 2007 Anderson D. M. G., Carolan V. A., Crosland S., Sharples K. R. and Clench M. R. (2007) Imaging the Distribution of Agrochemicals in Plants. ASMS (American Society for Mass Spectrometry), Sanibel Conference on Mass Spectrometry: Imaging Mass Spectrometry, Sanibel Island, Florida, USA.
- Anderson D. M. G., Carolan V. A., Crosland S., Sharples K. R. and Clench M. R. (2007) Imaging the Distribution of Agrochemicals in Plants. RSC (Royal Society of Chemistry), Glasgow, UK.
- Anderson D. M. G., , Carolan V. A., Crosland S., Sharples K. R. and Clench M. R. (2007) Imaging the Distribution of Agrochemicals in Plants. BMSS (British Mass Spectrometry Society), Edinburgh, UK,
- 2006 Anderson D. M. G., , Carolan V. A., Crosland S., Sharples K. R. and Clench M. R. (2006) The Development of a Method for Imaging the Distribution of Agrochemicals in Plants. EMS (Environmental Mass Spectrometry), Chester, UK.
- Anderson D. M. G., , Carolan V. A., Crosland S., Sharples K. R. and Clench M. R. (2006) The Development of a Method for Imaging the Distribution of Agrochemicals in Plants. ASMS (American Society for Mass Spectrometry), Seattle, USA.
- Anderson D. M. G., , Carolan V. A., Crosland S., Sharples K. R. and Clench M. R. (2006) The Development of a Method for Imaging the Distribution of Agrochemicals in Plants. RSC (Royal Society of Chemistry), Cork, Ireland.
- Anderson D. M. G., , Carolan V. A., Crosland S., Sharples K. R. and Clench M. R. (2006) The Development of a Method for Imaging the Distribution of Agrochemicals in Plants. Syngenta CASE Students Showcase, Jealotts Hill International Research Center.

Anderson D. M. G., , Carolan V. A., Crosland S., Sharples K. R. and  
Clench M. R. (2006) The Development of a Method for Imaging the  
Distribution of Agrochemicals in Plants IMSC (International Mass  
Spectrometry Conference), Prague, Czech Republic.

**Appendix 2: Examination of the Distribution of  
Nicosulfuron in Sunflower Plants by MALDI-MSI**

# Examination of the distribution of nicosulfuron in sunflower plants by matrix-assisted laser desorption/ionisation mass spectrometry imaging

David M. G. Anderson<sup>1</sup>, Vikki A. Carolan<sup>1</sup>, Susan Crosland<sup>2</sup>, Kate R. Sharples<sup>2</sup> and Malcolm R. Clench<sup>1\*</sup>

<sup>1</sup>Biomedical Research Centre, Sheffield Hallam University, Howard Street, Sheffield S1 1WB, UK

<sup>2</sup>Syngenta, Jealotts Hill International Research Station, Jealotts Hill, Bracknell RG42 6EY, UK

Received 19 December 2008; Revised 2 February 2009; Accepted 4 February 2009

Matrix-assisted laser desorption/ionisation mass spectrometry imaging (MALDI-MSI) has been used to image the distribution of the pesticide nicosulfuron (2-[[[(4,6-dimethoxypyrimidin-2-yl)aminocarbonyl]aminosulfonyl]-*N,N*-dimethyl-3-pyridinecarboxamide) in plant tissue using direct tissue imaging following root and foliar uptake. Sunflower plants inoculated with nicosulfuron were horizontally sectioned at varying distances along the stem in order to assess the extent of translocation; uptake via the leaves following foliar application to the leaves and uptake via the roots from a hydroponics system were compared. An improved sample preparation methodology, encasing samples in ice, allowed sections from along the whole of the plant stem from the root bundle to the growing tip to be taken. Images of fragment ions and alkali metal adducts have been generated that show the distribution of the parent compound and a phase 1 metabolite in the plant. Positive and negative controls have been included in the images to confirm ion origin and prevent false-positive results which could originate from endogenous compounds present within the plant tissue. Copyright © 2009 John Wiley & Sons, Ltd.

Studying the uptake and translocation of agrochemicals in plants is important in developing new active ingredients for weed and pest management. Autoradiography is an established methodology for assessing the absorption and translocation of agrochemicals following both uptake via the roots and absorption following foliar application. It provides a very sensitive method with quantifiable results.<sup>1</sup> A major limitation of this method, however, is that the synthesis of radiolabelled compounds is required. This is expensive and can be time consuming, and the results do not give any differentiation between the distribution of metabolites and the parent compound since images generated show the distribution of all compounds that contain the radio isotope. In addition there is a wish to move away from the safety issues involved in handling radiolabelled materials. The overall aim of this research project is to develop an analytical technique for the detection of the distribution and absorption rates of agrochemicals into plants without the use of radiolabelled compounds.

Matrix-assisted laser desorption/ionisation mass spectrometry imaging (MALDI-MSI) applications have been increasing rapidly in the last few years. MALDI-MSI was first developed by the Caprioli group in 1997.<sup>2</sup> This technique has been used to image the distribution of a wide range of

compounds, including proteins, lipids, pharmaceuticals, metabolites and other small molecules.<sup>3,4</sup> The first demonstration of the use of MALDI to directly study pharmaceutical compounds in animal tissue was performed by Troendle *et al.*,<sup>5</sup> where the anti-cancer drug paclitaxel was detected in a rat liver incubated in a solution containing paclitaxel and also in a dosed xenograft. They also detected the antipsychotic drug spiperone from spiked sections of rat liver tissue. These results suggested that MALDI-MSI could provide a powerful investigative tool for pharmaceutical research and development.

The Caprioli group in collaboration with Schering-Plough<sup>6</sup> reported the distribution of an anti-tumour drug in dosed mouse tumour tissue and rat brains. By using selected reaction monitoring (SRM), spectral interference from matrix and endogenous metabolites which limits the sensitivity of MALDI time-of-flight (TOF) MS for drug analysis was avoided. Images were generated from the product ions showing the distribution of the anti-tumour drugs in both tumour and brain tissue. MALDI-MSI has now progressed to the stage when it offers a complementary technology to autoradiography for imaging the distribution of xenobiotic compounds. Additional functionality is obtained since separate images for the distribution of the parent compounds and its metabolites in whole body tissue sections may be generated.<sup>7</sup>

MALDI-MSI and profiling have been widely used in the study of plant material. In 1997 Stahl *et al.*<sup>8</sup> employed MALDI-MS and high-performance anion-exchange chroma-

\*Correspondence to: M. R. Clench, Biomedical Research Centre, Sheffield Hallam University, Howard Street, Sheffield S1 1W, UK.

E-mail: m.r.clench@shu.ac.uk

Contract/grant sponsor: BBSRC CASE Award from Syngenta.

graphy (HPAEC) to analyse two high molecular weight fructans from *Dahlia variabilis* L. and also carried out direct tissue analysis on the epidermal and paraenchymal tissue of onion bulbs (*Allium cepa* L.). *Allium cepa* L. contains various oligomeric fructans and more than 50 compounds were detected from both techniques with masses ranging from 2000 to 10 000.

In 2004 Sluszný and Yeung<sup>9</sup> reported the probing of the biotic-abiotic boundary of plants using laser desorption/ionisation mass spectrometry (LDI-MS), by using transition metal salts, metal powders and colloidal suspensions to create ionised species via attachment of metal ions. The published data demonstrated that LDI-MS could be used to analyse cuticle waxes made up of long-chain non-polar hydrocarbons and that these could be identified by direct tissue analysis with nearly identical mass spectra being obtained by direct analysis and extraction.

Wu *et al.*<sup>10</sup> profiled the alkaloid distribution in four commonly used Chinese medicinal herbs using direct tissue analysis MALDI-MS. The results demonstrated the feasibility of using MALDI-MS to provide rapid and reliable plant component profiles by direct analysis of plant tissue. This obviated the degradation of the compounds of interest caused by traditional sample preparation methods. They also used the technique to study *Strychnos nux-vomica* seeds, profiling regions of the endosperm and epidermis without the need for complex sample preparation; clear differences were observed between the endosperm and epidermis regions with several additional alkaloids being found to be present in the epidermis region.<sup>11</sup>

Ng *et al.*<sup>12</sup> have demonstrated the spatial profiling of phytochemicals and secondary metabolites by direct analysis of herbal plant tissue using MALDI-MS. The results clearly differentiate the relative abundance of metabolites in different tissue regions including the cortex, phloem, xylem, and pith.

Robinson *et al.*<sup>13</sup> have generated images of carbohydrates from wheat stems. Hexose sugars present in wheat stems were identified using MALDI-MS and liquid chromatography/electrospray ion trap mass spectrometry and the images showed the distribution of these sugars within stem sections from both the longitudinal axis and the horizontal axis. Burrell *et al.*<sup>14</sup> generated images of a range of metabolites in wheat grains in positive and negative ion mode using  $\alpha$ -cyano-4-hydroxycinnamic acid (CHCA) and 2-mercaptoacridine as MALDI matrices, respectively. The images show the distribution and variation in abundance of metabolites in specific regions of a wheat grain at a picomolar concentration.

In a previous study we reported preliminary investigations into the determination of agrochemicals in soybean plants by MALDI-MSI.<sup>15</sup> Nicosulfuron is a member of the sulfonamide herbicides group which have been extensively used in cereal-growing regions following their introduction in the early 1980s. Sulfonamide herbicides are potent inhibitors of the enzyme acetolactate synthase (ALS) which is involved in branched-chain amino acid biosynthesis in plants. It is a thiamine pyrophosphate (TPP)-dependent enzyme which results in the condensation of pyruvate,  $\alpha$ -ketoglutarate and carbon dioxide in isoleucine

biosynthesis or the condensation of pyruvate molecules to form acetolactate and carbon dioxide in leucine and valine biosynthesis. ALS inhibitors are regarded as the most active group of herbicidal compounds found to date and display very high herbicidal activity in soil and following foliar application.<sup>16</sup>

In the work reported here our aim was to further refine methods of sample preparation for the examination of the translocation of agrochemicals in plants and to apply these to a study of the distribution of sulfonamide herbicides.

## EXPERIMENTAL

### Uptake of nicosulfuron via the roots (hydroponics experiment)

Sunflower plants were germinated and grown in multi-purpose potting compost until they had reached a height of 145 mm. The plants were then removed from the soil and washed before being introduced into a conical flask containing 1/2 strength Hoglands N°2 Basel salt solution. The solutions were spiked with nicosulfuron to give a concentration of 20 ppm, and the plants were left for 24 h before a further addition of nicosulfuron was made to give a final concentration of 40 ppm. The plants were then left for another 24 h before being removed and prepared for cryostat sectioning along the horizontal axes at 10 mm, 30 mm, 50 mm and 140 mm from the root bundle region. Control sections were taken from an undosed plant to be used as positive and negative controls; the positive controls were spiked with 1  $\mu$ L of a 1 mg/mL solution of nicosulfuron in acetonitrile.

### Absorption of nicosulfuron via foliar application

Sunflower plants were germinated and grown in potting compost until they had reached a height of 135 mm for the 24 h experiment and 200 mm for the 48 h experiment. Fifty aliquots of 1  $\mu$ L of a 1.25 mg/mL solution of nicosulfuron in 50:50 acetonitrile/0.1% Tween were applied to the tissue either side of the midrib vein of a leaf. The plants were then left for 24 and 48 h at 21°C with a relative humidity of 55% before being removed and prepared for cryostat sectioning along the horizontal axes at varying distances from the root bundle region. Control sections were taken from an undosed plant to be used as positive and negative controls; the positive controls were spiked with 2  $\mu$ L of a 2.5 mg/mL solution of nicosulfuron in acetonitrile.

### Section preparation for MALDI-MSI analysis

Sections were coated in CHCA (10 mg/mL 1.0% trifluoroacetic acid (TFA) in acetone) by an air-spray technique. The compressed air gun (Iwata Media Inc., Portland, OR, USA) was passed over the sample 15 times ensuring that the sample tissue did not get saturated and that an even coverage was achieved. Sectioned samples were then mounted onto a MALDI target using conductive tape.

### MALDI-MSI analysis

Appropriate areas of the plant sections were imaged using a 'Q-star Pulsar I' quadrupole time-of-flight mass spectrometer (Applied Biosystems/MDS Sciex, Concord,



ntario, Canada) fitted with an 'oMALDI 2' orthogonal ALDI source. For root uptake experiments an Nd:YAG ser was used at a power of 3.2  $\mu\text{J}$  and a repetition rate of 000 Hz. For the foliar applied samples a nitrogen laser was employed at a laser power of 35  $\mu\text{J}$  and a laser repetition rate of 20 Hz. Mass spectra were acquired by scanning over the range  $m/z$  150 to 1000 for the root uptake experiments and  $m/z$  150 to 500 for foliar application experiments. Images were obtained with a spatial resolution of 200  $\mu\text{m} \times 200 \mu\text{m}$  with an acquisition time of 5 s per pixel.

### Processing of MALDI-MSI data

All images were created using Applied Biosystems oMALDI Server 5.0 tissue imaging software. All images presented are normalised against a matrix fragment ion to reduce effects caused by matrix inhomogeneity. In all cases other than the 4 h foliar absorption experiment the ion chosen to act as the 'internal standard' for normalisation was  $m/z$  172.04. For the 24 h foliar absorption experiment the signals generated from the cyclised pyridylsulfonamide ion at  $m/z$  185.00 were of very low intensity and dividing this intensity by the intensity of the ion at  $m/z$  172.04 resulted in images with a low number of counts that were difficult to manipulate. In this case, instead of the ions at  $m/z$  172.04, the ion chosen for normalisation was  $m/z$  147.06, the  $^{13}\text{C}$  isotope of the CHCA fragment ion at  $m/z$  146. Use of this ion increased the intensity of the pixels in the resulting image making presentation easier.

## RESULTS AND DISCUSSION

The positive ion MALDI mass spectrum of nicosulfuron (Fig. 1(a)) exhibits a number of ions which can potentially be used to generate images, i.e. the  $[\text{M}+\text{H}]^+$  ion at  $m/z$  411.10,

the  $\text{Na}^+$  adduct at  $m/z$  433.06, the  $\text{K}^+$  adduct at  $m/z$  449.04 and fragment ions at  $m/z$  182.06 and 156.08. The fragment ion at  $m/z$  156.08 is clearly observed not only in spot samples, but also in tissue samples; therefore, it potentially allows the generation of clear MALDI-MS images for the distribution of nicosulfuron following either uptake via the roots or absorption following foliar application. A spectrum of the CHCA matrix (Fig. 1(b)) included for comparison shows how intense the ions arising from nicosulfuron are in comparison with the matrix ions.

A previous study by Sabadie<sup>17</sup> described the formation of breakdown products of nicosulfuron via alcoholysis and hydrolysis. This would potentially lead to a species of aminopyrimidyl structure (Fig. 2) of RMM 155 and is a possible source of the ion at  $m/z$  156.08 in Figs. 1(a) and 3. In a previous study conducted by electrospray ionization/tandem mass spectrometry, Lily *et al.*<sup>18</sup> reported that the major product ion observed under collision-induced dissociation (CID) for nicosulfuron was  $m/z$  182.06. This suggests that the ion observed at  $m/z$  156.08 in the work reported here may arise as a result of hydrolysis of the urea bond rather than by 'in-source' fragmentation. To confirm that the ion at  $m/z$  156.08 was being produced as a result of in-source fragmentation and did not originate from a compound formed by alcoholysis by the matrix solution or hydrolysis by water or TFA, nicosulfuron was analysed using just acetonitrile as a solvent. The nicosulfuron was dissolved in acetonitrile (2.5 mg/mL) and a saturated solution of CHCA in acetonitrile was employed as the matrix. The spectrum obtained (Fig. 3) shows the ion from the aminopyrimidine species as the base peak along with the  $[\text{M}+\text{H}]^+$ ,  $[\text{M}+\text{Na}]^+$  and  $[\text{M}+\text{K}]^+$  ions of nicosulfuron. Another potential source of the ion at  $m/z$  156.08 in plants is histidine. This has the same molecular formula as 2-amino-4,6-dimethoxypyrimidine ( $\text{C}_6\text{H}_9\text{N}_3\text{O}_2$ ) and it is present as an

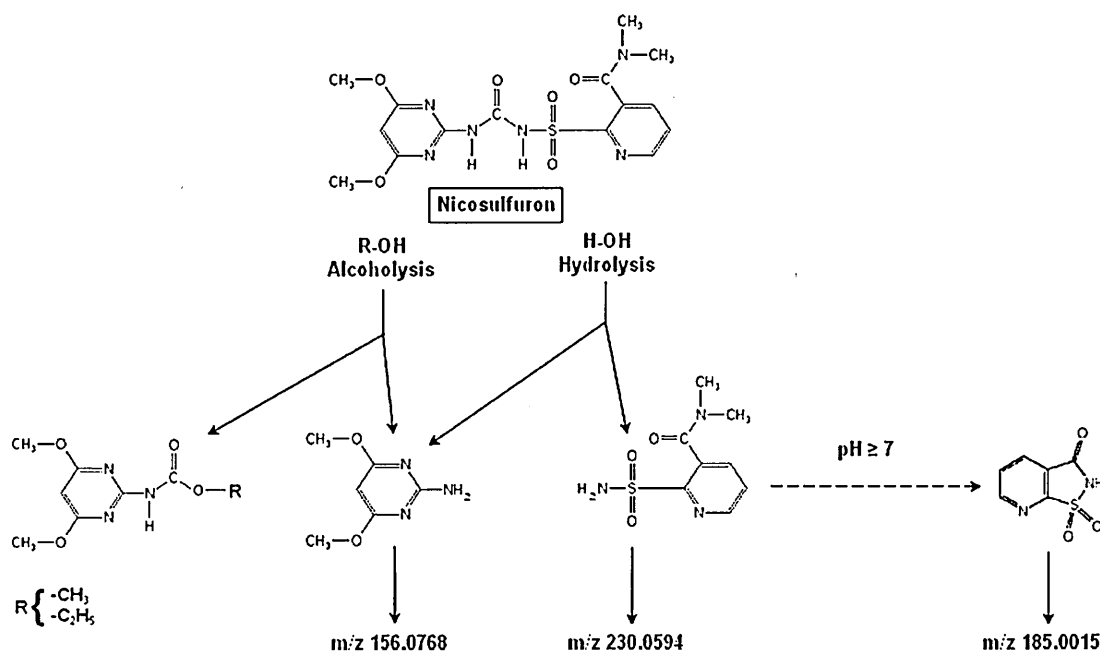


**Figure 2.** Alcoholysis and hydrolysis of nicosulfuron with resulting products. The  $m/z$  values given below are those for the protonated species used for detection.<sup>5</sup>

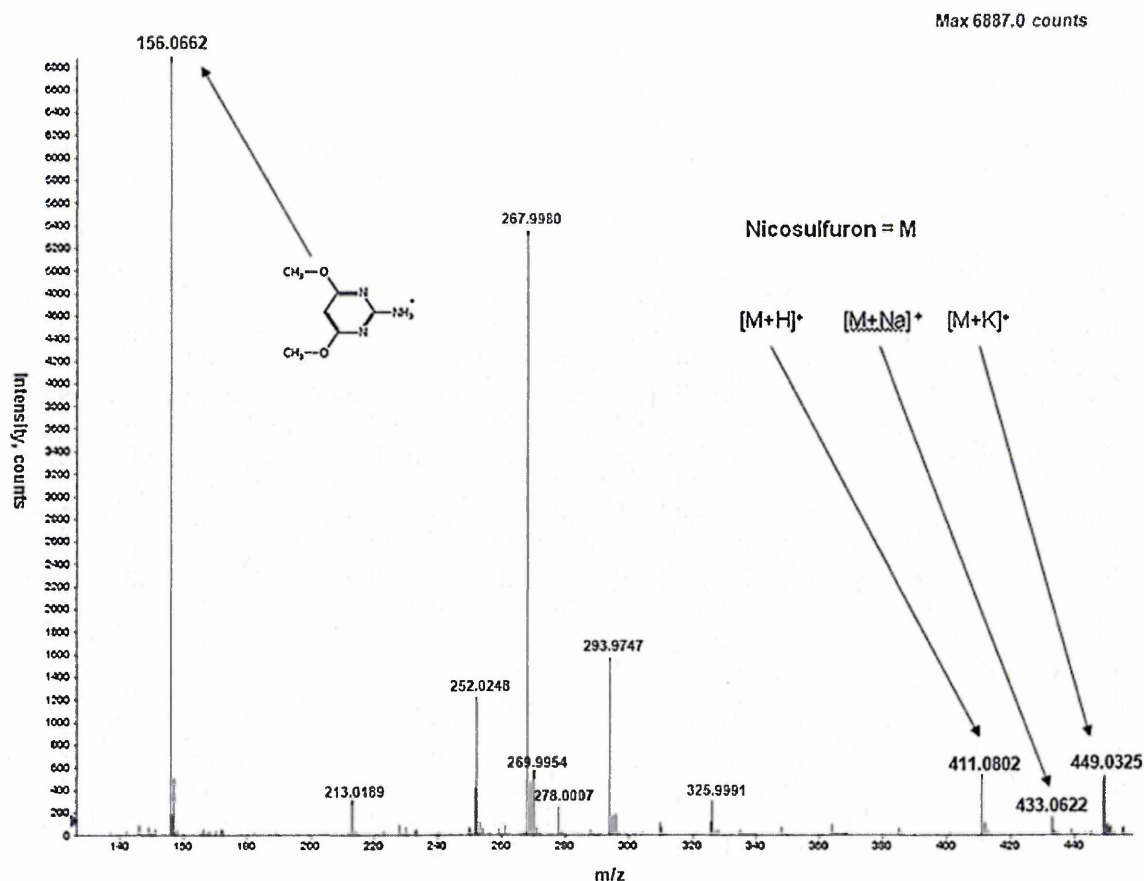


**Figure 3.** Positive ion MALDI mass spectrum of nicosulfuron (2.5 mg/mL in acetonitrile) obtained using CHCA (saturated solution in acetonitrile) as matrix. The  $[M+H]^+$  ion at  $m/z$  411.08, the sodium adduct at  $m/z$  433.06, the potassium adduct at  $m/z$  449.03 and the fragment ion  $m/z$  156.07 are readily observable.

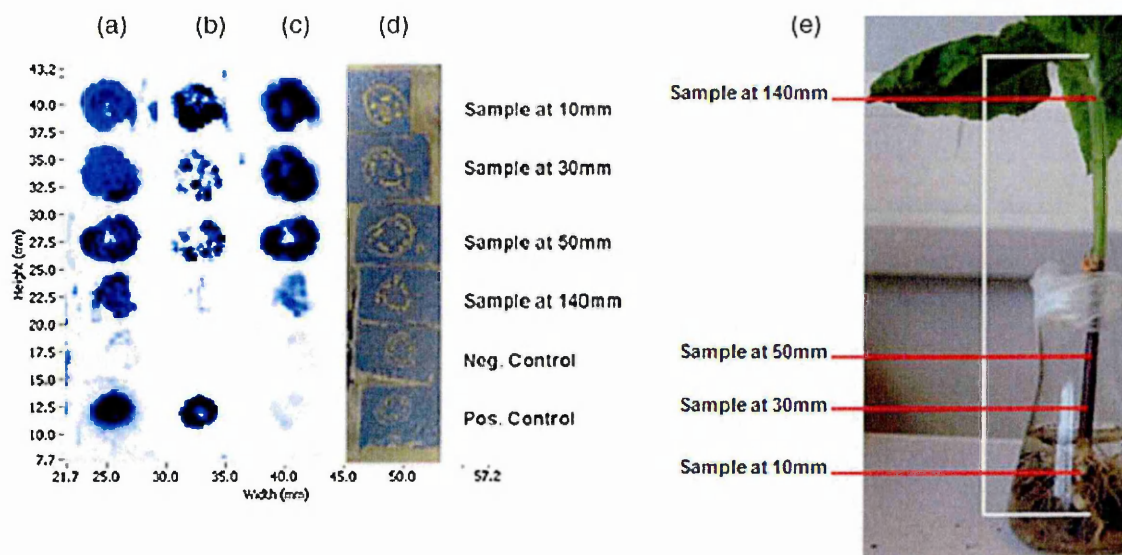


**Figure 4.** Cross-sections of a stem of a sunflower plant following uptake via the roots after a 48 h hydroponics experiment. (a) Image of nicosulfuron fragment ion at  $m/z$  156.08 (image range  $m/z$  156.068–156.081), normalised against CHCA  $m/z$  172.04 ion. (b) Image of cyclised pyridylsulfonamide at  $m/z$  185.00 (image range  $m/z$  185.001–185.009), normalised against CHCA  $m/z$  172.04 peak. (c) Image of nicosulfuron potassium adduct ion at  $m/z$  449.06 (image range  $m/z$  449.042–449.076), normalised against CHCA  $m/z$  172.04 ion. (d) Optical image indicating the orientation of the horizontal sections. (e) Optical image indicating region where horizontal sections were taken from hydroponics experiment. This figure is available in colour online at [www.interscience.wiley.com/journal/rcm](http://www.interscience.wiley.com/journal/rcm).

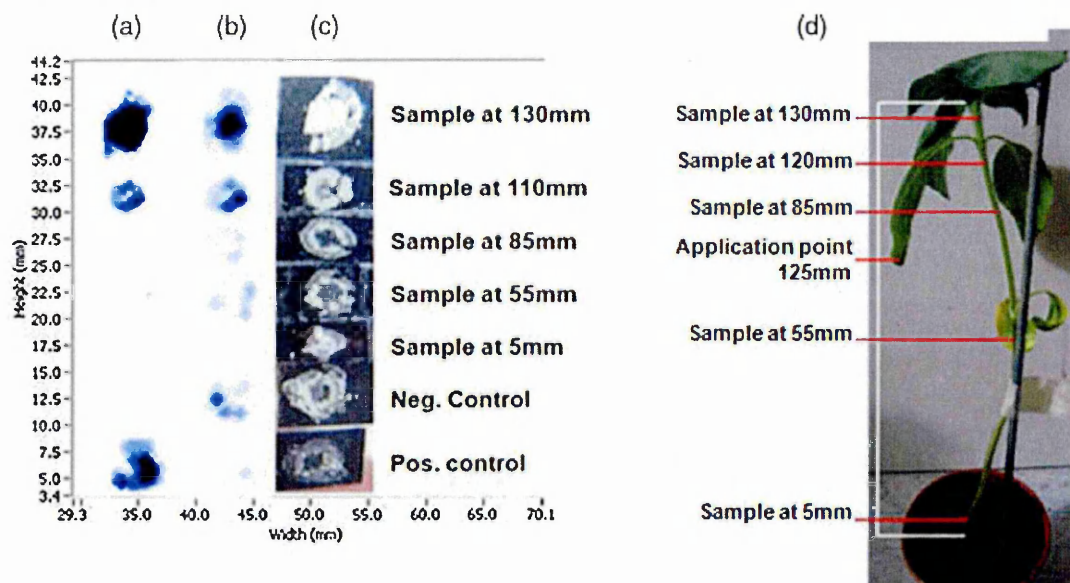


**Figure 5.** Cross-sections of a stem of a sunflower plant following uptake via the leaves after a 24 h foliar application experiment. (a) Image of nicosulfuron fragment ion at  $m/z$  156.08 (image range  $m/z$  156.068–156.081), and normalised against CHCA  $m/z$  172.04 ion. (b) Image of the cyclised pyridylsulfonamide metabolite ( $m/z$  185.00 (image range  $m/z$  185.001–185.009) and normalised against CHCA  $m/z$  147.06  $^{13}\text{C}$  fragment ion increasing the dynamic range for the intensity of the image). (c) Optical image indicating the orientation of the horizontal sections. (d) Optical image indicating region where horizontal sections were taken from hydroponics experiment. This figure is available in colour online at [www.interscience.wiley.com/journal/rcm](http://www.interscience.wiley.com/journal/rcm).

endogenous cellular metabolite as part of the histidine biosynthesis and methionine salvage pathway;<sup>19</sup> however, interference from histidine was not an issue in these experiments as indicated by the low signal in the negative control images.

Whilst the use of SRM techniques adds specificity to MALDI-MSI experiments, for the work reported here it was found that because the  $[\text{M}+\text{H}]^+$  ion of nicosulfuron was of relatively low abundance the sensitivity obtainable was not adequate to allow SRM experiments to be performed. Experiments were therefore conducted in full scan mode and a very narrow mass window (0.013  $m/z$  units) around the fragment ion of interest ( $m/z$  156.08) was used to ensure a degree of specificity. The inclusion of positive and negative controls also highlighted potential interferences.

Alcoholysis and hydrolysis of nicosulfuron causes breakdown of the urea part of the molecule and in fact results in the production of four products; a pyridylsulfonyl-carbamate (the exact molecular mass of which depends on the alcohol), the aminopyrimidine (RMM 155.08), as previously discussed, a pyridylsulfonamide (RMM 229.06) and a cyclised pyridylsulfonamide (RMM 184.00).<sup>17</sup>

Figure 4(a) shows the presence of the 2-amino-4,6-dimethoxypyrimidinyl fragment ion of nicosulfuron ( $m/z$  156.08) in all of the sample sections and the positive control. No interference from histidine can be seen in the negative control. These data show that after 48 h nicosulfuron has translocated around all the plant tissue following uptake via the roots. Confirmation of these findings is given in Fig. 4(b). This is generated from the potassium adduct at  $m/z$  449.06 using the matrix ion at  $m/z$  172.04 as an internal

standard. The presence of nicosulfuron is clearly indicated in the positive control and samples taken 10, 30 and 50 mm from the root tip, with a weak signal being also observed in the sample taken at 140 mm. Figure 4(c) shows the distribution of the phase 1 cyclised pyridylsulfonamide metabolite obtained using the protonated molecule at  $m/z$  185.00. This compound can be seen in the samples at 10, 30 and 50 mm clearly and some signal can be seen in the sample 140 mm from the root tip. The compound is not present in either the positive or the negative control, indicating that there is no endogenous compound at this mass and that production of this compound is a result of the hydrolysis of nicosulfuron in the plant transport system. Images generated from  $m/z$  230.06 (which corresponds to the  $[\text{M}+\text{H}]^+$  ion for the pyridylsulfonamide) (data not shown) exhibited a response from all of the samples including the negative control indicating the presence of an interfering endogenous compound.

Figure 5(a) shows the distribution of the 2-amino-4,6-dimethoxypyrimidinyl fragment ion of nicosulfuron ( $m/z$  156.08) in the stem sections of sunflower plants 24 h after foliar application of nicosulfuron. These data indicate that nicosulfuron has been absorbed and translocated to stem tissue above and slightly below the application point at 110 mm. The image generated from the ion at  $m/z$  156.08 shows that nicosulfuron is present in the sample at 130 mm and in the positive control with high intensity and also in the sample at 110 mm. Nicosulfuron was not detected in any of the other stem sections. Figure 5(b) shows the distribution of the phase 1 cyclised pyridylsulfonamide metabolite obtained using the protonated molecule at  $m/z$  185.00. As can be clearly seen the metabolite is present in the same areas as

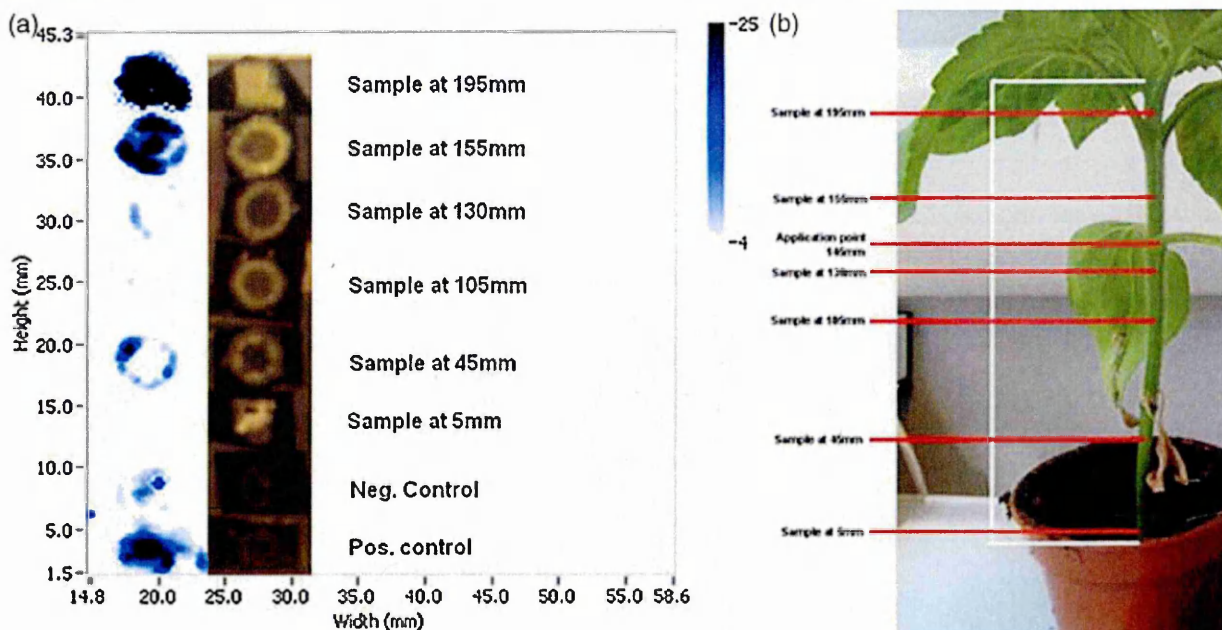


**Figure 6.** Cross-sections of a stem of a sunflower plant following uptake via the leaves after a 48 h foliar application experiment. (a) Image of nicosulfuron fragment ion at  $m/z$  156.08 (image range  $m/z$  156.068–156.08), and normalised against CHCA  $m/z$  172.04 ion. (b) Optical image indicating region where horizontal sections were taken from 48 h foliar applied experiment. This figure is available in colour online at [www.interscience.wiley.com/journal/rcm](http://www.interscience.wiley.com/journal/rcm).

nicosulfuron. An image for the potassium adduct in these samples could not be generated.

The image generated from  $m/z$  156.08 48 h after foliar application of nicosulfuron (Fig. 6) shows that nicosulfuron is present in the positive control and in the samples at 155 and 195 mm. This indicates that nicosulfuron has translocated towards the growing tips of the plant. A signal is also observed in the sample 45 mm along the stem due to translocation towards the growing tips of the roots.

## CONCLUSIONS

MALDI-MSI has been used to show the distribution of nicosulfuron following uptake via the roots, and absorption and translocation of nicosulfuron following foliar application after a 24 and 48 h time period. A structurally significant fragment ion was used to generate the images. The distribution of a nicosulfuron phase 1 metabolite which arises as a result of hydrolysis in the plant was also studied. Both the fragment ion and the metabolite are formed by breaking the urea bond in this substituted pyrimidinesulfonylurea herbicide.<sup>17</sup> Since this bond is common to all pyrimidinesulfonylurea herbicides it might be assumed that other herbicides from this group will behave in the same way. For the next stage of this project it is planned to repeat these experiments using other herbicides from the pyrimidinesulfonylurea group in order to develop a general method for imaging the distribution of substituted pyrimidinesulfonylurea herbicides in sunflowers using MALDI-MSI.

## Acknowledgements

The authors gratefully acknowledge funding for this project by a BBSRC CASE award from Syngenta.

## REFERENCES

- Rubio G, Sorgoná A, Lynch JP. *J. Exp. Bot.* 2004; **55**: 2269.
- Caprioli RM, Farmer TB, Gile J. *Anal. Chem.* 1997; **69**: 4751.
- Atkinson SJ, Prideaux B, Bunch J, Warburton KE, Clench MR. *Chim. Oggi* 2005; **23**: 5.
- Goodwin RJ, Pennington SJ, Pitt AR. *Proteomics* 2008; **18**: 3785.
- Troendle FJ, Reddick CD, Yost RA. *J. Am. Soc. Mass Spectrom.* 1999; **10**: 1315.
- Reyzer ML, Hsieh Y, Ng K, Korfmacher WA, Caprioli RM. *J. Mass Spectrom.* 2003; **38**: 1081.
- Stoekli M, Staab D, Schweitzer A. *Int. J. Mass Spectrom.* 2007; **260**: 195.
- Stahl B, Linos A, Karas M, Hillenkamp F, Steups M. *Anal. Biochem.* 1997; **246**: 195.
- Slusznyc C, Yeung ES. *J. Am. Soc. Mass Spectrom.* 2004; **16**: 107.
- Wu W, Liang Z, Zhao Z, Cai Z. *J. Mass Spectrom.* 2007; **42**: 58.
- Wu W, Gao C, Liang Z, Hu H, Zhao Z, Cai Z. *J. Pharm. Biomed. Anal.* 2007; **45**: 430.
- Ng K-M, Liang Z, Lu W, Tang H-W, Zhao Z, Che C-M, Cheng Y-C. *Anal. Chem.* 2007; **79**: 2745.
- Robinson S, Warburton K, Seymour M, Clench M, Thomas-Oates J. *New Phytol.* 2006; **173**: 438.
- Burrell MM, Earnshaw CJ, Clench MR. *J. Exp. Bot.* 2007; **58**: 757.
- Mullen AK, Clench MR, Crosland S, Sharples KR. *Rapid Commun. Mass Spectrom.* 2005; **19**: 2507.
- Ren T-R, Yang H-W, Gao X, Yang X-L, Zhou J-J, Cheng F-H. *Pest Manag. Sci.* 2000; **56**: 218.
- Sabadie J. *J. Agric. Food Chem.* 2002; **50**: 526.
- Lily T, Campbell DA, Bennett PK, Herion J. *Anal. Chem.* 1996; **68**: 3397.
- Li Y, Shrestha B, Vertes A. *Anal. Chem.* 2008; **80**: 407.